Functional Characterization of the SARS-CoV-2 Nucleocapsid Protein

DISSERTATION ZUR ERLANGUNG DES DOKTORGRADES DER NATURWISSENSCHAFTEN (DR. RER. NAT.)
DER FAKULTÄT FÜR BIOLOGIE UND VORKLINISCHE MEDIZIN DER UNIVERSITÄT REGENSBURG

vorgelegt von

Sabrina Babl

Aus Oberviechtach

Im Jahr 2024

Das Promotionsgesuch wurde eingereicht am:

12.06.2024

Die Arbeit wurde angeleitet von:

Prof. Dr. Gernot Längst

Unterschrift

(Babl Sabrina)

Content

Zusammenfassung

Ende 2019 verursachte SARS-CoV-2 eine weltweite Pandemie mit erheblichen Gesundheitsproblemen und hoher Morbidität und Mortalität. Das SARS-CoV-2 Nukleokapsid (N) Protein spielt eine entscheidende Rolle bei der viralen Replikation und Pathogenese. Diese Studie untersucht die Funktionen und Mechanismen des N Proteins, insbesondere seine Interaktionen mit Nukleinsäuren und Komponenten der Wirtszelloberfläche.

Eine Reihe biochemischer und biophysikalischer Experimente identifizierten funktionelle Domänen im N Protein, die für die RNA-Interaktion verantwortlich sind. Generell besteht das N Protein aus zwei strukturierten Domänen, der RNA-Bindungsdomäne (RBD) und der C-terminalen Domäne (CTD), die von intrinsisch ungeordneten Domänen (IDRs) flankiert und miteinander verbunden sind. Die RBD und IDR2 sind für die ssRNA Bindung entscheidend, während die RBD, IDR2 und CTD zusammen effizient dsRNA binden. Zudem besitzt das N Protein eine intrinsische RNA Chaperonaktivität, die für die RNA-Verpackung und -Faltung wesentlich ist. Die RBD, IDR2 und CTD sind für diese Funktion notwendig.

Eine vergleichende Analyse zwischen den Wuhan und Omikron BA.5 N Proteinvarianten zeigte signifikante Unterschiede in der RNA Chaperonaktivität. BA.5 N zeigte eine stark reduzierte Chaperonaktivität, die durch Proteinphosphorylierung wiederhergestellt werden konnte. Phosphorylierung verringert außerdem die RNA-Bindungsaffinität und erleichtert dadurch die RNA-Freisetzung ins Zytoplasma, was für die virale Replikation notwendig ist. Diese Ergebnisse deuten auf unterschiedliche Regulationsmechanismen zwischen den Varianten hin und betonen die Rolle der Phosphorylierung bei der RNA-Verpackung und -Freisetzung.

In der Studie wurde zudem ein neuartiger Mechanismus des N Proteins entdeckt, der eine Flüssig-Flüssig-Phasentrennung mit Heparin und Heparansulfat auf der Wirtszelloberfläche während der Infektion umfasst. Dies deutet auf eine Umgehung der Wirtsabwehr hin, indem Heparansulfat und Heparin abgeschirmt werden. Darüber hinaus löst das N Protein auf der Zelloberfläche die Freisetzung der proinflammatorischen Zytokine TNFα and IL-8 aus, was zu dem in COVID-19 Fällen beobachteten Zytokinsturm beitragen könnte.

Zusammengefasst bietet diese Studie ein detailliertes Verständnis des SARS-CoV-2 N Proteins, seiner Funktionen und potenziellen immunmodulatorischen Mechanismen. Sie schließt Wissenslücken über die grundlegenden Prozesse der SARS-CoV-2 Infektion und schafft dadurch eine Grundlage für zukünftige Forschungsarbeiten, die das N Protein als therapeutische Strategie untersuchen.

Abstract

In late 2019, SARS-CoV-2 caused a global pandemic with severe health issues, leading to widespread morbidity and mortality. The SARS-CoV-2 Nucleocapsid (N) protein is a multifunctional protein and crucial for viral replication and pathogenesis. This study comprehensively explored the intricate functions and mechanisms of the N protein, focusing on its interactions with nucleic acids and host cell surface components.

Through a series of biochemical and biophysical assays, distinct functional domains within the N protein responsible for its interaction with RNA, were identified. Generally, the N protein comprises two structured domains, the RNA-binding domain (RBD) and the C-terminal domain (CTD), which are flanked and interconnected by three intrinsically disordered regions (IDRs). The RBD in combination with the IDR2 were found to be essential for ssRNA binding, while the combined action of RBD, IDR2, and CTD facilitated efficient dsRNA binding. The N protein was discovered to harbor an intrinsic RNA chaperone activity. This activity is crucial for RNA packaging as well as for the efficient and accurate folding of the viral RNA genome. The experiments revealed the RBD, IDR2, and CTD to be essential for this function.

Comparative analysis between the Wuhan and Omicron BA.5 N protein variants revealed significant differences in RNA chaperone activity. The BA.5 N exhibited reduced chaperone activity, which can be restored by protein phosphorylation. Additionally, phosphorylation decreases RNA binding affinity, necessary for RNA release into the host cytoplasm to facilitate viral replication. These findings suggest distinct regulatory mechanisms between the variants and highlight the crucial role of phosphorylation in RNA packaging and release.

This study also uncovered a novel mechanism of the N protein involving extracellular liquid-liquid phase separation with heparin and heparan sulfate on the host cell surface during viral infection, suggesting another host evasion mechanism by shielding heparan sulfate, which is essential for antiviral immune response, and heparin, which is necessary for anti-coagulation during infection. Additionally, this study found that the cell surface bound N protein triggers the release of proinflammatory cytokines TNFα and IL-8, potentially contributing to the cytokine storm observed in COVID-19 cases.

In conclusion, this study provided a detailed understanding of the SARS-CoV-2 N protein regarding its intrinsic functions and potential immune modulatory mechanisms. It fills key knowledge gaps in the basic mechanisms of SARS-CoV-2 infection and established a foundation for future research aimed at targeting N as a therapeutic strategy.

1. Introduction

1.1. Viruses in general

“Viruses should be considered as viruses because viruses are viruses”. This statement made by Andre Lwoff in 1957, underscores the ongoing discourse within the scientific community aimed at precisely defining essential attributes of viral entities. Viruses share several fundamental characteristics that form the basis of contemporary viral classification. They are small entities, reliant on host cells for replication, and possess genetic material in the form of either DNA or RNA (Louten, 2016).

Virions exhibit significant variations in size, shape, molecular composition, structural organization, and complexity. In a very general and basic approach, they are broadly categorized into two groups based on their molecular composition: non-enveloped viruses and enveloped viruses, distinguished by the presence or absence of an outer lipid layer. Non-enveloped viruses feature a basic structure consisting solely of a protein shell, known as a capsid, containing the viral nucleic acid. Enveloped viruses, on the other hand, have their capsid and internal structures enclosed within a lipid bilayer, or envelope, with embedded proteins. Some enveloped virions display a multi-layered structure composed of organized lipid, protein, and nucleoprotein layers (Mateu, 2013).

Taking the variety of present viral genomes into account, the impressive work of David Baltimore in 1971 yielded a groundbreaking classification framework, now recognized as the "Baltimore classification", which categorizes viruses into six distinct classes based on their modes of genome transmission and gene expression patterns (Koonin et al., 2021). The classes include Class I: double-stranded DNA (dsDNA) viruses, Class II: single-stranded DNA (ssDNA) viruses, Class III: double-stranded RNA (dsRNA) viruses, Class IV: positive-sense (+) single-stranded RNA (ssRNA) viruses, Class V: negative-sense (-) ssRNA viruses, and Class VI: reverse-transcribing (RT) RNA viruses, encompassing those which encapsulate a (+) ssRNA genome and undergo replication via a DNA intermediate (Baltimore, 1971). Subsequently, a seventh class was incorporated following the characterization of hepadnaviruses, which harbor a dsDNA genome subject to replication through an RNA intermediate (Koonin et al., 2021).

Despite the extensive diversity observed within biological systems, particularly the preference of DNA as the primary hereditary molecule, the emergence and evolution of viruses bearing an RNA genome underscore a remarkable niche within this landscape. RNA viruses constitute a substantial fraction of viral diversity, characterized by distinctive genomic architectures and

replication mechanisms. Their prevalence and unique features make RNA viruses a focal point of interest in virology and molecular biology research (Baltimore, 1980).

The presence of RNA genomes in viruses not only provides flexibility in terms of genome size and structure but also allows viruses to generate genetic diversity, adapt quickly to new hosts, evade host immune responses and develop resistance to antiviral drugs as it has a heavily increased mutation rate compared to DNA genomes (Wolf et al., 2018). This increased mutation rate in RNA genomes is primarily due to the error-prone nature of RNA-dependent RNA polymerases (RdRp) and their lack of proof-reading mechanisms as well as the single-stranded nature of RNA, which contribute mainly to its flexibility and adaptation capabilities (Belshaw et al., 2007; Duffy, 2018; Kautz & Forrester, 2018).

As previously delineated, RNA viruses are categorically differentiated according to the nature of their RNA genome and the manner in which replication occurs. Specifically, these classifications encompass negative-sense ssRNA viruses (e.g. *Bornaviridae, Filoviridae, Pneumoviridae*), dsRNA viruses (e.g. *Birnaviridae, Reoviridae*), and positive-sense ssRNA viruses (e.g. *Coronaviridae*, *Flaviviridae, Picornaviridae*) with the special case of ssRNA viruses replicating through an DNA intermediate (e.g. *Retroviridae*) (Payne, 2017). The forthcoming chapter will center its discourse primarily on the family of *Coronaviridae*, elaborating upon their characteristics and mechanisms in greater depth.

1.2. Coronaviruses

Coronaviruses (CoVs), part of the *Coronaviridae* family within the *Nidovirales* order, are viruses with large RNA genomes ranging from 25 to 32 kilobases (kb). These enveloped, ssRNA viruses have caused various respiratory outbreaks such as severe-acute respiratory syndrome (SARS) and middle east respiratory syndrome (MERS). They derive their name from the distinctive spike proteins on their surface forming a crown-like shape. There are four genera of coronaviruses, each with different host infectivity: alpha (α) and beta (β) coronaviruses affect mammals, gamma (γ) coronaviruses infect avian species, and delta (δ) coronaviruses can infect both mammals and avian species. The β-CoV genus is further divided into four sub-genera/lineages: A, B, C, and D, and includes the largest known RNA viruses with genome sizes of approximately 27 – 30 kb (Weiss & Navas-Martin, 2005).

Since the mid-1960s, seven human coronaviruses (hCoVs) have been discovered (Figure 1). Among these, hCoV-OC43 and hCoV-HKU1 are classified as β-CoVs within lineage A, SARS-

CoV, and SARS-CoV-2 within lineage B and MERS-CoV within lineage C, while hCoV-229E and hCoV-NL63 belong to the α-CoVs group. These coronaviruses typically manifest as the common cold or mild upper respiratory tract infections. Conversely, β-CoVs from lineages B and C, are more pathogenic, causing severe respiratory illnesses that can lead to epidemics (Rabaan et al., 2023; Rajpal et al., 2022).

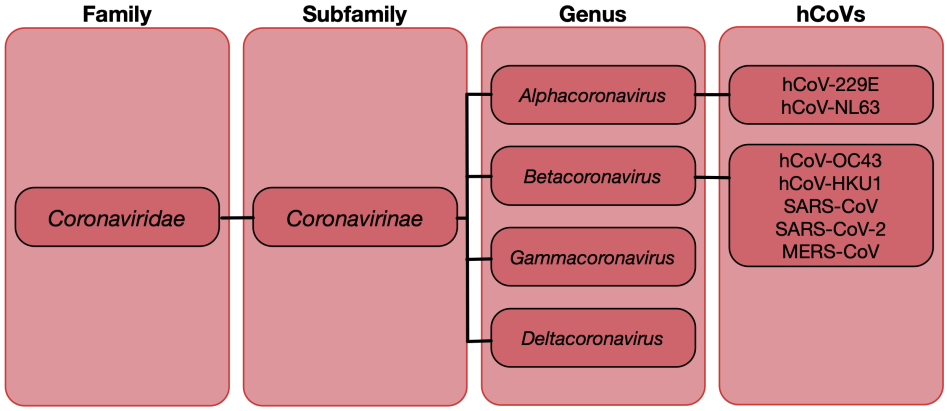

Figure 1: Classification of human coronaviruses

The taxonomic classification of *Coronaviridae* encompasses the subfamily *Coronavirinae*, which includes four genera: alpha-, beta-, gamma-, and deltacoronavirus. Among the alpha- and betacoronaviruses, seven distinct human coronaviruses have been identified to date. Specifically, hCoV-229E and hCoV-NL63 are classified within the alphacoronavirus genus, while hCoV-OC43, hCoV-HKU1, SARS-CoV, SARS-CoV-2, and MERS-CoV fall under the betacoronaviruses genus.

Coronaviruses initiate their infection by attaching to specific cellular receptors through the spike protein, a process that triggers a conformational change in the spike protein and facilitates fusion between the viral envelope and the host cell membrane. This fusion allows the release of the viral nucleocapsid, containing the viral RNA, into the host cell's cytoplasm (Weiss & Navas-Martin, 2005).

Once inside the cell, the viral genome is translated into two large polyproteins, pp1a and pp1ab, by the host cell machinery. The translation of pp1ab involves a ribosomal frameshift mechanism, occurring at a frequency of approximately 25 to 30% (Brian & Baric, 2005). These polyproteins are then processed by viral proteases, including papain-like proteases (PLpro or PLP) and a picornavirus 3C-like protease (3CLpro), into mature replicase proteins (Ziebuhr, 2005). The replicase proteins, along with other viral and host factors, initiate the replication of the viral genome. This process involves the synthesis of negative-strand RNA templates, which serve as templates for both full-length genomic RNA (gRNA) and subgenomic mRNAs (sgRNA). These sgRNAs, along with the full-length gRNA, contain a common leader sequence derived from the 5′ end of the genome (Di et al., 2018; La Monica et al., 1992). The mechanism behind the synthesis of these RNAs involves a unique discontinuous transcription mechanism,

where transcription-regulating sequences present in the gRNA regulate sgRNA synthesis (La Monica et al., 1992).

Subsequently, viral structural RNAs are synthesized from individual sgRNAs. After translation, viral proteins, including the nucleocapsid (N), membrane (M), envelope (E), and spike (S) proteins, are assembled at the Golgi intracellular membranes. The M and E proteins, along with other viral and cellular factors, facilitate viral budding, primarily occurring at the endoplasmic reticulum Golgi intermediate compartment (ERGIC). During assembly, the S protein interacts with the transmembrane segment of the M protein (Klumperman et al., 1994). N proteins complex with the viral RNA, forming helical structures and interact with the M protein, leading to budding into vesicles. Finally, the mature virus particles are transported to the cell surface, where they are released from the host cell, ready to infect neighboring cells and spread the infection further. This complex process ensures the successful replication and spread of the coronavirus within the host organism (Weiss & Navas-Martin, 2005).

1.3. SARS-CoV-2

The emergence and rapid global spread of the severe acute respiratory syndrome coronavirus 2 (SARS-CoV-2), the virus causing coronavirus disease 2019 (COVID-19), has led to a profound impact on human health, society, and the global economy. The virus was first identified in Wuhan, China, in late 2019 and quickly spread internationally causing millions of deaths and substantial morbidity (Hu et al., 2021).

All highly pathogenic human coronaviruses have had a zoonotic origin so far (Guan et al., 2003). Therefore, it is also proposed for SARS-CoV-2, although clarity on this matter is still lacking.

Bats are known reservoirs of SARS-like viruses. However, due to the significant evolutionary differences between SARS-CoV-2 and its closest animal relatives, direct transmission from bats to humans is unlikely. Instead, it is more plausible that the spillover event occurred in settings where densely populated areas interact with live animals susceptible to SARS-CoV-2 infection. These animals are often traded and sold for consumption in markets in Wuhan, which have been identified as key locations for SARS-CoV-2 transmission (Pagani et al., 2023; Pekar et al., 2022).

The evolution of SARS-CoV-2 has been characterized by the emergence of numerous variants driven by genetic mutation, recombination, and adaptation (Qin et al., 2022). This rapid

evolution has resulted in the identification of several variants, such as Alpha, Beta, Gamma, Delta, and Omicron besides the wild-type (Wuhan) strain (Kumar & Reji, 2023; Malden et al., 2021; F. Zhao et al., 2021). Concerns have arisen regarding the impact of these variants on vaccine efficacy and the immune response (Reeves et al., 2022). Additionally, the infectivity and lethality of these variants have varied, with some exhibiting higher infectivity than the original SARS-CoV-2 strain (Y. Lu et al., 2021). The ongoing mutation and evolution of SARS-CoV-2 have resulted in the circulation of multiple variants, with evidence of coinfection by different SARS-CoV-2 variants (Y. Li et al., 2021). Similar to other coronaviruses, the transmission of SARS-CoV-2 predominantly transpires through infected respiratory droplets, facilitated by direct, indirect, or close contact with infected individuals (Muralidar et al., 2020).

1.3.1. SARS-CoV-2 genome organization

SARS-CoV-2 is a positive-sense ssRNA virus that belongs to the family of betacoronaviruses with a virion diameter of 50-200 nm and a genome size of approximately 30 kb which is encoding about 29 proteins. Its genome exhibits a 79% nucleotide similarity to SARS-CoV and 50% to MERS-CoV, respectively (Calder et al., 2022; R. Lu et al., 2020). On its 5′ end, non-structural and accessory proteins are encoded, building up the basis of the viral particle (Figure 2), whereas the 3′ end of the genome harbors the coding sequences for the four structural proteins, namely the spike (S), membrane (M) and envelope (E) and nucleocapsid (N) protein (C. Wu et al., 2022; W. Wu et al., 2023).

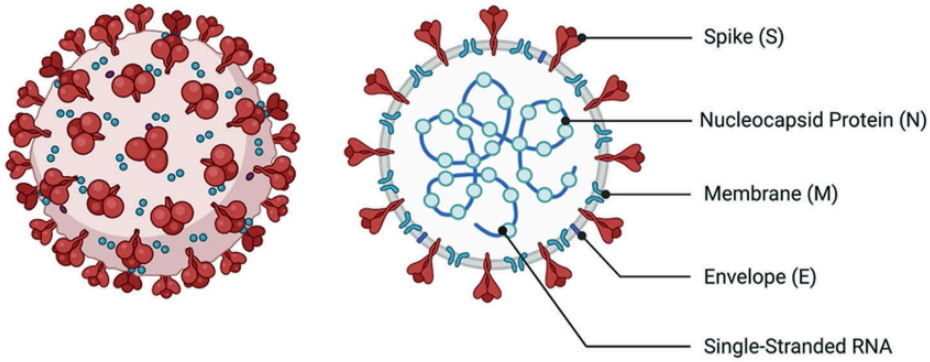

Figure 2: Schematic representation of the SARS-CoV-2 virion

SARS-CoV-2 consists of four essential structural proteins including spike (S), nucleocapsid (N), membrane (M), and envelope (E). Together with the ssRNA genome, these elements enable viral replication, virion assembly and spread of infection. Picture taken from Jamison et al., 2022

Since its discovery, the SARS-CoV-2 genome has demonstrated a significant genetic diversity, with over 7,123 unique single nucleotide mutations or modifications identified among 12,754 complete genome sequences obtained by September 2020. This accounts for approximately 29%

of the genome positions across more than 40,000 SARS-CoV-2 genomes globally (Fang et al., 2021). The host RNA editing machinery, including ADARs (Adenosine deaminases acting on RNA) targeting dsRNA to catalyze adenosine-to-inosine deamination and APOBECs (apolipoprotein B mRNA editing enzyme catalytic polypeptide) deaminating cytosine into uracil on ssRNA or ssDNA, may contribute to the observed mutations and modifications in the SARS-CoV-2 genome during virus infections (Gabriella, 2020).

The genome, represented in Figure 3, comprises 12 functional ORFs, with ORF1a and ORF1b collectively accounting for approximately 70% of the viral genome. These ORFs encode 16 Nsps, while the remaining 30% of the genome encodes the structural proteins (S, E, M, N) and six to eleven accessory proteins (ORF3a, b, c, 6, 7a, 7b, 8, 9b, 9c, 10) (Brant et al., 2021; Redondo et al., 2021). All 16 Nsps involved in viral transcription, replication, and immune evasion are cleavage products of two polyproteins, pp1a and pp1ab, which are derived from overlapping ORF1a and ORF1b, whereby translation of ORF1b is mediated by a -1 ribosomal frameshift (Kelly et al., 2021). The cleavage of these polyproteins by two viral proteases (Nsp3 and Nsp5) results in the production of the 16 Nsps. The structural and accessory proteins are translated from synthesized sgRNAs, which contain a 5'-TLS (transcription leader sequence) (Brant et al., 2021).

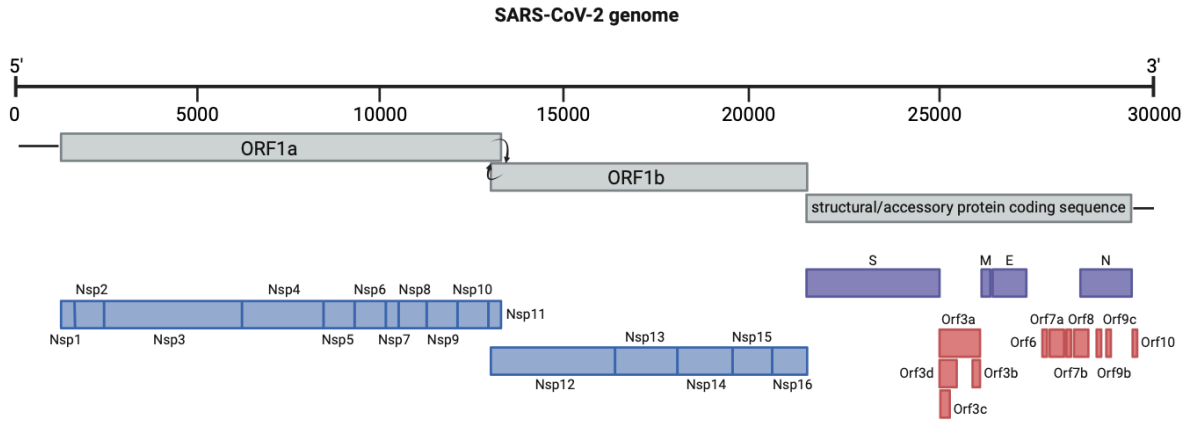

Figure 3: Organization of the SARS-CoV-2 genome

The SARS-CoV-2 genome comprises approximately 30,000 nt with 12 ORFs. ORF1a and ORF1b encode the viral Nsps (Nsp1-16), marked in blue, with both ORFs overlapping and ORF1b translation being mediated by a -1 ribosomal frameshift (indicated with arrows). The remaining 3′ part of the viral genome encodes the structural (S, M, E, N), represented in violet, and accessory proteins (Orf3a-Orf10), marked in red. Picture modified from Redondo et al., 2021

Similar to other RNA viruses, the folding of the SARS-CoV-2 genome into higher-order structures is crucial for its virulence and regulatory functions. The genome of SARS-CoV-2 contains well-defined RNA structural elements distributed across its entire length. While notably high levels of structured RNAs are present in the 5′ untranslated region (UTR) (61%)

and 3'UTR (41%), structured elements are also prevalent throughout the coding regions of the virus (Tavares et al., 2021). SARS-CoV-2 possesses not only the largest but also the most intricately structured RNA genome among RNA viruses. This high level of structural organization is comparable to other well-structured RNA viruses such as hepatitis C virus (HCV), where the ordered RNA structure is associated with a reduced activation of antiviral pathways, such as the interferon (IFN) response (Witteveldt et al., 2014). The condensed and structured configuration of SARS-CoV-2 potentially facilitates interactions between distant RNA structural elements. Such interactions could regulate various processes including replication, translation, and packaging, as observed in the case of HCV (Shetty et al., 2013).

The 5′UTR is highly conserved across coronaviruses (Figure 4), featuring five stem–loops (SL1–5) with crucial roles in viral replication, sgRNA production, and translational suppression evasion. Notably, SL5 contains the start codon of ORF1 and exhibits three additional stems (SL5A, SL5B, and SL5C). Furthermore, downstream of the 5′ UTR, three stem–loops (SL6–8) were identified (Lan et al., 2022).

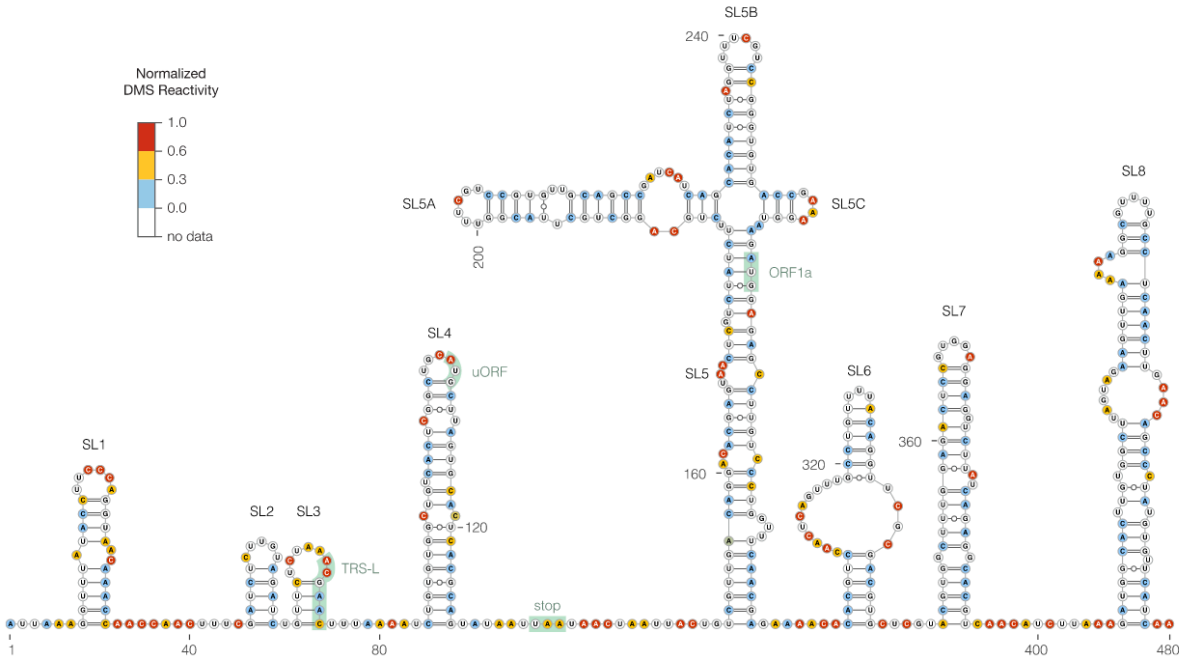

Figure 4: Secondary structure of the SARS-CoV-2 5′-UTR

Representation of the initial 480 nt of the SARS-CoV-2 genome, encompassing the 5′UTR (based on DMS reactivities observed in Vero cells). Nucleotides are marked according to their normalized DMS reactivities. Features highlighted comprise SL1-8, the TRS-L and the start codon of ORF1a. Picture taken from Lan et al., 2022

As other hCoVs, SARS-CoV-2 possesses a m^{7}G-cap structure at the 5' end of its genome and a polyadenylated (polyA) tail (30-60 nucleotides (nt) in length) at the 3' end. These features contribute to the stability of the genome and protect it from degradation by host exoribonucleases (Kim et al., 2020; Viswanathan et al., 2020). The viral 5'UTR spans 265 nt and

includes a 72-nt-long 5'-TLS sequence, which is, together with other cis-elements, involved in viral translation, sgRNA transcription and viral packaging (Miao et al., 2021).

On the other hand, the 3'-UTR encompasses 337 nt and contains the binding site for the RTC, which is crucial for viral replication and transcription of negative-sense RNA (J. Zhao et al., 2020).

1.3.2. Viral infection cycle

Following viral infection of the respiratory tract, the infection cycle starts with ACE2-mediated cell entry, followed by translation of non-structural proteins (Nsps), viral genome replication, translation of structural proteins, assembly of new virions, and ultimately, viral release, as illustrated in Figure 5 (W. Wu et al., 2023) and are described in further detail in the following subchapters.

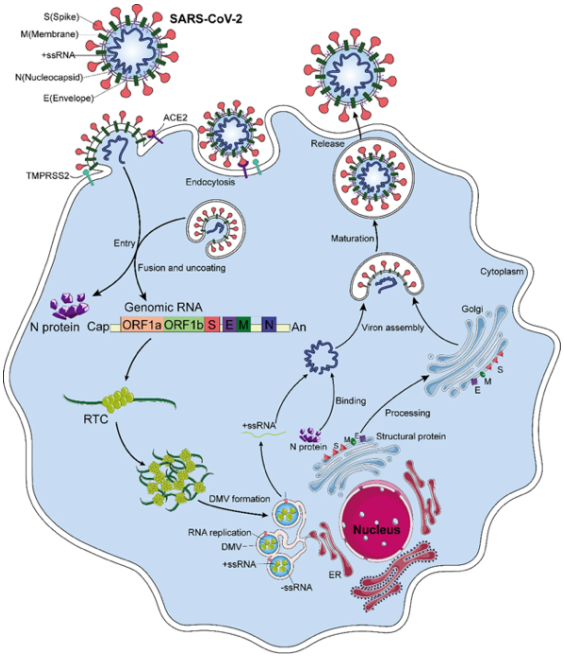

Figure 5: Infection cycle of SARS-CoV-2

Upon binding of the SARS-CoV-2 spike protein to the ACE2 receptor on the target cell, proteases, such as TMPRSS2, facilitate cleavage of the S protein, inducing fusion of the virus with the cell membrane. Alternatively, the virus can enter the cells via endocytosis. Subsequently, the N protein dissociates from the positive-strand RNA genome and is translated into the polyproteins pp1a and pp1ab. These polyproteins are processed into non-structural proteins (Nsp1-16), forming viral replication and transcription complexes (RTCs) that reshape the cell membrane to create replicating organelles (DMVs). DMVs, which are continuous with the endoplasmic reticulum, serve as the primary sites for viral RNA replication. Newly synthesized viral RNA exits DMVs through transmembrane pores for translation or virion assembly. Structural proteins translated from the genome are transported to the endoplasmic reticulum (ER) membrane and then to the ER-to-Golgi intermediate compartment (ERGIC). The positive-strand RNA wrapped by the N protein assembles with structural proteins S, M, and E, leading to the formation of new virions by budding into the ERGIC lumen. Finally, the progeny virions are released from the host cell. Picture taken from Wu et al. 2023

1.3.2.1. Viral cell entry

Subsequently to infection, viral entry occurs primarily via the angiotensin converting enzyme 2 (ACE2) receptor, which was originally identified as the receptor for SARS-CoV entry in 2003 (W. Li et al., 2003), allowing the virus to replicate and spread within the host. ACE2 functions as a carboxypeptidase, catalyzing the removal of a single amino acid from the C-terminus of its substrates (Jackson et al., 2022) .

The initial steps of viral entry involve attachment to the host cell membrane and membrane fusion, facilitated by the S protein (Figure 6). In this process, the S1 subunit of the S protein binds to ACE2, while the S2 unit anchors the S protein to the membrane (Hoffmann et al., 2020; Shang et al., 2020). This interaction, along with the cleavage of the S1 – S2 junction by furin (S. Xia et al., 2020) and the subsequent cleavage of the S2' site by transmembrane protease serine 2 (TMPRSS2) (Glowacka et al., 2011; Matsuyama et al., 2010), induces conformational changes in both S protein subunits. These changes lead to the formation of a fusion pore, allowing the viral genome to enter the cell cytoplasm. If TMPRSS2 expression is insufficient in the infected cell, the virus can alternatively enter through endocytosis. This process is followed by the activation of cathepsin-mediated S2' cleavage, leading to membrane fusion and subsequent viral release into the cell (Bayati et al., 2021).

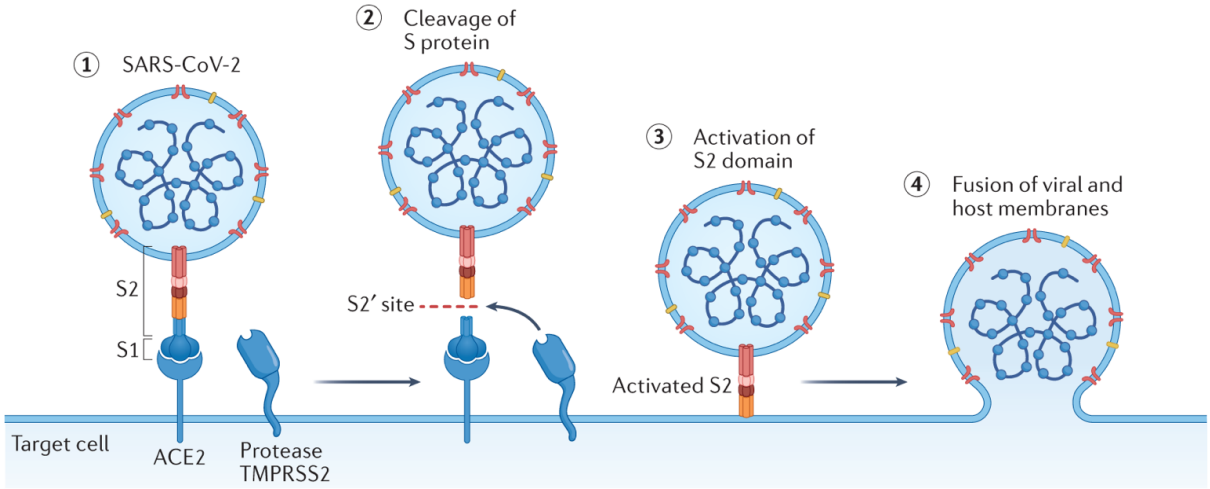

Figure 6: S protein-mediated entry into the host cell

The initial step involves the attachment of the S protein to the host cell receptor ACE2 through its S1 domain (1). Following this, TMPRSS2 cleaves the S protein (2), activating the S2 domain for fusion (3). Subsequently, the activated S2 domain facilitates fusion between the viral and host lipid bilayers, allowing the viral positive-sense, single-stranded RNA genome to enter the host cell (4). Picture taken from Lamers et al., 2022

1.3.2.2. Translation of non-structural viral proteins

The release of the SARS-CoV-2 genome into the host cell cytoplasm acts as a trigger for the start of a highly regulated viral gene expression program (V'kovski et al., 2021). As a first step, through translation of ORF1a and ORF1b, the polyproteins pp1a and pp1ab are produced (Finkel et al., 2021). The 16 Nsps are released from pp1a (Nsp1-11) and pp1ab (Nsp1-10, Nsp12-16), out of which 15 build the viral replication and transcription complex (RTC), including RNA-processing, RNA-modifying and RNA-proofreading enzymes. Synthesis of the viral RNA is performed by the viral RdRp (Nsp12) with help of its cofactors Nsp7 and Nsp8 (Emrani et al., 2021).

1.3.2.3. Transcription of new genetic material and viral assembly

The expression of viral Nsps triggers the biogenesis of viral replication organelles in the cytoplasm of the host cell, which create double membrane vesicles (DMVs), a protected environment, for the transcription of sgRNAs (Sawicki & Sawicki, 1995; V'kovski et al., 2021). Initially, genome replication is induced by the transcription of full-length negative-sense genomic copies, which serve as templates to produce positive-sense gRNAs, resulting in an even more increased expression of Nsps and formation of RTCs (Sola et al., 2015). Additionally, SARS-CoV-2 possesses a conserved leader sequence for the sgRNA transcription directed by viral RdRp. During negative-strand RNA synthesis, the RTC pauses transcription when encountering transcription regulatory sequences (TRSs) located upstream of most ORFs in the 3' region of the viral genome. These TRS elements act as termination sites for negative-strand RNA synthesis. Subsequently, synthesis restarts at a TRS adjacent to a leader sequence (TRS-L) situated approximately 70 nt from the 5' end of the genome (Di et al., 2018). This discontinuous process involves the interaction between complementary TRSs on the nascent negative strand RNA and the positive-sense TRS-L on the gRNA. Upon restart at the TRS-L region, a negative strand copy of the leader sequence is added to the nascent RNA, completing the synthesis of negative-strand sgRNAs. This discontinuous synthesis yields a set of negative-strand sgRNAs, serving as templates to produce a characteristic nested set of positive-sense sgRNAs that are subsequently translated into structural and accessory proteins (Di et al., 2018; Sola et al., 2015). Structural proteins involve the S, E, M and N protein, which will be discussed in more detail in following chapters. After sgRNAs are produced, Nsp16 and Nsp10 collaborate to methylate the 5′-end of viral mRNAs, forming a 5′-methyl-cap (Viswanathan et al., 2020). This modification promotes translation and shields the virus from the host immune response. Virus replication is thought to occur at perinuclear sites, where, similar to other positive-sense RNA viruses, structures derived from the endoplasmic reticulum (ER), such as DMVs, are formed. These DMVs, along with convoluted membranes and small open double-membrane spherules (DMSs), are interconnected (Pinto et al., 2022; V'kovski et al., 2021). Viral budding of SARS-CoV-2 likely takes place at compartments between the ER and Golgi apparatus, known as the ERGIC, similar to what has been observed in SARS-CoV (Stertz et al., 2007). Additionally, there is speculation that the virus may utilize lysosomes to facilitate egress from the host cell following viral replication (Ghosh et al., 2020).

1.3.3. SARS-CoV-2 non-structural proteins

Upon virus infection, the initial proteins synthesized are two polyproteins derived from ORF1a and ORF1b, encompassing a total of 16 Nsps. Nsp1, also known as the leader protein, inhibits host protein translation by binding to the 40S ribosome and blocks host mRNA export from the nucleus, hindering the synthesis of key immune response proteins while enhancing viral mRNA translation (Lapointe et al., 2021). Nsp2 is suggested to disrupt the host cell environment by binding to host PHB1 and PHB2 (prohibitin 1 and 2), which are involved in various cellular processes including cell cycle progression and apoptosis (Cornillez-Ty et al., 2009). Nsp3, a papain-like proteinase, facilitates the release of Nsp1 and Nsp2 from the polyproteins pp1a and pp1ab (Shin et al., 2020). Nsp4 interacts with Nsp3 and some host proteins, contributing to membrane rearrangement in order to form DMVs in conjunction with Nsp6 for viral replication (Angelini et al., 2013). Nsp5, the 3C-like proteinase, is essential for processing the polyproteins to yield mature Nsps (Roe et al., 2021). Nsp6 is involved in DMV formation for viral replication and in autophagosome generation and expansion, preventing the delivery of viral components for lysosome degradation (Cottam et al., 2011).

The peptide cofactors Nsp7 and Nsp8 form a complex with the RdRp Nsp12, enhancing its polymerase activity and forming the RTC (Te Velthuis et al., 2012). Nsp9 is involved in viral RNA replication, thereby activating Nsp8 and priming Nsp12 for RNA synthesis (Chandel et al., 2022). It positions itself near the membrane of the ER in host cells, where it interacts with a protein called nucleoporin 62 (Nup62), a structural protein which is part of the nuclear pore complex, hindering the entry of p65 into the nucleus. This mislocalization of p65 reduces the expression of genes regulated by NF-κb (nuclear factor κ-light-chain-enhancer of activated B cells), leading to a weakened immune response (Makiyama et al., 2022). Nsp10 interacts with Nsp14, a 3′-5′-exonuclease and S-adenosylmethionine (SAM)-dependent (guanine-N7) methyl transferase, and stimulates the activity of Nsp16, a 2′-O-methyltransferase (Decroly et al., 2011). The function of Nsp11 remains yet unclear but it might be involved in ribosomal frameshifting (Gadhave et al., 2021). Nsp13 functions as the viral helicase, unwinding RNA and possessing a 5′-triphosphatase activity necessary for mRNA capping (J. Chen et al., 2020). Nsp15 exhibits endonuclease activity, cleaving viral polyuridine sequences to evade host immune detection (Hong et al., 2021).

1.3.4. SARS-CoV-2 accessory proteins

The SARS-CoV-2 genome encodes also eleven accessory proteins which are playing significant roles in immune escape and viral pathogenesis.

ORF3a, the largest accessory protein of SARS-CoV-2, facilitates virus release and is crucial for viral replication and virulence. It interacts with the host immune system by promoting IL-1ß. (interleukin-1ß) secretion, leading to NF-κb signaling activation, inflammasome assembly, and apoptosis induction through caspase-3 activation (Redondo et al., 2021). ORF3b acts as a potent interferon agonist, suppressing type I-IFN induction (Konno et al., 2020). ORF3c is suggested to interact within the lipid bilayer by disrupting membrane-associated signaling activities (Finkel et al., 2021). ORF3d was shown to interact with the mitochondrial protein STOML2 (Stomatin Like 2) but further characterization is still missing (Gordon et al., 2020). The ORF6 protein of SARS-CoV-2 acts as a potent IFN antagonist. Its mechanism involves blocking the transportation of the transcription factor STAT (Signal Transducer and Activator of Transcription) from the cytoplasm to the nucleus, thereby inhibiting IFN activation (Miorin et al., 2020). ORF7a also possesses the capability to counteract the IFN-I response (H. Xia et al., 2020). ORF7b is suggested to disrupt certain cellular processes associated with leucin zipper formation and cell-cell adhesion (Fogeron et al., 2021). ORF8 antagonizes IFN signaling (Wong et al., 2018). ORF9b is an alternative ORF located within the gene coding for the N protein. Research on protein interactions revealed ORF9b interacting with a host mitochondrial import receptor which potentially influences the host immune response by impairing the IFN-I synthesis (Kreimendahl & Rassow, 2020). ORF9c seems to be involved in lipid remodeling, ER stress response and inhibition of IFN signaling (Dominguez Andres et al., 2020). ORF10 was shown to have no essential function in human CoV-2 infection (Pancer et al., 2020).

1.3.5. SARS-CoV-2 structural proteins

Besides the non-structural and accessory proteins, the genome of SARS-CoV-2 encodes for four structural proteins, the S, M, E and N protein, which play essential roles in viral assembly and the formation of new virions (C. Bai et al., 2022).

1.3.5.1. Spike, membrane and envelope proteins

The attachment of the virus to the host cell is facilitated by the S protein, which interacts primarily with cell surface receptors such as ACE2, initiating a fusion between viral and host

cell membranes for viral entry. SARS-CoV and SARS-CoV-2 S proteins share a 78% amino acid sequence homology and consist of the N-terminal S1 and the C-terminal S2 subunit (Walls et al., 2020). Two cleavage sites are located at the boundary of S1/S2, with furin cleavage being essential for viral entry into the target cell. The interaction with the ACE2 receptor for cell entry is facilitated by the receptor-binding domain (RBD), which is situated on the S1 subunit (S. Xia et al., 2020). After the binding of the RBD to ACE2, the second cleavage site on the S2 subunit is exposed and cleaved. In the S2 subunit, the HR1 and HR2 (heptad repeat 1 and 2 region) domains interact, forming an antiparallel six-helix bundle that constitutes the fusion core, facilitating the fusion of viral and host cell membranes (C. Bai et al., 2022).

The shape of the viral envelope is determined by the M protein, classified as a type III glycoprotein. Its central function lies in directing viral assembly through envelope formation and serving as the attachment matrix for nucleocapsid-mediated viral budding (C. Bai et al., 2022). Furthermore, research has revealed its capability to suppress the innate antiviral response by targeting specific signaling pathways (Fu et al., 2021). It inhibits the production of type I and III IFNs, aiding in evasion of the host's immune response (Y. Zheng et al., 2020). Additionally, M protein mediated apoptosis was observed, which potentially contributes to COVID-19 pathogenesis (Ren et al., 2021).

The E protein is widely preserved across coronaviruses and comprises a short hydrophilic N-terminal domain (NTD), a hydrophobic transmembrane domain (TMD), and an extensive hydrophilic C-terminal domain (CTD). It functions as a viroporin, potentially serving as a virulence factor by inducing host cell death and initiating a cytokine storm. Within the host cell, it predominantly localizes to the ERGIC, where it facilitates viral assembly and budding processes (Zhou et al., 2023).

1.3.5.2. Nucleocapsid protein

The N protein, highly abundant and immunogenic in SARS-CoV-2, is a homodimeric RNA-binding protein composed of 419 amino acids. As represented in Figure 7, it features two conserved and well-structured domains: the N-terminal domain (NTD/RBD) responsible for RNA binding and the C-terminal domain (CTD) facilitating protein dimerization and RNA binding. These domains are flanked and linked by intrinsically disordered regions (IDRs), with IDR2 serving as a serine-arginine-rich linker containing potential phosphorylation sites. The N-terminal IDR1, also known as the N-arm, and the C-terminal IDR3, referred to as the C-tail, contribute to the overall architecture and functionality of the protein. (Peng et al., 2020).

Figure 7: Schematic representation of the SARS-CoV-2 Nucleocapsid protein

The SARS-CoV-2 N protein comprises two distinct structured domains: the RNA binding domain (RBD)/N-terminal domain (NTD), highlighted in red, and the C-terminal domain (CTD), depicted in grey. The RBD is implicated in RNA interaction, while the CTD is crucial for protein oligomerization. These domains are connected by three intrinsically disordered regions (IDRs): IDR1, IDR2, and IDR3.

1.3.5.2.1. Structure of the Nucleocapsid protein

The structures of the SARS-CoV-2 NTD (Figure 8A) and CTD (Figure 8B) were intensively investigated. Structurally resembling other coronavirus N proteins, the NTD adopts a right-handed fist-like conformation. It is composed of a four-strand antiparallel β-fold core subdomain flanked by an annular or short 3_{10} helix and a prominent β-hairpin region formed by β2 and β3 chains (Figure 8A). Notably, this β-hairpin region exhibits considerable flexibility (Z. Bai et al., 2021; Dinesh et al., 2020). Analysis of the structure reveals the presence of a positively charged pocket at the interface between the basic hairpin and the core, which is believed to serve as a conserved RNA-binding site across human-infecting coronaviruses. Molecular modeling studies have shown that both dsRNA and ssRNA molecules can bind to this region, facilitated by the arginine residues R92, R107 and R149 (Dinesh et al., 2020). While the overall structure of the SARS-CoV-2 NTD shares similarities with other coronavirus NTDs, significant differences exist, particularly in the extension of the N-terminal loop and the flexibility of the β-hairpin region. These structural disparities, along with variations in electrostatic surface potentials and increased flexibility in N-terminal tail residues, may contribute to the accommodation of the high-order structure of the viral RNA genome (Kang et al., 2020). Numerous scientific studies have delved into the structural intricacies of the SARS-CoV-2 CTD. Typically, CTD monomers combine to form dimers, exhibiting varied structural conformations. Each monomer is characterized by a specific arrangement of five α-helices, two 3_{10}-helices, and two β-strands (Figure 8B). At the dimer interface, stability is achieved through intricate hydrogen bonding and hydrophobic interactions. Importantly, the structural architecture of the SARS-CoV-2 CTD closely resembles that of other coronaviruses, suggesting a conserved functionality, potentially involving RNA binding. Specific residues within the SARS-CoV-2 CTD have been implicated in RNA binding, contributing to the formation of a positively

charged region. Similarly to SARS-CoV, residues Arg319, Thr334, and Ala336 along the β1-β2 hairpin, were identified as part of RNA binding site present in the CTD (Zinzula et al., 2021).

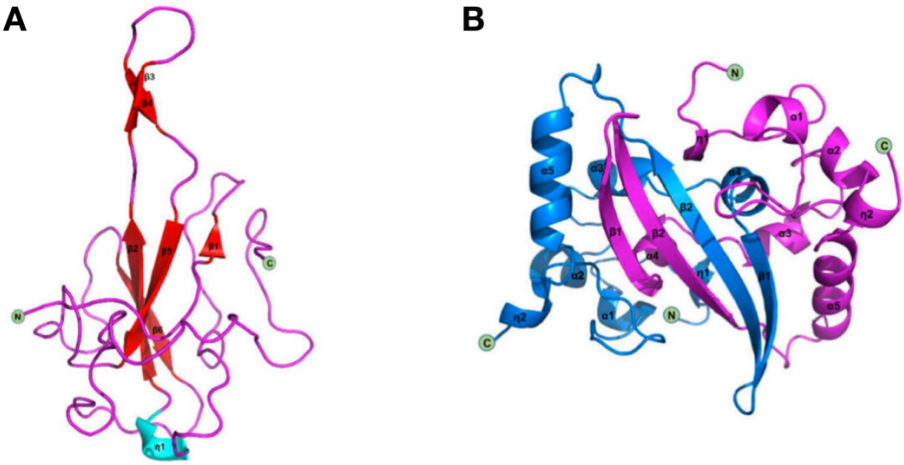

Figure 8: Structure of the Nucleocapsid NTD and CTD

(A) Cartoon representation of the NTD. The N-terminal domain (NTD/RBD) is structured with a core subdomain composed of four antiparallel β-strands (red). Adjacent to this core, there is either an annular or a short 3_{10} helix (turquoise). **(B)** Cartoon representation of the C-terminal domain (CTD). It exhibits a distinct configuration featuring five α-helices, two 3_{10}-helices, and two β-strands. Pictures taken from W. Wu et al., 2023

Notably, differences in electrostatic potential patterns exist among coronaviruses, which may influence their RNA recognition capabilities (W. Wu et al., 2023). Additionally, the CTD demonstrates self-binding properties, forming oligomers of various sizes depending on protein concentration. Furthermore, it plays a pivotal role in the formation of the N protein tetramer and is essential for liquid-liquid phase separation (LLPS) and NF-κB regulation (Z. Bai et al., 2021).

α-Helices and β-sheets constitute essential components of a protein's secondary structure, while IDRs are increasingly recognized for their significance in protein function. IDRs lack a fixed structure, making them flexible and adaptable for interactions with biological macromolecules such as RNA, DNA, and proteins. There are three IDRs in the N proteins of both, SARS-CoV and SARS-CoV-2: the N-terminal IDR1, central IDR2, and C-terminal IDR3 regions (Barik, 2020). Structural predictions suggest the IDR3 can adopt an α-helical conformation, potentially facilitating oligomerization. Furthermore, the conserved leucine-rich sequence within the IDR2, along with the adjacent serine/arginine-rich region, has been implicated in RNA-mediated LLPS and RNA binding. Additionally, the serine arginine rich IDR2 contains phosphorylation sites that regulate N protein function through interactions with viral and host proteins (H. Zhao et al., 2022).

1.3.5.2.2. Mechanisms and roles of N protein RNA interaction

In the final phases of viral replication, viruses face the critical task of genome packaging, ensuring the specific integration of their genetic material into newly formed virions amidst competition from various nucleic acid species in the host cell. Positive-strand RNA viruses typically excel at selectively incorporating their full-length gRNA while excluding other viral and host nucleic acids. In the context of coronaviruses, addressing the packaging issue entails the precise identification and selection of gRNA from a variety of viral sgRNAs, cellular mRNAs, and other RNA entities within infected cells, which typically is accomplished by the presence of genomic packaging signals (PS) (Masters, 2019). The PS in coronaviruses, initially identified in mouse hepatitis virus (MHV), was pinpointed to a 190-nt segment within the replicase gene (Makino et al., 1990). Further studies revealed a proposed 69-nt substructure within this segment as the minimal functional PS. Notably, the PS is only present in gRNA and not in the nested set of sgRNAs (Fosmire et al., 1992). Several studies have observed the packaging of RNA containing a potential PS into virus-like particles (VLPs) of SARS-CoV, SARS-CoV-2, and MERS-CoV. One potential PS was found in the Nsp15 gene region of SARS-CoV and SARS-CoV-2, resembling the PS in MHV gRNA. However, the MHV PS sequence is missing in SARS-CoV and SARS-CoV-2, and their putative PS lacks conserved RNA structural features found in other coronaviruses, hinting towards a different location in their genomes (Terasaki et al., 2023). Numerous studies have investigated potential PS positions within the SARS-CoV-2 genome, yielding conflicting findings (Syed et al., 2021a; Terasaki et al., 2023). Consequently, the PS of SARS-CoV-2 remains undetermined.

The N protein serves crucial functions in the coronavirus life cycle. Firstly, it assembles with gRNA to form the viral ribonucleic particle (vRNP) and facilitates vRNP packaging into virions by interacting with the other structural proteins at the ERGIC membrane (S. Lu et al., 2021). Secondly, the N protein localizes to RTCs during early infection stages, where it is suspected to aid in viral RNA synthesis and translation by recruiting host factors and promoting RNA template switching (Zúñiga et al., 2010). Each virus typically contains approximately 38 viral vRNPs, each likely comprising about 12 N proteins associated with approximately 600 nt of viral RNA. This implies that within a virus, there are around 500 N proteins bound to approximately 23,000 nt of RNA (Carlson et al., 2022).

Recently, LLPS, which plays a crucial role in organizing membrane-less organelles (MLOs), such as the nucleolus and stress granules, has been identified as the primary mechanism

governing the main functions of the N protein (Figure 9) (Dang & Song, 2022). In general, LLPS is driven by weak multivalent interactions, including hydrogen bonding and electrostatic forces, often involving proteins with IDRs. These weak multivalent interactions among macromolecules cause the system to minimize free energy by separating into distinct dense and dilute liquid phases, forming liquid droplets. LLPS is influenced by factors like concentration, temperature, and ionic strength, and is essential for various cellular functions and diseases (Gao et al., 2021).

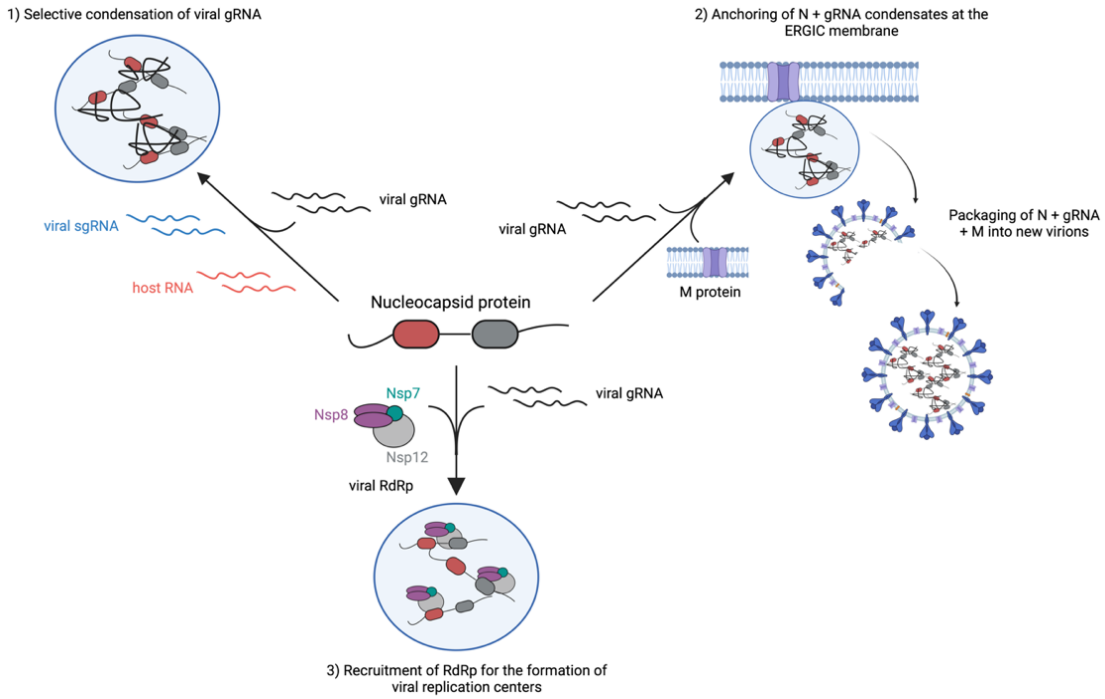

Figure 9: LLPS-mediated functions of the SARS-CoV-2 N protein

SARS-CoV-2 N protein functions reliant on LLPS. 1) Selective condensation of viral gRNA by excluding viral sgRNA as well as host RNA. 2) Anchoring of N-RNA condensates at the ERGIC membrane preparative for virus assembly. 3) Recruitment of the viral RdRp for the formation of replication centers. Picture modified from W. Wang et al., 2022

Several studies have explored the phase separation ability of CoV-2 N-RNA and have observed LLPS occurring with different RNA lengths, sequences, and concentrations. These findings imply a somewhat nonspecific phase separation behavior *in vitro* (Carlson et al., 2020; S. Lu et al., 2021; Savastano et al., 2020).

Various types of RNA, including nonviral RNA, can induce N protein LLPS *in vitro*, but the potency of induction and the properties of resulting condensates depend on the RNA type and length used. Iserman et al. observed that different regions of the SARS-CoV-2 genome exert distinct effects on N protein phase separation, with the 5' and 3' ends promoting LLPS while central regions promote solubilization (Figure 10). This behavior is strand-specific, suggesting a role in organizing viral RNA for efficient packaging and providing specificity for full-length genomic RNA over subgenomic and host-cell RNA (Iserman et al., 2020).

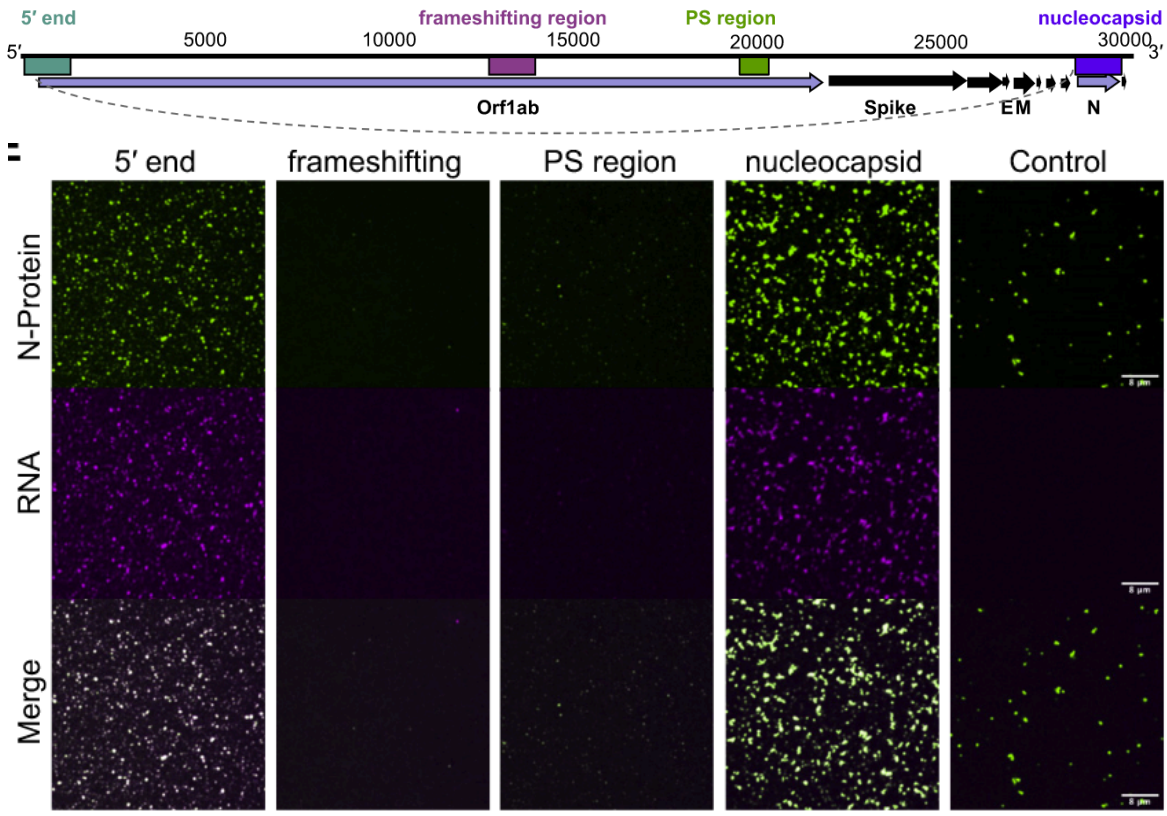

Figure 10: Sequence-specific N-RNA LLPS

RNA from different regions of the SARS-CoV-2 genome, including the 5′UTR (turquoise), frameshifting region (magenta), CoV-1 PS region (green), and nucleocapsid gene (purple), were evaluated for their ability to undergo LLPS with the nucleocapsid protein. Under identical conditions of protein and RNA concentration, and with comparable RNA lengths, LLPS was observed selectively with RNA derived from the 5′ end and the region encoding the nucleocapsid. Picture taken from Iserman et al., 2020

SARS-CoV-2, like other enveloped viruses, requires compacted gRNA to be encapsulated in a protein-decorated membrane to form mature virions, a process occurring at the ERGIC membrane. The transmembrane M protein of SARS-CoV-2 localizes to the ERGIC membrane, anchoring and organizing compacted gRNA at virion budding sites through interactions with other structural proteins (Boson et al., 2021). Co-LLPS between the N protein and gRNA fragments, as well as between the N protein and the M (aa104–222) protein, suggests a connection between N+gRNA condensation and their localization at intracellular sites. M co-LLPS occurs with the N protein but not with RNA, resulting in nonuniform condensates comprising an N + RNA "core" surrounded by a punctate M "shell". This suggests a model where the N protein serves as a bridge between mutually exclusive N + M condensates and N+gRNA condensates. The mechanistic role of the N protein as a bridge between condensates in aiming anchoring at the ERGIC for assembly remains unknown (S. Lu et al., 2021).

Several viruses induce the formation of viral replication centers, specialized compartments rich in proteins and nucleic acids essential for viral genome replication within host cells. These replication centers often exhibit liquid-like properties indicative of phase-separated condensates

(Etibor et al., 2021). In recent studies, condensates formed by the SARS-CoV-2 N protein and RNA were found to recruit components of the SARS-CoV-2 RdRp complex, responsible for replicating viral gRNA (Savastano et al., 2020).

1.3.5.2.3. Post-translational N protein modifications

The N protein of SARS-CoV-2 undergoes various post-translational modifications (PTMs), which play critical roles in its function and interactions with host factors. Phosphorylation is a key PTM that regulates RNA binding and alters the physical and chemical properties of the N protein (C. Wu et al., 2021). During early infection stages, cytoplasmic kinases rapidly phosphorylate the serine-arginine (SR) region of the N protein at multiple sites, facilitating its interaction with RNA helicase DDX1 and promoting structural RNA changes required for sgRNA transcription in the viral RTCs (Bouhaddou et al., 2020; Carlson et al., 2020; C.-H. Wu et al., 2014). This phosphorylation disrupts multivalent RNA-protein and protein-protein interactions, leading to the formation of liquid-like droplets that aid in viral genome processing (Carlson et al., 2020). However, during viral assembly, unphosphorylated N protein binds genomic RNA to form the compact nucleocapsid structure, which is then engulfed by ER membranes containing the S, E, and M proteins to form a mature virus (Carlson et al., 2022; Scherer et al., 2022).

Furthermore, phosphorylation of specific residues within the SR motifs, such as S176, S188, and S206, weakens RNA binding and influences the solution properties of protein-RNA complexes (C. Wu et al., 2021). The highly phosphorylated SR domain also modulates interactions between the N protein and viral Nsp3 proteins, as well as host proteins like glycogen synthase 3, CDK-1, and 14–3-3 proteins, impacting nucleoplasmic shuttling of the N protein (Bouhaddou et al., 2020; W. Wu et al., 2023). Moreover, phosphorylation of S/R residues in the IDR2 regulates discontinuous transcription, particularly affecting shorter sgRNA production in the early stages of replication (C. Wu et al., 2021; C.-H. Wu et al., 2014).

In addition to phosphorylation, methylation modifications, particularly at residues R95 and R177, influence RNA binding of the N protein. Methylation of R95 inhibits stress granule formation and affects nearby phosphorylation sites, indicating potential crosstalk between methylation and phosphorylation pathways (Cai et al., 2021). Similarly, glycosylation at N48 and N270 as well as acetylation at K75 modulate N protein interactions like LLPS with viral RNA and other proteins (Rump et al., 2021; S. Wang et al., 2021).

1.3.5.2.4. N protein – mediated host immune modulation

Upon SARS-CoV-2 infection, the immune system activates various pathways to combat the virus. Viral RNA sensors such as RIG-I and MDA5 recognize viral RNA and translocate to the mitochondria, where they bind to the mitochondrial antiviral signaling (MAVS) protein. This interaction forms a signalosome, leading to the phosphorylation and nuclear translocation of interferon regulatory factor (IRF) 3/7, thereby promoting the transcription of type I and III IFN genes (Yu et al., 2023). Upon the production of type I IFN, these signaling molecules bind to their receptors, triggering a series of intracellular events. This process involves the activation of tyrosine kinases within the cell, leading to the phosphorylation and subsequent activation of STAT 1/2. However, the presence of SARS-CoV-2 N protein disrupts this pathway by inhibiting the phosphorylation and nuclear translocation of STAT1/2 induced by type I IFN. Mechanistically, SARS-CoV-2 N protein directly binds to STAT1/2, interfering with their interaction with upstream tyrosine kinases and downstream activation of gene transcription of genes involved in antiviral response. CoV-2 N protein was also shown to bind to MAVS, inhibiting its activation and downstream IFN I and III production (Mu et al., 2020; Y. Zhao et al., 2021). Furthermore, the N protein hinders the recognition of viral RNA by binding to RIG-I and TRIM25 (tripartite motif protein 25), an E3 ligase involved in RIG-I activation, thereby blocking its activation and following IFN-ß production (K. Chen et al., 2020; Gori Savellini et al., 2021).

In response to viral infection, stress granules are formed, which facilitate the interaction between G3BP1 (Ras GTPase-activating protein-binding protein 1) and RIG-I, enhancing RIG-I activation. The N protein targets G3BP1 to inhibit stress granule formation, preventing the enhancement of RIG-I activation after infection (Z.-Q. Zheng et al., 2021).

1.3.6. Cellular response to SARS-CoV-2 infection and viral immune evasion

The host innate immune response to coronavirus infections involves the production of type I and type III interferons (IFN-I and IFN-III), as well as proinflammatory cytokines and chemokines (Kasuga et al., 2021). These responses are initiated by the recognition of viral pathogen-associated molecular patterns (PAMPs) and/or host danger-associated molecular patterns (DAMPs) by specialized cellular pattern recognition receptors (PRRs). In the case of SARS-CoV-2, RNA-based replication intermediates serve as major PAMPs, recognized by receptors like RIG-I-like (retinoic acid inducible gene I) receptors (RLRs) and Toll-like receptors

(TLRs) (Diamond & Kanneganti, 2022). RLRs, including RIG-I and MDA5 (melanoma differentiation-associated protein 5), sense different RNA structures, while TLRs detect extracellular viral components (Lester & Li, 2014; Thoresen et al., 2021). In the case of an SARS-CoV-2 infection, TLR7 and TLR8 bind G/U-rich viral ssRNA and induce proinflammatory cytokines (Jangra et al., 2021). Upon recognition, these receptors trigger a cascade of signaling events leading to the production of IFN-I and IFN-III. These interferons induce the upregulation of hundreds of interferon-stimulated genes (ISGs), which exert antiviral effects by inhibiting viral replication and transcription (R. Lin et al., 2000). Earlier research demonstrated that the cell entry of SARS-CoV-2 can be hindered by preventing the translocation from the endosomal membrane to the cytoplasm. This inhibition was achieved through the expression of two members of the ISG family: interferon-induced transmembrane protein 2 (IFITM2) and lymphocyte antigen 6 family member E (LY6E) (G. Shi et al., 2021; X. Zhao et al., 2020).

Viruses, including SARS-CoV-2, are reliant on host cells for energy and resources. To successfully infect a host, viruses must manipulate or deactivate various host pathways. SARS-CoV-2 employs diverse strategies to evade the host's antiviral response (Minkoff & tenOever, 2023).

Coronaviruses modify their RNA through capping and methylation to avoid host detection (Viswanathan et al., 2020). This process involves enzymatic reactions mediated by Nsp13, Nsp14, and Nsp16 (Y. Chen et al., 2009). As viral RNA synthesis progresses, dsRNA is present as an intermediate, triggering host immune activation. Nsp15 minimizes the accumulation of dsRNA (Frazier et al., 2021), while the virus induces the assembly of DMVs to compartmentalize viral replication and interfere with host sensors (Versteeg et al., 2007). Replication organelles (ROs) are formed, mediated by Nsp3, Nsp4, and Nsp6, which diminish host recognition of the virus infection. Optimal infection is achieved with a low multiplicity of infection to avoid excessive dsRNA formation before the formation of DMVs or translation of adequate levels of Nsp15 (Ricciardi et al., 2022).

After the establishment of viral ROs, SARS-CoV-2 transcripts exit these structures and enter the host cell cytosol for translation and virion assembly (D. Chen & Zhang, 2022). However, outside the protective ROs, the viral RNAs are vulnerable to detection by cellular sensors. To evade host immune responses, SARS-CoV-2 is targeting viral sensing processes and delaying the production of host antiviral defenses (Emrani et al., 2021). SARS-CoV-2 efficiently takes over host cells, with over 60% of cellular mRNA originating from the virus. This is facilitated by high

viral RNA levels and suppression of host mRNA by viral proteins like Nsp1, Nsp10, and Nsp14 (Fiege et al., 2021). The N protein, abundant in infected cells, may mask viral RNAs from detection. Additionally, it can interfere with the formation of stress granules, which are sites for viral RNA recognition by host sensors (Y. Zheng et al., 2022). SARS-CoV-2 proteins also target downstream factors in cellular signaling pathways involved in antiviral responses, such as MAVS, TBK1 (TANK binding kinase 1), and IRF3 (interferon regulatory factor 3), inhibiting their function and suppressing immune activation (H. Xia et al., 2020). Despite the virus inducing NF-κB activation, it specifically targets IRF3, preventing IFN-I induction (Freitas et al., 2022; W. Zhang et al., 2021).

Furthermore, blocking nuclear transport machinery offers a significant advantage for cytoplasmic pathogens. The nuclear pore complex (NPC) regulates nucleocytoplasmic transport and is hijacked by viruses to facilitate viral protein access to the nucleus (Cautain et al., 2015). SARS-CoV-2 proteins Nsp1, Nsp9, Nsp15 and ORF6 interact with the host nuclear transport machinery (Makiyama et al., 2022; K. Zhang et al., 2021). ORF6 inhibits nucleocytoplasmic transport by binding to Nup98 (Nucleoporin 98kD) and Rae1 (ribonucleic acid export 1), preventing the translocation of transcription factors and mRNA (Kato et al., 2021).

Another strategy of SARS-CoV-2 to enhance its viral fitness involves interfering with translation initiation and mRNA splicing processes. The virus' Nsp1 protein blocks mRNA entry into ribosomes, inhibiting protein synthesis (Banerjee et al., 2020; Thoms et al., 2020). Similarly, Nsp10, Nsp14 and Nsp16 disrupt host mRNA splicing, leading to a global inhibition of protein production (Hsu et al., 2021). Alternatively, Nsp1 protein might trigger the degradation of mRNAs lacking the 5′ viral leader sequence, thereby enabling preferential translation of viral mRNAs over cellular ones (Finkel et al., 2021).

Furthermore, SARS-CoV-2 targets protein trafficking by interacting with the signal recognition particle (SRP), a complex responsible for directing newly synthesized proteins to their proper destinations within the cell. Specifically, Nsp8 and Nsp9 bind to components of the SRP, disrupting its function and impairing the proper folding and secretion of host proteins (Banerjee et al., 2020).

These mechanisms not only contribute to the virus' ability to evade host immune responses but also enhance its replication and spread within the host cell. By interfering with fundamental cellular processes, SARS-CoV-2 ensures its survival and propagation, ultimately contributing to the severity of COVID-19.

1.3.7. SARS-CoV-2 variants

Following its emergence in late 2019 in Wuhan, SARS-CoV-2 has undergone various adaptations and phenotypic alterations during its evolution. The initial adaptation was characterized by a single substitution in the spike protein (D614G), leading to enhanced transmissibility observed in the subsequent alpha variant (Harvey et al., 2021). Most subsequent mutated variants primarily exhibit mutations in the spike protein. To date, the World Health Organization (WHO) has identified five SARS-CoV-2 variants as variants of concern (VOCs), all displaying enhanced transmissibility and immune evasion. These VOCs have become dominant in specific regions, such as alpha, beta, and gamma, or have rapidly spread globally, as observed with the delta and omicron sublineages. (Carabelli et al., 2023). The virus enters the host cell by cleaving at the furin cleavage site located at the S1-S2 junction of the S protein. Therefore, this cleavage site plays a crucial role in determining the high transmission rates and rapid spread of SARS-CoV-2 (S. Xia et al., 2020). Mutations within the furin cleavage site are believed to have boosted the transmissibility and fitness of the alpha and delta VOCs. However, the evolutionary success of the Omicron VOCs is not attributed to an optimized cleavage site. Instead, Omicron exhibits an altered entry phenotype along with substantial immune evasion, facilitating efficient infection of vaccinated or previously infected individuals (Carabelli et al., 2023). In contrast to pre-Omicron variants, which primarily enter the cell via the TMPRSS2-dependent pathway, Omicron predominantly enters the host cell via endocytosis, leading to altered infection dynamics. While the lower respiratory tract expresses higher levels of TMPRSS2, the upper respiratory tract has elevated levels of cathepsin, essential for viral endocytosis. Furthermore, cell entry mediated by TMPRSS2 is associated with syncytia formation, which correlates with a more severe clinical presentation of COVID-19. The predominant endocytic entry mechanism of Omicron may contribute to the less severe disease outcome observed with this variant (Willett et al., 2022).

Mutations detected within the M protein of Omicron BA.5 subvariant may potentially disrupt membrane integrity. Notably, the N protein of Omicron BA.5 exhibits mutations including P13L, ΔE21, ΔR32, and ΔS33 within the IDR1, E136D within the RBD, R203K and G204R within the IDR2, and S413R within the CTD. These mutations could be associated with altered RNA binding capabilities and inhibition of RNA-induced interferon expression, potentially influencing pathogenicity and viral fitness (Rana et al., 2022).

1.4. RNA chaperones

RNA molecules are central players in a range of cellular processes, serving as templates and major regulators of translation and actively regulating gene expression (Dai et al., 2020). Additionally, RNAs function as catalysators in the form of ribozymes, playing essential roles in nuclear architecture and chromatin organization (Thakur & Henikoff, 2020). For many viruses, RNA serves as the hereditary molecule, either in the form of a double-stranded or highly structured single-stranded RNA genome (Poltronieri et al., 2015).

The presence of RNA genomes in viruses provides them with flexibility in terms of genome size and structure and allows them to generate genetic diversity, adapt quickly to new hosts, evade host immune responses, and develop resistance to antiviral drugs due to its heavily increased mutation rate compared to DNA genomes (Wolf et al., 2018). This higher mutation rate in RNA genomes is primarily due to the error-prone nature of RdRps and their lack of proof-reading mechanisms as well as the single-stranded nature of RNA, which contribute mainly to its flexibility and adaptation capabilities (Belshaw et al., 2007; Duffy, 2018).

Single-stranded RNA molecules can adopt various structural conformations by exploiting different intramolecular base pair formations, resulting in distinct RNA folds. Moreover, the presence of non-canonical base pairs, tertiary interactions, and long-range interactions further expands the possible structural outcomes. The folding of RNA is a complex process that is influenced by various factors, including the nucleotide sequence, thermodynamic stability, and kinetic pathways which lead to differently stable RNA structures. The folding process isn't solely determined by thermodynamics, but kinetic factors and associated proteins also play a role. RNA molecules can get trapped in kinetic intermediates, leading to the formation of different metastable structures and off-pathway folding traps (Doetsch et al., 2011; Herschlag, 1995; Russell, 2008). However, since the proper RNA structure is essential for its biological function and interaction with other molecules, proteins evolved to resolve these folding traps and promote proper RNA folding (Ganser et al., 2019; Mathews et al., 2004).

The aforementioned proteins fall into one of three categories: RNA binding proteins that form stable complexes with RNA, RNA helicases that facilitate ATP-dependent unwinding of RNA, or RNA chaperones that alter RNA structure dynamically, similar to helicases (Doetsch et al., 2011; Herschlag, 1995).

RNA chaperones are proteins that assist in the proper folding of RNA molecules exhibiting a crucial role in structural biogenesis and function (Grohman et al., 2013; Mohr et al., 2002). These

proteins are characterized by a lack of sequence/structure specificity, transient RNA interactions, and no energy requirement for their function (Zúñiga et al., 2010). Unlike many protein chaperones, which require ATP as an energy source, RNA chaperones interact directly with RNA, going through cycles of unfolding and folding without requiring ATP (Semrad, 2011). An intriguing feature shared by RNA chaperones is the presence of IDRs within their protein structure (Tompa & Csermely, 2004; Woodson et al., 2018a). The IDRs of RNA chaperones, account for more than half of their amino acid residues, an unprecedented occurrence compared to other protein classes, underscoring their crucial role in the process of RNA chaperoning (Woodson et al., 2018a). The IDRs likely play different roles in RNA chaperones, either functioning as molecular recognition elements by acting as solubilizers and preventing aggregation of the misfolded substrate (typically for protein chaperones), or locally loosening the structure of the kinetically trapped RNA folding intermediate to facilitate its folding into the functional conformational state (Tompa & Csermely, 2004).

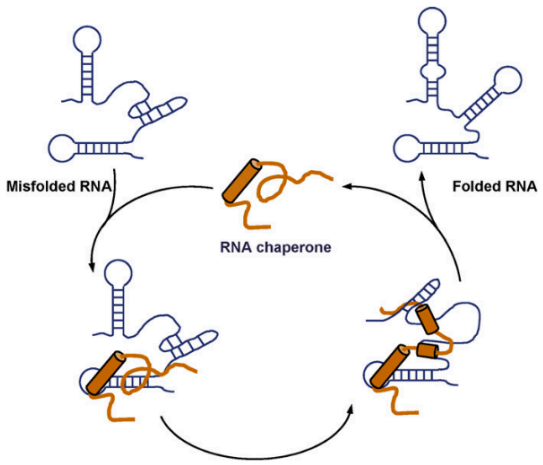

Figure 11: Schematic representation of the RNA chaperone mechanism

Initially, the RNA chaperone (orange) recognizes and binds the misfolded RNA (blue). Conformational changes in the RNA chaperone's IDRs lead to the entropy transfer from the protein to the RNA. The RNA can therefore overcome kinetic barriers and assume another structure while transferring entropy back to the IDRs of the RNA chaperone. These steps occur in various cycles until the RNA reaches its thermodynamically favorable structure and is releases from the RNA chaperone. Picture taken from Zúñiga et al., 2009

Driving RNA folding towards a thermodynamically stable and functional structure, is suggested to occur by a two-step entropy transfer mechanism, illustrated in Figure 11. In the first step, entropy is transferred from the protein to the substrate: the RNA chaperone binds to the misfolded RNA, re-organizing the IDRs of the protein and unfolding the RNA. In the second step, the entropy transfer occurs in the opposite direction, from the substrate to the protein: the RNA folds, whereas the chaperone's IDRs become unfolded again. These steps occur in many cycles of order-disorder until the proper folded RNA substrate is released (Tompa & Csermely, 2004; Zúñiga et al., 2009). IDRs were also shown to be drivers of LLPS and required to form RNA granules by interacting cooperatively with the folded domains of the protein (Y. Lin et al., 2017).

The number of identified RNA chaperones is steadily growing and they can be found in all kingdoms of life, ranging from procaryotic to higher eukaryotic organisms, as well as viruses, indicating their fundamental role in RNA metabolism and processing (Rajkowitsch et al., 2007). Within viruses, RNA chaperones have been identified in several viral families, including retroviruses, enteroviruses and coronaviruses (H. Xia et al., 2015; Zúñiga et al., 2010). The first RNA chaperone discovered was the nucleocapsid protein 7 (Ncp7) of the human immunodeficiency virus type 1 (HIV-1) (Herschlag et al., 1994; Tsuchihashi et al., 1993). RNA dimerization, encapsidation and the annealing of the primer tRNA to the initiation site of reverse transcription are promoted by Ncp7 (Morellet et al., 1992). Ncp7 contains two Zinc (Zn) finger motifs which are linked by basic amino acids and flanked by a highly basic N-terminus and a short C-terminus. An *in vivo* study investigating Ncp7 mutations showed both Zn finger motifs as well as the N-terminus and the linker being involved in RNA dimerization of the HIV-1 genome by a so-called RNA-RNA kissing mechanism (Aduri et al., 2013).

Another viral protein, the nucleocapsid protein of SARS-CoV has been described promoting viral RNA sequences to form hybrids by annealing nucleic acids and destabilizing RNA duplexes (McBride et al., 2014; Zúñiga et al., 2007a). The N protein of SARS-CoV-2 was also suggested to be a viral RNA chaperone (Savastano et al., 2020). However, functional proof and mechanistic studies are still missing.

1.5. Cell surface glycosaminoglycans

Glycosaminoglycans (GAGs) constitute a diverse family of linear, negatively charged polysaccharides, made up of repeating disaccharide units, typically ranging in a molecular weight from approximately 10-100 kDa. Found abundantly in various cell types, GAGs exhibit intricate structural complexities due to variations in residue types, glycosidic bond types, sulfation levels, sulfation positions, and chain lengths (D. Shi et al., 2021). There are five main types of GAGs, classified based on their composition and glycosidic linkage: nonsulfated GAGs like hyaluronic acid (HA), and sulfated GAGs such as heparin (H) and heparan sulfate (HS), chondroitin sulfate (CS), dermatan sulfate (DS), and keratan sulfate (KS). H and HS, characterized by their high sulfation, are of particular interest due to their diverse biological activities. With exception of HA, all GAGs are covalently attached to the core protein of proteoglycans (PGs) (Shriver et al., 2012).

While HS is distributed on various cell types, H is specifically present on the surface of mast cells. Despite their structural similarities, H tends to have a higher degree of sulfation compared to HS (Farrugia et al., 2018).

In glycobiology, GAGs play pivotal roles as signal molecules, structural components, and modulators of cellular activities (Vallet et al., 2021). They are involved in various biological processes, including embryonic development, extracellular matrix assembly, enzymatic regulation, ligand-receptor interactions, and cell signaling pathways. Furthermore, GAGs hold significant relevance in disease contexts such as cardiovascular disease, cancer, infectious diseases, neurodegenerative diseases, inflammatory responses, and wound healing (D. Shi et al., 2021). Their predominantly ionic interactions with proteins influence a wide range of physiological processes (Morla, 2019).

In addition to chemokines, selectins, and cell surface receptors, GAGs, particularly HS, play a significant role in inflammation. Inflammation describes the body's reaction to foreign material intrusion or injury. Specific immune cell surface receptors identify PAMPs and DAMPs released from injured cells, thereby triggering a signaling cascade constituting the inflammatory response. This cascade includes processes such as leukocyte recruitment, adhesion, and transmigration at the inflammation site (Parish, 2006).

Furthermore, GAGs are widely recognized for their role in interacting with chemokines, facilitating chemokine dimerization and enhancing chemokine receptor binding, directly influencing inflammatory processes. These interactions are essential to the antiviral immune response. Chemokines are crucial for fighting viral infections by recruiting both innate and adaptive immune cells to infection sites. They also boost the cytotoxic capabilities of these cells and their capacity to produce antiviral agents (Melchjorsen et al., 2003). However, certain viruses produce chemokine binding proteins, disrupting GAG binding to evade the chemokine-mediated immune response, thereby modulating leukocyte migration to the infection site (Thompson et al., 2017).

Viruses like HIV-1, HCV, HPV (human papillomavirus), and SARS-CoV-2 exploit electrostatic interactions between the negatively charged HS chains and the basic residues on their surface or capsid proteins. This strategy enhances their concentration on the host cell surface during infection, facilitating binding to target entry receptors (De Pasquale et al., 2021). For HIV, interaction of the viral gp120 envelope protein with HS prior to CD4 (cluster of differentiation 4) receptor recognition is crucial for the accumulation of viral particles at the cell surface (Pomin

et al., 2017). Moreover, various serotypes of HPV rely on binding to heparan sulfate proteoglycans (HSPGs) for attachment to host cells and subsequent processing of the HPV capsid protein essential for cell entry (Richards et al., 2013).

Furthermore, studies have demonstrated that for SARS-CoV-2, HSPGs act as the initial anchoring sites on the host cell surface (Figure 12). Efficient cell entry requires the binding of the S protein to both HS and the ACE2 receptor. The interaction with HS facilitates the initial contact between the virus and the host cell, leading to an increased concentration of virus particles on the cell surface and enhanced access to the entry receptor ACE2. Additionally, research suggests that HS may play a role in the endocytic entry of SARS-CoV-2, as knocking out genes involved in HSPG biosynthesis prevents viral endocytosis. (Q. Zhang et al., 2020).

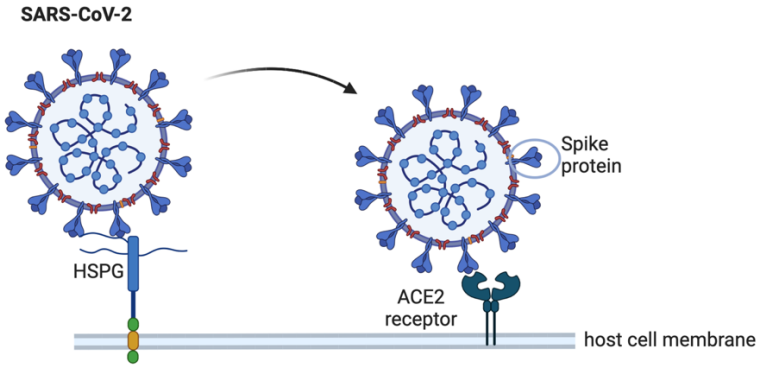

Figure 12: Schematic illustration of S-HSPG interaction for cell entry

Heparan sulfate proteoglycans (HSPGs) serve as the primary anchoring sites on the host cell surface after SARS-CoV-2 infection. The interaction with HS facilitates the initial contact between the virus and the host cell, promoting the accumulation of virus particles on the cell surface and facilitating access to the entry receptor ACE2, followed by conformational changes of the S protein and viral uptake.

A study by López-Muñoz et al. highlights the significance of H and HS in SARS-CoV-2 infection by not only facilitating viral entry by binding to the S protein but also interacting with the viral N protein. Upon infection, intracellular N proteins translocate to the cell surface, where it covalently binds to H and HS but not to other sulfated GAGs. This bound N protein is then distributed to neighboring cells. Moreover, the study demonstrates the high-affinity binding of N protein to several chemokines. The binding to both H/HS and chemokines gives an hint in potential N-mediated impairment of the host's immune response upon SARS-CoV-2 infection (A. López-Muñoz, 2022).

1.6. Thesis outline

Considering the global health crisis which resulted by the outbreak of SARS-CoV-2 and the respective COVID-19 pandemic, a comprehensive understanding of the virus and its associated disease is essential for effective infection prevention and the development of therapeutics. Therefore, the primary aim of this thesis is to comprehensively investigate the biochemical and biophysical properties of the SARS-CoV-2 nucleocapsid protein, with a focus on elucidating its mechanisms of RNA binding, its contribution to viral genome structuring, and its influence on modulating host immune responses. The first aspect involves the investigation of the RNA binding properties of the nucleocapsid protein, aiming to identify the protein domains harboring the intrinsic affinity and specificity, thereby shedding light on the crucial step of RNA packaging. Furthermore, unraveling the role of the nucleocapsid protein in structuring the viral genome and elucidating the underlying mechanisms of the generation and maintenance of the viral secondary structure, is another goal of the project. Furthermore, this thesis explores the immunomodulatory role of the nucleocapsid protein on the host immune response to SARS-CoV-2 infection to gain a deeper insight into the molecular mechanisms through which the nucleocapsid protein interacts with host factors and influences immune signaling pathways. Through these investigations, the overall objective is to advance the understanding of the virus-host interaction to facilitate the development of strategies for infection control for SARS-CoV-2 and further upcoming viruses.

2. Material and methods

2.1. Material

2.1.1. Chemicals

Table 1: Chemicals

Chemical	Distributor
0.5% Trypsin-EDTA (10x)	Gibco
Acetic acid	Roth
Agar	Roth
Agarose UltraPure™	Invitrogen
Ampicillin	Roth
APS	Sigma Aldrich
Bacto™ Tryptone	BD Biosciences
Bacto™ Yeast Extract	BD Biosciences
Benzamidine	Sigma Aldrich
BlueEasy Prestained Protein Marker	Nippon Genetics
Boric acid	Babochem. International
Bromphenol blue	Merck
BSA	Sigma Aldrich
CH_3COONH_4	Merck
Chloramphenicol	Sigma Aldrich
Coomassie Brilliant Blue G-250	Thermo Fisher Scientific
Coomassie Brilliant Blue R-250	Thermo Fisher Scientific
DAPI	Sigma Aldrich
DMSO water free	Merck
dNTPs 10 mM each	New England Biolabs
DTT	Roth
DY-647P1	Dyomics
EDTA	Merck
Ethanol tech./p.A.	Sigma Aldrich
Gene Ruler 1kb Plus DNA Ladder	Thermo Fisher Scientific
Glycerol 99 %	Roth
Glycogen	Roche
HCl 37 %	VWR
Heparan sulfate sodium salt from bovine kidney	Merck
Heparin sodium salt from porcine intestinal mucosa	Merck
HEPES	Roth
Imidazole	Roth

Chemical	Distributor
Isopropanol p.A.	VWR
Kanamycin	Roth
KCl	Roth
KH_2PO_4	Merck
Methanol p.A.	VWR
$MgCl_2$	Merck
Na_2HPO_4	Roth
NaCl	Roth
NaOH	VWR
NativeMark™ unstained protein standard	Invitrogen
NativePAGE™ 4-16 % Bis-Tris-gels	Invitrogen
NT-647-His labeling dye	NanoTemper
Orange G	Sigma Aldrich
Paraformaldehyde	Roth
Penicillin-Streptomycin (10,000 U/ml)	Gibco
Pluronic F-127	Sigma Aldrich
Polybrene	Sigma Aldrich
Protein Assay Dye Reagent Concentrate	Bio-Rad
Protein Assay Dye Reagent Concentrate	Bio-Rad
RNase free	Apex Chemicals and Reagents
Rotiphorese Gel 30	Roth
SDS	Roth
ß-Mercaptoethanol	Merck
SYBR Safe DNA Gel Stain	Invitrogen
TEMED	Roth
Tris	Roth
Urea	Roth

2.1.2. Kits

Table 2: Kits

Kit	Distributor
CyQUANT™ LDH Cytotoxicity Assay	Invitrogen
LEGENDplex™	BioLegend
Monolith His-Tag Labeling Kit RED-tris-NTA	NanoTemper
Plasmid Plus Midi Kit	Qiagen
PureLink™ HiPure Plasmid Filter Maxiprep Kit	Invitrogen
QIAEX II Gel extraction Kit	Qiagen
QIAprep Spin Miniprep Kit	Qiagen
ReliaPrep™ RNA Clean-Up and Concentration System	Promega

Kit	Distributor
RiboMAX™ Large Scale RNA Production Systems	Promega
Zero Blunt™ TOPO™ PCR Cloning Kit	Life Technologies

2.1.3. Oligonucleotides

Table 3: DNA Oligonucleotides

Name	Sequence (5′→ 3′)	Description	Manufacturer
SBp#060	GGAGATATACATATGAG	CoV-2 N_IDR1 fw	Sigma Aldrich
SBp#061	TCTCAGTGGTGGTGGTG	CoV-2 N_IDR3 rev	Sigma Aldrich
SBp#063	TACATATGCCGAATAATACCGCAAGCTG	CoV-2 N_RBD fw	Sigma Aldrich
SBp#064	TGCTCGAGAACGGTCTGACCCTGTTG	CoV-2 N_IDR2 rev	Sigma Aldrich
SBp#065	GTGGATCCGAAGGTAGCCGTGGT	CoV-2 N_IDR2 fw	Sigma Aldrich
SBp#066	ATCTCGAGGGCATAAAAACCTTTCG	CoV-2 N_RBD rev	Sigma Aldrich
SBp#073	GAAGGAGATATACATATGACCAAAA AAAGCGCAGCAGAAG	CoV-2 N_CTD fw	Sigma Aldrich
SBp#074	GTGGTGGTGGTGCTCGAGCGGAAATG TTTTATAGGC	CoV-2 N_CTD rev	Sigma Aldrich

Table 4: RNA Oligonucleotides

Name	Sequence (5′→ 3′)	Description	Manufacturer
GFP-PS9	Nt 20,080-21,272 of SARS-CoV-2 3′UTR	Putative packaging signal 9 (PS9) of SARS-CoV-2 (Addgene #177944)	IVT
RNA2	CUGCACCUCAUGGUCAUGUUAUGGUU	SARS-CoV-2 nt 498-520	Sigma Aldrich
RNA20	UUCGUCCGGGUGUGACCGAAAGGUAA	SARS-CoV-2 nt 239-264	Sigma Aldrich
RNA21	UUACCUUUCGGUCACACCCGGACGAA	Complementary to RNA20	Sigma Aldrich
RNA22	CAUAAUAAGAGGCUGGAUUUUUGGUA	SARS-CoV-2 nt 21,859-21,884	Sigma Aldrich
RNA23	UACCAAAAAUCCAGCCUCUUAUUAUG	Complementary to RNA22	Sigma Aldrich
RNA3	AACCAUAACAUGACCAUGAGGUGCAG	Complementary to RNA2	Sigma Aldrich
RNA6	CUGCACCUCAUGGUC	SARS-CoV-2 nt 498-512	Sigma Aldrich

Name	Sequence (5′→ 3′)	Description	Manufacturer
RNA7	GACCAUGAGGUGCAG	Complementary to RNA6	Sigma Aldrich

2.1.4. Proteins/Enzymes

Table 5: Proteins and enzymes

Protein/Enzyme	Manufacturer/Producer
Phusion Polymerase	New England Biolabs
Restriction Enzymes	New England Biolabs
SARS-CoV-2 N_WT	SB – Längst Lab
SARS-CoV-2 N_BA.5	SB – Längst Lab
SARS-CoV-2 N_WT_PM	SB – Längst Lab
SARS-CoV-2 N_BA.5_PM	SB – Längst Lab
SARS-CoV-2 N_RICI	SB – Längst Lab
SARS-CoV-2 N_IRIC	SB – Längst Lab
SARS-CoV-2 N_RIC	SB – Längst Lab
SARS-CoV-2 N_IRI	SB – Längst Lab
SARS-CoV-2 N_RI	SB – Längst Lab
SARS-CoV-2 N_CI	SB – Längst Lab
SARS-CoV-2 N_IC	SB – Längst Lab
SARS-CoV-2 N_RBD	SB – Längst Lab
SARS-CoV-2 N_CTD	SB – Längst Lab
T4 DNA Ligase	New England Biolabs
Taq Polymerase	Längst Lab

2.1.5. Plasmids and G-blocks

Table 6: Plasmids

Plasmid	Insert	Producer
pCDNA3.1-GFP-PS9	Putative packaging signal of SARS-CoV-2 fused to GFP	Addgene
pCR™ Blunt II-TOPO®		Invitrogen
pET21a(+)_SARS-CoV-2_N_BA.5	Full-length SARS-CoV-2 Omicron BA.5 nucleocapsid protein	S. Babl – Längst Lab
pET21a(+)_SARS-CoV-2_N_BA.5_PM	Phosphomimic full-length SARS-CoV-2 Omicron BA.5 nucleocapsid protein	S. Babl – Längst Lab
pET21a(+)_SARS-CoV-2_N_CI	SARS-CoV-2 Wuhan N lacking the IDR1/RBD/IDR2	S. Babl – Längst Lab
pET21a(+)_SARS-CoV-2_N_IC	SARS-CoV-2 Wuhan N lacking the IDR1/RBD/IDR3	S. Babl – Längst Lab
pET21a(+)_SARS-CoV-2_N_IRI	SARS-CoV-2 Wuhan N lacking the CTD/IDR3	S. Babl – Längst Lab
pET21a(+)_SARS-CoV-2_N_IRIC	SARS-CoV-2 Wuhan N lacking the IDR3	S. Babl – Längst Lab

Plasmid	Insert	Producer
pET21a(+)_SARS-CoV-2_N_RBD	SARS-CoV-2 Wuhan N RBD	S. Babl – Längst Lab
pET21a(+)_SARS-CoV-2_N_RI	SARS-CoV-2 Wuhan N lacking the IDR1/CTD/IDR3	S. Babl – Längst Lab
pET21a(+)_SARS-CoV-2_N_RIC	SARS-CoV-2 Wuhan N lacking the IDR1/IDR3	S. Babl – Längst Lab
pET21a(+)_SARS-CoV-2_N_RICI	SARS-CoV-2 Wuhan N lacking the IDR1	S. Babl – Längst Lab
pET21a(+)_SARS-CoV-2_N_WT	Full-length SARS-CoV-2 Wuhan (wildtype) nucleocapsid protein	E. Silberhorn – Längst Lab
pET21a(+)_SARS-CoV-2_N_WT_PM	Phosphomimic full-length SARS-CoV-2 Wuhan (wildtype) nucleocapsid protein	S. Babl – Längst Lab
pRSF-Duet1_SARS-CoV-2_N_CTD	SARS-CoV-2 Wuhan N CTD	Baumeister Lab

Table 7: G-blocks

G-block	Insert	Manufacturer
SB#060s	SARS-CoV-2 Omicron BA.5 N protein	IDT
SB#061s	SARS-CoV-2 Omicron BA.5 N protein phosphomimic	IDT
SB#062s	SARS-CoV-2 Wuhan N protein phosphomimic	IDT

2.1.6. Bacterial strains

Table 8: Bacterial strains

Bacterial strain	Application	Producer
DH5α	General cloning	Längst Lab
JM-109	General cloning	Längst Lab
One Shot™ BL21-AI™	Protein expression	Längst Lab (Invitrogen)

2.1.7. Cell lines

Table 9: Mammalian cell lines

Cell line	Cell type	Tissue	Source
HFF	fibroblast human	foreskin	Work group Prof. H. Wodrich (University of Bordeaux)
MCF-7	epithelial human	breast adenocarcinoma	Work group Prof. M. Kreutz (University hospital)
U2OS	epithelial human	bone osteosarcoma	Work group Prof. H. Wodrich (University of Bordeaux)

2.1.8. Buffers/solutions and media

If not mentioned otherwise, all buffers and media are prepared with water.

Table 10: Buffers and solutions

Buffer/solution	Composition
2xLLPS buffer	100 mM HEPES [pH 7.4] 200 mM NaCl 0.02 % (v/v) Pluronic F-127
Ampicillin (1000x)	50 mg/ml Ampicillin
Annealing buffer (10x)	200 mM Tris-HCl [pH 7.6] 500 mM NaCl 20 mM MgCl2
Chaperone reaction buffer	10 mM Tris [pH 7.6] 50 mM NaCl 0.01% (v/v) Pluronic F-127
Chaperone STOP solution	20 mM Tris [pH 7.6] 2.5 % (w/v) SDS 50 % (v/v) Glycerol 50 mM EDTA
Chloramphenicol (1000x)	50 mg/ml Dissolve in EtOH
Coomassie staining solution	0.25 % (w/v) Coomassie Brilliant Blue R-250 0.25 % (w/v) Coomassie Brilliant BlueG-250 50 % (v/v) Methanol 10 % (v/v) Acetic acid
Elution buffer	50 mM HEPES [pH 7.4] 500 mM NaCl 250 mM Imidazole 10% (v/v) Glycerol
EMSA buffer N-H/HS interactions	50 mM HEPES [pH 7.4] 100 mM NaCl 0.01% (v/v) Pluronic F-127
EMSA buffer N-RNA interactions	0.5x PBS 0.01% Pluronic F-127 5 % (v/v) Glycerol
EX-x buffers	10 mM Tris-HCl [pH 7.6] 1 mM EDTA 1.5 mM MgCl2 10 % (v/v) Glycerol x mM NaCl
His-Tag-Labeling buffer	1x PBS
Kanamycin (1000x)	50 mg/ml Kanamycin
Lämmli buffer (6x)	350 mM Tris-HCl [pH 6.8] 10 % (w/v) SDS 30 % (v/v) Glycerol 5 % (v/v) ß-mercaptoethanol 0.2 % (w/v) Bromphenolblue
Lysis buffer	50 mM HEPES [pH 7.4] 500 mM NaCl 20 mM Imidazole

Buffer/solution	Composition
	10% (v/v) Glycerol 6 M Urea
MST buffer	50 mM Tris-HCl [pH 7.6] 300 mM NaCl 0.1 % (v/v) Pluronic-F127
Orange G loading dye (6x)	10 mM EDTA 50 % (v/v) Glycerol 0.03 % (w/v) Orange G
PBS (10x)	1.37 M NaCl 27 mM KCl 100 mM Na2HPO4 18 mM KH2PO4 pH adjusted to 7.4
SDS Lower Buffer (4x)	1.5 M Tris-HCl [pH 8.8] 0.4 % (w/v) SDS
SDS Running buffer (10x)	25 mM Tris 200 mM Glycerol 0.1 % (w/v) SDS
SDS Upper Buffer (4x)	0.5 M Tris-HCl [pH 6.8] 0.4 % (w/v) SDS
SEC buffer	50 mM HEPES [pH 7.4] 500 mM NaCl 10% Glycerol
TBE (5x)	450 mM Tris 450 mM Boric acid 10 mM EDTA
Tris-HCl	1 M Tris Titrate to required pH with HCl
Wash buffer	50 mM HEPES [pH 7.4] 500 mM NaCl 20 mM Imidazole 10% (v/v) Glycerol 6 M Urea

Table 11: Media

Media	Composition
LB medium	1 % (w/v) Bacto Tryptone 0.5 % (w/v) Bacto Yeast Extract 1 % (w/v) NaCl Autoclave
LB agar plates	LB medium 2 % (w/v) Agar Autoclave Cool to ca. 60°C while stirring, add required antibiotic (50 µg/ml) Pour into petri dishes

Media	Composition
TY medium (2x)	1.6 % (w/v) Bacto Tryptone 1 % (w/v) Bacto Yeast Extract 0.5 % (w/v) NaCl Adjust to pH 7.0 with NaOH Autoclave
DMEM GlutaMAX™, low glucose	Gibco™ Supplemented with 10% FCS (Gibco™)
DMEM, high glucose, GlutaMAX™ Supplement	Gibco™ Supplemented with 10% FCS (Gibco™)

2.1.9. Consumables

Table 12: Consumables

Consumable material	Distributor
Amicon Ultra Centrifugal Filters	Merck
Cell culture plates (24-Well)	Sarstedt
Dialysis membrane (6-8k MWCO)	Spectrum laboratories
Falcon tubes 15 ml, 50 ml	Sarstedt
Filter tips (10, 20, 200, 1000 µl)	Sarstedt
Glass Pasteur pipettes 230 mm	Brand
HiLoad 16/600 Superdex 75 pg	GE Healthcare
Low bind reaction tubes 1.5 ml	Sarstedt
Monolith NT.115 Capillaries (Standard/Premium)	NanoTemper
Ni-NTA beads	Qiagen
Nitrile Gloves	neoLab
Parafilm	Pechiney
Pierce™ High Capacity Endotoxin Removal Spin Column (0.25 ml)	Thermo Scientific
Pipette tips (10, 20, 200, 1000 µl)	Sarstedt
Plastic cuvettes	Sarstedt
Poly-Prep Chromatography Columns, 10 ml	Bio-Rad
Prometheus NT.48 Series High Sensitivity Capillaries	NanoTemper
Prometheus NT.48 Series Standard Capillaries	NanoTemper
Reaction tubes 0.2 ml	Kisker Biotech
Reaction tubes 1.5 ml; 2 ml	Sarstedt
Screenstar Microplate, 384-well	Greiner Bio-one
Serological pipettes 2 ml, 5 ml, 10 ml, 25 ml, 50 ml	Sarstedt
Syringes	BD Biosciences
XCell SureLock Mini gel cassettes	Invitrogen
Zeba™ Spin Desalting Columns 7K MWCO, 0.5 ml	Thermo Scientific
µ-Slide 8-Well ibiTreat	ibidi

2.1.10. Laboratory equipment

Table 13: Laboratory equipment

Equipment	Distributor
-20°C freezer	Bosch
-80°C freezer	Sanyo
100x objective (BZ-PA100, Plan Apochromat 100X Oil)	Keyence
37°C incubator	Memmert
40x objective (BZ-PF40L Plan Fluorite 40X LD PH)	Keyence
4x objective (BZ-PF04P, Plan Fluorite 4x PH)	Keyence
Agarose gel chamber	University of Regensburg
ÄKTApure	GE Healthcare
Autoclave	Zirbus
Bacterial shakers	Eppendorf, HT Infors
Bioruptor Ultrasonicator	Diagenode
BZ-X800 fluorescent microscope	Keyence
C1000 Touch™/S1000™ Thermal Cycler	Bio-Rad
Cell culture CO_2 incubator	Binder
Centrifuges	Beckman Coulter
Confocal microscope	Leika
Cy5 filter. (BZ-X Filter Cy5)	Keyence
DAPI filter (BZ-X Filter DAPI)	Keyence
Gel Shaker Polymax 1040	Heidolph
GelStick Imager	Intas
HERAsafe™ KS Biological Safety Cabinet	Thermo Fisher Scientific
Ice machine	Ziegra
Magnetic stirrer	Heidolph
Microwave	Sharp
Monolith NT.115^{Pico}	NanoTemper
NanoDrop One	Thermo Fisher Scientific™
Neubauer Counting Chamber	Roth
PeqStar PCR Cycler	PeqLab
pH meter	Knick
Pipetboy	Eppendorf
Pipettes 2 µl, 10 µl, 20 µl, 200 µl, 1000 µl	Gilson
Power Supply	GE Healthcare
Prometheus NT.48 nanoDSF	NanoTemper
Prometheus Panta DLS	NanoTemper
PureLab Ultra	ELGA LabWaters VWS
Reax top vortexer	Heidolph
Refrigerator	Liebherr

Equipment	Distributor
Tabletop centrifuge	Eppendorf
Typhoon FLA 9500	Fujifilm
Ultrasonics™ Sonifier™ SFX250	Branson
UVP PCR Hepa Workstation	Analytik Jena

2.1.11. Software

Table 14: Software

Software	Source
BioRender	https://app.biorender.com/
BZ-X800 analysis software	Keyence
Epson Scan	Seiko Epson Corporation
Fiji 2.9.0/1.54f	https://imagej.net/software/fiji/downloads
Geneious 11.0.5	http://www.geneious.com
Microsoft Office 2021 Mac	Microsoft
MO. Affinity Analysis	NanoTemper
NT. Control	NanoTemper
OmniGraffle 7.21	http://www.omnigroup.com/Omnigraffle/
R 4.3.2	R foundation for Statistical Computing, 2023
R.Studio 2023.12.0+369	Posit software, PBC
Typhoon FLA 9500 control software	Fujifilm
Unicorn 7.0	GE Healthcare

2.1.12. R packages

Table 15: R packages

R package	Application	Source
dplyr	Data manipulation	Wickham et al., 2023
forcats	Working with categorial variables	Wickham, 2023
ggplot2	Data visualization	Kassambara, 2023
ggpubr	'ggplot2' based publication ready plots	Kassambara, 2023
grDevices	R graphics devices and support for base and grid graphics	R Core Team, 2023
RColorBrewer	Color palettes	Neuwirth, 2022
tidyverse	Transformation and presentation of data	Wickham et al., 2019

2.2. Methods

2.2.1. DNA methods

2.2.1.1. Restriction enzyme hydrolysis of DNA

DNA digestion using restriction enzymes was conducted either for analytical purposes, such as positive clone identification, or for preparative DNA fragment preparation for cloning.

Table 16 illustrates the pipetting protocols for both types of reactions. Analytical digestions were subjected to a 1h incubation at 37°C, while preparative digestions were left overnight at the same temperature.

Table 16: Restriction digestion mixtures

Component	Analytical	Preparative
DNA	~ 100 ng	5000 ng
10x CutSmart	1 µl	4 µl
Restriction enzyme	0.5 µl each	1 µl each
H_2O	Ad 10 µl	Ad 40 µl
Total volume	10 µl	40 µl

2.2.1.2. Ligation of DNA fragments

T4 DNA Ligase was used to ligate the digested vector and DNA insert fragments. Concentrations were determined using nanodrop measurements. A molar ratio of 1:10 (vector:insert) was chosen and ligation occurred at room temperature (RT) for a minimum of 1h before transformation (2.2.1.7). Half of the ligation mixture was used for transformation. Refer to Table 17 for the pipetting scheme of the ligation reaction.

Table 17: Ligation mixture

Component	Required amount
Vector DNA	100 ng
Insert DNA	x ng
10x T4 Ligase buffer	1 µl
T4 DNA Ligase	0.5 µl
H_2O	Ad 10 µl
Total volume	10 µl

2.2.1.3. TOPO cloning

The linear IDT G-block DNA fragments (Table 7) were preserved by cloning into the pCR™ Blunt II-TOPO® vector using the Zero Blunt® TOPO® PCR Cloning Kit. Next, specific DNA

inserts were PCR-amplified (2.2.1.4), analyzed by agarose gel electrophoresis (2.2.1.6) and purified via gel elution (2.2.1.8.5) if nonspecific products were detected. Clean PCR products were directly employed for TOPO cloning. Subsequently, either 4 µl of gel-eluted PCR product or 1 µl of fresh PCR product was utilized for TOPO reaction (Table 18). The reaction was incubated for 30 minutes at room temperature and subsequently transformed into JM-109 chemically competent cells.

Table 18: TOPO cloning reaction

Component	Volume	
Gel eluted PCR product	4 µl	/
Fresh PCR product	/	1 µl
Salt solution	1 µl	1 µl
H_2O	/	3 µl
pCR™II-Blunt-TOPO®	1 µl	1 µl
Total volume	6 µl	

2.2.1.4. Polymerase chain reaction (PCR)

Polymerase chain reaction (PCR) was performed to amplify DNA fragments required for cloning attempts. Inserts for N (truncation-) protein sequence cloning were produced by PCR. Each reaction comprised 5x Phusion buffer, dNTPs, forward and reverse primers, template DNA, and the Phusion polymerase (NEB). Primer and template selection depended on the fragment to be generated, with a typical range between 55 and 65°C. A standard PCR setup and PCR program for amplification are shown in Table 19 and Table 20. PCR samples were run in a Bio-Rad C1000 Touch™ /S1000™ PCR cycler.

Table 19: PCR setup

Reagent	Volume
5x Phusion buffer	10 µl
dNTPs (10 mM)	1 µl
Primer fw (10 µM)	2.5 µl
Primer rev (10 µM)	2.5 µl
Phusion Polymerase	0.5 µl
Template DNA (1 ng/µl)	5 µl
H_2O	Ad 50 µl
Total volume	50 µl

Table 20: PCR program

Step	Temperature	Duration	Cycles
Initial	95°C	5′	
Denaturation	95°C	30s	
Annealing	55-65°C	30s	30
Extension	72°C	30s	
Final	72°C	10′	
Hold	12°C	∞	

2.2.1.5. Colony PCR

Colony PCR was performed to quickly identify positive clones. Initially, a colony was picked and suspended in water, followed by the addition of the PCR master mix, inclusive of Taq

polymerase, Taq buffer, forward and reverse primer, and dNTPs (Table 21). The primer used for the colony PCR were depending on the template. The PCR protocol is outlined in Table 22. Positive clones were used for inoculation of bacterial liquid cultures to perform DNA isolation (2.2.1.8).

Table 21: Colony PCR set-up

Reagent	Volume
10x Taq buffer	5 µl
dNTPs (10 mM)	0.5 µl
Primer fw (10 µM)	2.5 µl
Primer rev (10 µM)	2.5 µl
Taq polymerase	1 µl
H_2O + colony	38.5 µl
Total volume	50 µl

Table 22: Colony PCR program

Step	Temperature	Duration	Cycles
Initial	95°C	5′	
Denaturation	95°C	30s	30
Annealing	63°C	30s	
Extension	72°C	30s	
Final Extension	72°C	10′	
Hold	12°C	∞	

2.2.1.6. Agarose gel electrophoresis

Agarose gel electrophoresis was carried out for analytical and preparative analysis of DNA fragments, utilizing agarose gels of varying percentages based on the experimental needs. A standard 1 % agarose gel was prepared by solving 0.5 g of agarose in 50 ml of 1x TBE by heating. To visualize DNA, 5 µl of SYBR Safe (ThermoFisher Scientific) (1: 10,000) was added to the gel. DNA samples were mixed with 6x Orange G loading dye prior to loading onto the gel. The GeneRuler 1kb Plus DNA Ladder (ThermoFisher Scientific) served as a DNA standard. Agarose gel electrophoresis occurred for 30 min at 120 V in 1x TBE buffer and was documented with the Intas GelStick Imager.

2.2.1.7. Transformation of chemically competent *E. coli*

For plasmid transformation, a 50 µl aliquot of chemically competent *E. coli* was thawed on ice. Subsequently, 100 ng of DNA or 5 µl of a ligation mix (2.2.1.2) was added. The tube was gently flicked 4-5 times to ensure thorough mixing of cells and DNA. The mixture was then incubated on ice for 20 minutes. Afterwards, heat shock was applied at 42°C for 40s followed by a 5 min incubation on ice. Subsequently, cells were resuspended in 200 µl of LB_0 and then incubated for 1 hour at 37°C. The entire suspension was plated onto pre-warmed selection plates and left to incubate overnight at 37°C.

2.2.1.8. Isolation and purification of DNA

2.2.1.8.1. Small-scale preparation of DNA

To carry out a small-scale DNA preparation, 5 ml LB medium supplemented with the suitable antibiotic was inoculated with a single bacterial colony and left to incubate overnight at 37°C. The isolation of plasmid DNA was conducted using the QIAprep Spin Miniprep Kit from QIAgen, following the manufacturer's instructions. The DNA was eluted in 50 µl of EB buffer.

2.2.1.8.2. Mid-scale preparation of DNA

To carry out a mid-scale DNA preparation, 50 ml LB medium supplemented with the suitable antibiotic was inoculated with a single bacterial colony and left to incubate overnight at 37°C. The isolation of plasmid DNA was conducted using the QIAprep Plasmid Plus Midi Kit from QIAgen, following the manufacturer's instructions. The DNA was eluted in 100 µl of EB buffer.

2.2.1.8.3. Large-scale preparation of DNA

To carry out a large-scale DNA preparation, 500 ml LB medium supplemented with the suitable antibiotic was inoculated with a 5 ml preculture of a single bacterial colony and left to incubate overnight at 37°C. The isolation of plasmid DNA was conducted using the PureLink HiPure Plasmid Filter Maxiprep Kit from Invitrogen, following the manufacturer's instructions. The DNA was eluted in 200 µl of EB buffer.

2.2.1.8.4. Precipitation of PCR-generated DNA fragments

To eliminate any remaining dNTPs and primers, PCR products underwent purification via isopropanol precipitation using ammonium acetate. All samples, identified with the correct band size, were combined in a suitable reaction tube. Subsequently, 0.8x volumes of isopropanol, 1/3 volumes of 7.5 M ammonium acetate, and 1 µl per ml of PCR sample of 2% glycogen were added. After thorough mixing and incubation for 20 minutes to overnight at -20°C, the samples were centrifuged for 30 minutes at 15,000 rcf and 4°C. The resulting pellet was washed twice with 70% ethanol, with centrifugation steps in between (15,000 rcf, 15 minutes, 4°C). Finally, the pellet was air-dried and dissolved in 100 µl of EB buffer.

2.2.1.8.5. DNA isolation from agarose gels

Following the separation of DNA fragments on an agarose gel (2.2.1.6), the fragments of interest were carefully excised using a sharp scalpel. Subsequently, the gel slices containing the DNA were purified using the QIAquick Gel Extraction Kit from QIAgen, following the manufacturer's instructions.

2.2.1.9. Quantification of DNA

DNA concentration and purity measurements were performed using a Nanodrop spectrophotometer. Prior to sample measurements, the device was blanked with 1-2 µl of sample buffer. For concentration determination, a small volume of 1-2 µl of DNA is required. Absorbance at wavelengths of 260 nm, where DNA absorbs light, and 280 nm, where proteins absorb light, was detected. The ratio of absorbance at 260 nm to 280 nm provides an indication of DNA purity, with values around 1.8 considered optimal for pure DNA.

2.2.2. RNA methods

2.2.2.1. Annealing of dsRNA

To anneal two ssRNAs, equimolar ratios (1 µM each) of unlabeled and labelled ssRNA were mixed in annealing buffer (100 mM HEPES pH 7.4, 100 mM NaCl, 10 mM $MgCl_2$). The mixture was heated to 95°C for 2 min and allowed to slowly cool down to 25°C. The annealed dsRNA sample was analyzed on an 8% native polyacrylamide gel and visualized using the Typhoon™ FLA 9500 (GE Healthcare) fluorescent readout.

2.2.2.2. *In vitro* transcription (IVT) and purification of RNA

In order to study protein-RNA interaction, longer RNA fragments were transcribed *in vitro* from a linearized template using the RiboMax T7 Transcription kit (Promega) according to the manufacturer's instructions. Each reaction contained 1 µg of linearized template to generate either unmodified or Cy3/Cy5-labelled RNA, with setup protocols outlined in Table 23 and Table 24. During IVT, Cy3/Cy5 was incorporated by using Cy3/Cy5-labelled UTP at a ratio of 1:10 compared to unmodified UTP.

Table 23: IVT setup for unmodified RNA

Reagent	Volume
T7 buffer 5x	6 µl
rNTPs (25 mM ATP, CTP,	7.5 µl
UTP (25 mM)	5 µl
Linearized template	x µl
Enzyme mix	2 µl
H_2O	Ad 30 µl
Total volume	30 µl

Table 24: IVT setup for fluorescently labelled RNA

Reagent	Volume
T7 buffer 5x	6 µl
rNTPs (25 mM ATP, CTP,	7.5 µl
UTP (25 mM)	5 µl
UTP-Cy3/Cy5 (5 mM)	0.5 µl
Linearized template	x µl
Enzyme mix	2 µl
H_2O	Ad 30 µl
Total volume	30 µl

The IVT reaction was incubated for 3 h at 37°C followed by a DNase digestion (1 µl/µg of template) for 15 min at 37°C. Afterwards, RNA was purified using the ReliaPrep Kit (Promega) following the manufacturer's instructions. Successful IVT and purification was confirmed by analyzing samples on an 1% agarose gel.

2.2.3. Protein methods

2.2.3.1. Expression of SARS-CoV-2 nucleocapsid proteins

The SARS-CoV-2 nucleocapsid protein and its protein truncations were produced using *E. coli* BL21-AI™ One Shot™ chemically competent cells. Bacterial transformation followed the protocol outlined in 2.2.1.7. Subsequently, 2-3 colonies were selected from the transformation plate and inoculated into a 3 ml $2xTY_{Amp/Cam}$ pre-culture, which was then allowed to grow for 2-3 hours. The main culture, consisting of 500 ml $2xTY_{Amp/Cam}$, was inoculated with the pre-culture and maintained at 30°C until the OD_{600} reached a range of 0.5 to 0.8. Protein expression was induced by supplementing the growth medium with 0.5 g/L arabinose and 1 mM IPTG. The induced culture was then incubated for 16 hours at 20°C. Post-expression, cells were pelleted for 30 minutes at 15,000 g at 4°C, followed by snap freezing in liquid nitrogen for storage at -80°C until purification.

2.2.3.2. Purification of SARS-CoV-2 nucleocapsid proteins

2.2.3.2.1. Ni-NTA purification

As a first step, expression pellets were resuspended in a denaturing buffer (50 mM HEPES pH 7.4, 500 mM NaCl, 20 mM Imidazole, 6 M Urea) to facilitate cell lysis. The sample underwent three cycles of freeze and thaw with liquid nitrogen and warm water. Afterwards, sonication

was performed for 5 min at 30 % amplitude using the Branson Ultrasonics™ Sonifier™ SFX250. Following sonication, the bacterial lysate was centrifuged for 45 min at 15,000 g at 4°C. The supernatant was then transferred to a fresh falcon tube and mixed with 2 ml of Ni-NTA agarose beads (QIAGEN), followed by overnight incubation at 4°C with gentle rotation. Prior to this, the beads were prepared by discarding the storage solution and equilibrating them with the lysis buffer. The following day, the sample was passed through a 10 ml gravity flow column, and the flow through was collected. The beads were washed three times with wash buffer (50 mM HEPES pH 7.4, 500 mM NaCl, 20 mM Imidazole, 6 M Urea) followed by elution in four steps with 1 ml elution buffer (50 mM HEPES, 500 mM NaCl, 250 mM Imidazole, 6 M Urea) each. Purification success was assessed by analyzing samples on an SDS gel (2.2.3.3). Elution fractions containing the pure protein of interest were pooled and dialyzed into SEC buffer (50 mM HEPES pH 7.4, 500 mM NaCl, 10% glycerol) before further applications. While full-length nucleocapsid proteins from the Wuhan WT and the Omicron BA.5 variant underwent further gel filtration chromatography (2.2.3.2.2), all truncated proteins were directly utilized for further applications following Ni-NTA purification. Concentration of the truncation proteins was determined (2.2.3.5) after which they were aliquoted, snap frozen in liquid nitrogen and stored at -80°C.

2.2.3.2.2. Size exclusion chromatography

As an additional purification step, full-length nucleocapsid proteins from both the Wuhan WT and Omicron BA.5 strains, were subject to size exclusion chromatography (SEC). Therefore, proteins were applied to a Superdex 16/600 75 pg (GE Healthcare) gel filtration column connected to the ÄKTApure system (GE Healthcare). Size exclusion was carried out in SEC buffer (50 mM HEPES pH 7.4, 500 mM NaCl, 10% glycerol) utilizing the protocol outlined in Table 25.

Table 25: SEC purification protocol

Purification step	**Settings**	
Method setting	Technique	SEC
	Column type	HiLoad 16/600 Superdex 75 pg
	Column volume	120.637 ml
	Pressure limit pre-column	0.5 MPa
	Pressure limit delta-column	0.3 MPa
	Flow rate	1 ml/min
	Inlet	A1, B1
	UV wavelength	UV 1: 280 nm UV 2: 260 nm

Equilibration	UV Monitor	Reset
	Flow rate	As method settings; 1 ml/min
	Inlets	A1, B1 (0%)
	Volume	0.2 CV
Sample application	Flow rate	1 ml/min
	Sample injection	Inject sample from loop Fill loop: manual load Loop type: capillary loop Empty loop with 2 ml
	Fractionate	Waste
Elution	Flow rate	1 ml/min
	Inlets	A1, B1 (0%)
	Volume	1.1 CV
	Start Fractionation	After 0.2 CV
	Fractionate	Fraction collector; 2 ml

The gel elution fractions were analyzed on an SDS gel and those containing the desired pure protein were pooled and the concentration was measured. Subsequently, the protein was either divided into aliquots or concentrated using Amicon Ultra Centrifugal Filters (Merck) before aliquoting. Protein aliquots were snap frozen in liquid nitrogen and stored at -80°C.

2.2.3.3. SDS PAGE

Sodium dodecyl sulfate polyacrylamide gel electrophoresis (SDS-PAGE) was performed to assess the quantity and purity of proteins under denaturing conditions. For the purified SARS-CoV-2 nucleocapsid (truncation-) proteins, the percentage of the SDS gel varied depending on protein size, typically 12% or 15% separating gel with a 4% stacking gel for each. Gels were prepared in Novex XCell SureLock Mini gel cassettes by filling them up to ¾ with separating gel and overlaying them with isopropanol. Upon polymerization, the isopropanol was removed, and the cassettes were filled with the stacking gel, with 10-well combs inserted. The compositions of separating and stacking gel are provided in Table 26.

Table 26: Composition of SDS gels

Component	Separating gel (12%)	Separating gel (15%)	Stacking gel (4%)
Rotiphorese Gel 30	2.4 ml	3.0 ml	250 µl
SDS lower buffer (4x)	1.5 ml	1.5 ml	-
SDS upper buffer (4x)	-	-	380µl
20% APS	30 µl	30 µl	7.5 µl
TEMED	6 µl	6 µl	1.5 µl
H_2O	2.06 ml	1.46 ml	870 µl
Total volume	6 ml	6 ml	1.5 ml

Prior to running the SDS-PAGE, samples were mixed with 6xLämmli and denatured at 100°C for 10 min. Meanwhile, the running chamber was filled with 1x SDS running buffer, the cassette

was inserted, and the comb removed. Typically, 10 µl of sample and 2 µl of the BlueEasy Protein ladder for size estimation were applied to the gel. The gel was run at 300 V and 45 mA per gel for 45 minutes. Following the run, the gel was stained with Coomassie staining solution for approximately 5 min and destained in H_2O by repeated heating, subsequently. Fully destained gels were documented using a conventional office scanner.

2.2.3.4. Native PAGE

NativePAGE 4-16% Bis-Tris-gels (Invitrogen™) were used to identify the native protein size and the oligomerization status of N (truncation-) proteins under non-denaturing conditions. In contrast to SDS PAGE, where SDS is used to denature the proteins and charge them negatively in order to migrate towards the anode, Native PAGE is based on the usage of Coomassie G-250 as a molecule for charge displacement, whereby the protein stays in its native conformation. Of each protein, 5 µg were applied to the native gels along with 5 µl of the NativeMark™ (Invitrogen™) unstained protein standard. Native PAGE was performed for 2h at 150V.

2.2.3.5. Quantification of proteins

To quantify protein concentration, the Bradford assay was used. This assay relies on the interaction between protein molecules and Coomassie dye under acidic conditions, resulting in a color change. The Protein Assay Dye Reagent Concentrate (Bio-Rad) was diluted 1:5 with ddH2O. Each sample was assessed by filling a plastic cuvette with 1 ml of Bradford reagent. Bovine serum albumin (BSA) was utilized as a standard for generating a calibration curve, with various concentrations (0 mg, 1 mg, 2.5 mg, 5 mg, 15 mg, and 50 mg) prepared by adding 10 µl of ddH2O and different amounts of BSA to the cuvettes. For determination of the desired protein concentration, 2 to 10 µl of protein solution were tested. A cuvette containing only water served as a blank for the spectrophotometer. Absorption readings of the samples were taken at 450 nm and 590 nm. The results were analyzed in Microsoft Excel, where the A590/A450 ratio was calculated for each sample. The quotient obtained from the cuvette with 0 mg/ml BSA was subtracted from each sample's ratio to obtain corrected values. Subsequently, each total BSA amount was divided by the corresponding corrected A590/A450 ratio, and an average was computed. The total protein amount was then determined by multiplying the corrected values of the protein samples by this average. Finally, the protein concentration was calculated by dividing the total amount by the volume used.

2.2.3.6. Buffer exchange of proteins by dialysis

Following Ni-NTA purification of N (truncation-)proteins, the present imidazole needed to be removed for further applications, and samples were dialyzed into SEC buffer (50 mM HEPES pH 7.4, 500 mM NaCl, 10 % glycerol). Depending on the molecular weight of the protein, dialysis membranes with a molecular weight cut-off of either 6-8 kDa or 12-14 kDa (Spectrapor) were used. The samples were filled into the dialysis tubing and placed into a beaker containing the desired buffer at 4°C. Buffer was exchanged at least three times with a final overnight dialysis step.

2.2.3.7. Fluorescent protein labelling

Fluorescent labelling of the nucleocapsid (truncation-) proteins was required to study interactions with heparin, heparan sulfate, or RNA in EMSA or LLPS experiments as well as for immunofluorescent imaging on cells. Labelling occurred either at present lysine residues or at the attached C-terminal 6xHis tag.

For lysine labelling, protein and DY647-P1 dye (Dyomics) were mixed in a 1:1 ratio in 100 µl 2xLLPS buffer (100 mM HEPES pH 7.4, 200 mM NaCl, 0.02% Pluronic F-127) and incubated for 30 min at RT in the dark. A typical labelling reaction contained 25-50 µM of protein with equal amounts of 647-dye. Afterwards, any remaining free dye was removed by passing the labelling sample through Zeba™ Spin Desalting Spin Columns 7K MWCO (Thermo Scientific™). Following centrifugation at 1,500 g for 1.5 min, the fluorescently labelled protein was either used directly or stored at -20°C.

His-tag labelling was performed using the His-Tag Labeling Kit RED-tris-NTA 2nd Generation (NanoTemper) according to the manufacturer's instructions. A total of 200 nM N protein was mixed with a total of 100 nM NT-647-His labelling dye in a volume of 100 µl PBS. The sample was then incubated for 30 min at RT in the dark and subsequently centrifuged (10 min, 15,000 g, 4°C). Following centrifugation, the labelled protein was either used directly or stored at -20°C.

2.2.3.8. Endotoxin removal

To eliminate any potentially attached endotoxin residues remaining from bacterial expression of the N protein, endotoxin removal was performed prior to immune assays. For this, Pierce High-Capacity Endotoxin Removal Spin Columns were used for this purpose, following the

manufacturer's instructions. Afterwards, both Wuhan wildtype and Omicron BA.5 N proteins were stored in endotoxin-free PBS.

2.2.4. Methods to study protein interactions

2.2.4.1. Nano differential scanning fluorimetry (nanoDSF)

Nano differential scanning fluorimetry (nanoDSF) is a technique used to monitor protein stability by detecting changes in intrinsic fluorescence, particularly from tryptophan and tyrosine residues, at 330 and 350 nm, along a given temperature gradient. In a hydrophobic environment, such as within a folded protein, tryptophan residues exhibit an emission maximum at 330 nm. As the protein unfolds at a certain temperature, the tryptophan residues initially facing inwards become exposed to the hydrophilic environment, resulting in an emission maximum of 350 nm. By plotting the fluorescence signals of the 350/330 nm ratio, the onset, peak, and completion of protein unfolding can be determined.

In this study, nanoDSF was used to determine overall protein stability of all N (truncation-) proteins, also as part of protein quality control, and to investigate the changes in protein stability and affected protein domains upon heparin or heparan sulfate binding. Additionally, inhibitors, directed against N and heparin/heparan sulfate LLPS, received from an inhibitor library screen, were analyzed by nanoDSF.

For each measurement, 10 µM of protein was prepared in a total of 20 µl assay buffer (50 mM HEPES pH 7.4, 100 mM NaCl, 0.01% Pluronic F-127) with or without 5 µM heparin/heparan sulfate being present and split into two Prometheus High Sensitivity Capillaries (NanoTemper). Capillaries were loaded into the Prometheus NT.48 device (NanoTemper). Measurements were carried out at 60-85% laser intensity, depending on the protein used, and an unfolding temperature range from 25-95°C with 1°C/min followed by a subsequent vice versa refolding ramp.

2.2.4.2. Dynamic light scattering (DLS)

Dynamic light scattering (DLS) is a technique used to determine the sizes of particles in the scale of nm to µm in solution. Specifically, DLS measures the translational diffusion coefficient, which is correlated with the hydrodynamic radius of a particle. At its core, DLS observes fluctuations in the intensity of scattered light caused by particles undergoing Brownian motion. A laser irradiates the sample, scattering light in all directions as it encounters molecules in

solution. The scattered light from each particle interacts with that from others, creating a net intensity of scattered light detected. As particles constantly change positions due to diffusion, intensity fluctuations are detected by the sensor. The timescale of these fluctuations reveals the diffusion behavior of solvated particles, whereby smaller particles exhibit faster fluctuations, while larger particles show slower ones.

Hereby, DLS was used to determine N (truncation-) protein particle sizes and to identify interaction with heparin/heparan.

For each measurement, 10 µM of protein were mixed with 5 µM heparin or heparan sulfate in a total volume of 20 µl assay buffer (50 mM HEPES pH 7.4, 100 mM NaCl, 0.01% Pluronic F-127). Each sample was measured in duplicates by filling 10 µl in Prometheus High Sensitivity Capillaries (NanoTemper). Measurements were carried out at 100% laser intensity at 37°C.

2.2.4.3. MicroScale Thermophoresis (MST)

MicroScale Thermophoresis (MST) measures the binding affinity between molecules in solution by tracking their movement along a temperature gradient. It is based on changes in fluorescent markers to monitor thermophoresis, influenced by molecular size, charge, and solvation. The technique uses an infrared laser to generate the temperature gradient. By observing fluorescence intensity changes, MST aims to quantify the binding of molecules, providing insights into interaction kinetics.

In this study, MST was used to determine binding affinities for the various N (truncation-) proteins towards ssRNA and dsRNA. A constant amount of Cy5-fluorescent RNA was used and the protein of interest was titrated in a 1:2 dilution series in a total volume of 10 µl. Titration ranges for the protein (Table 27), RNA amount (Table 28), and associated LED power for fluorophore emission were determined based on the specific protein and RNA used. The MST assay buffer consisted of 50 mM HEPES, 100 mM NaCl and 0.01%/0.1% Pluronic F-127, depending on the specific RNA. The reactions were incubated for 30 min at RT before being loaded into NT.115 Standard Capillaries (NanoTemper) and analyzed using the Monolith NT.115^{Pico} device (NanoTemper). All measurements were performed in duplicates, with each including two technical replicates, applying a MST power of 40, temperature settings of 22°C or 25°C, and an MST On time of 30 sec. The LED power was adjusted to yield fluorescence counts ranging between 10,000 and 20,000. EC_{50} or K_D determination of the affinity measurement was carried out at 2.5 s MST On Time.

Table 27: Start concentration proteins

Protein name	Concentration
N_WT	40 µM
N_WT_PM	30 µM
N_BA.5	40 µM
N_BA.5_PM	30 µM
N_RICI	40 µM
N_IRIC	40 µM
N_RIC	40 µM
N_IRI	40 µM
N_RI	40 µM
N_CI	30 µM
N_IC	40 µM
N_RBD	40 µM
N_CTD	40 µM

Table 28: RNA concentration

RNA name	Concentration
ssRNA3-Cy5	20 nM
dsRNA3-Cy5	20 nM
ssRNA20-Cy5	5 nM
dsRNA20-Cy5	5 nM
ssRNA22-Cy5	5 nM
dsRNA22-Cy5	5 nM

2.2.4.4. Electrophoretic mobility shift assay (EMSA)

Electrophoretic mobility shift assay (EMSA) is a technique to study protein-nucleic acid and other protein interactions. Typically, a labelled nucleic acid is incubated with the protein of interest. Upon protein binding to the ligand, a shift in the electrophoretic mobility can be detected when applying the sample to a gel. This shift is due to the larger size and altered charge of the established complex compared to the free labelled sample.

2.2.4.4.1. Interactions of the N protein with nucleic acids

In order to study the interaction capabilities of the N (truncation-) proteins with RNA, either single- or double-stranded fluorescently labeled RNA3, was incubated with various concentration of protein. A reaction contained 20 nM of RNA3-Cy5 along with increasing concentrations of protein, ranging from 0.035 µM to 18 µM, in a total of 10 µl assay buffer (0.5x PBS, 0.01% Pluronic F-127, 5 % glycerol). The mixtures were incubated for 90 min at RT. Afterwards, the reaction samples were loaded onto 1 % agarose gels and electrophoresed in 1x TBE for 30 min at 100 V. Gel analysis was done by scanning with the Cy5 laser of the Typhoon™ FLA 9500 fluorescent scanner (GE Healthcare).

2.2.4.4.2. Interaction of the N protein with heparin/heparan sulfate

To detect interactions between the N protein and heparin/heparan sulfate in EMSA, 647-labelled N protein was used. For the reaction, 500 nM N protein was mixed with increasing concentrations of heparin/heparan sulfate, ranging from 0.006 µM to 3.3 µM, in assay buffer (50 mM HEPES pH 7.4, 100 mM NaCl, 0.01% Pluronic F-127). Reactions were incubated for 2h at RT and then applied to a 1.5% agarose gel. Gel electrophoresis occurred at 120 V for 30 min in 1x TBE before being analyzed using the Cy5 laser of the Typhoon™ FLA 9500 fluorescent scanner (GE Healthcare).

2.2.4.4.3. Interaction of the N protein with RNA and heparin/heparan sulfate

To investigate the interaction between the N protein with heparin/heparan sulfate along with RNA, the experiment followed the setup described in 2.2.4.4.3. but with the addition of 40 nM *in vitro* transcribed (2.2.2.2), Cy3-labelled, GFP-PS9 RNA. RNA was visualized by detection with the incorporated Cy3 laser of the Typhoon™ FLA 9500 (GE Healthcare).

2.2.4.5. Chaperone Assay

The chaperone assay, originally developed by Zúñiga et al., 2007 to examine the RNA chaperone activity of N protein in SARS-CoV, was modified for the N protein of SARS-CoV-2 in our laboratory (Bachelor Thesis Julia Seidel, 2021). An RNA master mix, containing two complementary ssRNAs, each labelled with different fluorophores, was heated for 1 min at 95°C and subsequently snap cooled at 4°C. Afterwards, the protein of interest was added to the mixture in a total volume of 10 µl reaction buffer (10 mM Tris pH 7.6, 50 mM NaCl, 0.01% Pluronic F-127). The samples were incubated for 3 min at RT, and reaction was stopped by adding 1 µl of STOP solution (20 mM Tris pH 7.6, 2.5 % SDS, 50 % glycerol, 50 mM EDTA). The samples were then applied onto 6% native polyacrylamide gels and run for 45 min at 100 V in 0.4x TBE. This general experimental setup applies to all experiments described in this section.

2.2.4.5.1. Chaperone assay of the N protein with RNA

Different RNAs were used to assess the RNA chaperone activity of the N protein. One complementary consisted of ssRNA3-Cy3 and ssRNA6-Cy5, of which 100 nM of RNA3-Cy3 were mixed with 125 nM ssRNA6-Cy5. For ssRNA20-Cy5 and ssRNA21, 100 nM ssRNA20-Cy5

and 125 nM ssRNA21 were used. RNA master mixes were incubated with 0.0016 μM to 1 μM of N protein.

2.2.4.5.2. Chaperone assay in presence of inhibitors

The N protein's RNA chaperone activity in presence of N-RNA LLPS inhibitors was investigated. Specifically, 100 nM RNA3-Cy3 and 125 nM RNA6-Cy5 were mixed with 500 nM of N protein in presence of increasing inhibitor concentrations, ranging from 10 – 80 μM.

2.2.4.6. *In vitro* liquid-liquid phase separation (LLPS)

Liquid-liquid phase separation (LLPS) is a phenomenon where certain molecules within a solution segregate into distinct liquid phases. This process is driven by various factors such as molecular interactions, protein conformational changes, and environmental conditions like concentration and temperature. LLPS is important in cellular biology, particularly in forming membraneless organelles such as nucleoli.

In the present study, an *in vitro* LLPS approach was used to examine the interaction between N and RNA as well as between N and heparin/heparan sulfate. Additionally, specific LLPS inhibitors were characterized regarding their impact in this established assay. All further described LLPS experiments were carried out in a 384-well plate with a total well volume of 12 μl. Reactions were incubated for 2h at RT or 37°C before observing droplet formation using fluorescent microscopy (Keyence BZ-X800, Cy5 filter) at 4x (BZ-PF04P Plan Fluorite 4x PH, Keyence) and 40x (BZ-PF40LP Plan Fluorite 40X LD PH, Keyence) magnification. Exposure times were adjusted depending on the labelled interaction partner.

2.2.4.6.1. LLPS of N protein with RNA

For N-RNA interaction studies, each well contained a total 2 μM of ssRNA3 or dsRNA3 spiked with 100 nM of Cy5-labelled RNA and increasing concentrations of N (truncation-) proteins, ranging from 0.25 μM to 8 μM. Reactions were set up in 20 mM Tris pH 7.6, 250 mM NaCl, 0.01% Pluronic F-127.

For determination of LLPS inhibitor function on the assay, 2 μM of N protein was mixed with 100 nM RNA3-Cy5, in the presence of 1.25 μM of inhibitor. As the inhibitors are dissolved in DMSO, the total DMSO concentration was adjusted to 1 % in each well.

2.2.4.6.2. LLPS of N protein with heparin/heparan sulfate

For N-heparin/heparan sulfate studies, each well contained 500 nM N (truncation-) protein with a ratio of Cy5-labelled to unlabelled protein of 1:4 and increasing concentrations of heparin/heparan sulfate, ranging from 0.02 μM to 5 μM. Reactions were set up in 50 mM HEPES pH 7.4, 100 mM NaCl and 0.01% Pluronic F-127. When various N (truncation) proteins were compared, a constant heparin concentration of 50 nM and heparan sulfate concentration of 100 nM was used.

For determination of LLPS inhibitor function on the assay, 500 nM of N protein was mixed with either 50 nM heparin or 100 nM heparan sulfate, in the presence of 6.25 – 100 μM inhibitor. As the inhibitors are dissolved in DMSO, the total DMSO concentration was adjusted to 1 % in each well.

2.2.4.6.3. LLPS inhibitor screen for N-heparin/heparan sulfate interaction

In order to interfere with N-heparin/heparan sulfate LLPS, an inhibitor screen directed against this interaction was performed in collaboration with the Fraunhofer Institute for Toxology and Experimental Medicine (ITEM) Regensburg.

Preparation of assay ready plates from compound library (done by Silvia Materna-Reichelt, Fraunhofer ITEM)

A compound library of 2645 bioactive compounds were purchased from Selleckchem (L1700) in 96-well format. The stock concentration was 10 mM and the drugs were dissolved in either DMSO or water. The library was reformatted into 384-well format, 8 different 384-well source plates were created in ECHO compatible low dead volume plates (Beckman, # 001-16128).

From each of the eight 10 mM stock concentration source plates, 24 nl were transferred into 384-well assay plates (PerkinElmer, # 6057300) in columns 1-22 using an acoustic liquid handler (Labcyte, Echo® 550). From a second ECHO compatible low dead volume plates, 24 nl DMSO (negative control) was transferred into column 23 and 120 nl 10 mM S2485 (positive control) was transferred into column 24. The plates were thermally sealed (Agilent, PlateLoc Thermal Microplate Sealer) and stored at -20°C until usage.

Screening set-up (done by Sabrina Babl and Silvia Materna-Reichelt)

Each of the LLPS binding partners – heparin or heparan sulfate – was screened in a single run at 20 µM final compound concentration. The final DMSO concentration was 1%. Library containing assay ready plates were thawed from -20°C.

The assay mixes were prepared in LLPS buffer (50 mM Hepes at pH 7.4, 100 mM NaCl, 0.01% Pluronic-F127). For heparin assay mix, 50 nM of heparin and 375 nM of unlabeled BA.5 N-protein as well as 125 nM of 647-labelled BA.5 N-protein were mixed prior addition to assay ready plates. For heparan sulfate assay mix, 100 nM of heparan sulfate and 375 nM of unlabelled BA.5 N-protein as well as 125 nM of 647-labelled BA.5 N-protein were mixed freshly. Using a liquid dispenser (Multidrop Combi, Thermo Scientific™), 12 µl of the appropriate assay mix were added to column 24 of all library plates first. To the remaining mix, DMSO was added to a final concentration of 0.8%. Of this mix, 12 µl were added to columns 1-23. The plates were sealed using a transparent sealing tape and the plate lid was put. After 3h incubation in the dark, the plates were imaged using a high-content imaging platform (PerkinElmer, Operetta CLS) in confocal mode at 40x magnification using a water-immersion objective.

Data analysis (done by Durdam Das, Fraunhofer ITEM)

Primary data analysis for extraction of morphological and intensity droplet features per well was performed using Harmony software (PerkinElmer) – building block "find spots" method B. For the final data analysis using R-script, a 2pt-normalization was performed for each feature. From the percent of control (POC) values of relevant features identified by PCA, a score (median of the POC values) was calculated to identify primary hits.

2.2.5. Cell-based methods

2.2.5.1. Cell culture maintenance

Mammalian cell lines MCF-7, U2OS and HFF were used for cell culture experiments within this study. After thawing, MCF-7 were maintained in DMEM, low glucose, GlutaMAX™ Supplement (Gibco™), supplemented with 10 %. HFF cells were maintained in DMEM, high glucose, GlutaMAX™ Supplement (Gibco™), supplemented with 10 % FCS. U2OS were maintained in DMEM, high glucose, GlutaMAX™ Supplement (Gibco™), supplemented with 10 % FCS. All cells were kept at conditions of 37°C and 5 % CO_2.

Cells were split when they reached approximately 85% confluence, typically at a ratio of 1:4 twice a week. The splitting process involved aspirating the medium, rinsing the cells with 1x PBS, trypsinizing with a 0.05% Trypsin solution in 1x PBS, and then incubating them for three minutes at 37°C, 5% CO2. Trypsin was neutralized with four times the volume of the respective medium, and the cells were transferred into a fresh flask. All reagents were pre-warmed to 37°C before usage.

2.2.5.2. Seeding of cells

To prepare cells for experiments, they were trypsinized as described in 2.2.5.1. Afterwards, cells were centrifuged for 3 min at 1000 g and the cell pellet resuspended in fresh medium. Cell counting was done using a Neubauer counting chamber. Approximately 100 µl of cell suspension was transferred to the chamber and cell number in all four small squares was counted and divided by four. The resulting number corresponds to the cell count multiplied with 10^4 per milliliter of cell suspension. Depending on the experiment and according to the determined cell count, cells were seeded into specific culture plates.

2.2.5.3. Immunofluorescence

For immunofluorescence experiments, MCF-7 cells were seeded into µ-Slide 8 Well ibiTreat (ibidi) with 9 x 10^4 cells/ml and 300 µl cell suspension per well. The cells were left to adhere for 24 h at 37°C and 5 % CO_2. For polybrene treatment of cells, in order to neutralize the cell surface, 10 µg/ml polybrene were added to the well and incubated for 1h at 37°C, 5% CO_2. Prior to protein addition, cells were washed with 1x PBS. The experiment itself was carried out with a total of 500 nM 647-labelled N (truncation-) protein in a total volume of 200 µl 1x PBS. Medium was aspirated, the protein solution was added to the corresponding well and incubated for 30 min at 37°C, 5 % CO_2. Afterwards, protein solution was removed, and cells washed three times with 1x PBS prior to cell fixation. Cells were then fixed in 400 µl of 4 % PFA for 15 min at RT. Fixation solution was aspirated and cells were washed three times with 1x PBS. Afterwards, cell nucleoli were stained with 200 µl DAPI solution (5 µg/ml) for 5 min at room temperature. Cells were once again washed three times with 1x PBS.

Visualization of the immunofluorescence was carried out using fluorescent microscopy (Keyence BZ-X800) with phase contrast, Cy5 and DAPI filters at 100x magnification (BZ-PA100 Plan Apochromat 100X Oil, Keyence). Exposure times were adjusted accordingly for each fluorophore.

2.2.5.4. Fluorescence recovery after photobleaching (FRAP)

Fluorescence recovery after photobleaching (FRAP) experiments and their analyses were carried out by Nicolas Landrein (Work group of Prof. H. Wodrich, University of Bordeaux).

One day prior to the experiment, cells were seed into ibidi 6-well slides with 400,000 cells/ml in DMEM, GlutaMAX™, high glucose (Gibco™) and incubated over night at 37°C, 5% CO_2. Prior imaging, the medium was exchanged to complete Fluorobrite™ medium (Gibco™), supplemented with 10% FCS, 1% PenStrep and 25 mM HEPES pH 6.9 and incubated for 1h at 37°C, 5% CO_2. A total of 500 nM of 647-labeled N protein (Wuhan and Omicron BA.5, provided by our laboratory) were added to the cells. FRAP analysis was performed with an SP5 Leica confocal microscope using the Leica FRAP mode. Bleaching of the N protein signal was done at approximately 75% laser power. Postbleach recovery was imaged every 10s for 640s. The intensity of fluorescence is measured in the FRAP area and bleach corrected and normalized to the non-FRAP area. Graphs were generated using jupyter notebook.

2.2.5.5. Protein-mediated cytokine release

N protein-mediated cytokine release assays using LEGENDplex™ (BioLegend) and following analyses were carried out by Antonia Senninger (Work group Prof. R. Wagner, University Hospital Regensburg).

For the assay, 50,000 THP-1 cells per ml were seeded into 96-well plates in 100 µl RPMI-0 medium (Gibco™) and incubated over night at 37°C, 5% CO_2.

On the day of the experiment, the SARS-CoV-2 Wuhan and Omicron BA.5 N proteins were diluted in a 1:2 dilution series starting at 4 µM in 220 µl RPMI-0 medium in a 96-well plate.

Performed in duplicates, 100 µl of the N protein dilutions were transferred to wells with THP-1 cells, leading to a maximum N concentration of 2 µM. Mixtures were incubated for 2h, 4h, 8h, and 24h at 37°C, 5% CO_2. The supernatant was harvested by centrifugation at 300 g for 5 min and subsequently transferred to -80°C until cytokine release measurement. Measurement of released cytokines upon N incubation was performed using the LEGENDplex™ Pre-defined Panel 'Human Inflammation Panel 1', according to the manufacturer's instructions by flow cytometry. Analysis was carried out using the LEGENDplex™ data analysis software.

2.2.6. Quantification, analysis and visualization of data

2.2.6.1. Quantification of LLPS with Fiji

Obtained LLPS microscopy data were analyzed using the Fiji software. For this, a Fiji macro was designed in our laboratory, which automatically counts the formed liquid droplets.
This macro first scans the input directory for required image files which end with "40x.tif. For each matching file, the script follows then a series of image processing steps.
First, a main output directory ("FIJI LLPS Analysis") is created, within the input directory, in which various other subfiles are created. For each image file, the script sets a scale for the picture and adds a scale bar for reference. Next, background subtraction is performed using rolling ball with a radius of 5 pixels. Particles within a size range of 0-3000 pixels and a circularity range of 0-1.0 are analyzed. Next, the particles become colored and counted. Results were visualized with R (2.2.6.3). The analysis results, including particle measurements, are saved as CSV files. The full Fiji Macro script used for this analysis is available under the following link: **https://git.uni-regensburg.de/bas29017/sars-cov-2-nucleocapsid-project.git**

2.2.6.2. Quantification of RNA chaperone activity with Fiji

In order to work out differences in the N (truncation-) protein's RNA chaperone efficiency, assays were quantified using Fiji. The efficiency was determined by the ratio of single-stranded to double-stranded RNA in each lane. For this, each lane was delineated with a rectangle by using the 'Select First Lane' and 'Select Next Lane' function of Fiji. Afterwards, the function 'Plot Lanes' was utilized to generate histograms of the intensities. Next, areas corresponding to the RNA lane were selected by drawing lines and this area was measured using the 'Wand' tracing tool. For each lane, the proportion of dsRNA intensity compared to the total RNA intensity was calculated. Data visualization was done in R (2.2.6.3).

2.2.6.3. Data visualization with R

Data visualization was conducted using R. The R packages used to analyze data and create visualizations are listed in Table 15. Visualizations were designed to illustrate key findings based on the raw data obtained from MST, LLPS, EMSA and DLS. The full R scripts and corresponding datasheets for each figure are available under the following link to enable replication of the visualizations presented in this study:

https://git.uni-regensburg.de/bas29017/sars-cov-2-nucleocapsid-project.git

3. Results

3.1. Generation of SARS-CoV-2 nucleocapsid proteins

To gain further insight into the properties of the SARS-CoV-2 N protein, N proteins of both the original Wuhan strain and the later prevalent Omicron BA.5 strain were prepared. Additionally, a selection of N truncation variants derived from the Wuhan N protein were produced. Throughout this thesis, the N protein from the Wuhan strain is referred to as wildtype (WT) N and that from the Omicron BA.5 strain is referred to as BA.5 N. Furthermore, phosphomimetic variants of both WT and BA.5 N were generated to facilitate further functional analysis.

3.1.1. Generation of the SARS-CoV-2 Wuhan full-length N protein

Following the successful cloning of the full-length WT N protein sequence into the pET21a(+) expression vector (done by Elisabeth Silberhorn), subsequent steps involved expression and purification of the N protein, in accordance with the methodology outlined in sections 2.2.3.1 and 2.2.3.2.

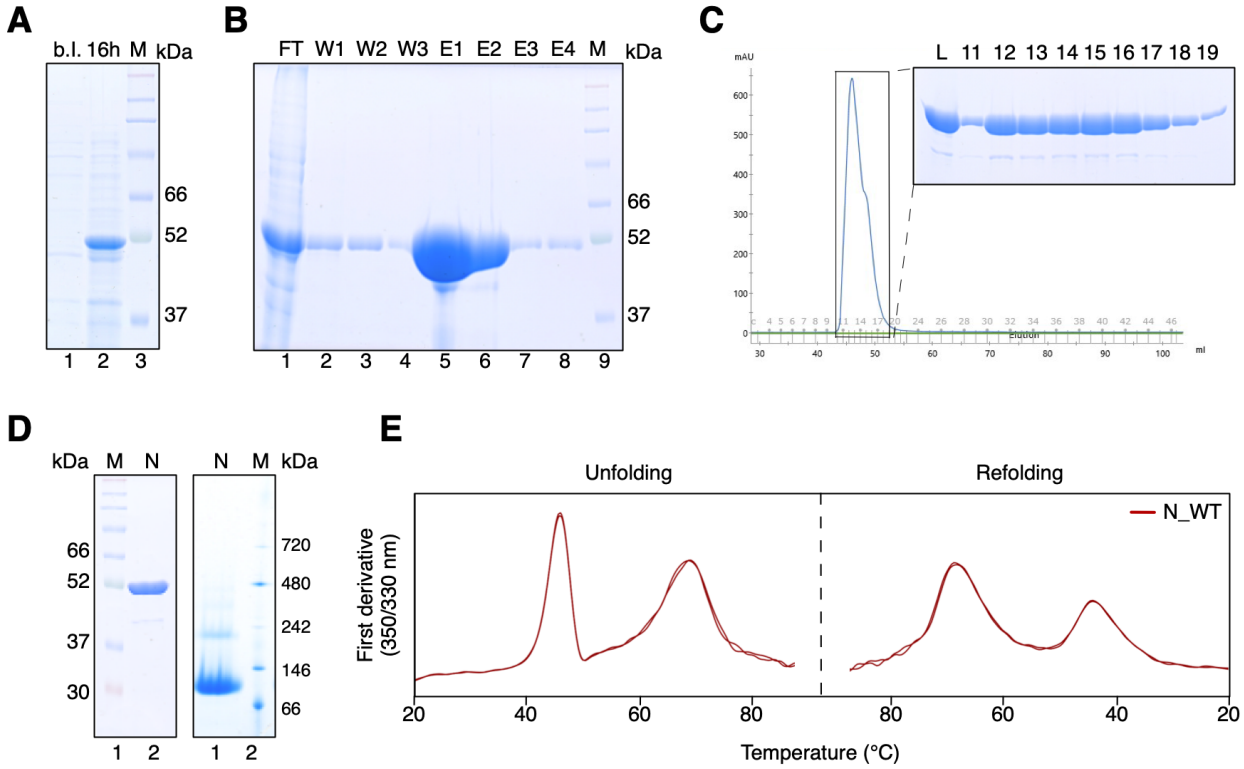

Figure 13: Generation and quality assessment of the SARS-CoV-2 wildtype N protein

(A) 12% SDS gel of recombinant WT N expression. Lane 1 represents sample before induction (b.I.), while lane 2 displays the recombinantly expressed WT N protein 16h after induction, with an estimated molecular weight of 46 kDa. M = Blue Easy Prestained Protein Marker (Nippon Genetics) **(B)** 12% SDS gel of Ni-NTA purification of the WT N protein. Samples of FT (lane 1), W1-3 (lanes 2-4), and E1-4 (lanes 5-8) were applied to the gel. All samples contain

the protein of interest with a maximum elution observed in fractions E1 and E4. The protein size is consistent with the estimated molecular weight, which is 46 kDa. FT = flow through, W = wash, E = elution, M = Blue Easy Prestained Protein Marker (Nippon Genetics). **(C)** Chromatogram and SDS gel of WT N SEC. Elution starts at approximately 43 ml and continues until 53 ml, with fractions 11-19 depicted on the SDS gel. Each fraction contains the protein of interest. L = Load (pooled elution fractions of Ni-NTA purification). **(D)** SDS and native protein gels of SEC-purified WT N protein. The SDS gel (left) exhibits a single distinct band of protein (lane 2). M = Blue Easy Prestained Protein Marker (Nippon Genetics). The native gel (right) displays the native state of the protein, with N present in a majorly dimeric form, as well as in higher oligomeric forms (lane 1). M = Native Mark Proteinstandard (Invitrogen™). **(E)** NanoDSF analysis of WT N. The first derivative of the 350/330 nm ratio along a temperature gradient from 20 – 85°C is shown. WT N protein exhibits two peaks. The first T_M peak at 45°C for the RBD and the second one at 68°C for the CTD of the protein. Refolding of the individual domains with decreasing temperature shows similar T_M peaks as the unfolding.

The expression of the protein resulted in a significant overexpression of N, as evidenced by the presence of an intense protein band observed at the estimated molecular weight of 46 kDa (Figure 13A, lane 2). Purification of the protein utilizing its His tag revealed high and pure amounts of eluted protein in elution fractions E1 and E2 (Figure 13B, lanes 5 and 6). Typically, an expression volume of 800 ml yielded approximately 30 mg of protein. Further purification via size exclusion chromatography (SEC) was conducted for the full-length N proteins. Elution of the protein occurred after approximately 43 ml to 53 ml with a small shoulder appearing in elution fraction 15. Analysis of elution fractions 11 to 19 via SDS gel for analysis confirmed the presence of pure N protein in each lane, with negligible low-molecular-weight contaminants (Figure 13C). Following purification, fractions were pooled, and the final N protein batch underwent analysis via both SDS (Figure 13D, left) and a native (Figure 13D, right) PAA gel electrophoresis. The SDS gel exhibited a single prominent protein band at the expected molecular weight of 46 kDa (lane 2), while in the native state, the predominantly dimeric form of the N protein was observed with a molecular weight of approximately 92 kDa (lane 1). Molecular weights were calculated according to the amino acid constitution. Additionally, the ability of the N protein to form higher oligomers was observed. The N protein contains the two well-structured domains, the RBD and CTD, in addition to highly flexible IDRs. The protein's stability, which is indicative of its quality, can be monitored by thermal unfolding of the structured domains with nanoDSF (2.2.4.1). NanoDSF employs intrinsic tryptophan residues at 330 and 350 nm to monitor protein unfolding over a defined temperature gradient. This study revealed thermal melting temperatures (T_M) of 45°C for the RBD and 68°C for the CTD along with the capacity to properly refold upon a decrease in temperature (Figure 13E).

3.1.2. Generation of SARS-CoV-2 N truncation proteins and variants

In order to identify the location of specific functions of the N protein, a series of truncated proteins lacking one or more specific domains were generated along with the full-length protein of the Omicron BA.5 variant.

Figure 14 illustrates the proteins, which were generated and utilized in this study, with N_WT depicted for reference, showcasing its structured RBD (red) and CTD (grey) domains flanked by the N-terminal IDR1 and the C-terminal IDR2 and linked by the IDR2. Truncated protein nomenclature is based on the remaining domains. Thus, N_RICI lacks the IDR1, N_IRIC the IDR3, N_RIC the IDR1 and IDR3, N_CI the IDR1, RBD and IDR2, N_IC the IDR1, RBD and IDR3, N_IRI the CTD and IDR3, N_RI the IDR1, CTD and IDR3. For N_RBD and N_CTD, only the structured domains were generated. N_BA.5 is analogous to the schematic structure of N_WT.

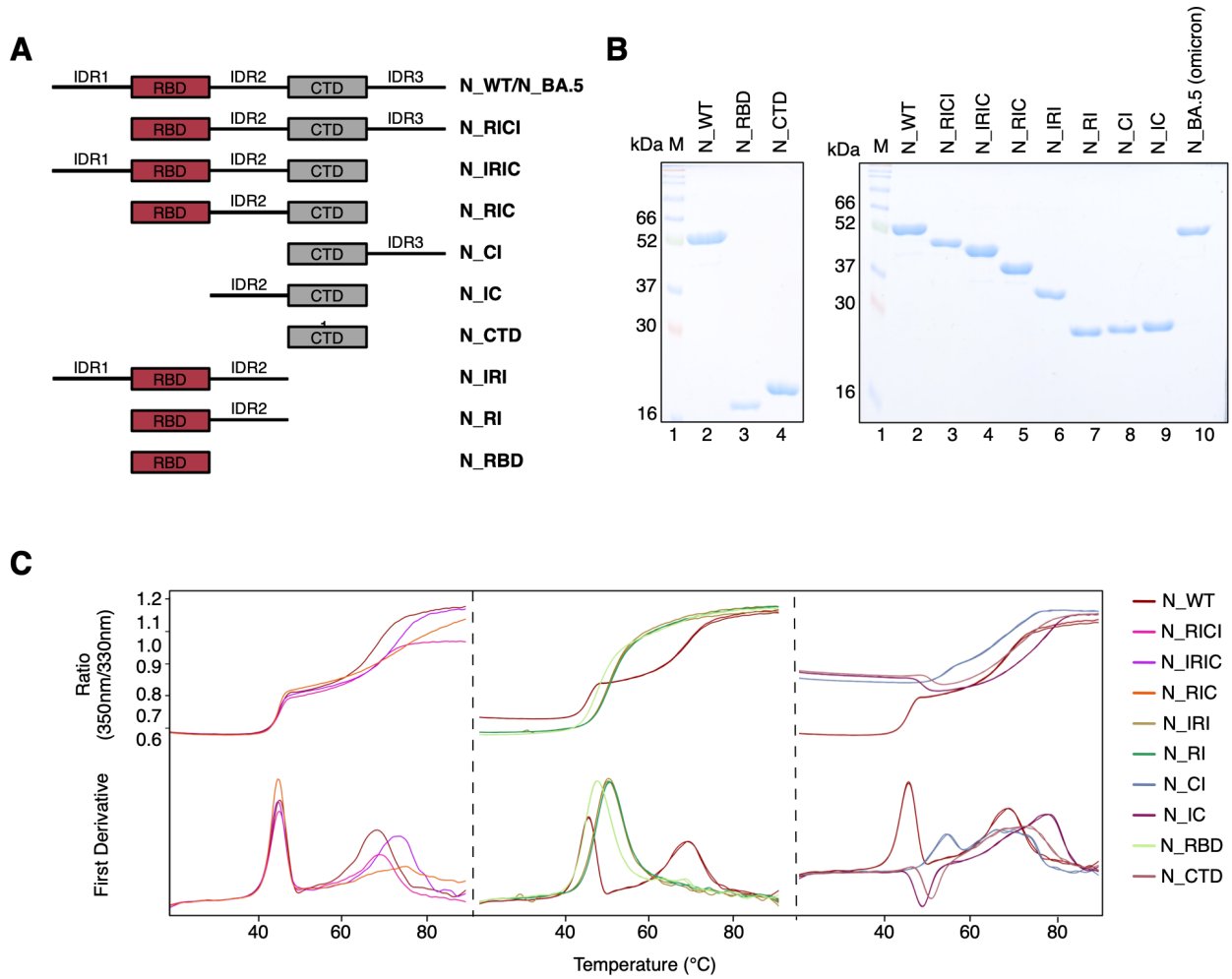

Figure 14: Generated N (truncation) proteins and their respective folding properties

(A) Schematic representation of the generated SARS-CoV-2 N (truncation) proteins with their corresponding nomenclature. Designation of the protein is based on the remaining domains. N = nucleocapsid, R = RBD, I = IDR, C = CTD. **(B)** SDS-PAGE gel analysis of purified recombinant N (truncation) proteins. A total of 2 µg of each protein was applied to a 15% SDS gel. The observed protein bands align with the calculated molecular weights.

(C) Assessment of protein stability of N (truncation) proteins using nanoDSF. 10 μM of each protein were loaded into Prometheus™ NT.48 Standard Capillaries (NanoTemper) and subjected to a temperature gradient ranging from 25-95°C using the Prometheus™ NT.48 device (TanoTemper). The unfolding process was monitored in real-time by measuring changes in the intrinsic tryptophan fluorescence at 350 nm and 330 nm. The ratio of these wavelengths and the corresponding first derivative were employed to ascertain the T_M of the specific folded protein domains. For N_WT (dark red), the structured RBD and CTD domains unfold at 45°C and 68°C, respectively. The truncation of specific protein regions resulted in alterations of the unfolding behavior.

All N protein truncations and the BA.5 variant were expressed and purified in accordance with the methodology described in sections 2.2.3.1 and 2.2.3.2 and as mentioned in section 3.1.1. The truncation proteins were not subjected to additional SEC purification but were pooled, aliquoted and stored at -80°C after Ni-NTA purification. For the generated proteins, similar amounts were subjected to SDS (Figure 14B) and native PAA gel analysis (Supplementary Figure 1A,B). For each protein, a specific single protein band can be observed in SDS-PAGE, which corresponds to the estimated molecular weight of the respective protein. The calculated molecular weights of the proteins without the His tag were determined according to the amino acid constitution and are as follows: 46 kDa for N_WT and N_BA.5, 41 kDa for N_RICI, 42 kDa for N_IRIC, 36 kDa for N_RIC, 27 kDa for N_IRI, 22 kDa for N_RI, 20 kDa for N_CI, 22 kDa for N_IC, 15 kDa for N_CTD, and 14 kDa for N_RBD.

Prior to functional assays, the generated proteins underwent correct folding assessment by nanoDSF (Figure 14C). As previously stated in 3.1.1, N_WT (dark red) displays two distinct peaks for the RBD and CTD. The single folded domains N_RBD (light green) and N_CTD (brown) exhibit a single T_M peak and comparable T_M values to N_WT, indicating similar folding and stability properties. N_RICI (pink) behaves similarly to N_WT while N_IRIC (purple) and N_RIC (orange) exhibit a rightward shift of the CTD T_M. N_IRI (olive) and N_RI (green), which lack the CTD, exhibited an elevated T_M of the RBD compared to N_RBD and N_WT. The CTD peak of N_IC (dark purple) shifted 5°C to the right, while N_CI (grey-blue) retained the CTD T_M of N_CTD. Overall, the structured domains remained folded in the N truncation variants, with changes in the T_M indicating a stronger interaction between the remaining domains. Furthermore, all of the generated proteins were capable of refolding after thermal unfolding (Supplementary Figure 1C), making them suitable for further functional studies.

3.1.3. Generation of phosphomimetic variants of the SARS-CoV-2 Wuhan and Omicron BA.5 N protein

To address the functional role of post-translational phosphorylation on the activity of the SARS-CoV-2 N protein within both the Wuhan and Omicron BA.5 variants, pseudo-phosphorylated N

proteins were generated. Given the absence of natural post-translational modifications in proteins expressed in *E. coli*, pseudo-phosphorylation was introduced by mimicking the phosphorylation status by substituting specific serine and threonine residues with aspartic acid in order to obtain negatively charged residues. These substitutions were chosen based on documented phosphoproteomic analyses (Yaron et al., 2022). The exchanged amino acids included S23, T141, S176, S180, T198, S201, S202, S206 in the case of N_WT and S23, T138, S173, S177, S180, S195, S198, S202, S203 in the case of N_BA.5.

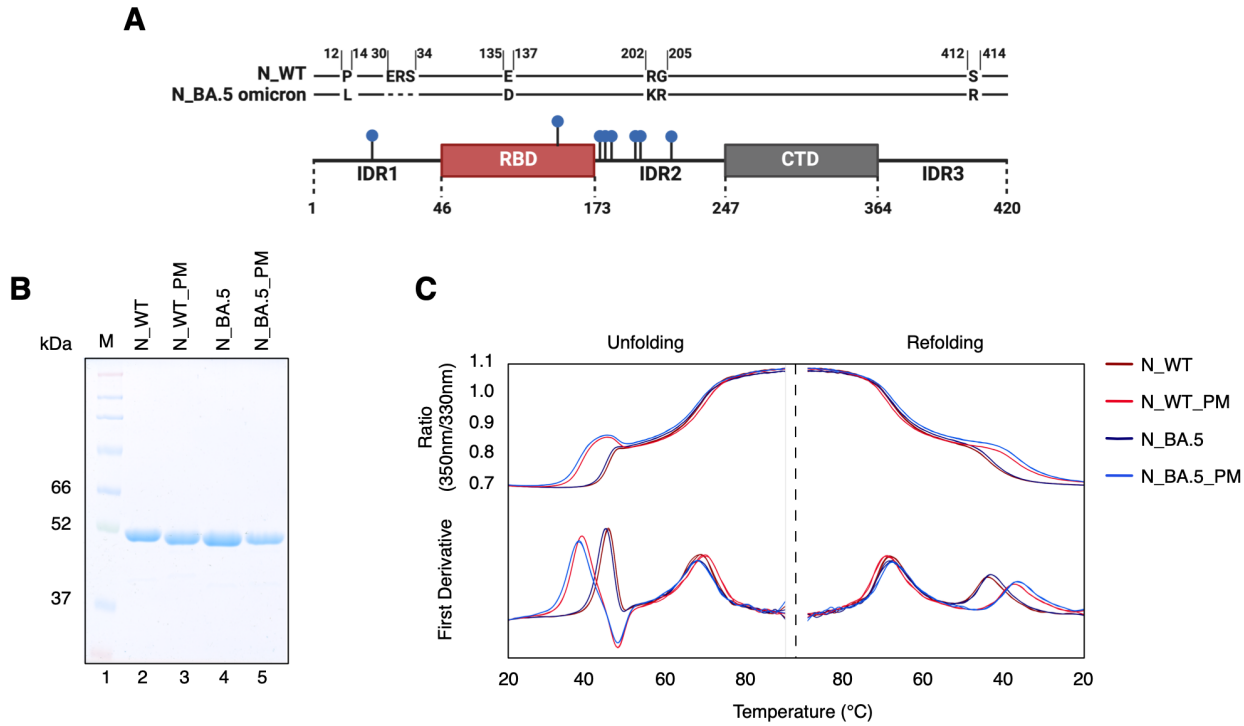

Figure 15: Generation of phosphomimetic WT and BA.5 N proteins

(A) Schematic representation of sequence differences between WT N and Omicron BA.5 N. In contrast to N_WT, N_BA.5 harbors P13L, Δ31-33, E136D, R203K, G204R, S413R). To mimic the phosphorylated state of the N protein, specific serine and threonine residues were substituted by aspartic acid (pseudo-phosphorylation). For N_WT, S23, T141, S176, S180, T198, S201, S202, and S206 and, for N_BA.5, S23, T138, S173, S177, S180, T195, S198, S202, and S203, with regard to sequence deletions and mutations, were substituted by aspartic acid. The locations of these sites are indicated by blue dots and are primarily situated in the IDR2, with one site in the RBD and one in the IDR1. **(B)** Unmodified (N_WT, N_BA.5) and pseudo-phosphorylated (N_WT_PM, N_BA.5_PM) N proteins were recombinantly expressed in *E. coli* and purified via Ni-NTA and subsequent SEC. Of each protein, 2 µg were applied to a 10% SDS gel, with the protein bands aligning the calculated molecular weight of 46 kDa. **(C)** Protein stability was evaluated by monitoring the unfolding and refolding properties of the unmodified and pseudo-phosphorylated N proteins by nanoDSF. 10 µM of each protein were loaded into Prometheus™ NT.48 Standard Capillaries (NanoTemper) and analyzed by a temperature gradient ranging from 25-95°C in the Prometheus™ NT.48 nanoDSF device (NanoTemper). N_WT (dark red) and N_BA.5 (dark blue) samples demonstrate the anticipated unfolding and refolding characteristics. N_WT_PM (red) and N_BA.5_PM (blue) samples exhibit a leftward shift of the RBD peak, while the CTD peak remains stable.

For both, WT and BA.5 N, the residues were selected in accordance with the deletions and mutations within the BA.5 N protein sequence, as illustrated in Figure 3A. The BA.5 N protein contains the P12L, Δ13-33, E136D, R203K, G204R and S413R mutations. Selected amino acid substitutions are shown in Figure 15, indicated by blue dots and are primarily clustered within

the serine-arginine rich IDR2, with additional modifications in the IDR1 and RBD. Following the established expression and purification protocols detailed in section 3.1.1, phosphomimetic variants of N_WT (N_WT_PM) and N_BA.5 (N_BA.5_PM) were successfully expressed and purified. SDS gel analyses (Figure 15B) confirmed the purity of the purified phosphomimetic proteins, with the observed molecular weights consistent with the calculated one of 46 kDa. NanoDSF (2.2.4.1) analyses (Figure 15C) revealed insights into the thermal stability of these variants. Notably, while both N_WT_PM (light red) and N_BA.5_PM (light blue) displayed overall stability comparable to their unmodified counterparts (N_WT, dark red and N_BA.5, dark blue), a distinct reduction in the stability of the RBD for both phosphomimetic N proteins was observed, indicated by a left shifted peak corresponding to a T_M below 40°C. Remarkably, this effect was confined to the RBD, leaving the stability of the CTD unaffected by pseudo-phosphorylation.

3.2. RNA binding characteristics of the SARS-CoV-2 N protein

The N protein of SARS-CoV-2 plays a pivotal role in the packaging of viral RNA a process essential for the assembly of new virions during infection. The interaction of the N protein with viral RNA and the LLPS-mediated RNA packaging have been extensively studied (Iserman et al. 2020). However, this study represents the first comprehensive characterization of the RNA binding capabilities and the functionality of the N protein in this context.

3.2.1. Double-stranded RNA is the preferred substrate for the SARS-CoV-2 N protein

SARS-CoV-2 is a ssRNA virus, and previous studies have demonstrated the N protein interacting with ssRNA (Dinesh et al., 2020; Iserman et al., 2020). However, it is crucial to acknowledge that a significant portion of the viral genome exists in highly structured dsRNA formations. To gain further insight into the N protein's interaction with dsRNA, comparative binding analyses were conducted using both EMSA (2.2.4.4.1, Supplementary Figure 2A) and MST (2.2.4.3) techniques. These analyses involved 26-nt long RNAs derived from three distinct locations within the viral genome (RNA3, RNA20, RNA22) in the form of either ss- or dsRNA. Specifically, the sequence of RNA3 is located in the ORF1a, RNA20 sequence in the 5'UTR, and RNA22 sequence in the S gene.

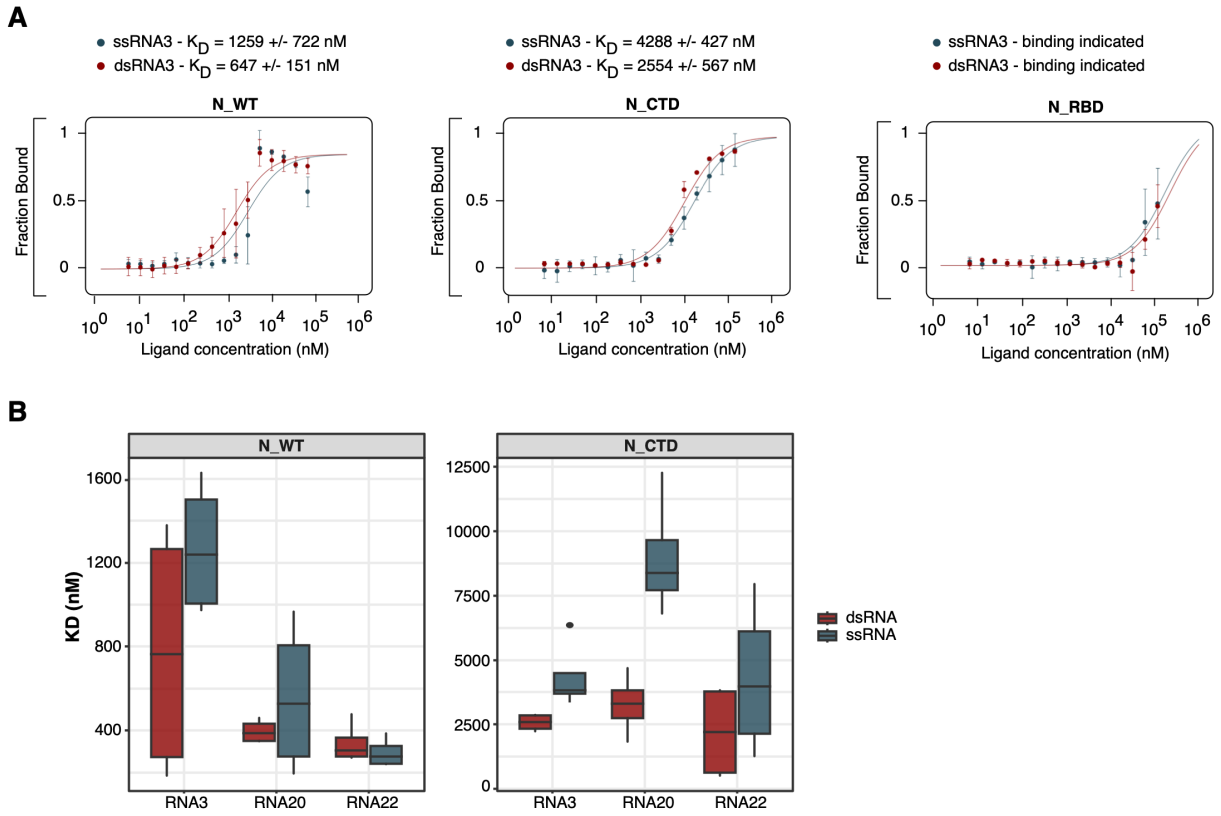

Figure 16: Preferred dsRNA binding of the SARS-CoV-2 N and its C-terminal domain

(A) The binding affinities of N_WT, N_CTD and N_RBD to either ssRNA3 (blue-grey) or dsRNA3 (red) were determined using MST. The MST traces and the respective K_D values and the K_D confidence are provided in the figure for reference. The plots are presented with the ligand (protein) concentration on the x-axis and the fraction bound on the y-axis. For N_WT, the K_D values were 1259 +/- 722 nM for ssRNA3 and 647 +/- 151 nM for dsRNA3. For N_CTD, K_D values were 4288 +/- 427 nM for ssRNA3 and 2554 +/- 567 nM for dsRNA3. However, only an indication for binding could be detected. **(B)** Comparative boxplot of three different SARS-CoV-2 RNAs (RNA3, RNA20, RNA22) in single-stranded (blue-grey) and double-stranded (red) form for N_WT and N_CTD based on MST data. Each boxplot contains four MST runs. Each boxplot represents the interquartile range (IQR), with the median indicated by a horizontal line inside the box. The upper and lower whiskers extend to a maximum of 1.5 times above and below the upper and lower quartiles, respectively. Outliers beyond this range are depicted as individual data points. The x-axis represents the RNA while the y-axis indicates the K_D. The dimensions of the y-axis differ between N_WT and N_CTD. For each RNA, dsRNA is bound with a similar or even higher affinity than ssRNA.

MST measurements were performed following the methodology outlined in 2.2.4.3. The resulting MST traces, along with the calculated K_D values and their K_D confidence intervals for ssRNA3 and dsRNA3 binding of N_WT, N_CTD and N_RBD with RNA3 are presented in Figure 16A. The experiment unveiled binding affinities with a K_D of 1259 nM for ssRNA and 647 nM for dsRNA for N_WT. However, it is noteworthy that the standard deviation (SD) for dsRNA3 measurements was relatively high (Figure 16B). For N_CTD, a K_D of 4288 nM for ssRNA and 2554 nM for dsRNA was determined, whereas for N_RBD, only an indicated binding could be observed. Further analysis extended to RNA20 and RNA22, with summarized results presented in Figure 16B, depicting the K_D and the SD for all individual measurements. A comparable trend is observed for RNA20, with N_WT exhibiting a binding affinity of 425 nM to ssRNA20 and 398 nM to dsRNA20, whereas N_CTD displayed a binding affinity of 8535 nM to

ssRNA20 and 3300 nM to dsRNA20. Interestingly, for RNA22, N_WT binding does not appear to be affected by the presence of RNA in double-stranded form. In contrast, there was a slight enhancement in the binding affinity of N_CTD to dsRNA20. Supplementary Figure 2B, Supplementary Table 2 and Supplementary Table 3 provide individual MST traces, K_D and K_D confidence values for the proteins' binding to RNA20 and RNA22, respectively. Overall, the findings suggest that dsRNA is the preferred substrate for binding by the SARS-CoV-2 N protein, as evidenced by the majority of measurements.

3.2.2. RBD-IDR2-CTD harbors the RNA binding ability of the protein

Despite the well-documented overall function of the SARS-CoV-2 N protein in RNA binding, and the identification of dsRNA as the preferred substrate in this study, the specific domains responsible for its RNA binding ability remain largely unknown. To address this gap, a set of N protein truncation proteins was generated as described in section 3.1.2, and their binding behavior both ssRNA and dsRNA (Supplementary Figure 3A, B) was analyzed in comparison to that of the WT N protein. Comparative analyses of all truncation proteins were carried out using MST (2.2.4.3) approaches with the 26 nt long RNA3. This allowed a comprehensive assessment of the RNA binding behavior of each truncation variant in comparison to the WT N protein.

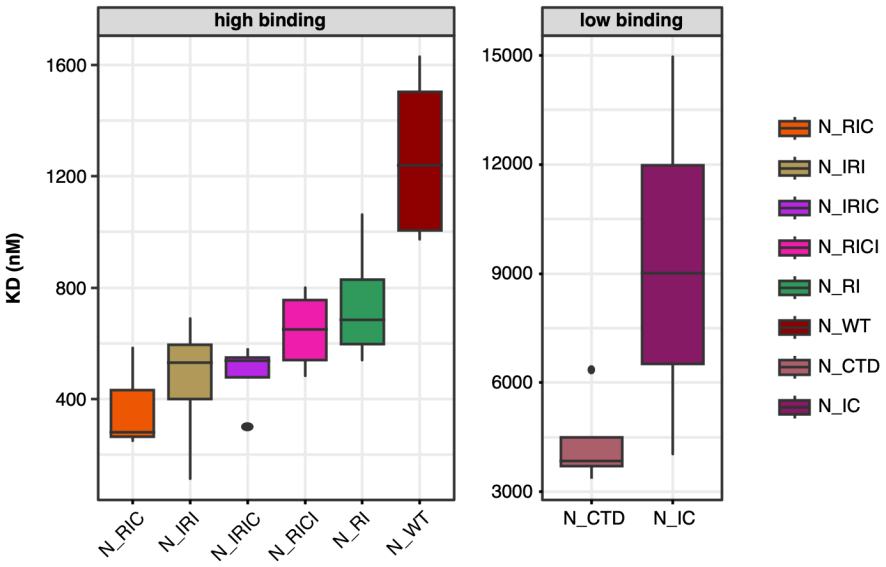

Figure 17: Binding properties of N truncation proteins to ssRNA3

A comparative boxplot of N (truncation) proteins binding properties towards ssRNA3 based on MST data. Each boxplot contains four MST measurements, each with its individual K_D value being fitted together. Each boxplot represents the interquartile range (IQR), with the median indicated by a horizontal line inside the box. The upper and lower whiskers extend to a maximum of 1.5 times above and below the upper and lower quartiles, respectively. Outliers that fall outside this range are depicted as individual data points. The proteins are divided into two groups, designated as "high binding" and "low binding", based on their K_D values. Proteins with no or only indicated binding are excluded from the analysis. The x-axis represents the protein, while the y-axis displays the K_D. The

dimensions of the y-axis differ between the groups. Proteins are arranged in order of their median K_D value. The majority of truncation proteins (N_RIC (orange), N_IRI (beige), N_IRIC (purple). N_RICI (pink), N_RI (green)) bind similar or even with higher affinity to ssRNA while N_CTD (brown) and N_IC (dark purple) display lower binding.

Figure 17 presents the binding affinities of the N truncation protein to ssRNA3, sharing K_D values, along with the SD of the single MST measurements. In this analysis, non-binding proteins were excluded, and the binding proteins were categorized into two groups: "high binding" and "low binding" truncation proteins. The provided measurements indicate that N_IRIC (purple), N_RICI (pink), N_RIC (orange), N_IRI (beige) and N_RI (green) display similar and, in some cases, even stronger binding to ssRNA3 compared to N_WT (dark red). Conversely, N_IC (dark purple) and N_CTD (brown) exhibited only low binding characteristics. K_D values and the corresponding K_D confidence intervals for proteins are provided in Supplementary Table 1. This analysis suggests that the minimal protein domains necessary for ssRNA3 binding are N_RIC and N_RI.

Further examination of N_RIC and N_RI revealed differences in ssRNA3 and dsRNA3 binding of the truncation proteins (Figure 18)

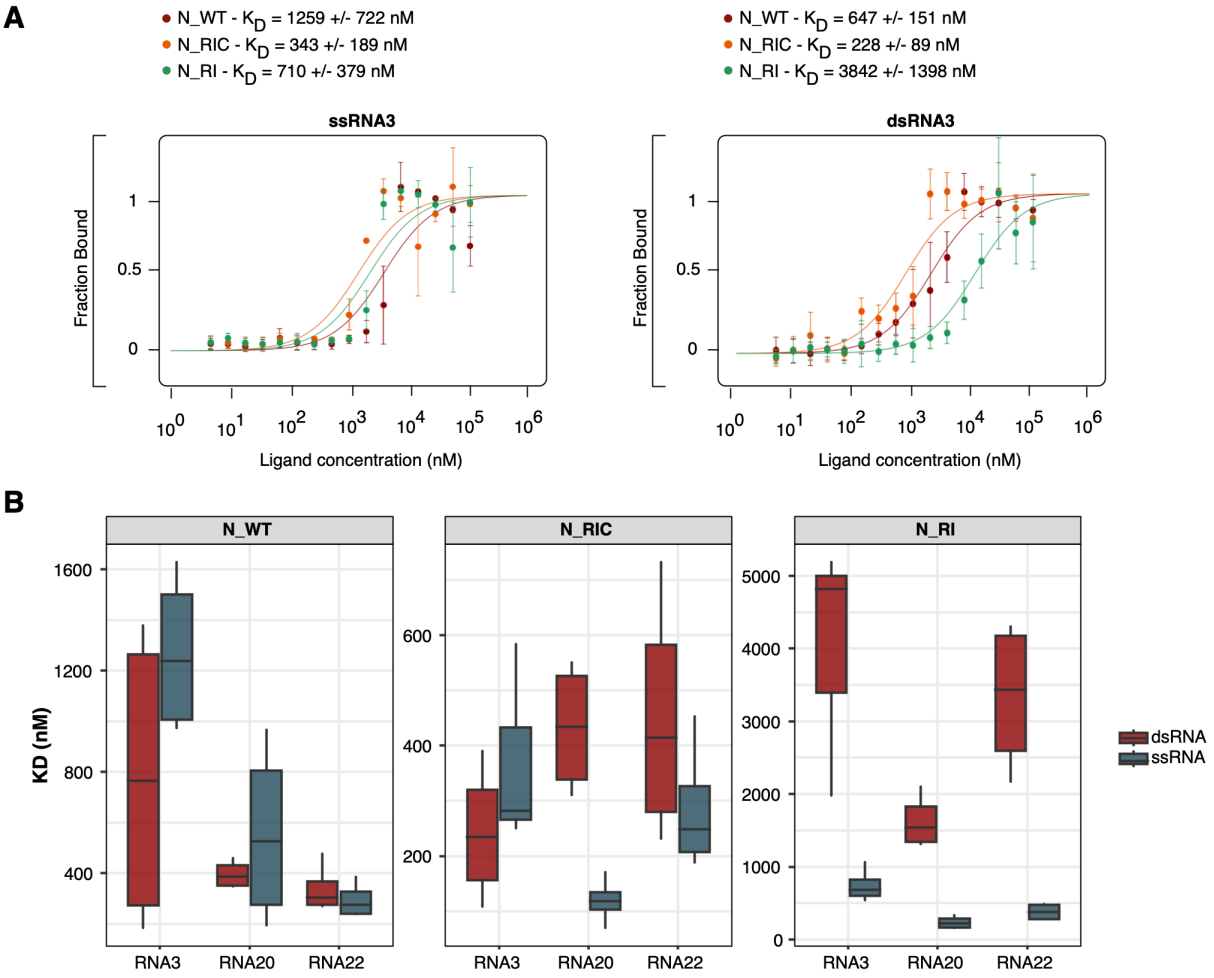

Figure 18: Comparative ss and dsRNA binding of N_WT, N_RIC, and N_RI

(A) The binding affinities of N_WT (red), N_RIC (orange) and N_RI (green) to either ssRNA3 (left) or dsRNA3 (right)

were determined using MST. The MST traces and the respective K_D values and the K_D confidence are provided in the figure. The plots are presented with the ligand (protein) concentration on the x-axis and the fraction bound on the y-axis. The K_D values for ssRNA3 are given as follows: 1259 +/- 722 nM for N_WT, 343 +/- 189 nM for N_RIC and 710 +/- 379 nM for N_RI. For dsRNA3 the K_D values are 647 +/- 151 nM for N_WT, 228 +/- 89 nM for N_RIC and 3842 +/- 1396 nM for N_RI. For ssRNA3, N_RIC and N_RI display higher RNA binding affinity than N_WT. With regard to dsRNA3, only N_RIC exhibits a higher binding affinity, whereas the affinity of N_RI has decreased. **(B)** Comparative boxplot of three different SARS-CoV-2 RNAs (RNA3, RNA20, RNA22) in single-stranded (blue-grey) and double-stranded (red) form for N_WT, N_RIC and N_RI based on MST data. Each boxplot contains four MST runs. Each boxplot represents the interquartile range (IQR), with the median indicated by a horizontal line inside the box. The upper and lower whiskers extend to a maximum of 1.5 times above and below the upper and lower quartiles, respectively. The x-axis represents the RNA while the K_D is indicated on the y-axis. The dimensions of the y-axis differ for N_WT, N_RIC and N_RI. The binding affinity of N_RI to dsRNA is observed to decrease in each case.

A comprehensive analysis of the N_RIC and N_RI truncation proteins regarding their RNA binding characteristics was conducted using MST. The data revealed high-affinity binding to both ssRNA3 and dsRNA3 for N_RIC (orange), with K_D values of 343 nM and 228 nM, respectively. In contrast, the N_RI (green) protein exhibited high affinity for ssRNA3 (710 nM), while the binding affinity for dsRNA3 is strongly reduced (3842 nM) (Figure 18A, B). This trend was consistent across RNA20 and RNA22. For N_RIC, similar binding affinities for ssRNA (grey-blue) and dsRNA (dark red) were observed, comparable to the N_WT binding behavior. However, for N_RI, in all cases, the binding affinity decreased with dsRNA (Figure 18B). MST traces of binding towards ssRNA3 and dsRNA3 for other N protein truncation proteins as well as comparative dsRNA3 analysis are provided in Supplementary Figure 3A, B, with an overview of the K_D values and K_D confidence intervals available in Supplementary Table 1. Except for N_IRI and N_RI, the trend of higher dsRNA3 binding is consistent for all N truncation proteins (Supplementary Figure 3C). Collectively, the data indicate that the minimal protein domain required for ssRNA binding is N_RI, whereas for dsRNA it is N_RIC.

3.2.3. SARS-CoV-2 Wuhan and Omicron BA.5 N proteins display different RNA binding abilities

Following the initial outbreak of the SARS-CoV-2 Wuhan strain in 2019, emergence of the Omicron variants has been notable, becoming predominant in new infections. These strains exhibit differences in various aspects, including their modes of transmissibility and disease severity (Gili & Burioni, 2023). To gain a deeper understanding of the molecular mechanisms underlying the observed differences, investigations into RNA binding characteristics were undertaken. The interaction of the N proteins with RNA was analyzed through MST measurements (2.2.4.3) using the 26 nt long RNA3, RNA20 and RNA22. These analyses aimed to provide insights into the differential RNA binding behaviors of the N protein across these

two different strains and shed light on potential molecular determinants contributing to their distinct biological properties.

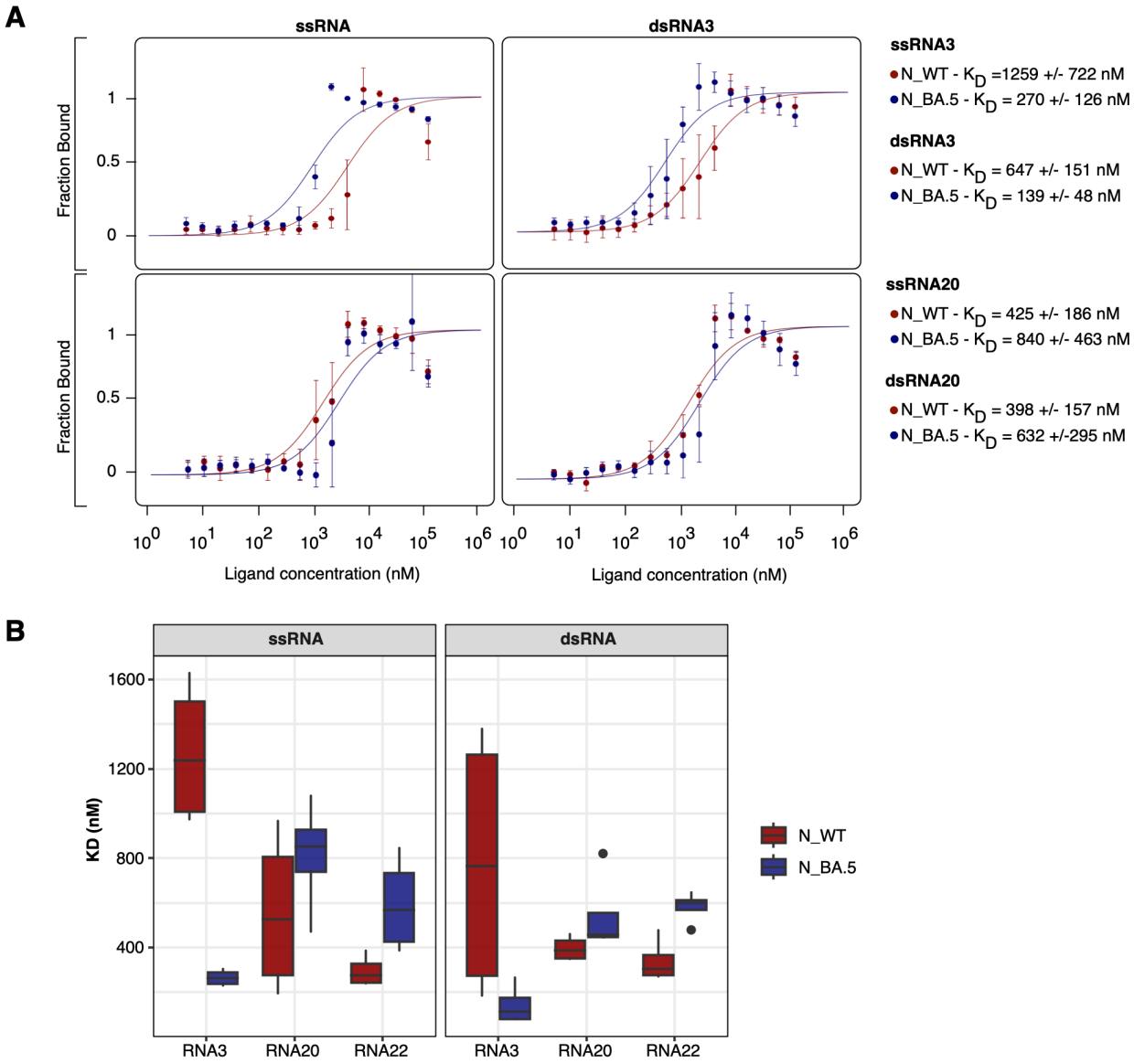

Figure 19: RNA binding differences of the WT and Omicron BA.5 N proteins

(A) The binding affinities of N_WT (red) and N_BA.5 (blue) to either RNA3 (top) or RNA20 (bottom) in single-stranded (left) or double-stranded (right) conformation, were determined using MST. The MST traces and the respective K_D values and the K_D confidence are provided in the figure. The plots are presented with the ligand (protein) concentration on the x-axis and the fraction bound on the y-axis. The K_D values for ssRNA3 are as follows: 1259 +/- 722 nM for N_WT, 270 +/- 126 nM for N_BA.5. For dsRNA3 the K_D values are 647 +/- 151 nM for N_WT and 139 +/- 48 nM for N_BA.5. K_D values for ssRNA20 are 425 +/- 186 nM for N_WT and 840 +/- 463 nM for N_BA.5. For dsRNA20, K_D values are 398 +/- 157 nM for N_WT and 632 +/- 295 nM for N_BA.5. RNA3 is bound with higher affinity by N_BA.5 while for RNA20, N_WT displays a slightly higher binding affinity. **(B)** Comparative boxplot of three different SARS-CoV-2 RNAs (RNA3, RNA20, RNA22) in single-stranded (left) and double-stranded (right) form for N_WT (red) and N_BA.5 (blue) based on MST data. Each boxplot contains four MST runs. Each boxplot represents the interquartile range (IQR), with the median indicated by a horizontal line inside the box. The upper and lower whiskers extend to a maximum of 1.5 times above and below the upper and lower quartiles, respectively. Outliers beyond this range are depicted as individual data points. The x-axis of the plots represents the RNA, while the y-axis represents the K_D. In all cases, dsRNA is bound with higher affinity than ssRNA. The enhanced binding of N_BA.5 to RNA is only observable for RNA3, while for RNA20 and RNA22, N_BA.5 binds with similar or lower affinity to the RNA.

For RNA3, a notable trend towards higher affinity binding of N_BA.5 (blue; K_D ssRNA: 270 nM, dsRNA: 139 nM) compared to N_WT (red; K_D ssRNA: 1259 nM, dsRNA: 647 nM) was observed, as depicted in Figure 19 A and B. However, this difference is not evident in the case of RNA20 and RNA22. Rather, it is apparent that N_WT binds more strongly to these RNAs. With regard to RNA20, N_WT exhibits ssRNA binding affinities of 425 nM compared to 840 nM for N_BA.5, while dsRNA binding affinities of 398 nM for N_WT and 632 nM for N_BA.5 (Figure 19B). This variation in RNA binding specificity between the two proteins suggests that viral N proteins may engage in distinct mechanisms for RNA binding and packaging.

3.2.4. Pseudo-phosphorylation impairs RNA binding activity of the N protein

Posttranslational modifications are known to exert significant regulatory effects on the SARS-CoV-2 infection cycle. Notably, the N protein undergoes phosphorylation at specific stages, including prior to genome replication (Carlson et al., 2020). In this study, it was aimed to investigate the impact of pseudo-phosphorylation on the RNA binding activity of both the Wuhan and Omicron BA.5 N proteins. The generation of phosphomimetic proteins was detailed in section 3.1.3. and RNA analysis was performed by MST measurements (2.2.4.3) using the 26 nt long ssRNA3 (Figure 20). This approach allowed to examine how the introduction of phosphomimetic modifications impairs the RNA binding capabilities of these two N protein variants, shedding light on potential functional alterations induced by phosphorylation events.

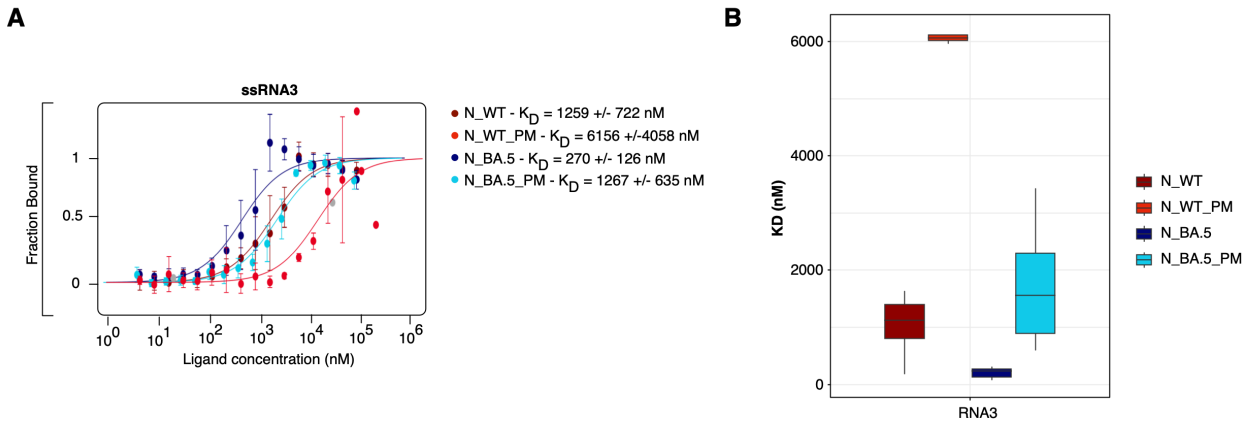

Figure 20: Impact of pseudo-phosphorylation on the RNA binding capability of the N protein

(A) The binding affinities of N_WT (dark red), N_WT_PM (red), N_BA.5 (dark blue) and N_BA.5_PM (light blue) to ssRNA3 were determined using MST. The MST traces and the respective K_D values and the K_D confidence are provided in the figure. Plots are presented with the ligand (protein) concentration on the x-axis and the fraction bound on the y-axis. The K_D values for ssRNA3 are as follows: 1259 +/- 722 nM for N_WT, 270 +/- 126 nM for N_BA.5, 6156 +/- 4058 nM for N_WT_PM and 1267 +/- 635 nM for N_BA.5_PM. Pseudo-phosphorylation has been observed to decrease the binding affinity of both N_WT and N_BA.5. **(B)** Comparative boxplot of ssRNA3 binding affinity of N_WT (dark red), N_WT_PM (red), N_BA.5 (dark blue) and N_BA.5_PM (light blue) based on MST data. Each boxplot contains four MST runs. Each boxplot represents the interquartile range (IQR), with the median indicated by a horizontal line inside the box. The upper and lower whiskers extend to a maximum of 1.5 times above and below the upper and lower quartiles, respectively. The x-axis represents the RNA while the K_D is indicated on the y-axis.

RNA is bound with lower affinity when the N protein is pseudo-phosphorylated.

The individual MST measurements were fitted and are represented in Figure 20A, displaying the K_D along with the respective K_D confidence intervals of the fit. The same measurements are directly compared with the K_D value and the SD of all individual measurements in Figure 20B. The pseudo-phosphorylation of both proteins led to a notable reduction in RNA binding affinity relative to the native proteins. In the context of the WT protein, N_WT_PM exhibited a nearly 5-fold decrease in binding affinity from 1259 nM (N_WT, dark red) to 6159 nM (N_WT_PM, red). A similar trend was observed in the context of Omicron BA.5, with an almost 5-fold decrease in binding affinity from 270 nM (N_BA.5, dark blue) to 1267 nM (N_BA.5_PM, light blue). Interestingly, N_BA.5_PM displayed a binding affinity to ssRNA3 similar to that of N_WT, suggesting differential regulation of the RNA interaction between the Wuhan and Omicron BA.5 strains. Nevertheless, it is evident that phosphorylation exerts a detrimental effect on the RNA binding affinity of both variants of the N protein.

3.3. RNA chaperone function of the SARS-CoV-2 N protein

As outlined in the introduction section 1.4, RNA molecules are central players in numerous biological processes, but their functions often depend on their intricate structures. RNA chaperones play a crucial role in facilitating RNA folding and structural transitions. Notably, the genome of SARS-CoV-2 exhibits a highly structured architecture, with significant portions adopting double-stranded configurations (Lan et al., 2022). The SARS-CoV-2 N protein's remarkable affinity for dsRNA, which was highlighted in chapter 3.2.1, raises intriguing questions about its potential role beyond simple RNA binding. The fact that various RNA viruses packaging proteins possess an RNA chaperone function, which was also already shown for N of SARS-CoV (Zúñiga et al., 2007b), together with the presented increased efficiency in dsRNA interaction, suggests a plausible function as an RNA chaperone, capable of mediating RNA structural changes and promoting the assembly of ribonucleoprotein complexes.

3.3.1. The SARS-CoV-2 N protein is an RNA chaperone

The N protein is recognized for its crucial involvement in RNA binding and packaging, yet its additional functions within the viral infection cycle remain largely unexplored. Thus, this study seeks to gain insight into the RNA folding and viral genome structuring abilities of the N protein, aiming to bridge knowledge gaps in our fundamental understanding of how the N protein influences viral function, fitness and pathogenesis.

In order to test for a potential RNA chaperone activity of the SARS-CoV-2 N protein, an assay, previously described by Zúñiga et al. (2007), demonstrating the chaperone activity of the SARS-CoV-2 N protein, was adjusted for the purposes in this study (2.2.4.5). This established assay involves the use of two complementary ssRNAs, with at least one of them being fluorescently labeled. The ssRNAs were mixed, denatured at 95°C to ensure single-strandedness, followed by rapid cooling to 4°C. This RNA mix was incubated for 3 minutes in presence or absence of varying concentrations of the N protein. Following the incubation period, an SDS-containing STOP solution was added to denature the N protein and terminate the reaction. The chaperone reaction mixture was applied onto a native PAA gel (2.2.3.4). In instances where the N protein contributes to RNA hybridization, the intensity of the ssRNA band decreases slightly while the intensity of the dsRNA band increases the more protein is present (Figure 21A).

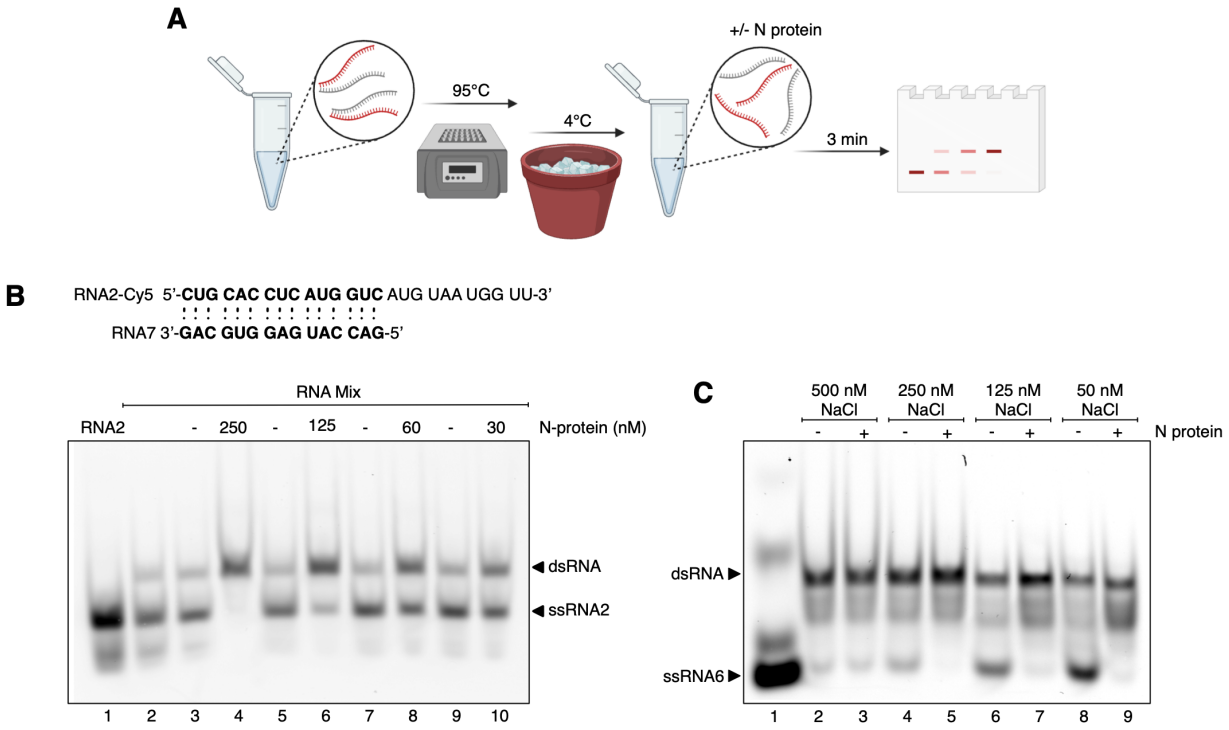

Figure 21: SARS-CoV-2 N hybridizes ssRNA to dsRNA

(A) Schematic workflow of the established RNA chaperone assay. Two complementary ssRNA, with at least one being fluorescently labeled, were mixed, denatured at 95°C for 2 min and rapidly cooled down to 4°C on ice. Subsequently, samples were incubated for 3 min at 25°C in presence or absence of N_WT protein. Reaction was terminated by adding a stop-buffer containing SDS for protein denaturation. Samples were then applied to a native PAA gel and analyzed by fluorescent readout using the Typhoon™ FLA 9500 reader (GE Healthcare). **(B)** Analysis of N_WT RNA chaperone activity. Complementary ssRNA2-Cy5 and ssRNA7 were mixed and incubated in presence (lanes 4, 6, 8 and 10) or absence (lanes 2, 3, 4, 7 and 9) of N protein. Following completion of the reaction, samples were applied to a native 6% PAA gel. RNA hybridization was enhanced in presence of SARS-CoV-2 N protein, with detectable enhancement observed at 30 nM of added protein and increasing dsRNA intensity the more protein was added. Lane 1 served as a ssRNA2-Cy5 control. **(C)** RNA chaperone activity of N_WT was assessed under varying salt concentrations in the reaction buffer. An RNA mix (ssRNA3, ssRNA6-Cy5) was incubated in absence (lanes 2, 4,

6, 8) or presence (lanes 3, 5, 7, 9) of N_WT. RNA chaperoning occurred efficiently at 50 mM (lane 9), 125 mM (lane 7) and 250 mM (lane 5) of NaCl in the reaction. At 500 mM of present NaCl (lane 3), RNA hybridization was not detectable compared to the control (lane 2). Gels of B and C are taken from the Bachelor thesis of Julia Seidel, 2021.

In this study, the complementary ssRNA2-Cy5 and ssRNA7 were employed and the assay was performed with increasing concentrations of N_WT (Figure 21B). As a baseline, the efficiency of spontaneous RNA hybridization without additional protein was also assessed (lanes 2, 3, 5, 7, 9). The results reveal that the addition of N protein indeed enhanced RNA hybridization in a concentration dependent manner, with a noticeable effect observed at concentrations as low as 30 nM (lane 10). Notably, at a concentration of 250 nM of N_WT (lane 4), complete annealing of ssRNA to dsRNA occurred within 3 minutes, as evidenced by a substantial increase in dsRNA band intensity and the disappearance of the ssRNA band. It is noteworthy that RNA chaperone activity and RNA binding are connected with RNA binding and RNA chaperoning occurring at similar concentration ranges (Supplementary Figure 4C). Moreover, increased binding of RNA correlated with more efficient RNA chaperone activity of the WT N protein, underscoring the significance of robust RNA binding as a prerequisite for effective RNA chaperoning. Furthermore, despite SARS-CoV-2 being ssRNA virus, N exhibits a binding affinity to DNA and is capable facilitating annealing of complementary ssDNA strands, further highlighting its role in structurig the viral genome in a partial double-stranded form. However, the DNA chaperone activity is comparatively weaker than that observed for RNA, with DNA hybridization slowly starting at approximately 500 nM of protein, where also DNA binding saturation is reached (Supplementary Figure 4A, B). Additionally, the RNA chaperone mechanism appears to be sensitive to the ionic environment. While the assay is typically performed at 50 mM NaCl, increasing NaCl concentrations up to 500 mM hinder N protein-mediated RNA hybridization (Figure 21C). This is evidenced by a lack of change in ssRNA or dsRNA band intensity between the samples with and without N protein at 500 mM salt concentration (lanes 2, 3), whereas RNA chaperone activity persisted at other salt concentrations. Interestingly, overall N protein stability is unaffected by elevated salt concentration, with minor effects observed up to 1.6 M of NaCl (Supplementary Figure 4E). Additionally, RNA binding is observable at higher NaCl concentrations up to 500 mM, as indicated by nanoDSF, wherein ssRNA addition still induces an effect in RBD and CTD stability of the N protein (Supplementary Figure 4D). In conclusion, these findings contribute to the understanding that the SARS-CoV-2 N protein functions as an RNA chaperone during the viral

life cycle, a process that is, to some extent, influenced by the overall salt concentration within the system.

3.3.2. RBD-IDR2-CTD harbors the intrinsic RNA chaperone activity

For many viral RNA chaperones, the disordered domains play a crucial role in the efficient folding of RNAs (Herschlag, 1995). As the SARS-CoV-2 N protein contains approximately 50% of predicted disorder, reflected by three IDRs flanking the RBD and the CTD, the function of the IDRs and the specific domains harboring the RNA chaperone activity are aimed to be studied. Therefore, the N truncation proteins outlined in section 3.1.2, were used to analyze and quantify their specific RNA chaperone activities.

In order to delineate the involvement of different protein domains in RNA chaperoning, complementary ssRNA3 and ssRNA6-Cy5 were mixed, and a constant amount of the various proteins was added to identify the regions being most efficient in RNA hybridization (section 2.2.4.5.1). Prior to this analysis, the RNA chaperone activity of each individual truncation protein was titrated to determine suitable quantities for comparative assessment (Supplementary Figure 5A), leading to a protein concentration of 250 nM of each protein to use for the comparative chaperone assay. As depicted in an illustrative assay gel (Figure 22A) and statistically analyzed (Figure 22B, section 2.2.6.3), diminished chaperone activity was observed for N_CI, N_IC, N_CTD, N_IRI, N_RI and N_RBD (Figure 22A, lanes 7, 8, 9, 10, 11, 12) in comparison to N_WT (Figure 22A, lane 3; Figure 22B dark red) and the RNA mix control (Figure 22A lane 2; Figure 22B black). Notably, N_CI (grey-blue), N_IC (dark purple) and N_RBD (light green) exhibited a significant reduction in the chaperone activity relative to N_WT, with the percentage of dsRNA provided, while the differences observed for the remaining N truncation proteins were not statistically significant.

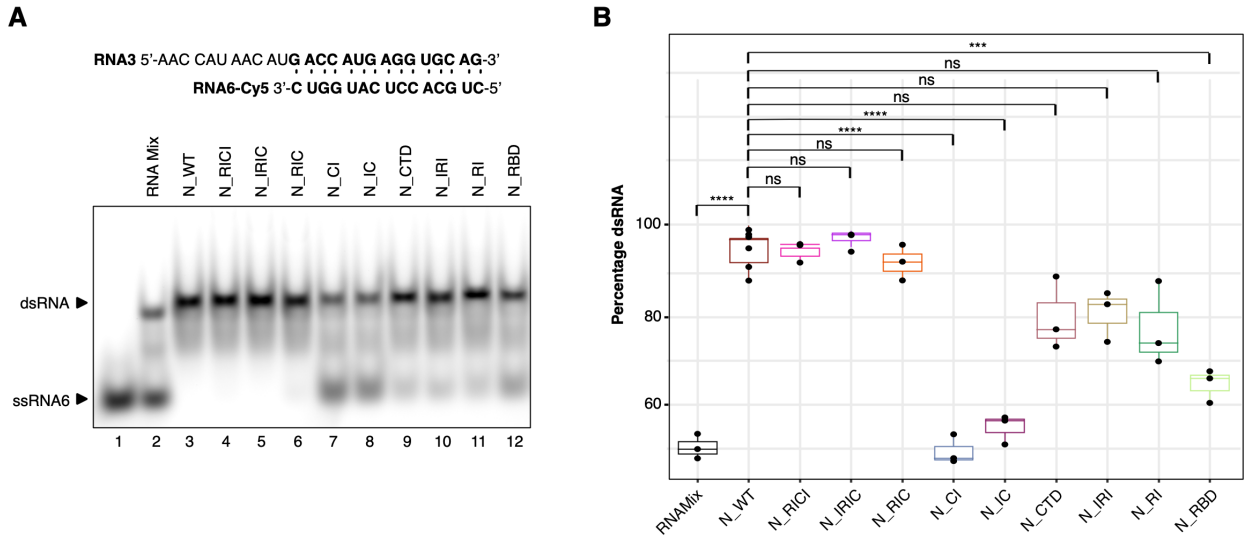

Figure 22: RBD-IDR2-CTD harbors the N protein's RNA chaperone activity

(A) RNA chaperone assay comparing the activity of N truncation proteins at equimolar protein concentrations. An RNA Mix (ssRNA3, ssRNA6-Cy5) was incubated in the absence (lane 2) or presence (lanes 3-12) of 250 nM N (truncation) protein for 3 min at 25°C. Afterwards, samples were analyzed on a 6% native PAA gel and visualized by fluorescent readout using the Typhoon™ FLA 9500 reader (GE Healthcare). The RNA Mix (lane 2) served as a control for spontaneous RNA hybridization, while N_WT (lane 3) represented the fully hybridized state. Additional complete RNA annealing was observed for N_RICI (lane 4), N_IRIC (lane 5) and N_RIC (lane 6). Partial hybridization was detectable for N_CTD (lane 9), N_IRI (lane 10), N_RI (lane 1), and N_RBD (lane 12). Only weak hybridzation was observable for N_CI (lane 7) and N_IC (lane 8). **(B)** Boxplot representing the percentage of hybridized dsRNA. RNA band intensities were analyzed using Fiji. Each boxplot contains three biological replicates of the chaperone assay. Each boxplot represents the interquartile range (IQR), with the median indicated by a horizontal line inside the box. The upper and lower whiskers extend to a maximum of 1.5 times above and below the upper and lower quartiles, respectively. The x-axis represents the respective N truncation protein, while the percentage of dsRNA is indicated on the y-axis. Highly significant differences in dsRNA formation were observed between the RNAMix control (black) and N_WT (dark red). Significant differences to N_WT in RNA annealing efficiency were observed for N_CI (grey-blue), N_IC (dark purple) and N_RBD (light green). Observed differences for the other proteins relative to N_WT were statistically not significant (n.s.). Statistical analysis was performed by applying a t-test using the Benjamini-Hochberg (BH) procedure. 'n.s.' = 0.05 < p; '*' = 0.05 <= p >0.01; '**' = 0.01 <= p > 0.001; '***' = 0.001 <= p > 0.0001; '****' = 0.0001 <= p.

The N truncation proteins N_RICI, N_IRIC and N_RIC (Figure 22A, lanes 4, 5, 6, Figure 22B pink, purple and orange) exhibited comparable hybridization efficiency to the wildtype N protein (Figure 22A, lane 3; Figure 22B dark red). Interestingly, the presence of IDRs adjacent to the CTD resulted in a decrease in chaperone efficiency, whereas IDRs adjacent to the RBD enhanced its chaperoning abilities. Analysis using a second pair of ssRNAs (ssRNA20/ssRNA21), derived from the 5'UTR of SARS-CoV-2, led to a similar trend, with a overall reduced RNA annealing efficiency Supplementary Figure 5B, C). Considering these observations, the minimal protein domains capable of high-efficiency RNA hybridization comprise the RBD-IDR2-CTD (N_RIC), indicating the IDR2 as the primary IDR involved in the RNA chaperoning process.

3.3.3. Pseudo-phosphorylation impairs Omicron BA.5 but not Wuhan N protein's RNA chaperone activity

Building upon the current understanding of the distinct RNA binding properties observed between the Wuhan and Omicron BA.5 variants of the N protein, in the following chapter, a focus to explore potential disparities in their RNA chaperone activities is set. Given the established differences in their RNA binding affinities (3.2.3 and 3.2.4), investigating their roles as RNA chaperones presents an avenue to unravel further adaptations in their functional dynamics. Furthermore, for known RNA chaperones like the RNA binding protein La, protein phosphorylation has been demonstrated to impact their RNA chaperone activity (Kuehnert et al., 2015). Also, the presence of disordered regions in RNA chaperones, is often associated with the presence of phosphorylation sites (Habchi et al., 2014), suggesting a potential role for phosphorylation in the RNA chaperone mechanism. However, whether and how protein phosphorylation affects the RNA hybridization activity of the SARS-CoV-2 N protein remains elusive. To address these questions, N_WT, N_BA.5, and their respective pseudo-phosphorylated variants N_WT_PM and N_BA.5_PM were subjected to analysis in the established chaperone assay.

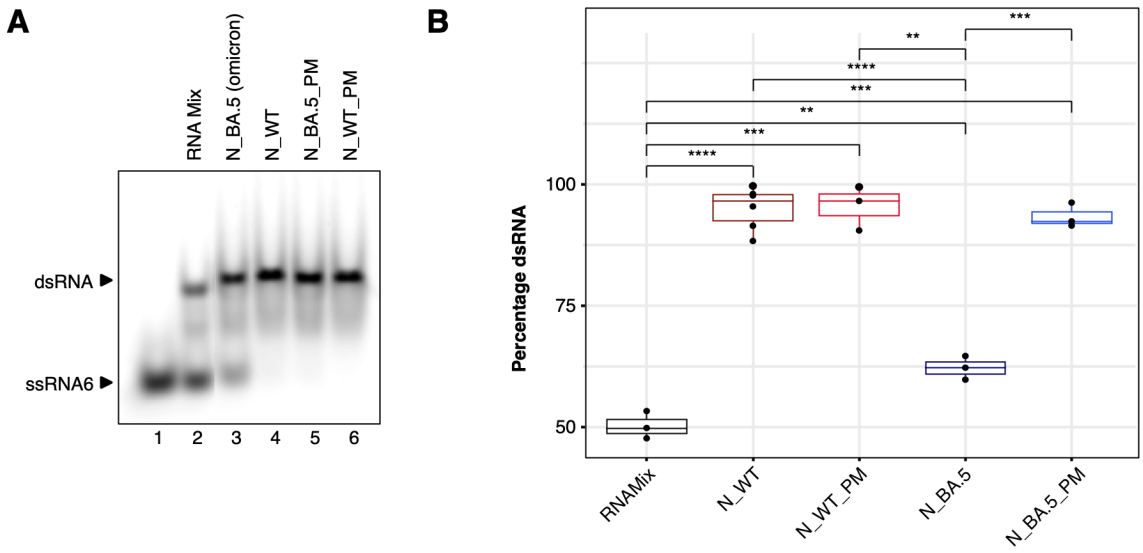

Figure 23: RNA chaperone characteristics of Wuhan and Omicron BA.5 N and their respective phosphomimetic variants

(A) RNA chaperone assay comparing the activity of Wuhan and Omicron BA.5 N proteins along with their respective phosphomimetic variants at equimolar protein concentrations. An RNA Mix (ssRNA3, ssRNA6-Cy5) was incubated in the absence (lane 2) or presence of 250 nM N_BA.5 (lane 3), N_WT (lane 4), N_BA.5_PM (lane 5) or N_WT_PM (lane 6) for 3 min at 25°C. Afterwards, samples were analyzed on a 6% native PAA gel and visualized by fluorescent readout using the Typhoon™ FLA 9500 reader (GE Healthcare). RNA Mix (lane 2) served as a control for spontaneous RNA hybridization, while N_WT (lane 4) represented the fully hybridized state. Additional complete RNA annealing was observed for N_WT_PM (lane 6) and N_BA.5_PM (lane 5). Partial hybridization was detectable for N_BA.5 (lane 3).

(B) Boxplot representing the percentage of hybridized dsRNA. RNA band intensities were analyzed using Fiji. Each boxplot contains three biological replicates of the chaperone assay. Each boxplot represents the interquartile range (IQR), with the median indicated by a horizontal line inside the box. The upper and lower whiskers extend to a maximum of 1.5 times above and below the upper and lower quartiles, respectively. The x-axis represents the respective N truncation protein, while the percentage of dsRNA is indicated on the y-axis. The difference in dsRNA formation is highly significant between the RNAMix control (black) and N_WT (dark red). Significant enhancement of dsRNA formation was detectable for all N protein variants compared to the RNAMix (black) with N_BA.5 (dark blue) exhibiting the least significant enhancement among the proteins. Each protein was also statistically compared to the other proteins. Non-significant (n.s.) comparisons were not visualized in the plot. Each protein variant displayed a significant difference in dsRNA formation compared to N_BA.5. While N_WT_PM did not differ from N_WT, N_BA.5_PM restored the RNA chaperone activity of N_BA.5. Statistical analysis was performed by applying a t-test using the Benjamini-Hochberg (BH) procedure. 'n.s.' = 0.05 < p; '*' = 0.05 <= p >0.01; '**' = 0.01 <= p > 0.001; '***' = 0.001 <= p > 0.0001; '****' = 0.0001 <= p.

In order to elucidate the RNA chaperone mechanisms of the N protein within the two SARS-CoV-2 strains and the impact of protein phosphorylation, complementary ssRNA3 and ssRNA6-Cy5 were co-incubated with equimolar amounts (250 nM) of the different proteins to identify differences between the SARS-CoV-2 protein variants (section 2.2.4.5.1). In a preliminary experiment, the RNA chaperone activity of all individual proteins was titrated to determine suitable quantities for comparative analysis (Supplementary Figure 6A, B). Chaperone assays were performed on a native PAA gel (Figure 23A), and the results from three biological replicates were statistically analyzed and represented as boxplots in Figure 23B. In the case of both N_WT (lane 4) and N_WT_PM (lane 6), no differences in activity of RNA annealing were observed, as evidenced by complete dsRNA formation. The enhanced RNA annealing activity of N_WT (dark red) and N_WT_PM (light red) relative to the RNA mix control (black) was statistically significant, suggesting that pseudo-phosphorylation does not affect the function of the Wuhan N protein. Surprisingly, the Omicron BA.5 N protein exhibited distinct behavior. The unmodified N_BA.5 (lane 3) displayed reduced chaperone activity, indicated by residual unhybridized ssRNA in the gel. The difference in dsRNA formation between the RNAMix control (black) and N_BA.5 (dark blue) was significant, as was the difference between N_WT (dark red) and N_BA.5, highlighting a genuine difference in chaperoning behavior between these two protein variants. Interestingly, the pseudo-phosphorylated Omicron BA.5 protein (N_BA.5_PM, lane 5, blue) restored the RNA chaperone efficiency comparable to that of the Wuhan N protein, evidenced by a single, intense dsRNA band in the gel. The significant difference in the percentage of dsRNA between the RNAMix control (black) and N_BA.5 (dark blue) further supports this observation. A similar trend was obsered for another ssRNA pair (ssRNA20/ssRNA21), with the exception that the phosphomimetic variants of both N_WT and N_BA.5 did not achieve full RNA hybridization (Supplementary Figure 6C, D). This surprising finding demonstrates that phosphorylation

modulates the chaperone activity of different SARS-CoV-2 N protein variants, underscoring the potential role of phosphorylation in regulating RNA chaperoning during viral infections.

3.3.4. Inhibition of liquid-liquid phase separation does not affect the RNA chaperone activity

The accurate folding of the viral RNA genome is likely essential for the viral life cycle and its infectivity. A comprehensive understanding of the RNA chaperone mechanism and its role in RNA genome folding of SARS-CoV-2 may pave the way for the development of effective antiviral drugs. Consequently, novel N protein-directed inhibitors, which were identified through a small molecule library screen conducted in collaboration with the Fraunhofer ITEM, were examined. These inhibitors interact with the N protein, specifically blocking N-mediated liquid-liquid phase separation (LLPS) with RNA. As outlined in section 3.3.1, RNA interaction and binding form the foundation for efficient RNA chaperone activity, and drugs targeting the N-RNA interaction may also interfere with the chaperone activity if these mechanisms are connected. Among the identified inhibitors, A7 (GSK J4 HCl), G22 (NSC348884) and N13 (Cloxiquine) efficiently disrupt N-RNA interaction, mediated by droplet formation. This disruption is evidenced by the formation of droplets in the absence of inhibitor, whereas little to no droplet formation was observed in presence of 1.25 μM of the respective inhibitor (Figure 24A, section 2.2.4.5.2).

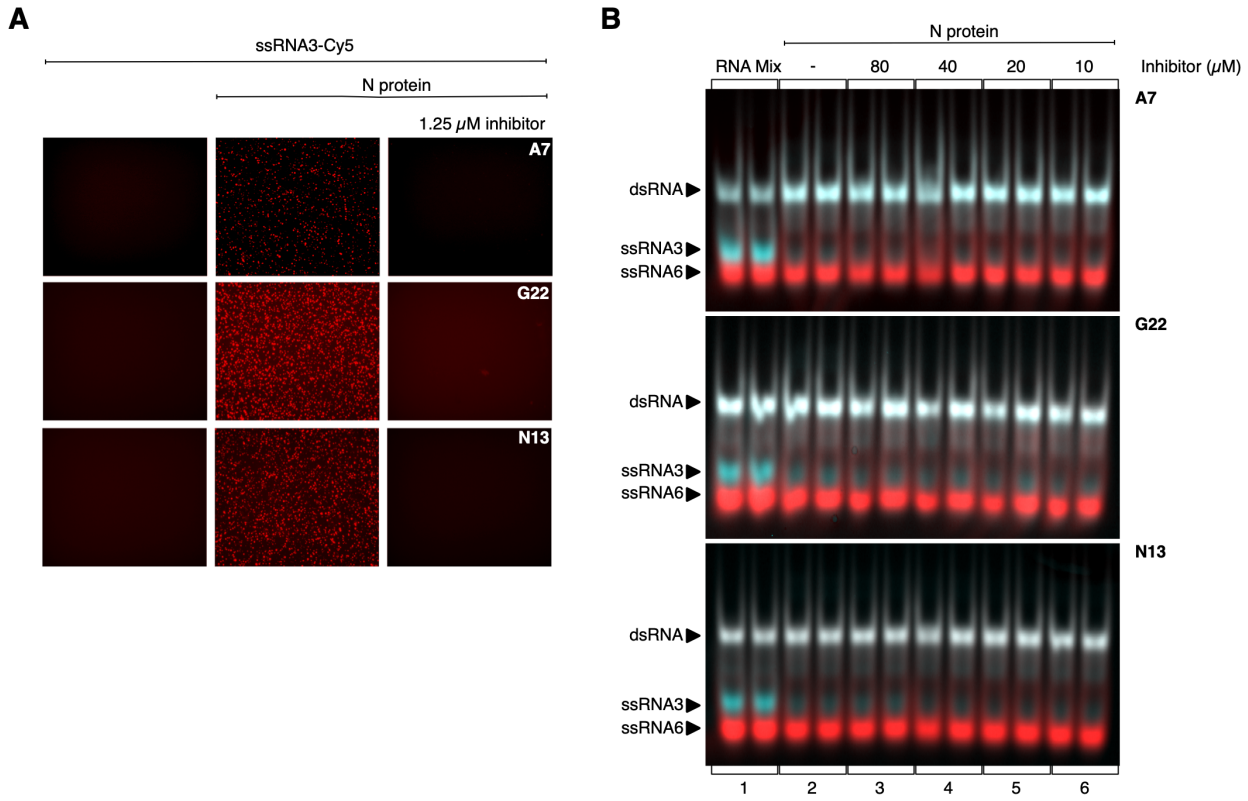

Figure 24: LLPS inhibitors do not impair the RNA chaperone activity of the N protein

(A) LLPS experiments were conducted using 100 nM of ssRNA3-Cy5, which were incubated with 2 μM of N_WT, in the presence or absence of 1.25 μM A7, G22 or N13 inhibitor. After a 2h incubation at 25°C, droplet formation was visualized by fluorescent microscopy at 40x magnification. While droplet formation was observed in the presence of N protein, addition of inhibitor led to depletion of droplet formation in each case. **(B)** RNA chaperone activity of N_WT was investigated in presence of LLPS inhibitors A7 (top), G22 (middle) and N13 (bottom). The RNA Mix (ssRNA3-Cy3, ssRNA6-Cy5; lane 1) was incubated with N_WT in the absence (lane 2) or presence of various inhibitor concentrations: 80 μM (lane 3), 40 μM (lane 4), 20 μM (lane 5) and 10 μM (lane 6). While the presence of N protein led to a full dsRNA hybridization, evidenced by a total loss of ssRNA3-Cy3 signal, the added inhibitors did not show any effect on the chaperone efficiency of N_WT.

The characterization of the inhibitors by nanoDSF revealed that these do directly interact with N and induce slight changes in the T_M values of N_WT without devastating he overall protein integrity (Supplementary Figure 7), indicating a direct interaction between the protein and the compound. In terms of the inhibitors' effect on the RNA chaperone function of the wildtype N protein, the assay was performed in presence of increasing concentrations of the inhibitors (Figure 24B). The N protein itself efficiently facilitated RNA hybridization (lane 2) and even in the presence of inhibitor (lanes 3-6), RNA hybridization persisted, as evidenced by the loss of ssRNA3 signal relative to the RNA Mix control (lane 1). Although inhibitors A7, G22, and N13 interact with the RBD or CTD, which are implicated in efficient chaperoning, and are capable of disrupting N protein-mediated LLPS, they do not affect the protein's chaperone activity. These results suggest that the RNA chaperone mechanism operates independently of LLPS-mediated N-RNA interaction.

3.4. The SARS-CoV-2 N protein interacts with cell surface heparin and heparan sulfate

The identification of an interaction between the SARS-CoV-2 N protein and cell surface glycosaminoglycans heparin (H) and heparan sulfate (HS) post-infection suggests a potential extracellular function of N in modulating host immunity (A. López-Muñoz, 2022). However, while the presence of extracellular N and its interaction with these molecules has been established, a detailed biochemical and biophysical characterization of this interaction is lacking. The upcoming chapter aims to receive a more detailed understanding of the N protein H/HS interaction, seeking to unravel its significance within the viral infection cycle. This extracellular interaction extends beyond the conventional roles of the N protein in RNA binding and packaging, potentially shedding light on novel functions crucial for SARS-CoV-2 pathogenesis.

3.4.1. The N protein displays different interaction modes with heparin/heparan sulfate

In an initial investigation, the interaction of the N protein towards H/HS was explored in regards of detecting binding through EMSA, assessing the impact of ligand binding on the overall protein stability through nanoDSF, and examining changes in particle size upon ligand interaction via dynamic light scattering (DLS) (Figure 25).

To evaluate the binding abilities of N_WT towards H/HS, EMSA (2.2.4.4.2) experiments were conducted. A 647-fluorescently labeled N_WT was used, and H/HS were titrated to the protein (Figure 25A). A noticeable shift upon H/HS addition was observed, with H binding (top) starting at approximately 50 nM of protein (lane 8), while HS binding (bottom) commenced at around 200 nM (lane 6), reaching saturation at 800 nM of protein. Given that the N protein is typically associated with RNA, it was of particular interest if the protein is capable of binding both, H/HS and RNA simultaneously. Consequently, fluorescently labeled N_WT (red) was preincubated with *in vitro* transcribed Cy3-labelled GFP-PS9 RNA (green) to form a complex and H/HS was subsequently added in increasing amounts (2.2.4.4.3, Figure 25B). Differences were noted between H and HS interactions. Notably, with low concentrations of H, RNA remained strongly bound by N_WT, as indicated by the yellow appearance of the band (lanes 11-14). However, RNA dissociation occurred at approximately 100 nM, followed by exclusive binding of H by the N protein, evident from the green RNA signal at the size of the RNA alone

(lane 1) and a downward shift in the N_WT signal, corresponding to the N-H control (lane 5). In contrast, for HS, no release of RNA was detected even with increasing HS concentration, suggesting simultaneous binding of both HS and RNA to the protein (lanes 6-14). In order to exclude an possible interaction between RNA and H/HS, both were co-incubated, resulting in no shift (lane 2). Additionally, N_WT (lane 4), RNA and N_WT (lane 3), as well as H/HS and N_WT (lane 5), were incubated in concentrations ensuring full binding, serving as further controls. These binding analyses suggests the presence of a trimeric complex consisting of N, RNA and H, until a specific threshold concentration is reached, and the formation of a complex that persists for HS.

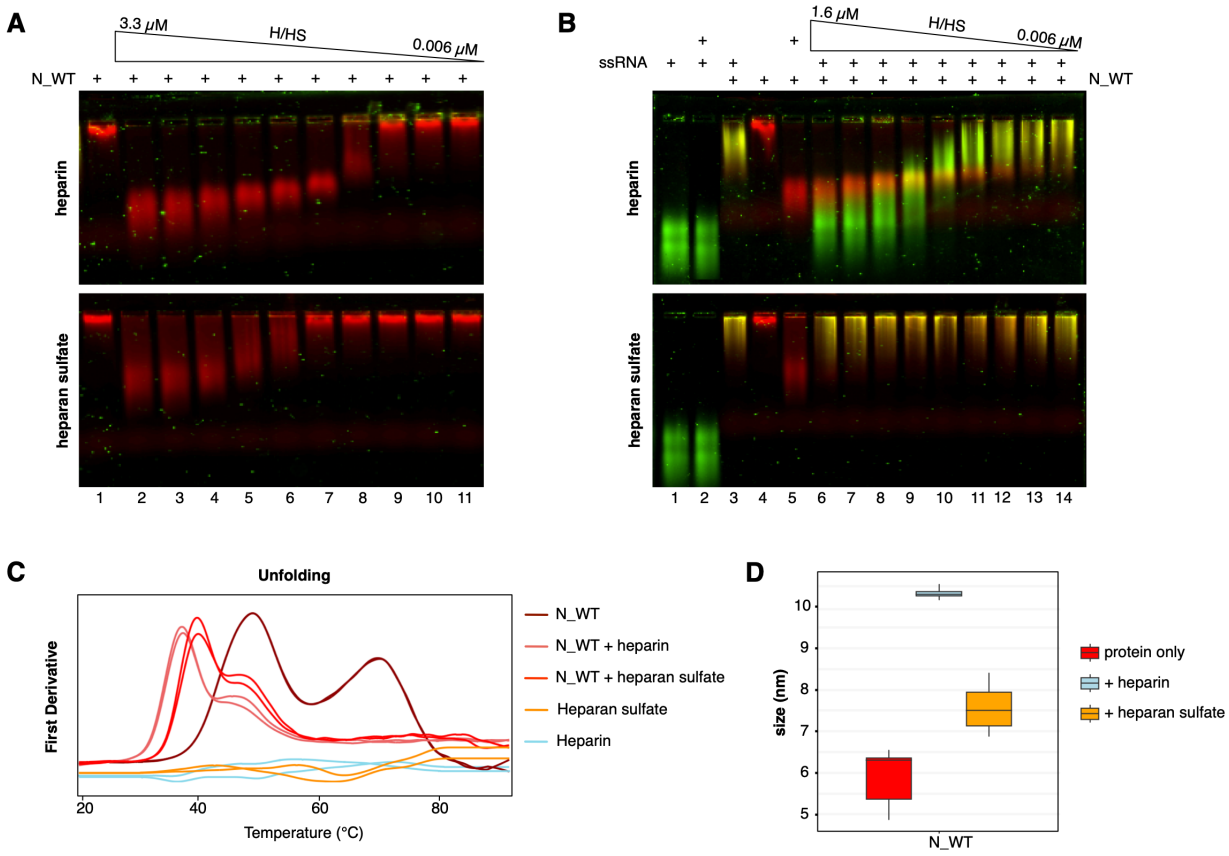

Figure 25: SARS-CoV-2 N interacts differently with heparin and heparan sulfate

(A) Electromobility Shift Assays (EMSA) of N_WT with either heparin (H) or heparan sulfate (HS) on a 1.5% agarose gel. N_WT was fluorescently labeled with DY-647. The reaction was set up with 500 nM 647-N_WT mixed with increasing concentrations of H/HS from 0.006 – 3.3 µM and incubated for 2h at RT in assay buffer (50 mM HEPES pH 7.4, 100 mM NaCl, 0.01% Pluronic F-127). Fluorescent readout occurred with the Cy5 laser of the Typhoon™ FLA 9500 fluorescent scanner (GE Healthcare). 647-N_WT was applied as a control in lane 1. Increasing concentrations of H/HS led to a shift in the fluorescent signal, suggesting interaction of N_WT with H/HS.
(B) Electromobility Shift Assays (EMSA) of N_WT with Cy3-RNA (*in vitro* transcribed GFP-PS9) and either heparin (H) or heparan sulfate (HS) on a 1.5% agarose gel. N_WT was fluorescently labeled with DY-647. The reaction was set up with 500 nM 647-N_WT mixed with increasing concentrations of H/HS from 0.006 – 1.6 µM and incubated for 2h at RT in assay buffer (50 mM HEPES pH 7.4, 100 mM NaCl, 0.01% Pluronic F-127). Fluorescent readout occurred with the Cy5 laser of the Typhoon™ FLA 9500 fluorescent scanner (GE Healthcare). 647-N_WT was applied as a control in lane 1. RNA and H are simulteneously bound by N_WT until a treshold concentration of approximately 100 nM H at which RNA got released. N_WT, HS and RNA persist bound independently of HS concentration. **(C)** Protein stability was evaluated by monitoring the unfolding and refolding properties of the N_WT alone (dark red) and with H (light

red) and HS (red) addition by nanoDSF. 10 µM of N_WT with or without 5 µM of H/HS as well as 5 µM of H (light blue) or HS (orange) alone were loaded into Prometheus™ NT.48 Standard Capillaries (NanoTemper) and analyzed by a temperature gradient ranging from 20-85°C in the Prometheus™ NT.48 nanoDSF device (NanoTemper). H/HS alone displayed a backround signal. Addition of H/HS to N_WT led to a leftward shift of the RBD T_M along with the disappearance of the CTD melting peak. **(D)** Boxplot representing the particle size of N_WT alone (red) as well as with H (light blue) and HS (orange) addition. Each boxplot contains four individual DLS measurements. Each boxplot represents the interquartile range (IQR), with the median indicated by a horizontal line inside the box. The upper and lower whiskers extend to a maximum of 1.5 times above and below the upper and lower quartiles, respectively. The x-axis represents N_WT, while the particle size in nm is indicated on the y-axis. Addition of H/HS led to an increase in particle size.

To gain further insights into how the interaction with H/HS influences the N protein, nanoDSF measurements were performed (2.2.4.1). As illustrated in Figure 25C, N_WT (dark red), as a control, exhibited two T_M peaks at the expected temperatures. Upon addition of both H and HS, a destabilization of the RBD was observed, indicated by a left shift of the RBD peak (T_M below 40°C), which is more pronounced for H (light red) compared to HS (red), accompanied by a disappearance of the CTD peak in both cases. Notably, H (light blue) and HS (orange) themselves did not exhibit any peaks and appear as background. These ligands seem to interact with both structured domains of the protein. Further DLS analysis (2.2.4.2 ,Figure 25D), aimed at providing insights into the influence on particle size upon ligand binding, revealed an approximate size of 6 nm for N_WT (red) without any ligand bound. However, H binding induced an increase in size to around 10 nm (light blue) and HS to approximately 7.5 nm (orange), indicative of complex formation. As stable complexes of H and HS were only formed at 37°C, all DLS measurements were conducted at this temperature. In summary, the SARS-CoV-2 N protein interacts with H/HS, exhibiting diverse interaction modes, as inferred from EMSA and DLS analyses.

3.4.2. The interaction with heparin/heparan sulfate is mediated by LLPS

When 647-labeled N_WT was introduced to U2OS cells, accumulation of N_WT on the cell surface was observable within seconds until several hours post-treatment (Figure 26A). This attachment exhibited a highly dynamic appearance, characterized by a non-uniform distribution resembling droplet-like shape. This suggested a potential interaction between the N protein and H/HS via an extracellular liquid-liquid phase separation (LLPS) mechanism. To further elaborate on this interaction, an *in vitro* LLPS assay was established. In this assay, 500 nM of 647-labeled N_WT (with a labeled to unlabeled N ratio of 1:4) was co-incubated with either 50 nM of H or 100 nM of HS in the 1xLLPS assay buffer containing 50 mM HEPES pH 7.4, 100 mM NaCl, and 0.01% Pluronic. Following a 2h incubation at room temperature, droplet formation was visualized using fluorescent microscopy (Keyence BZ-X800) with the Cy5 filter. Indeed, upon examination with both 4x and 40x magnification, liquid droplets have formed, indicated by the presence of red dots in Figure 26B. This hallmark of LLPS, droplet formation was observed to occur with a specific ligand concentration range and was temperature-dependent (Supplementary Figure 13 and Supplementary Figure 17).

The presence of LLPS on the cell surface was confirmed by fluorescence recovery after photobleaching (FRAP), as outlined in section 2.2.5.4 (Figure 26C). The assay and data analysis were conducted by Nicolas Landrein from the work group of Prof. H. Wodrich at the University of Bordeaux. Following fluorescence bleaching of N_WT-647 on the cell surface of U2OS cells, the fluorescent signal returned with a half-time (t_half) of 137 seconds. This rapid recovery suggests a highly dynamic exchange of fluorescent proteins on the cell surface, indicative of an actual LLPS mechanism. The dynamic behavior observed supports the hypothesis that the SARS-CoV-2 N protein can undergo extracellular phase separation with glycosaminoglycans.

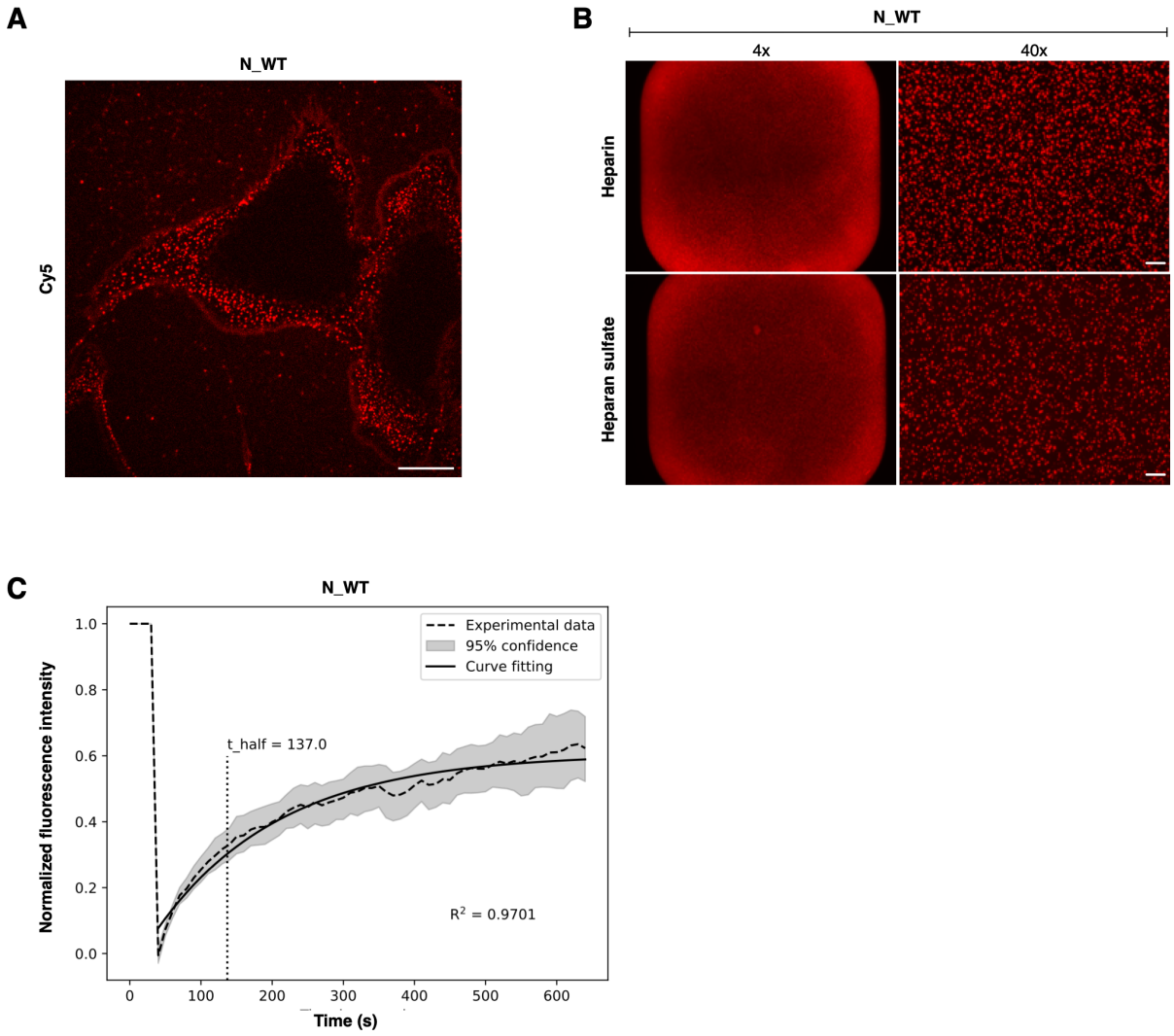

Figure 26: Interaction of SARS-CoV-2 N with heparin and heparan sulfate is mediated by liquid-liquid phase separation

(A) Confocal microscropy image of 647-labeled N_WT on U2OS cells. 500 nM of fluorescently labeled N_WT was introduced to U2OS cells and protein attachment was monitored in real-time. N_WT attached to the cell surface of U2OS within a few seconds post-treatment and was detectable for several hours. The present image depicts the state 10 min post-treatment. N_WT took the shape of droplets on the cell surface. Scale bar: 25 µm
(B) Interaction with N_WT and heparin (H) or heparan sulfate (HS) was elaborated using an *in vitro* LLPS assay. To conduct this, a constant concentration of 500 nM N protein (with a ratio of 1:4 of 647-labeled to unlabeled N_WT) was mixed with either 50 nM heparin (H) or 100 nM heparan sulfate (HS) in a total volume of 12 µl 1x LLPS buffer (50 mM HEPES pH 7.4, 100 mM NaCl, 0.01% Pluronic F-127). Droplet formation was visualized using fluorescent microscopy (Keyence BZ-X800) with the Cy5 filter at 4x (BZ-PF04P Plan Fluorite 4x PH, Keyence) and 40x magnification (BZ-PF40LP Plan Fluorite 40X LD PH, Keyence). Formation of liquid droplets was detectable for both H and HS and can be visualized at 4x and 40x magnification. **(C)** Normalized fluorescence intensity of the N_WT-647 signal on U2OS cells was measured in a fluorescence recovery after photobleaching (FRAP) experiment. Following fluorophore bleaching, fluorescence was monitored for 640 seconds. The half-time (t_half) for fluorescence recovery to 50% of the initial intensity was calculated to be 137 seconds post-photobleaching. The recovery of the fluorescent signal of N_WT indicates a dynamic LLPS mechanism. Figure C was kindly provided by Nicolas Landrein, University of Bordeaux.

3.4.3. RBD-IDR2-CTD as the key domains of heparin/heparan sulfate interaction

As the interaction with H/HS, mediated by extracellular LLPS on the cell surface, unveils a novel function of the N protein distinct from RNA binding and packaging, revealing the protein domains essential for this function became of particular interest. Therefore, the set of N truncation proteins (3.1.2 and 3.1.3) were examined to assess their interaction with both H and HS in terms of particle size, LLPS ability, and binding to the cell surface.

In DLS analyses, an interaction with H/HS was detectable for most N truncation proteins, as evidenced by a shift in particle size (Figure 27A) The boxplot presents four individual size measurements for each protein per condition, with detailed data and size distribution properties presented in Supplementary Figure 8 and Supplementary Figure 9. The different N (truncation) proteins are depicted in red boxes, with added H shown in light blue boxes and with added HS in orange boxes. With the exception of N_IC, interaction with HS induced a conformational change leading to a larger particle size. An identical pattern was detectable for H, with exception of N_CI. Notably, for N_CI, interaction was only detectable with HS. In general, a stronger change in particle size was observable for N-H interaction compared to N-HS. In the case of N_IRI, interaction with H led to the formation of a complex with an approximate size of 23 nm, more than double the size of the complexed formed with other truncation proteins. Regarding N_RI, the protein did not exhibit a consistent particle size when combined with HS, as reflected by a notable scatter in standard deviation. Nevertheless, interaction with H/HS induced a change in particle size, underscoring the influence of these ligands on the protein's conformation.

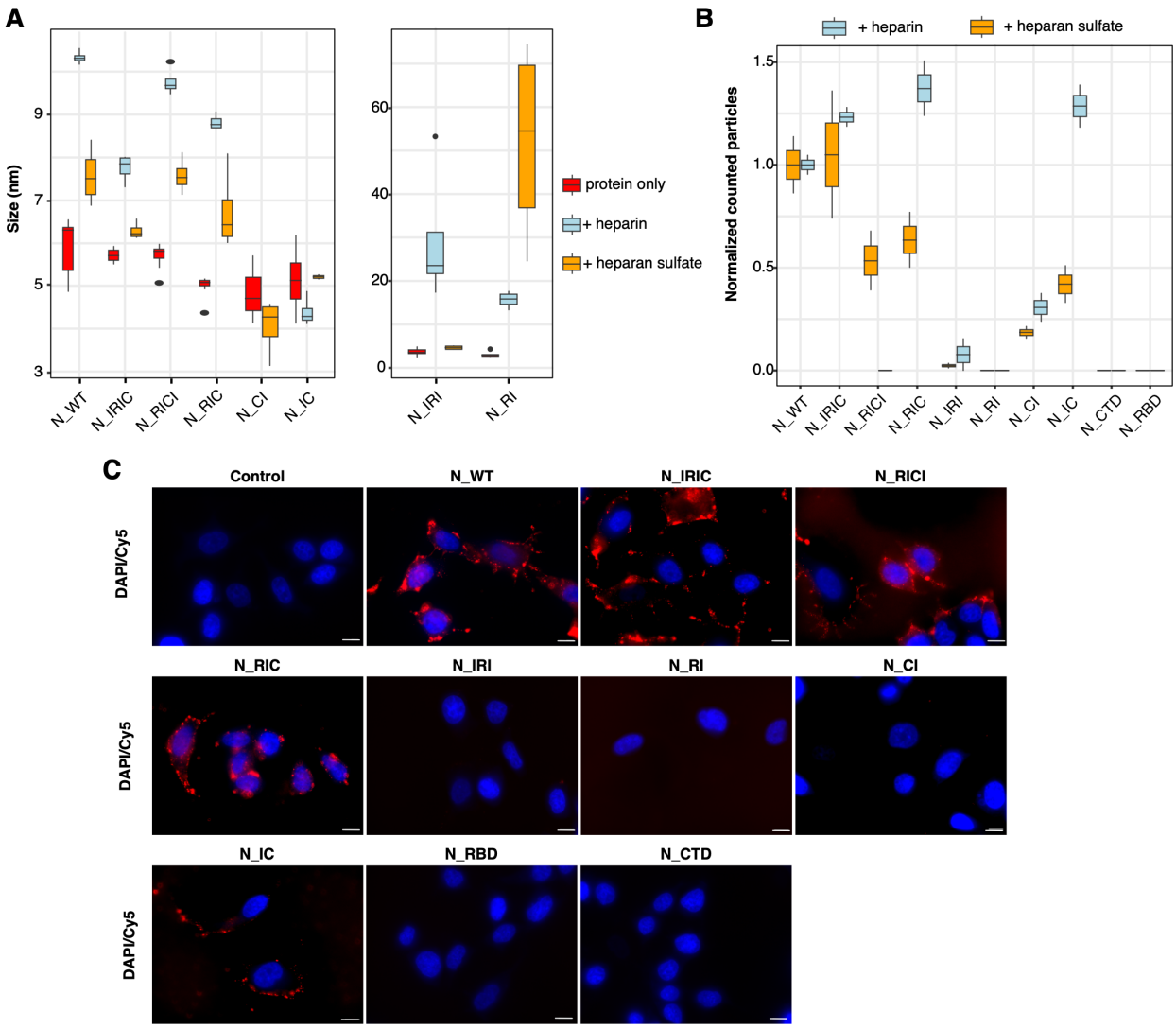

Figure 27: Characteristics of heparin/heparan sulfate interaction of N truncation proteins

(A) Boxplot representing the particle size of the N truncation proteins alone (red) as well as with H (light blue) and HS (orange) addition. Each boxplot contains four individual DLS measurements. Each boxplot represents the interquartile range (IQR), with the median indicated by a horizontal line inside the box. The upper and lower whiskers extend to a maximum of 1.5 times above and below the upper and lower quartiles, respectively. Outliers beyond this range are depicted as individual data points. The x-axis represents the respective N truncation protein, while the particle size in nm is indicated on the y-axis. Addition of H led to an increase in particle size true for most N truncation proteins with exception of N_IC. Addition of HS also led to an increase in particle size for most proteins except for N_CI. N_CI only displayed interaction with HS. For N_RI, in combination with HS, no distinct particles were formed resulting in a broad standard deviation of the box. **(B)** Boxplot representing the normalized counted particles/droplets of the N truncation proteins alone and in combination with H (light blue) and HS (orange) from liquid-liquid phase separation (LLPS). Each boxplot contains two individual LLPS approaches. Each boxplot represents the interquartile range (IQR), with the median indicated by a horizontal line inside the box. The upper and lower whiskers extend to a maximum of 1.5 times above and below the upper and lower quartiles, respectively. The x-axis represents the respective N truncation protein, while the normalized counted particles are indicated on the y-axis. Observed formed droplets were counted with Fiji and the LLPS formation of N_WT was set as the baseline. Counted particles of each N truncation protein were normalized to the counted particles of N_WT for each ligand. No droplet formation was detectable for N_RI, N_RBD, and N_CTD. Weak droplet formation was observable for N_IRI, N_IC and N_CI whereby N_IC forms efficiently droplets with H but not with HS. N_RICI only forms droplets with HS. **(C)** Immunofluorescence images of MCF-7 cells treated with 647-labeled N truncation proteins. MCF-7 cells were incubated with a total of 500 nM of each 647-labeled protein for 20 min at 37°C, 5% CO_2. Cells were fixed with 4% PFA, the cell nucleus was stained with DAPI, and fluorophore signals were checked by fluorescent microscopy using the Keyence BZ X-800 with the 100X Oil objective (Keyence, BZ-PA100). N_WT, N_RICI, N_IRIC, N_RIC and N_IC showed a 647-N protein signal. The other N truncation proteins did not show a signal on the cell surface. Untreated cells stained with DAPI served as a control. Scale bar = 25 µm.

Regarding the investigation of the LLPS properties, all N truncation proteins were analyzed at identical concentrations of each protein, H and HS, in order to directly compare the efficacy of phase separation with N_WT. The boxplot in Figure 27B depicts the counted droplets of each truncation protein bound to either H (light blue) or HS (orange), normalized to the WT N protein (Supplementary Figure 10). The analysis combined two individual LLPS experiments. N truncation proteins lacking the CTD (N_IRI, N_RI), exhibited no phase separation with H/HS, while those lacking the RBD (N_CI, N_IC) retained some capacity for LLPS, but still reduced compared to proteins containing the RBD and CTD. Remarkably, N_IC demonstrated a comparable interaction with H to N_WT. Nevertheless, N_RIC emerged as the most proficient protein in interacting with both H and HS, effectively mediating phase separation. Surprisingly, N_RICI appeared incapable to promote LLPS with H, presenting a distinct behavior compared to other truncation proteins. Even though the required protein domains for LLPS formation were analyzed, understanding the behavior of N truncation proteins in binding to the cell surface remained elusive. To address this, the N truncation proteins were fluorescently labeled with a 647 dye, and their binding to the cell surface of MCF-7 cells was observed and visualized by fluorescent microscopy (Figure 27C). As heparin is absent on MCF-7 cells, the analysis focused on binding to HS. Immunostaining images revealed results consistent to the phase separation abilities of the N truncation proteins. A fluorescent signal was observable for N_WT, N_IRIC, N_RICI, N_RIC and N_IC. Notably, N_RICI, despite not demonstrating LLPS with HS, still showed binding to the cell surface. Conversely, N_CI, which exhibited some LLPS-mediated droplet formation with HS, did not yield a signal in immunostaining. Individual fluorescent channels and phase contrast images are available in Supplementary Figure 11. In summary, N_RIC emerges as the protein fragment most capable in interacting with H and HS, with N_IC also demonstrating interaction to a certain extent, underscoring the importance of the IDR2 in this context.

3.4.4. Omicron BA.5 and Wuhan N proteins display similar interaction abilities towards heparin/heparan sulfate

The N proteins of the Wuhan and the Omicron BA.5 variants of SARS-CoV-2 exhibit distinct modes of RNA binding (3.2.3) and RNA chaperone activity (3.3.3). Given the potential implications of their interaction with cell surface H and HS in modulating the host immune system, understanding the differences between these SARS-CoV-2 variants is crucial for understanding the viral pathogenesis.

Interaction with H resulted in a reduction in RBD stability, with a T_M below 40°C and the disappearance of the CTD peak (Figure 28B, light blue), compared to N_BA.5 (dark blue), being in line with the observations for N_WT. This interaction with H appears to affect both folded domains, the RBD and the CTD of N_BA.5, similar to N_WT. Additionally, consistent with N_WT, particle size analysis (Figure 28A) showed an increase in size upon H (light blue) and HS (orange) addition compared to the protein alone (red). Nevertheless, the change in detectable particle size due to HS interaction was weaker for N_BA.5. Each box represents four individual measurements obtained through DLS for each condition and exemplary DLS size distribution data can be referenced from Supplementary Figure 8 and Supplementary Figure 9.

647-fluorescently labelled N_BA.5 showed a detectable signal when applied to MCF-7 cells, indicating its presence on the cell surface (Figure 28C). This binding appears to be driven by ionic interactions, as evidenced by the lack of binding of N_WT and N_BA.5 on MCF-7 cells pretreated with polybrene, which neutralizes the cell surface (Supplementary Figure 12). Furthermore, N_BA.5 exhibited similar LLPS trends as N_WT (Figure 28D). N_BA.5 phase separates in a smaller concentration range with H (dark blue), whereby LLPS discontinues at 150 nM of H, while phase separation occurs across the entire concentration range with HS (blue). Droplet formation with H is reduced compared to N_WT (dark red), which showed a nearly 4-fold higher range of H interaction in which LLPS is observable. However, for HS, N_BA.5 does not significantly differ from N_WT (red) in terms of the counted particles. These plots were generated from two individual LLPS experiments, and exemplary LLPS pictures are provided in Supplementary Figure 13. In the case of H and HS, the N protein variants did not exhibit significant differences in their interaction modes.

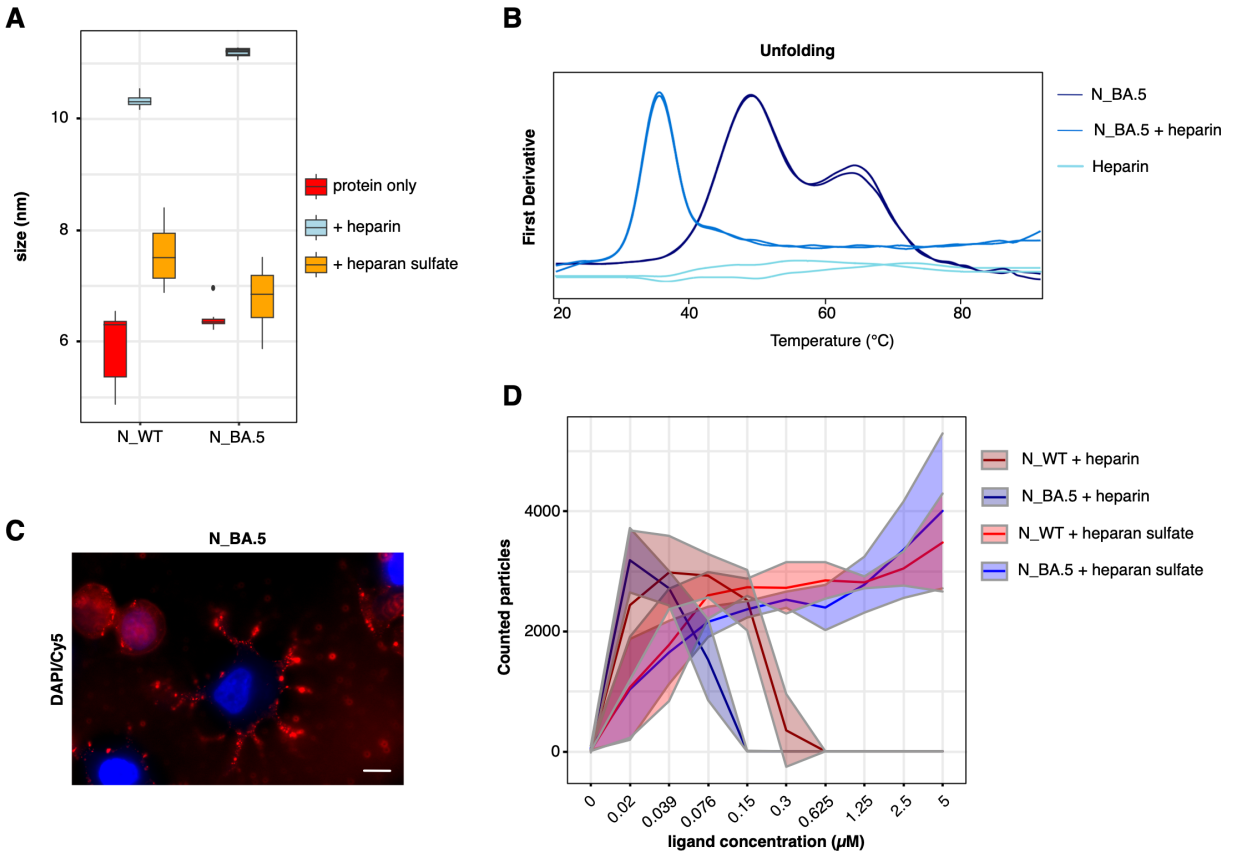

Figure 28: Interaction of Omicron BA.5 N with heparin and heparan sulfate

(A) Boxplot representing the particle size of N_WT and N_BA.5 alone (red) as well as with H (light blue) and HS (orange) addition. Each boxplot contains four individual DLS measurements. Each boxplot represents the interquartile range (IQR), with the median indicated by a horizontal line inside the box. The upper and lower whiskers extend to a maximum of 1.5 times above and below the upper and lower quartiles, respectively. Outlier beyond this range are displayed as single data points. The x-axis represents the respective protein, while the particle size in nm is indicated on the y-axis. For both proteins, addition of H/HS led to a increase in particle size. **(B)** Protein stability was evaluated by monitoring the unfolding and refolding properties of the N_BA.5 alone (dark blue) and with H (blue) addition by nanoDSF. 10 µM of N_BA.5 with or without 5 µM of H as well as 5 µM of H (light blue) alone were loaded into Prometheus™ NT.48 Standard Capillaries (NanoTemper) and analyzed by a temperature gradient ranging from 20-85°C in the Prometheus™ NT.48 nanoDSF device (NanoTemper). H alone displayed a background signal. Addition of H to N_BA.5 led to a leftward shift of the RBD T_M along with the disappearance of the CTD melting peak. **(C)** Immunofluorescent staining of MCF-7 cells with 647-labeled N_BA.5. Cells were treated with a total of 500 nM 647-labeled protein and incubated for 20 min at 37°C, 5% CO_2. Cells were fixed in 4% PFA and stained with DAPI. Fluorescence signals were analyzed by fluorescent microscopy (Keyence BZ-X800) using the 100X Oil objective (Keyence, BZ-PA100). Binding of N_BA.5 to the cell surface was observed. Scale bar = 25 µm. **(D)** Line plot of analyzed LLPS abilities of N_WT with H (dark red) and HS (red) as well as N_BA.5 with H (dark blue) and HS (blue). The number of droplets was counted with Fiji and are displayed in the y-axis. Ligand (H/HS) concentration (0 – 5 µM) is displayed on the x-axis. Standard deviation is illustrated as a slightly transparent ribbon. Both N_WT and N_BA.5 form droplets with HS in a broader concentration range than with H.

This mechanism of extracellular N protein H/HS interaction along with further chemokine interaction impairing the host immune response (A. López-Muñoz, 2022), presents a crucial immune-modulating mechanism during viral infection. Recognizing the potential significance of this interaction, a collaboration with the Fraunhofer ITEM, in particular with Dr. Nataša Stojanović Gužvić, Silvia Materna-Reichelt and Durdam Das, regarding a screen of LLPS directed inhibitors against the N_BA.5 H/HS interaction was set up (2.2.4.6.3). Given the

prevalence of the Omicron BA.5 variant over the diminished Wuhan strain, N_BA.5 was chosen for the screening process. Preparation of the tools and small-scale test LLPS experiments were conducted from our laboratory while the large-scale screen, containing 2,500 compounds, was carried out jointly with Silvia Materna-Reichelt at the Fraunhofer ITEM. Bioinformatic analysis of the screening results was done by Durdam Das, leading to the identification of promising drug targets, which were ordered from Selleckchem for further processing. These positive hits underwent further validation to assess their effects on N_BA.5, N_BA.5 with H, and N_BA.5 with HS in our laboratory (Supplementary Figure 14). The validation LLPS experiments revealed that most of the drugs primarily interfered with N_BA.5 alone, causing protein aggregation (A). However, inhibitors B12 (Fenticonazole Nitrate), K9 (RAF265), and D5 (Nelfinavir Mesylate) exhibited exceptional behavior in this regard. At the highest concentration of 100 μM, droplet formation was notably reduced in the presence of specific inhibitors, such as M15 (NVP-BHG712), G15 (SU11274), P13 (SGI-1027), C21 (Eltrombopag Olamine), D5, and K9 (B and C). When the inhibitor concentration was lowered to 50 μM, only G15, P13, and D5 showed a lack of droplet formation for both H and HS. Additionally, selected inhibitors P13 and D5 underwent testing to assess their inhibition of N_WT and N_BA.5 binding to the cell surface of MCF-7 cells (Supplementary Figure 15). Surprisingly, these inhibitors displayed a reduced signal when combined with N_WT and N_BA.5. Notably, inhibitor P13 even induced cell death when combined with N_BA.5. In summary, while these inhibitors did not seem suitable for interfering with LLPS-mediated N H/HS interaction, a subsequent screen involving 10,000 compounds is currently underway, offering the potential to identify additional promising candidates.

3.4.5. Efficient interaction of pseudo-phosphorylated N proteins with heparin/heparan sulfate is temperature-dependent

In previous sections, the role of pseudo-phosphorylation was explored in regulating the interaction between the N protein and RNA. Extending this investigation to the interaction between the N protein and H/HS, N_WT_PM and N_BA.5_PM were analyzed regarding their interaction modes. Consistent with the findings of unmodified proteins, the addition of H (orange, blue) to either N_WT_PM (red) or N_BA.5_PM (dark blue) resulted in further destabilization of the RBD (Figure 29B) As outlined in chapter 1.1.3., pseudo-phosphorylation alone induced a leftward shift of the RBD T_M, and ligand interaction enhanced this effect,

resulting in a T_M of approximately 30°C. Particle size analysis (Figure 29A) indicated that pseudo-phosphorylated N proteins exhibited weaker size discrepancies upon H (light blue) or HS (orange) binding compared to the unmodified N proteins. For N_WT_PM, both H and HS addition did not strongly influence particle size, indicating a weak interaction. For N_BA.5_PM, H/HS interaction resulted in a smaller complex with a stronger H induced effect observable compared to HS.

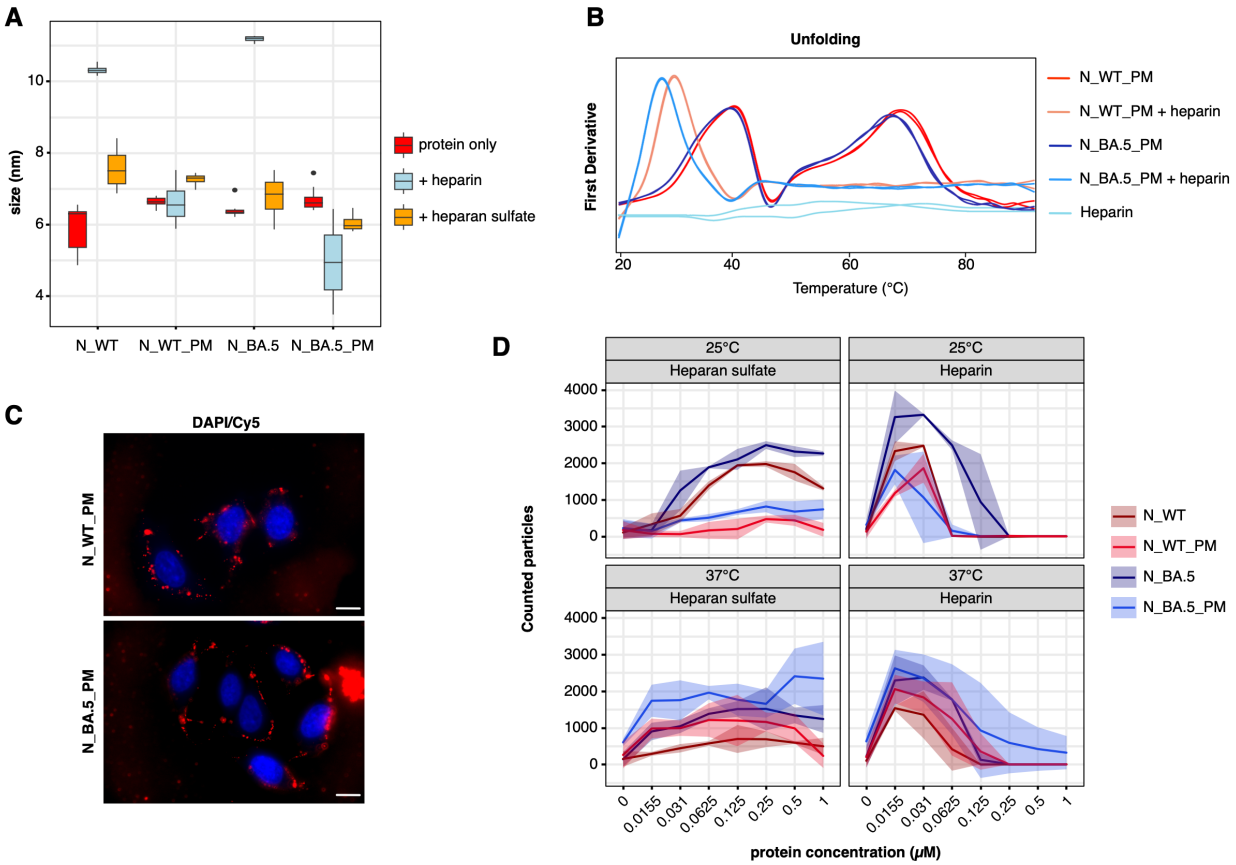

Figure 29: Interaction of pseudo-phosphorylated N proteins with heparin and heparan sulfate

(A) Boxplot representing the particle size of N_WT, N_WT_PM, N_BA.5 and N_BA.5_PM alone (red) as well as with H (light blue) and HS (orange) addition. Each boxplot contains four individual DLS measurements. Each boxplot represents the interquartile range (IQR), with the median indicated by a horizontal line inside the box. The upper and lower whiskers extend to a maximum of 1.5 times above and below the upper and lower quartiles, respectively. Outlier beyond this range are displayed as single data points. The x-axis represents the respective protein, while the particle size in nm is indicated on the y-axis. Addition of H/HS led to an increase in particle size the proteins except for N_BA.5_PM, for which a decrease in particle size was observable. For N_WT_PM, addition of H did not result in a size shift. **(B)** Protein stability was evaluated by monitoring the unfolding and refolding properties of N_WT_PM (red) and N_BA.5_PM (dark blue) and in addition with H (orange, blue) by nanoDSF. 10 µM of protein with or without 5 µM of H as well as 5 µM of H (light blue) alone were loaded into Prometheus™ NT.48 Standard Capillaries (NanoTemper) and analyzed by a temperature gradient ranging from 20-85°C in the Prometheus™ NT.48 nanoDSF device (NanoTemper). H alone displayed a background signal. Addition of H to both proteins led to a leftward shift of the RBD T_M along with the disappearance of the CTD melting peak. **(C)** Immunofluorescent staining of MCF-7 cells with 647-labeled N_WT_PM and N_BA.5_PM. Cells were treated with a total of 500 nM 647-labeled protein and incubated for 20 min at 37°C, 5% CO_2. Cells were fixed in 4% PFA and stained with DAPI. Fluorescence signals were analyzed by fluorescent microscopy (Keyence BZ-X800) using the 100X Oil objective (Keyence, BZ-PA100). Binding of both N_WT_PM and N_BA.5_PM to the cell surface was observed. Scale bar = 25 µm. **(D)** Line plot of analyzed LLPS abilities of N_WT (dark red), N_WT_PM (red), N_BA.5 (dark blue) and N_BA.5_PM (blue) with HS (left) as well as H (right) at 25°C (top) and 37°C (bottom). The number of droplets was counted with Fiji and are displayed in the y-axis. Ligand (H/HS) concentration (0 – 1 µM) is displayed on the x-axis. Standard deviation is displayed as a slightly

transparent ribbon. In contrast to N_WT and N_BA.5, N_WT_PM and N_BA.5_PM were just capable of efficient droplet formation at 37°C.

Pseudo-phosphorylation did not seem to affect the binding of N_WT_PM and N_BA.5_PM to the cell surface of MCF-7 cells, as the signal of the 647-fluorescently labeled protein was still detectable (Figure 29C, Supplementary Figure 16). While the intensity appeared slightly weaker compared to N_WT or N_BA.5, signal intensity quantification is lacking. Nevertheless, both proteins retained their ability to bind to the cell surface.

Additionally, both N_WT_PM and N_BA.5_PM displayed droplet formation in presence of H/HS, although the temperature seemed to play a role (Figure 29D). The analysis is based on two individual LLPS experiments (Supplementary Figure 17). At 25°C, N_WT_PM (red) and N_BA.5_PM (blue) exhibited a weaker droplet formation with both H and HS compared to N_WT (dark red) and N_BA.5 (dark blue). However, performing the assay at 37°C resulted in an increased number of counted droplets for the pseudo-phosphorylated N proteins compared to the unmodified ones. In conclusion, pseudo-phosphorylation seems to have minimal impact on the H/HS interaction. However, differences in the LLPS efficiency were observed, particularly concerning the required temperature. These findings suggest nuanced alterations in the interaction modes of pseudo-phosphorylated N proteins with H/HS compared to their unmodified counterparts.

3.4.6. Extracellular N protein induces a proinflammatory cytokine release

López-Muñoz et al. suggested the extracellular N may be transported from expressing to non-expressing cells, interfering with the proinflammatory cytokines produced upon viral infection, by interacting with H and HS on the cell surface. In collaboration with Prof. Ralf Wagner and Antonia Senninger from the Institute of Clinical Microbiology and Hygiene at the University Hospital Regensburg, the impact of extracellular applied SARS-CoV-2 N protein onto the immune response was investigated. Therefore, endotoxin-free N_WT and N_BA.5 were provided by our laboratory. The residual endotoxin in the protein samples was quantified by the University Hospital, resulting in concentrations of 0.661 EU/ml for N_WT and 0.095 EU/ml for N_BA.5. Experimental processing and data analysis was conducted by Antonia Senninger. Immune competent THP-1 cells were treated with various amounts of N protein, and cytokine release was monitored over 24 h using the LEGENDplex™ assay kit (section 2.2.5.5.).

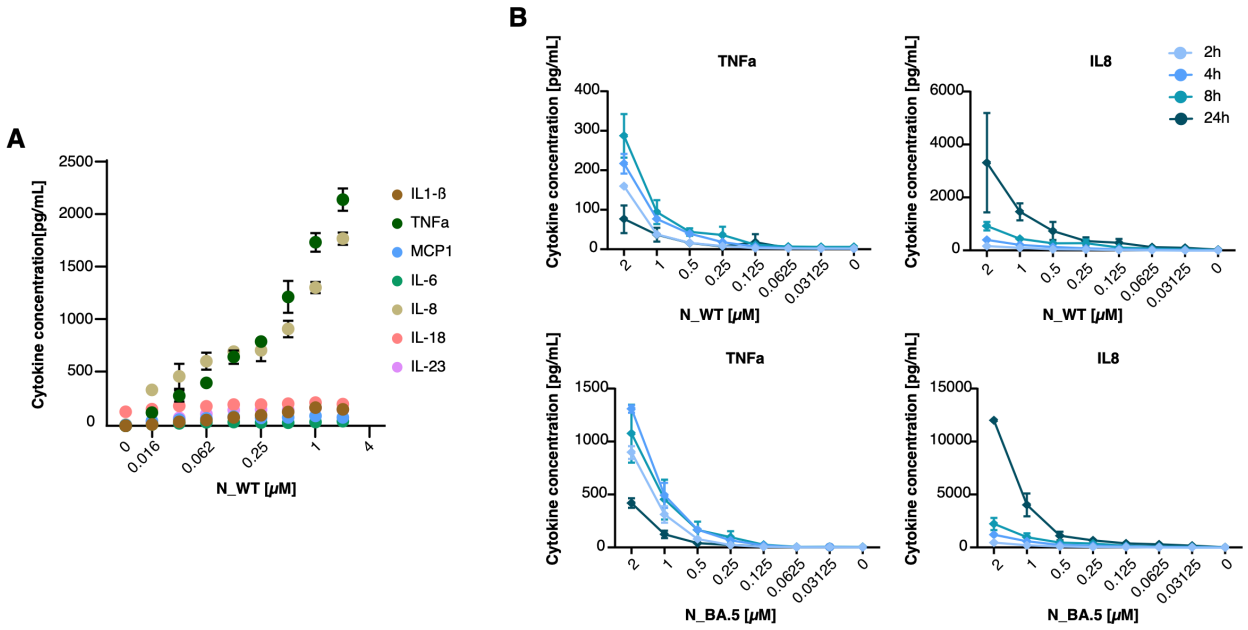

Figure 30: Stimulation of THP-1 cells with N_WT and N_BA.5 induces cytokine release

(A) THP-1 cells were stimulated with increasing concentrations of N_WT, ranging from 0 – 2 µM. Following treatment, cells were incubated for 24h at 37°C and 5% CO_2. Afterwards, supernatant was collected, and cytokine release was quantified. Treatment with N_WT resulted in a dose-dependent release of IL-8 (beige) and TNFα (dark green). The release of other cytokines was not stimulated by N_WT. **(B)** THP-1 cells were stimulated with increasing concentrations of N_WT (top) and N_BA.5 (bottom), ranging from 0-2 µM. The release of TNFα and IL-8 was monitored over a 24h period, with sample collection after 2, 4, 8, and 24h. A stable release of TNFα was detected as early as 2h post-stimulation, while the peak concentration of IL-8 was observed at 24 h post-stimulation. N_BA.5 induced a stronger cytokine compared N_WT. Figures were kindly provided by Antonia Senninger.

The presence of SARS-CoV-2 N protein alone resulted in a dose-dependent increase in TNFα (green) and IL-8 (beige) release (Figure 30A), both of which are proinflammatory cytokines. TNFα was strongly elevated after 2 - 8h (light – medium blue) of incubation with N protein, while IL-8 release took up to 24 h (dark blue) post-stimulation to reach its peak concentration. Interestingly, N_BA.5 appeared to induce a stronger TNFα and IL-8 release compared to N_WT (Figure 30B). To ensure that the observed cytokine release was not due to residual lipopolysaccharide (LPS), a titration of LPS was performed. The results showed that the maximum concentration of LPS remaining in the protein samples did not induce cytokine release (data not shown), thus ruling out LPS as the cause. Given that the N protein itself causes the release of proinflammatory cytokines from extracellular interactions, suggests an additional host modulating function within the viral infection and pathogenesis.

4. Discussion

The SARS-CoV-2 N protein plays a fundamental role in the viral infection cycle, engaging in interactions with both viral RNA and host cellular components. The protein is crucial for proficient RNA packaging and virus assembly and was shown to possess immune modulatory properties (A. López-Muñoz, 2022; S. Lu et al., 2021; Y. Zhao et al., 2021). This study aimed to elucidate the mechanistic details of these interactions, focusing on RNA binding and RNA chaperone activity, as well as interactions with the cell surface glycosaminoglycans heparin and heparan sulfate. Key findings identified and characterized the protein domains harboring the fundamental functions of RNA binding, chaperoning and interaction with glycosaminoglycans, differences between the N proteins of the Wuhan and the Omicron BA.5 strain and the importance of phosphorylation in the context of infection.

4.1. Interaction of the SARS-CoV-2 N protein with nucleic acids

Directly after the entering the host cell, the N protein disassociates from the RNA to enable genome replication. Importance of the N protein regarding its RNA interaction abilities re-emerges in the final phases of viral replication, when it comes to viral genome packaging and the formation of vRNPs (S. Lu et al., 2021). In order to obtain a deeper understanding of the mechanistic nature of the interaction of the N protein with RNA, this study provides the first comprehensive characterization of the N protein, focusing on specific protein domains harboring the protein's RNA binding affinity and specificity. Furthermore, we are the first to demonstrate that the SARS-CoV-2 N protein possesses an intrinsic RNA chaperone activity, indicating that it not only packages the viral genome but also plays a role in facilitating the formation of viral RNA secondary structures.

4.1.1. RNA binding abilities of the SARS-CoV-2 N protein

RNA binding characteristics have been extensively studies by various research groups over the past few years and the N protein has been found to bind to various nucleic acid types and sequences with micromolar affinities, regardless of the sequence, highlighting its ability to interact with different types of RNA and DNA (Zinzula et al., 2021).

In general, the SARS-CoV-2 N protein demonstrated a highly cooperative binding behavior, elucidating the high standard deviation observed, particularly evident in RNA3 interaction (Figure 16B). For clarity, N_WT was also depicted with its K_D, although cooperative binding

typically requires evaluation using the Hill equation. Notably, EC_{50} determination by Hill evaluation was conducted (data not shown), yielding similar binding affinities as the K_D evaluation for N_WT. As the primary objective of the study was to compare the RNA binding affinity of various N truncation proteins rather than to illustrate the cooperativity of the N protein binding, the focus remained on determining binding affinity using K_D determination. Cooperative binding refers to a scenario where the binding of one RNA molecule of a protein enhances the binding affinity of subsequent molecules. The highly cooperative nature of N protein binding arises, in part, from protein's ability to multimerize, thereby creating a scaffold for further stable RNA binding once the first RNA has bound to the N protein (Zeng et al., 2020).

The findings of this study regarding the binding to different RNA species align with observations by Zinzula et al., wherein the full-length N_WT exhibited RNA binding affinities in the high nanomolar to low micromolar range (section 3.2.1). However, variations in binding affinity were noted depending on the location of the RNA within the viral genome. While binding to RNA3 (nt 498-520) showed affinities in the micromolar range, binding towards RNA20 (nt 239–264) and RNA22 (nt 21,859-21,884) exhibited approximately 2-fold higher affinities. Coronaviruses are known to demonstrate different binding affinities for specific genomic regions, with high-affinity binding often associated with interactions at suggested packaging signals. Although specific packaging signals analogous to those identified in other coronaviruses, such as within the Nsp15 gene of MHV (Makino et al., 1990), have yet to be pinpointed for SARS-CoV (Hsin et al., 2018; Masters, 2019) and SARS-CoV-2 (Syed et al., 2021b; Terasaki et al., 2023), various studies have proposed potential regions within the genome.

For instance, Syed et al. claimed the presence of a packaging signal within nucleotides 20,080 – 22,222 of SARS-CoV-2 (Syed et al., 2021b). Additionally, for TGEV, a packaging signal was identified in the 5'UTR of the virus, whereby it could not be narrowed down to a specific window (Escors et al., 2003). Despite this, RNA20, located in the 5'UTR of SARS-CoV-2, also exhibited higher binding, suggesting a potential packaging signal also in this part of the genome.

While coronaviruses are commonly believed to possess a single specific packaging signal, RNA bind and seq (RNBS) analyses conducted in our laboratory (Master thesis Andreas Berger, 2020, Master thesis Julia Seidel, 2024) revealed the accumulation of the N protein at specific loci across the entire genome (data not shown), indicating more than one packaging signal or

positioning sequence involved in N protein array formation during genome packaging. The observed variations in RNA binding affinities towards RNA3, RNA20, and RNA22 by N_WT are consistent with the observed N_WT accumulation patterns throughout the viral genome, as identified through RNBS. The lower binding affinity towards RNA3 as well as the higher binding affinities towards RNA20 and RNA22, correlate positively with the accumulation of N_WT in RNBS (Figure 31). This correlation suggests the presence of several packaging signals or positioning sequences within the viral genome that facilitate the formation of an N protein array during genome packaging.

While previous studies have investigated the RNA binding capacity of the SARS-CoV-2 full-length N protein and its individual RBD and CTD, a comprehensive analysis of the specific regions responsible for RNA interaction has been lacking. Most research has claimed that the primary domain for RNA binding in SARS-CoV-2 is the RBD, with the CTD playing a supportive role in ensuring high affinity RNA binding through its oligomerization capabilities (Dinesh et al., 2020; Ye et al., 2020). However, our findings diverge from this consensus, as we did not observe efficient binding of the RBD to the RNA sequences used in this study. Conversely, while the CTD alone exhibited at least weak RNA binding, our RNA binding affinity studies highlighted the importance of IDRs in facilitating efficient RNA binding. Specifically, the RBD-IDR2 (N_RI) was found being sufficient for ssRNA interaction, while the RBD-IDR2-CTD (N_RIC) demonstrated efficient dsRNA binding (section 3.2.2). IDRs in viral RNA binding proteins are known to establish conserved electrostatic interfaces with RNAs, facilitating the RNA binding (Ivanyi-Nagy et al., 2005). While previous studies on for SARS-CoV identified IDR1-NTD as sufficient for RNA binding, being enhanced by the presence of the IDR2 and CTD (C.-Y. Chen et al., 2007; Woo et al., 2019), our study identified the IDR2 as the main IDR involved in RNA binding. Furthermore, both N_RIC and N_RI exhibited higher binding affinities to RNA than N_WT, suggesting that additional IDRs may contribute to fine-tuning this interaction to prevent excessive binding that could potentially impair viral replication and assembly.

The results obtained also suggest a preferential binding of most N truncation proteins to dsRNA, except for N_IRI and N_RI, even though SARS-CoV-2 is an ssRNA virus. The ssRNA genome of SARS-CoV-2 is indeed highly structured and possesses an approximate content of secondary structure of 61% and 41% in the 5'UTR and 3'UTR, respectively, with also an high content of structural elements throughout the coding regions of the genome (Tavares et al.,

2021). The binding to dsRNA besides RNA speaks also for the high structural flexibility and versatility in nucleic acid binding, potentially adopting to dynamic changes in RNA conformations during the viral life cycle. Furthermore, during viral infection, the presence of dsRNA, generated during viral replication, is a key activator of the host immune system. Notably, dsRNA was found to be produced as an intermediate during viral replication in SARS-CoV-2 (Frazier et al., 2021) The innate immune system is able to discriminate between host and viral RNA based on the presence of dsRNA, as host cells do typically not produce dsRNA (Takeuchi & Akira, 2009). The viral dsRNA is recognized by PAMPs, which activate an TLR3-induced IFN response (Abad & Danthi, 2020; Kawai & Akira, 2010). Additionally, SARS-CoV-2 N protein was shown to impair the formation of stress granules (SG) during infection (Z.-Q. Zheng et al., 2021). SGs are cytoplasmic aggregates of stalled translation pre-initiation complexes that form in response to stress conditions like viral infections. Typically, the formation of SGs is triggered by the phosphorylation of the translation initiation factor eIF2α by PKR (protein kinase R) (Reineke & Lloyd, 2015). Accumulation of dsRNA during viral infection leads to the activation of PKR, followed by eIF2α phosphorylation and SG formation. SGs harbor various functions for antiviral activity, as they can sequester viral RNAs, thereby preventing them from being translated into viral proteins and inhibiting viral replication (White & Lloyd, 2012). They can also modulate the immune system as components within SG can interact with components of antiviral signaling pathways, enhancing the antiviral response (Z.-Q. Zheng et al., 2021). Therefore, a high affinity interaction of the N protein towards dsRNA could also represent a protective function by safeguarding viral RNA from host immune recognition and degradation thereby promoting viral replication.

Another potential explanation for the enhanced dsRNA binding affinity of the N protein is its newly discovered function as an RNA chaperone. In this role, the protein assists in the proper folding of viral RNA, which is essential for efficient viral replication and packaging. Given that the viral genome can adopt various secondary structures, including dsRNA entities, the N protein may facilitate the remodeling of RNA into a thermodynamically favored conformation, thereby ensuring proper function and replication (Rajkowitsch et al., 2007). This additional function adds complexity to the role of the N protein in viral RNA metabolism and highlights its importance in the viral life cycle.

4.1.2. RNA chaperone abilities of the SARS-CoV-2 N protein

It is not uncommon for viral packaging proteins to exhibit RNA chaperone activity, a phenomenon observed in various viral systems (Woodson et al., 2018b). Among these, the HIV-1 Ncp7 stands out as one of the most extensively studied examples (Aduri et al., 2013). Prior investigations also have shed light on the RNA chaperone activity of packaging proteins in coronaviruses, particularly the N protein of SARS-CoV (Zúñiga et al., 2007b). However, the specific mechanism underlying RNA chaperone activity in coronaviruses remained unclear.

This study is the first highlighting an RNA chaperone activity of the N protein of SARS-CoV-2, a virus that shares approximately 90% sequence homology with SARS-CoV (McBride et al., 2014). The data obtained demonstrate that the SARS-CoV-2 N protein efficiently enhances the hybridization of SARS-CoV-2 ssRNA as well as ssDNA *in vitro* (section 3.3.1), indicating a distinct intrinsic RNA chaperone activity. There appears to be an interdependence between RNA binding affinity and the structuring of viral RNA, as efficient RNA hybridization requires conditions of stable RNA interaction. While typically, the RNA is stabilized by protein binding, chaperoning requires the destabilization of RNA in a thermodynamically unfavorable folding state, which initially appears controversial. A relevant analogy can be drawn with the RNA chaperone StpA (Suppressor of td phenontype A) of *E. coli*, which combines both RNA binding and RNA chaperone properties with a notable sensitivity to ionic strength for RNA binding. Remarkably, it has been shown that the RNA chaperone activity of StpA primarily stems from transient RNA binding rather than a tight binding (Mayer et al., 2007). This model of requiring weak RNA interaction for RNA chaperone activity is supported by the results obtained in this study. RNA annealing was already observed at RNA concentrations where no detectable RNA binding occurred. Nevertheless, the chaperone activity is positively correlated with the protein's binding efficiency and the corresponding K_D. Additionally, StpA binding to RNA was shown to be highly dependent on electrostatic interactions (Mayer et al., 2007), a characteristic also observed for the SARS-CoV-2 N protein. A loss in the N protein's chaperone activity was detected starting at 500 nM of salt, while the overall integrity of the protein remained intact, and spontaneous hybridization of ssRNA increased with rising salt concentrations. This suggests a mechanism wherein RNA can fold into different secondary structures in the absence of the N protein, which may be stabilized by high salt concentration through shielding the negatively charged phosphate groups. However, this also highlights the N protein's crucial role in maintaining accurate RNA folding and function.

To gain a deeper understanding of the underlying mechanism of RNA chaperoning, the annealing activity of the N truncation proteins was investigated. The protein regions harboring the RNA chaperone activity could be narrowed down to the amino acids 46-364 of the N protein corresponding to the RBD-IDR2-CTD (N_RIC, section 3.3.2). This region comprises the two structured domains RBD and CTD which are connected via the IDR2, still harboring the characteristics of RNA binding, especially for dsRNA, and protein dimerization. IDRs were shown to play essential roles in the activity of RNA chaperones as they undergo cycles of unfolding and folding with their substrate (Herschlag, 1995; Tompa & Csermely, 2004). Studies revealed the importance of the IDR1 in promoting LLPS with RNA and showed that its deletion alters the RNA concentration range in which sufficient droplet formation can occur (Zachrdla et al., 2022). LLPS was shown to play an important role in viral transcription, replication, cellular signaling or stress response, but this study shows that the RNA chaperoning mechanism is independent of LLPS, evidenced by LLPS inhibitors being non-functional in RNA chaperone assays (section 3.3.4). The obtained results present evidence that the IDR2 of the N protein harbors not only the RNA binding activity but also the RNA chaperone activity of the protein, contributing to at least two separate nucleic acid related functions in the viral infection cycle. While the IDR1 and IDR3 of the N protein also in part contribute to the chaperone mechanism, deletion of either or both IDRs, while retaining the RBD and CTD, did not impact the N protein's RNA chaperone activity (section 3.3.2). A review published by Mittag & Parker picks up on the regulation of protein function by the IDRs, underlining the concept of IDRs regulating protein function contextually. IDRs can positively modulate protein function for further interactions or negatively affect protein function by competing for binding partners (Mittag & Parker, 2018). The present results suggest the existence of a dynamic interplay between the IDRs and the structured domains, thereby regulating intrinsic RNA chaperone properties. While IDRs positively influence the annealing efficiency of the RBD, adding either the IDR2 or IDR3 to the CTD results in a weakening of the chaperone activity. In combination with the structured RBD and CTD, the IDR2 is majorly required for the RNA chaperone activity of the SARS-CoV-2 N protein.

Conclusively, the SARS-CoV-2 N protein could be identified as a multifunctional RNA binding protein, not only being involved in viral genome packaging but also in structuring viral gRNA. Switching between these functions might be essential for the viral life cycle as varying genome structures are required for the individual steps of viral reproduction.

4.1.3. Functional differences between the Wuhan and the Omicron BA.5 N protein

While the SARS-CoV-2 Wuhan strain marked the onset of the pandemic, exhibiting high transmissibility and significant morbidity and mortality, the Omicron strain with BA.5 as a sublineage, emerged quickly during SARS-CoV-2 evolution. This subvariant is characterized by increased transmissibility and partial resistance to neutralizing antibodies gained from vaccination or previous infection. Higher breakthrough infections were detected resulting from an enhanced ability of immune escape. Even though Omicron BA.5 resulted in less severe disease outcome compared to earlier strains, the rapid spread posed as a challenge for public health (Gili & Burioni, 2023; Reeves et al., 2022; Willett et al., 2022).

As the Omicron lineage evolved, it adapted to its environment through a high mutation rate, leading to significant changes in its genome, including the N protein sequence. In the investigated subvariant BA.5, notable mutations include P21L, Δ13-33, E136D, R203K, G204R, and S413R. These mutations are distributed across the entire N protein.

With the aim of directly comparing the RNA interaction abilities of the Wuhan and the Omicron BA.5 N protein, we found that both N proteins exhibit distinct differences with regard to RNA binding and RNA chaperone activity. For RNA3, the binding affinity of N_BA.5 is at least 4-fold higher than that of N_WT. In contrast, for RNA20 and RNA22, the binding affinity of N_BA.5 is 2-3-fold lower compared to N_WT (section 3.2.3). BLASTn alignment of the RNA sequences used, which were derived from the original Wuhan genome sequence, against the Omicron BA.5 genome sequence (Genkbank: OP984772.1), revealed a C3U point mutation in the used RNA20 sequence. This point mutation, along with additional mutations within N_BA.5, may lead to changes in either RNA or protein structure, thereby reducing the binding affinity towards the Wuhan RNA sequence. Specifically, the amino acid exchanges in the BA.5 N protein, such as E136D, R203K, and G204R, are located in the RI region, which is essential for efficient ssRNA binding. These mutations might have induced structural changes in the binding pocket, adapting to the genome mutations in the BA.5 sequence. This could explain the lowered affinity towards RNA20 but not towards RNA22, as no mutations within the BA.5 RNA22 genome sequence were found by BLAST analysis.

As depicted for N_WT in section 4.1.1., the high binding affinities of N_WT towards RNA20 and RNA22 correlate positively with an accumulation of N_WT in these regions of the viral genome. This pattern is also observable for N_BA.5 (Figure 31). At genome locations where lower binding affinity was found (RNA20, RNA22), there is a corresponding reduction or

absence of N_BA.5 accumulation. Conversely, RNA3, which is bound with high affinity, shows accumulation of the BA.5 N protein in RNBS. These observations suggest that the positioning of N_WT and N_BA.5 on the viral genome is regulated differently. The differences in binding affinities and accumulation patterns between N_WT and N_BA.5 indicate that mutations in the N protein and RNA sequence may lead to distinct regulatory mechanisms for genome packaging and viral protein positioning in the Wuhan and Omicron BA.5 variant.

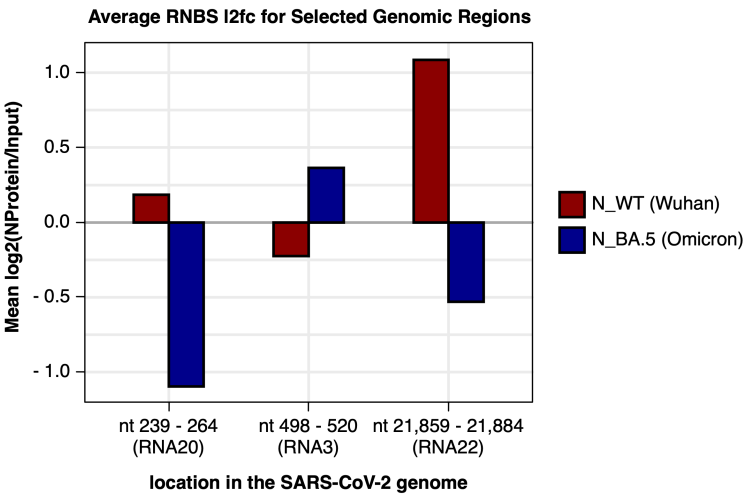

Figure 31: Average log2 fold change of SARS-CoV-2 genomic regions in RNBS

Average log2 fold change of N_WT (dark red) and N_BA.5 (dark blue) accumulation on specific SARS-CoV-2 genomic regions including RNA20 (nt 239-264), RNA3 (nt 498-520) and RNA22 (nt 21,859 – 21,884). Mean log2 fold change is displayed on the y-axis while the genomic region is shown on the x-axis. While a positive log2 fold change, therefore an accumulation of N_WT can be observed for RNA3 and RNA22, N_BA.5 is underrepresented in these regions. For RNA3, N_BA.5 represents an accumulation whereas N_WT does not effectively bind to this location.

Interestingly, the RNA chaperone activity of N_BA.5 was notably impaired compared to N_WT (section 3.3.3). This effect was observed for both RNA3 and RNA20 substrates. While N_WT demonstrated high efficiency in hybridizing RNA3, its efficiency for RNA20 was slightly reduced. In contrast, the activity of N_BA.5 was significantly diminished for both RNA3 and RNA20 when compared to N_WT. There appears to be a connection between RNA binding affinity and chaperone activity. As previously discussed, RNA chaperone activity requires relatively weak binding to facilitate multiple rounds of RNA release and binding, allowing proper folding. If the binding is too tight, the RNA may not be released efficiently, impeding the folding-unfolding cycles necessary for correct folding. In the case of N_BA.5, the affinity for RNA3 is approximately 200 nM, which might be too strong for effective RNA chaperone activity. For RNA20, where N_BA.5 has a lower affinity compared to N_WT, N_WT efficiently facilitates chaperoning, though less efficiently than with RNA3. However, N_BA.5 shows no change in efficiency with RNA20. This phenomenon could potentially be attributed to the point mutation present in RNA20, suggesting that the Omicron BA.5 variant is unable to correctly fold the sequence of the Wuhan strain. Thus, the differences in RNA chaperone activity between N_WT and N_BA.5 underscore the potential impact of specific mutations on the functional

capabilities of the N protein as well as the connection between RNA binding and RNA chaperoning.

4.1.4. Impact of pseudo-phosphorylation on the RNA interaction

Post-translational modifications such as phosphorylation of the N protein play a fundamental role in the SARS-CoV-2 infection cycle, particularly concerning viral replication. In early stages of infection, cytoplasmic kinases rapidly phosphorylate the SR region of the N protein at multiple sites, which facilitates its interaction with RNA helicase DDX1, thereby promoting structural RNA changes required for sgRNA transcription in the viral RTCs (Bouhaddou et al., 2020; Carlson et al., 2020; C.-H. Wu et al., 2014). Consequently, this phosphorylation disrupts multivalent RNA-protein and protein-protein interactions, leading to the formation of liquid-like droplets that play a crucial role in viral genome processing (Carlson et al., 2020).

While the SARS-CoV-2 N protein comprises up to 32 putative phosphorylation sites (Cheng et al., 2023), eight phosphorylation sites, which were chosen in this study based on an overlap from various phosphoproteomic analyses (Yaron et al., 2022), were pseudo-phosphorylated in this study. Pseudo-phosphorylation involves substituting specific serine and threonine residues with aspartic acid (**N_WT**: S23, T141, S176, S180, T198, S201, S202, S206; **N_BA.5**: S23, T138, S173, S177, S180, T195, S198, S202, S203), thereby introducing negative charges that mimic the phosphorylation state of the protein. Due to the E136D mutation within the N_BA.5 protein, an additional aspartic acid residue, and therefore an extra negative charge, is present in N_BA.5 but not in N_WT. RNA binding affinity of phosphomimetic N proteins was observed to decrease by approximately 5-fold compared to their unmodified protein counterparts (section 3.2.4.). This observation aligns with findings from a study involving the N protein of SARS-CoV, which also demonstrated a decrease in RNA binding efficiency upon phosphorylation, as phosphorylation introduces additional negative charges onto the protein, which can lead to electrostatic repulsion with the negatively charged RNA, thereby reducing overall binding affinity (Carlson et al., 2020). Another possible explanation for this reduction in binding affinity is that the pseudo-phosphorylation induces conformational changes that alter the protein's binding capabilities. Indeed, we detected decreased RBD stability due to pseudo-phosphorylation (section 3.1.3). Given that the RBD, in combination with the IDR2, is primarily responsible for ssRNA binding, these findings suggest that pseudo-phosphorylation affects to overall protein structure and thereby the protein's RNA binding characteristics. Phosphorylation of IDRs in RNA binding proteins has been shown to have a high impact on

their functionality (Modic et al., 2024) and most pseudo-phosphorylation sites in the used SARS-CoV-2 N proteins within this study are located in the IDR2.

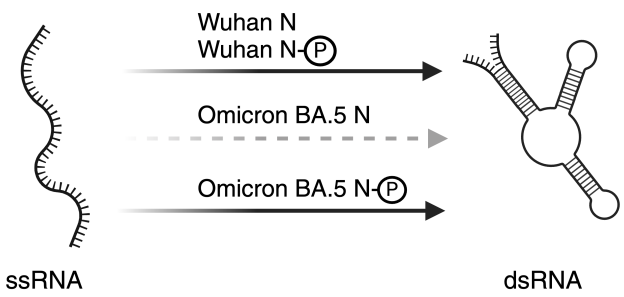

Figure 32: Impact of pseudo-phosphorylation on RNA chaperone activity of N

While Wuhan N is capable of fully hybridizing ssRNA to dsRNA, N of Omicron BA.5 showed strongly reduced RNA chaperone activity. This activity could be restored by mimicking the phosphorylation status of BA.5 N, whereby pseudo-phosphorylation did not show any effect on Wuhan N, suggesting distinct RNA chaperone regulations, required for viral pathogenesis of these strains.

In terms of RNA chaperone activity, where N_BA.5 exhibited reduced RNA annealing efficiency, mimicking the phosphorylation status of the protein restored its annealing activity to wildtype levels (Figure 32). Interestingly, this phosphomimetic modification did not alter the properties of N_WT. As discussed in the previous chapter, we propose a connection between RNA binding affinity, RNA accumulation on the viral genome, and the RNA chaperone activity of the respective protein. N_BA.5 exhibited reduced RNA chaperone activity with RNA3 but displayed high binding affinity, which potentially explains the reduced RNA hybridization abilities. In contrast, N_BA.5_PM binds RNA3 with an affinity of approximately 1200 nM, which is comparable to the affinity of N_WT towards RNA3. Given that N_WT demonstrated efficient RNA hybridization, N_BA.5_PM similarly enhances RNA annealing. N_WT_PM with an RNA3 binding affinity of approximately 6000 nM, does not alter RNA chaperone activity. Since N_WT already exhibits full annealing capacity and shows transient RNA binding, a further decrease of RNA binding does not seem to influence its chaperone activity.

Overall, these findings indicate that the RNA chaperone activity of the N protein is finely tuned by its RNA binding affinity and is significantly influenced by its phosphorylation status in the context of Omicron BA.5.

4.2. Interaction of the SARS-CoV-2 N protein with cell surface heparin and heparan sulfate

The cell surface glycosaminoglycans heparin (H) and heparan sulfate (HS) are crucial in numerous physiological processes, including cell signaling, tissue repair, viral infections, and inflammation (D. Shi et al., 2021). HS, in particular, which is present on various cell types, interacts with growth factors, cytokines, and mediates leukocyte adhesion and migration (Melchjorsen et al., 2003). For many viruses, HS serves as an attachment site, facilitating the accumulation of the viral particles at the cell surface for cell entry (Pomin et al., 2017). Studies have shown that for SARS-CoV-2, HS serves as the initial anchoring site on the host cell surface by binding of the S protein to HS and the ACE2 entry receptor (Q. Zhang et al., 2020). Interestingly, not only the S protein was found to interact with HS but also the N protein. The N protein, typically present in the cytosol of infected cells, has been observed on the cell surface. Through an as-yet-unknown mechanism, the N protein is released by SARS-CoV-2 infected cells and binds to neighboring uninfected cells via interaction with H and HS (A. López-Muñoz, 2022). This study aimed to further analyze the interaction of the N protein with H and HS *in vitro*, identifying the specific protein domains responsible for these interactions. Furthermore, we are among the first to demonstrate that liquid-liquid phase separation occurs extracellularly and that this LLPS-mediated interaction impairs the host immune response upon SARS-CoV-2 infection.

4.2.1. Functional characteristics of the glycosaminoglycan interaction

Initially, this study aimed to evaluate the functional biochemical and biophysical characteristics of the SARS-CoV-2 N protein interaction with H and HS. Techniques such EMSA, DLS, nanoDSF, and LLPS were employed to gain a deep understanding of the interaction modes. As our results revealed, binding affinities and interaction modes varied along H and HS.

EMSAs demonstrated a stronger initial affinity for N towards H compared to HS, suggesting a more robust early-stage interaction of N with H (3.4.1). Specifically, binding of the N protein to H occurred at lower concentrations (starting at 50 nM) than to HS (starting at 200 nM). When the N protein was complexed with RNA, H could displace the RNA at higher concentrations, indicating a competitive interaction. Conversely, HS allowed simultaneous binding with RNA, suggesting a more cooperative interaction. These results imply the formation of a trimeric complex involving the N protein, RNA, and H/HS.

The impact of ligand binding on the overall stability of the N protein was assessed using nanoDSF. H binding resulted in greater destabilization of the RBD compared to HS binding, as indicated by a more pronounced left shift of the RBD T_M. This suggests that H induces more significant conformational changes within the N protein. Additionally, DLS revealed that, in general, H binding led to a larger increase in particle size (from 6 nm to approximately 10 nm) compared to HS binding (from 6 to approximately 7.5 nm), indicating that H promotes more excessive cross-linking or multimerization of the N protein, potentially forming larger and more stable complexes.

The differential interaction of the N protein with H and HS likely reflects specific structural adaptations. Heparin, with its higher degree of sulfation (Shriver et al., 2012), facilitates stronger and more stable binding through potentially multiple electrostatic interactions. In contrast, HS was shown to display higher bending capacity and flexibility (Khan et al., 2013), which might allow the N protein to bind simultaneously to both HS and RNA over a broader concentration range compared to H.

While a kind of interaction could be detected for almost every N truncation protein in DLS, functional LLPS and immunofluorescence experiments revealed the required protein domains for H/HS interaction. These analyses showed that efficient droplet formation as well as the attachment to the cell surface require the presence of the CTD. N truncation proteins lacking the CTD exhibited limited LLPS capabilities and no cell surface binding, highlighting a crucial role of the CTD in the context of H/HS interaction. Interestingly, the N_IC truncation protein, which lacks the structured RBD but retains the IDR2, also significantly contributes to these interactions. In general, the RBD-IDR2-CTD seems to be the protein domains harboring the main function of H/HS interaction as LLPS as well as immunofluorescence are most efficient containing both structured domains with the IDR2. RBD-IDR2-CTD seem to harbor the general functions of the N protein as N_RIC was also shown to be in charge of nucleic acid interaction (sections 3.2.2 and 3.3.2). However, interactions with heparin could not be assessed in immunofluorescence assays using MCF-7 cells, as these cells only present HS on their surface.

The importance of the RBD and the IDR2, is supported by previous studies which have identified a H binding site within the RBD of the N protein by NMR, located at the motif GKMDL (amino acids 99-104). An additional second perturbation was shown within the IDR2, (amino acids 217-224) (Schiavina et al., 2022). These findings support the involvement of these regions in GAG interactions. However, this study did not explore potential interactions

involving the CTD, nor did it provide comparative data for HS, limiting the interpretation of these results for our context.

4.2.2. Extracellular liquid-liquid phase separation dependent mechanism of interaction

Besides the development of membrane-bound organelles such as the ER, cells also contain membraneless organelles such as nucleoli. While membrane-bound organelles encapsulate specific proteins, nucleic acids and other molecule, limiting molecular exchange with the cytoplasm, membraneless structures do not have any restricted space allowing molecular exchange with the surrounding cytoplasm. LLPS is a mechanism which became broadly accepted within the scientific community to control the formation of these membraneless compartments (Banani et al., 2017; B. Wang et al., 2021). LLPS is primarily driven by proteins containing IDRs, which are often capable of binding RNA or DNA, thereby facilitating multivalent weak interactions between biopolymers. The IDRs are believed to interact with ligands and the solution, thereby altering the local structure and physical properties. This means, the occurrence of LLPS is influenced by the total concentration of the present biomolecules and the environmental conditions such as temperature, ionic strength, or pH. Below a critical concentration, the system stays in a single-phase regime. Once a specific threshold concentration is reached, a two-phase regime develops by the occurrence of LLPS where molecules interact to form liquid droplets (Gao et al., 2021). LLPS in biological systems typically occurs intracellularly, resulting in the formation of nucleoli, Cajal bodies, stress granules, and other structures (Banani et al., 2017). The SARS-CoV-2 N protein is known to undergo LLPS with RNA, efficiently facilitating viral genome packaging and modulating the host immune system (S. Wang et al., 2021).

The present study is among the first's demonstrating extracellular LLPS within biological systems, particularly in the context of viral infections. We found that the interaction of the N protein with H and HS induces LLPS both *in vitro* as well as extracellularly with HS on the cell surface of U2OS cells, as evidenced by FRAP experiments performed under physiological conditions (section 3.4.2). Extracellular LLPS is an open field in current research, and no prior studies have examined this phenomenon in the context of viral infections. However, a recent study by Xue et al. provided evidence of the LLPS involving the basic fibroblast growth factor (bFGF) on the cell surface, dependent on its interaction with HS. Similar to the N protein of SARS-CoV-2, bFGF can be released from cells and are transported to nearby cells where it is

sequestered by HSPGs. This interaction forms a ternary complex with FGFR (fibroblast growth factor receptor), inducing droplet formation and facilitating efficient signal transduction. This study suggests that extracellular LLPS is involved in signal transduction for processes like tissue regeneration and wound healing (Xue et al., 2022).

Given the absence of studies on extracellular LLPS in the viral context, this study is the first to demonstrate this mechanism for the N protein of SARS-CoV-2. LLPS involving the N protein and HS may alter the physical properties of the cell surface, such as its rigidity or surface charge. These alterations could affect cell-cell interactions, receptor signaling, and the presentation of viral antigens to immune cells, thereby modulating the host immune response. However, these potential roles in viral pathogenesis will be explored in chapter 4.2.3.

4.2.3. Biological function of the interaction of SARS-CoV-2 N with heparin and heparan sulfate in viral pathogenesis

The cell surface expression of viral RNA- and DNA-binding proteins is a well-known phenomenon for various viruses, including influenza virus (VIRELIZIER et al., 1977), HIV-1 (Ikuta et al., 1989), and measles virus (Laine et al., 2003), among others. These proteins often play roles in modulating the host immune response. Additionally, it appears to be common for betacoronaviruses, such as HCoV-OC43 or MHV, to be exported to the cell surface and interact with H/HS, suggesting an evolutionarily conserved strategy for host immune modulation (A. D. López-Muñoz et al., 2023).

While heparin is only localized in and on specific cell types like mast cells (MC), heparan sulfate is broadly distributed across various cell types in the human body. The differential interaction modes of the SARS-CoV-2 N protein with H and HS suggest distinct functional roles within the viral infection cycle. Specifically, these interactions may play a unique role in MC-rich environments, potentially modulating immune responses during infection. MCs, typically known for their role in allergic reactions, are also present in the respiratory tract. These cells contain high levels of heparin and are activated upon SARS-CoV-2 infection, contributing to the pathology of COVID-19. Activation of MC leads to the release of inflammatory mediators, including histamine, cytokines and various chemokines. Elevated concentration of these have been observed in COVID-19 cases, characterized by a hyperinflammatory immune response, often known as “cytokine storm”, which is associated with severe disease outcome and long-COVID (Brock & Maitland, 2021; Weinstock et al., 2021). There are several potential

mechanisms through which SARS-CoV-2 infections can lead to the activation of MC. These include the direct binding of the S protein to MCs (González-Alvarez et al., 2024), the interaction of the PDZ (PSD-95/Dlg/ZO-1), which has been found in E and N proteins (Batiha et al., 2022), by viral activation of TLRs, or through cytokine or chemokine signaling (Meyerholz & Reznikov, 2022). During viral infections, MC activation results in the release of inflammatory cytokines and antiviral chemokines, which subsequently activate antiviral pathways to combat the infection (Graham et al., 2015). Additionally, the expression of TLR3, which recognizes viral dsRNA, by MC, among others, was observed post-infection, further triggering antiviral signaling pathways (Burke et al., 2008). Activation of MC also leads to the release of heparin, which has anticoagulant properties counteracting the hypercoagulable state observed in SARS-CoV-2 infected patients (Guilarte et al., 2017; Kempuraj et al., 2020). The data obtained in this study suggests a mechanism of SARS-CoV-2 pathogenesis that involved the indirect impairment of MCs and downstream pathways through the N protein. Our findings indicate that the N protein triggers the release of the pro-inflammatory cytokines TNFα and IL-8, by binding to monocytes (THP-1 cells), likely through extracellular interaction with HS. In combination with the N protein's ability to interact with heparin, it may initiate a cycle that leads to hyperinflammation and increased coagulation abnormalities, contributing to the thrombosis observed in COVID-19 patients (Figure 33 **(1)** and **(2)**). MCs do not only release TNFα upon activation but can also become activated in response TNFα (Brzezihka-Blaszczyk, 1997). Following infection, when the N protein is released into the extracellular space, it induces the release of TNFα and IL-8 from monocytes. This released TNFα could potentially activate MCs, triggering further release of immune mediators, such as TNFα and IL-9, as well as heparin. Given the N protein's active and strong interaction with heparin, which is crucial for inhibiting coagulation induced by infection, it may disrupt this mechanism by sequestering heparin upon release. Especially the LLPS-mediated interaction of H and N, trapping H within liquid droplets, actively shields H from its intended functions. This suggests a supportive role of the N protein in virus-induced thrombosis observed in COVID-19 patients. Moreover, as hyperactivating of MC and the release of inflammatory cytokines and chemokines are associated with long-COVID, the TNFα release triggered by the N protein may exacerbate this effect. An additional increase in cellular concentrations of TNFα and IL-8, beyond those derived from MC, could further intensify this response, leading to a cytokine storm and overstimulation of the host's immune system. As already mentioned, MCs present TLR3 on their surface, which can detect extracellular viral dsRNA, potentially originating from apoptotic cells. As discussed

in chapter 4.1.1, N protein binds dsRNA and therefore can potentially shield it from TLR3 detection (Figure 33 **(3)**). Especially, due to the existence of a trimeric complex consisting of N, RNA, and H/HS, N can interact with H/HS independently of shielding RNA from detection and downstream antiviral responses. An additional mechanism explaining the existence of a trimeric complex is its potential role in facilitating the spread of SARS-CoV-2 genetic information. The N protein has been shown to mediate the entry of RNA or DNA into neighboring cells following cell surface attachment. This occurs through ACE2-independent, STEAP2 (six-transmembrane epithelial antigen of prostate-2) receptor dependent endocytosis, facilitating viral gene expression (J.-L. Wu et al., 2023). The interaction of N with H/HS could assist in increasing the N-RNA concentration on the cell surface prior to RNA internalization (Figure 33 **(4)**).

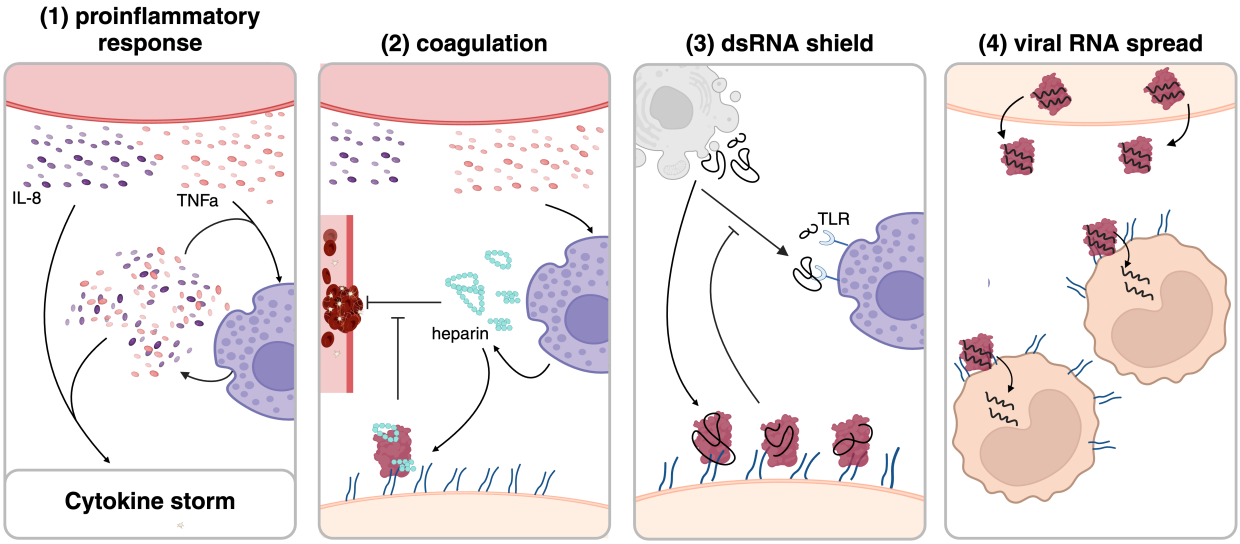

Figure 33: Biological relevance of cell surface interaction between N and H/HS in viral pathogenesis

The interaction between the SARS-CoV-2 N protein and heparin/heparan sulfate, after the export of N to the cell surface of infected cells, may lead to various immune-modulatory processes.
(1) Induction of a proinflammatory response. Interaction of N and HS on monocytes (red) triggers to the release of proinflammatory cytokines IL-8 and TNFα. TNFα may potentially activate mast cells (MC, purple), which further release cytokines. This may result in a circle of activation and cytokine release, leading to a cytokine storm, overwhelming the host's immune system.
(2) Promotion of coagulation. The activation of MCs through cytokine release mediated by N – HS interaction, leads to the release of heparin. Heparin is required to inhibit infection-mediated coagulation and subsequent thrombosis. Cell surface N (red) may, attached to HS (blue), potentially intercept heparin, thereby promoting the appearance of thrombosis.
(3) The N protein serves as an dsRNA shield. Infected apoptotic cells (grey) release viral dsRNA (replication intermediate), which would normally trigger an antiviral response via TLRs (toll-like receptors) on cells such as MCs. N protein, interacting with HS on the cell surface, particularly by forming liquid droplets, can bind the dsRNA, effectively hiding it from detection by TLRs. The formation of condensates may further prevent the detection.
(4) Function as a mechanism for viral spread. The N protein may also be exported bound to viral RNA. Interaction with HS on neighboring cells facilitates the uptake of RNA via endocytosis, promoting viral replication and spread to nearby cells.

The release of TNFα and IL-8 induced by N protein mediated monocyte stimulation plays a pivotal role in eliciting cellular responses to viral infections. Accumulation of TNFα triggers the interaction with its two receptors: TNFR-1 and TNFR-2 (Tumor necrosis factor receptor 1 and 2). Upon TNFR-1 activation, signaling cascades including NF-κB and MAPK are initiated, promoting inflammation, cytokine production (Wajant & Siegmund, 2019), and apoptosis (Micheau & Tschopp, 2003). In contrast, TNFR-2 signaling typically promotes proinflammatory responses through the NF-κB pathway (J.-H. Shi & Sun, 2018). Notably, NF-κB hyperactivation, resulting from excessive cytokine production, can lead to severe inflammation and respiratory complications, as observed in severe COVID-19 cases (Birra et al., 2020). The N protein-mediated TNFα release may contribute this process, causing an excessive production of TNFα, leading to cytokine overproduction and subsequently resulting in lung damage or pulmonary fibrosis, or even death due to immune overstimulation in severe COVID-19 outcomes (Mohd Zawawi et al., 2023).

Following SARS-CoV-2 infection, the host immune system responds to the detection of viral RNA with an early IFNα response to establish a robust antiviral state. Nevertheless, SARS-CoV-2 has evolved immune evasion mechanism to dysregulate this IFN response. Viral proteins such as Nsp1, Nsp5, and Nsp12 has been identified as key players disrupting the host's IFNα release (Znaidia et al., 2022). Interestingly, IL-8 has been observed displaying inhibitory effects on the antiviral activity of IFNα (Khabar et al., 1997). Typically, COVID-19 patients often exhibit elevated levels of various cytokines, with IL-8 playing a pivotal role (Biava et al., 2023). Our findings demonstrate that THP-1 cells exposed to SARS-CoV-2 N protein, exhibit increased IL-8 release, suggesting a potential inhibitory mechanism against the host's antiviral response. Notably, other viruses like cytomegalovirus (CMV), influenza A virus, and poliovirus, among others, have been shown to induce IL-8, pointing towards a general viral modulatory mechanism (Khabar et al., 1997).

López-Muñoz et al. not only identified the interaction between N protein and H and HS on the cell surface but also discovered interactions with a spectrum of 64 human cytokines and chemokines, such as CXCL4, CXCL9, CXCL10, and CXCL11. Importantly, their study revealed that N binds chemokines at their GAG binding site, thereby interfering with their ability to bind to HS (A. López-Muñoz, 2022). Chemokines play crucial roles in chemotaxis, orchestrating the movement of leukocytes towards sites of inflammation by establishing a gradient along the endothelium. This gradient is maintained by the binding of released chemokines to endothelial HS, preventing their dispersion by blood flow (Collins & Troeberg, 2018). Our findings suggest

a potential mechanism by which N assists in blocking chemotaxis. Through interaction of N with HS in an LLPS dependent manner, HS becomes trapped in liquid droplets, thereby being inaccessible for chemokine binding and establishing a gradient essential for leukocyte guidance.

4.3. Conclusion and Outlook

Throughout this study, we have gained profound insight into the multifaceted functions of the SARS-CoV-2 N protein, shedding light on its interaction with nucleic acids, revealing an intrinsic RNA chaperone activity, and unveiling extracellular LLPS as a previously unknown mechanism in viral infection and pathogenesis, which modulates the host's immune response (Figure 34). These findings significantly contribute to the field of coronavirus and particularly SARS-CoV-2 research.

Investigations into the RNA binding properties of the N protein delineated distinct functional domains responsible for its interaction with different RNA species. The RBD and IDR2 were collectively identified as crucial for binding ssRNA, whereas RBD-IDR2-CTD facilitated efficient binding to dsRNA. Moreover, our findings uncovered an RNA chaperone mechanism within the SARS-CoV-2 N protein, primarily localized in the RBD-IDR2-CTD region, essential for facilitating proper folding of the viral genome. Significantly, we observed notable differences between the Wuhan and the Omicron BA.5 N proteins of SARS-CoV-2 concerning their nucleic acid interactions. Phosphorylation also emerged as a crucial regulator of efficient RNA structuring in the Omicron BA.5 context., indicating distinct regulatory mechanism which have evolved for viral fitness of these strains.

Furthermore, we elucidated the interaction of the N protein with H and HS on the cell surface mediated by extracellular LLPS, suggesting a novel mechanism for modulating the host immune responses during viral infection. We identified the RBD-IDR2-CTD as the primary protein domains harboring this function for interaction. Notably, these domains were found to play the essential role in the overall N protein functions, suggesting the protein's IDR1 and IDR3 providing supportive functions for fine-tuning the critical regulatory tasks within the viral infection cycle.

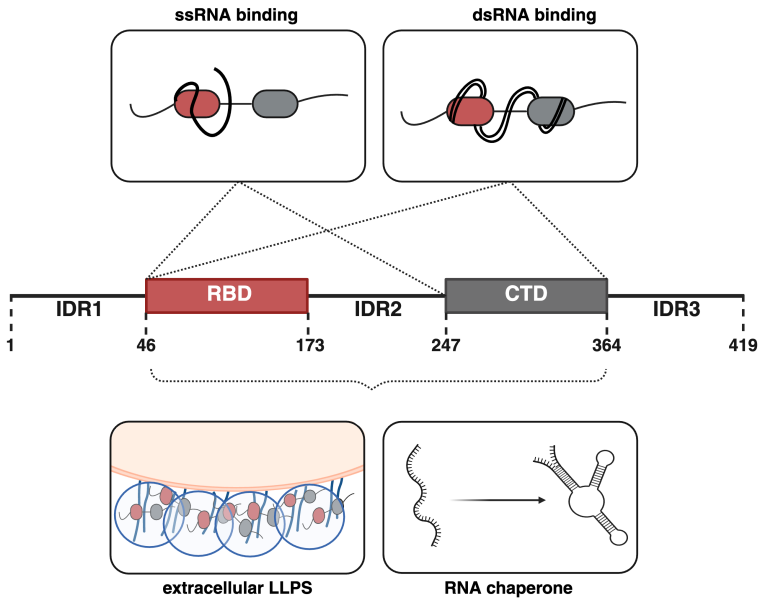

Figure 34: Uncovered N protein functions

Additional functions and specific domains harboring important roles of the SARS-CoV-2 N protein were revealed during this study. The N protein binds ssRNA and dsRNA with N_RI necessary for efficient ssRNA and N_RIC required for dsRNA interaction. The N protein harbors an intrinsic RNA chaperone activity, thereby facilitating proper folding of the viral genome. The interaction with heparin and heparan sulfate on the host cell surface is mediated by liquid-liquid phase separation and may modulate the host immune response upon infection. The function of RNA chaperone activity as well as of the interaction with H/HS are located within the RBD-IDR2-CTD.

Additionally, our data on N protein-mediated TNFα and IL-8 release contribute to the understanding of immune modulatory events during SARS-CoV-2 infection, adding to the known repertoire of immune evasion mechanisms.

Looking forward, further research could focus on investigating the structural basis of N protein interactions and identifying key amino residues involved in binding interfaces using techniques such as NMR (nuclear magnetic resonance) spectroscopy or cryo-electron microscopy. The roles of IDRs within the proteins could be validated, for instance, by exchanging the key IDR2 with IDR1/IDR3 to identify essential amino acid constitution or position for function. Furthermore, investigating key phosphorylation sites for N protein function, particularly for Omicron BA.5 N RNA chaperone activity, could provide valuable insights. *In vivo* studies could involve generating recombinant viruses with Wuhan and Omicron BA.5 background, substituting the N proteins between strains, and analyzing viral fitness, viability and pathogenesis. Additionally, examining the immune response upon heparin interaction on heparin-expressing cells and conducting inhibitor screens against N and H/HS interaction may yield potential therapeutic targets.

In conclusion, this comprehensive study of the multifaceted functions of the SARS-CoV-2 N protein has revealed novel insights into the protein's interplay with viral RNA, host cell components, and immune regulatory mechanisms. By unraveling the molecular mechanisms underlying the N protein interactions, this study added important knowledge to our fundamental understanding of SARS-CoV-2 infection, replication, and pathogenesis through viral-host interactions.

5. References

1) Abad, A. T., & Danthi, P. (2020). Recognition of Reovirus RNAs by the Innate Immune System. *Viruses*, *12*(6), 667. https://doi.org/10.3390/v12060667
2) Aduri, R., Briggs, K. T., Gorelick, R. J., & Marino, J. P. (2013). Molecular determinants of HIV-1 NCp7 chaperone activity in maturation of the HIV-1 dimerization initiation site. *Nucleic Acids Research*, *41*(4), 2565–2580. https://doi.org/10.1093/nar/gks1350
3) Angelini, M. M., Akhlaghpour, M., Neuman, B. W., & Buchmeier, M. J. (2013). Severe Acute Respiratory Syndrome Coronavirus Nonstructural Proteins 3, 4, and 6 Induce Double-Membrane Vesicles. *mBio*, *4*(4), e00524-13. https://doi.org/10.1128/mBio.00524-13
4) Bai, C., Zhong, Q., & Gao, G. F. (2022). Overview of SARS-CoV-2 genome-encoded proteins. *Science China Life Sciences*, *65*(2), 280–294. https://doi.org/10.1007/s11427-021-1964-4
5) Bai, Z., Cao, Y., Liu, W., & Li, J. (2021). The SARS-CoV-2 Nucleocapsid Protein and Its Role in Viral Structure, Biological Functions, and a Potential Target for Drug or Vaccine Mitigation. *Viruses*, *13*(6), 1115. https://doi.org/10.3390/v13061115
6) Baltimore, D. (1971). Expression of Animal Virus Genomes. *BACTERIOL. REV.*, *35*.
7) Baltimore, D. (1980). EVOLUTION OF RNA VIRUSES. *Annals of the New York Academy of Sciences*, *354*(1), 492–497. https://doi.org/10.1111/j.1749-6632.1980.tb27988.x
8) Banani, S. F., Lee, H. O., Hyman, A. A., & Rosen, M. K. (2017). Biomolecular condensates: Organizers of cellular biochemistry. *Nature Reviews Molecular Cell Biology*, *18*(5), 285–298. https://doi.org/10.1038/nrm.2017.7
9) Banerjee, A. K., Blanco, M. R., Bruce, E. A., Honson, D. D., Chen, L. M., Chow, A., Bhat, P., Ollikainen, N., Quinodoz, S. A., Loney, C., Thai, J., Miller, Z. D., Lin, A. E., Schmidt, M. M., Stewart, D. G., Goldfarb, D., De Lorenzo, G., Rihn, S. J., Voorhees, R. M., … Guttman, M. (2020). SARS-CoV-2 Disrupts Splicing, Translation, and Protein Trafficking to Suppress Host Defenses. *Cell*, *183*(5), 1325-1339.e21. https://doi.org/10.1016/j.cell.2020.10.004
10) Barik, S. (2020). Genus-specific pattern of intrinsically disordered central regions in the nucleocapsid protein of coronaviruses. *Computational and Structural Biotechnology Journal*, *18*, 1884–1890. https://doi.org/10.1016/j.csbj.2020.07.005
11) Batiha, G. E.-S., Al-kuraishy, H. M., Al-Gareeb, A. I., & Welson, N. N. (2022). Pathophysiology of Post-COVID syndromes: A new perspective. *Virology Journal*, *19*(1), 158. https://doi.org/10.1186/s12985-022-01891-2
12) Bayati, A., Kumar, R., Francis, V., & McPherson, P. S. (2021). SARS-CoV-2 infects cells after viral entry via clathrin-mediated endocytosis. *Journal of Biological Chemistry*, *296*, 100306. https://doi.org/10.1016/j.jbc.2021.100306
13) Belshaw, R., Pybus, O. G., & Rambaut, A. (2007). The evolution of genome compression and genomic novelty in RNA viruses. *Genome Research*, *17*(10), 1496–1504. https://doi.org/10.1101/gr.6305707
14) Biava, M., Notari, S., Grassi, G., Bordi, L., Tartaglia, E., Agrati, C., Cimini, E., Sberna, G., Nicastri, E., Antinori, A., Girardi, E., Vaia, F., Maggi, F., & Lalle, E. (2023). In Vitro and In Vivo Crosstalk between Type I IFN and IL-8 Responses in SARS-CoV-2 Infection. *Microorganisms*, *11*(11), 2787. https://doi.org/10.3390/microorganisms11112787

15) Birra, D., Benucci, M., Landolfi, L., Merchionda, A., Loi, G., Amato, P., Licata, G., Quartuccio, L., Triggiani, M., & Moscato, P. (2020). COVID 19: A clue from innate immunity. *Immunologic Research*, *68*(3), 161–168. https://doi.org/10.1007/s12026-020-09137-5

16) Boson, B., Legros, V., Zhou, B., Siret, E., Mathieu, C., Cosset, F.-L., Lavillette, D., & Denolly, S. (2021). The SARS-CoV-2 envelope and membrane proteins modulate maturation and retention of the spike protein, allowing assembly of virus-like particles. *Journal of Biological Chemistry*, *296*, 100111. https://doi.org/10.1074/jbc.RA120.016175

17) Bouhaddou, M., Memon, D., Meyer, B., White, K. M., Rezelj, V. V., Correa Marrero, M., Polacco, B. J., Melnyk, J. E., Ulferts, S., Kaake, R. M., Batra, J., Richards, A. L., Stevenson, E., Gordon, D. E., Rojc, A., Obernier, K., Fabius, J. M., Soucheray, M., Miorin, L., … Krogan, N. J. (2020). The Global Phosphorylation Landscape of SARS-CoV-2 Infection. *Cell*, *182*(3), 685-712.e19. https://doi.org/10.1016/j.cell.2020.06.034

18) Brant, A. C., Tian, W., Majerciak, V., Yang, W., & Zheng, Z.-M. (2021). SARS-CoV-2: From its discovery to genome structure, transcription, and replication. *Cell & Bioscience*, *11*(1), 136. https://doi.org/10.1186/s13578-021-00643-z

19) Brian, D. A., & Baric, R. S. (2005). Coronavirus Genome Structure and Replication. In L. Enjuanes (Ed.), *Coronavirus Replication and Reverse Genetics* (Vol. 287, pp. 1–30). Springer Berlin Heidelberg. https://doi.org/10.1007/3-540-26765-4_1

20) Brock, I., & Maitland, A. (2021). *Mast Cells and COVID-19: A case report implicating a role of mast cell activation in the prevention and treatment of Covid-19*. https://doi.org/10.21203/rs.3.rs-330667/v1

21) Brzezihka-Blaszczyk, E. (1997). *Tumor necrosis factor a (TNF-a) activates human adenoidal and cutaneous mast cells to histamine secretion*. 139–143.

22) Burke, S. M., Issekutz, T. B., Mohan, K., Lee, P. W. K., Shmulevitz, M., & Marshall, J. S. (2008). Human mast cell activation with virus-associated stimuli leads to the selective chemotaxis of natural killer cells by a CXCL8-dependent mechanism. *Blood*, *111*(12), 5467–5476. https://doi.org/10.1182/blood-2007-10-118547

23) Cai, T., Yu, Z., Wang, Z., Liang, C., & Richard, S. (2021). Arginine methylation of SARS-Cov-2 nucleocapsid protein regulates RNA binding, its ability to suppress stress granule formation, and viral replication. *Journal of Biological Chemistry*, *297*(1), 100821. https://doi.org/10.1016/j.jbc.2021.100821

24) Calder, L. J., Calcraft, T., Hussain, S., Harvey, R., & Rosenthal, P. B. (2022). Electron cryotomography of SARS-CoV-2 virions reveals cylinder-shaped particles with a double layer RNP assembly. *Communications Biology*, *5*(1), 1210. https://doi.org/10.1038/s42003-022-04183-1

25) Carabelli, A. M., Peacock, T. P., Thorne, L. G., Harvey, W. T., Hughes, J., COVID-19 Genomics UK Consortium, De Silva, T. I., Peacock, S. J., Barclay, W. S., De Silva, T. I., Towers, G. J., & Robertson, D. L. (2023). SARS-CoV-2 variant biology: Immune escape, transmission and fitness. *Nature Reviews Microbiology*. https://doi.org/10.1038/s41579-022-00841-7

26) Carlson, C. R., Adly, A. N., Bi, M., Howard, C. J., Frost, A., Cheng, Y., & Morgan, D. O. (2022). Reconstitution of the SARS-CoV-2 ribonucleosome provides insights into genomic

RNA packaging and regulation by phosphorylation. *Journal of Biological Chemistry*, *298*(11), 102560. https://doi.org/10.1016/j.jbc.2022.102560

27) Carlson, C. R., Asfaha, J. B., Ghent, C. M., Howard, C. J., Hartooni, N., Safari, M., Frankel, A. D., & Morgan, D. O. (2020). Phosphoregulation of Phase Separation by the SARS-CoV-2 N Protein Suggests a Biophysical Basis for its Dual Functions. *Molecular Cell*, *80*(6), 1092-1103.e4. https://doi.org/10.1016/j.molcel.2020.11.025
28) Cautain, B., Hill, R., De Pedro, N., & Link, W. (2015). Components and regulation of nuclear transport processes. *The FEBS Journal*, *282*(3), 445–462. https://doi.org/10.1111/febs.13163
29) Chandel, V., Sharma, P. P., Raj, S., Choudhari, R., Rathi, B., & Kumar, D. (2022). Structure-based drug repurposing for targeting Nsp9 replicase and spike proteins of severe acute respiratory syndrome coronavirus 2. *Journal of Biomolecular Structure and Dynamics*, *40*(1), 249–262. https://doi.org/10.1080/07391102.2020.1811773
30) Chen, C.-Y., Chang, C., Chang, Y.-W., Sue, S.-C., Bai, H.-I., Riang, L., Hsiao, C.-D., & Huang, T. (2007). Structure of the SARS Coronavirus Nucleocapsid Protein RNA-binding Dimerization Domain Suggests a Mechanism for Helical Packaging of Viral RNA. *Journal of Molecular Biology*, *368*(4), 1075–1086. https://doi.org/10.1016/j.jmb.2007.02.069
31) Chen, D., & Zhang, H. (2022). Autophagy in severe acute respiratory syndrome coronavirus 2 infection. *Current Opinion in Physiology*, *29*, 100596. https://doi.org/10.1016/j.cophys.2022.100596
32) Chen, J., Malone, B., Llewellyn, E., Grasso, M., Shelton, P. M. M., Olinares, P. D. B., Maruthi, K., Eng, E. T., Vatandaslar, H., Chait, B. T., Kapoor, T. M., Darst, S. A., & Campbell, E. A. (2020). Structural Basis for Helicase-Polymerase Coupling in the SARS-CoV-2 Replication-Transcription Complex. *Cell*, *182*(6), 1560-1573.e13. https://doi.org/10.1016/j.cell.2020.07.033
33) Chen, K., Xiao, F., Hu, D., Ge, W., Tian, M., Wang, W., Pan, P., Wu, K., & Wu, J. (2020). SARS-CoV-2 Nucleocapsid Protein Interacts with RIG-I and Represses RIG-Mediated IFN-β Production. *Viruses*, *13*(1), 47. https://doi.org/10.3390/v13010047
34) Chen, Y., Cai, H., Pan, J., Xiang, N., Tien, P., Ahola, T., & Guo, D. (2009). Functional screen reveals SARS coronavirus nonstructural protein nsp14 as a novel cap N7 methyltransferase. *Proceedings of the National Academy of Sciences*, *106*(9), 3484–3489. https://doi.org/10.1073/pnas.0808790106
35) Cheng, N., Liu, M., Li, W., Sun, B., Liu, D., Wang, G., Shi, J., & Li, L. (2023). Protein post-translational modification in SARS-CoV-2 and host interaction. *Frontiers in Immunology*, *13*, 1068449. https://doi.org/10.3389/fimmu.2022.1068449
36) Collins, L. E., & Troeberg, L. (2018). Heparan sulfate as a regulator of inflammation and immunity. *Journal of Leukocyte Biology*, *105*(1), 81–92. https://doi.org/10.1002/JLB.3RU0618-246R
37) Cornillez-Ty, C. T., Liao, L., Yates, J. R., Kuhn, P., & Buchmeier, M. J. (2009). Severe Acute Respiratory Syndrome Coronavirus Nonstructural Protein 2 Interacts with a Host Protein Complex Involved in Mitochondrial Biogenesis and Intracellular Signaling. *Journal of Virology*, *83*(19), 10314–10318. https://doi.org/10.1128/JVI.00842-09
38) Cottam, E. M., Maier, H. J., Manifava, M., Vaux, L. C., Chandra-Schoenfelder, P., Gerner, W., Britton, P., Ktistakis, N. T., & Wileman, T. (2011). Coronavirus nsp6 proteins generate

autophagosomes from the endoplasmic reticulum via an omegasome intermediate. *Autophagy*, *7*(11), 1335–1347. https://doi.org/10.4161/auto.7.11.16642

39) Dai, X., Zhang, S., & Zaleta-Rivera, K. (2020). RNA: Interactions drive functionalities. *Molecular Biology Reports*, *47*(2), 1413–1434. https://doi.org/10.1007/s11033-019-05230-7
40) Dang, M., & Song, J. (2022). CTD of SARS-CoV-2 N protein is a cryptic domain for binding ATP and nucleic acid that interplay in modulating phase separation. *Protein Science*, *31*(2), 345–356. https://doi.org/10.1002/pro.4221
41) De Pasquale, V., Quiccione, M. S., Tafuri, S., Avallone, L., & Pavone, L. M. (2021). Heparan Sulfate Proteoglycans in Viral Infection and Treatment: A Special Focus on SARS-CoV-2. *International Journal of Molecular Sciences*, *22*(12), 6574. https://doi.org/10.3390/ijms22126574
42) Decroly, E., Debarnot, C., Ferron, F., Bouvet, M., Coutard, B., Imbert, I., Gluais, L., Papageorgiou, N., Sharff, A., Bricogne, G., Ortiz-Lombardia, M., Lescar, J., & Canard, B. (2011). Crystal Structure and Functional Analysis of the SARS-Coronavirus RNA Cap 2′-O-Methyltransferase nsp10/nsp16 Complex. *PLoS Pathogens*, *7*(5), e1002059. https://doi.org/10.1371/journal.ppat.1002059
43) Di, H., McIntyre, A. A., & Brinton, M. A. (2018). New insights about the regulation of Nidovirus subgenomic mRNA synthesis. *Virology*, *517*, 38–43. https://doi.org/10.1016/j.virol.2018.01.026
44) Diamond, M. S., & Kanneganti, T.-D. (2022). Innate immunity: The first line of defense against SARS-CoV-2. *Nature Immunology*, *23*(2), 165–176. https://doi.org/10.1038/s41590-021-01091-0
45) Dinesh, D. C., Chalupska, D., Silhan, J., Koutna, E., Nencka, R., Veverka, V., & Boura, E. (2020). Structural basis of RNA recognition by the SARS-CoV-2 nucleocapsid phosphoprotein. *PLOS Pathogens*, *16*(12), e1009100. https://doi.org/10.1371/journal.ppat.1009100
46) Doetsch, M., Schroeder, R., & Fürtig, B. (2011). Transient RNA-protein interactions in RNA folding: Transient RNA-protein interactions in RNA folding. *FEBS Journal*, *278*(10), 1634–1642. https://doi.org/10.1111/j.1742-4658.2011.08094.x
47) Dominguez Andres, A., Feng, Y., Campos, A. R., Yin, J., Yang, C.-C., James, B., Murad, R., Kim, H., Deshpande, A. J., Gordon, D. E., Krogan, N., Pippa, R., & Ronai, Z. A. (2020). *SARS-CoV-2 ORF9c Is a Membrane-Associated Protein that Suppresses Antiviral Responses in Cells* [Preprint]. Bioinformatics. https://doi.org/10.1101/2020.08.18.256776
48) Duffy, S. (2018). Why are RNA virus mutation rates so damn high? *PLOS Biology*, *16*(8), e3000003. https://doi.org/10.1371/journal.pbio.3000003
49) Emrani, J., Ahmed, M., Jeffers-Francis, L., Teleha, J. C., Mowa, N., Newman, R. H., & Thomas, M. D. (2021). SARS-COV-2, infection, transmission, transcription, translation, proteins, and treatment: A review. *International Journal of Biological Macromolecules*, *193*, 1249–1273. https://doi.org/10.1016/j.ijbiomac.2021.10.172
50) Escors, D., Izeta, A., Capiscol, C., & Enjuanes, L. (2003). Transmissible Gastroenteritis Coronavirus Packaging Signal Is Located at the 5J End of the Virus Genome. *J. VIROL.*, *77*.
51) Etibor, T., Yamauchi, Y., & Amorim, M. (2021). Liquid Biomolecular Condensates and Viral Lifecycles: Review and Perspectives. *Viruses*, *13*(3), 366. https://doi.org/10.3390/v13030366

52) Fang, S., Li, K., Shen, J., Liu, S., Liu, J., Yang, L., Hu, C.-D., & Wan, J. (2021). GESS: A database of global evaluation of SARS-CoV-2/hCoV-19 sequences. *Nucleic Acids Research*, *49*(D1), D706–D714. https://doi.org/10.1093/nar/gkaa808

53) Farrugia, B. L., Lord, M. S., Melrose, J., & Whitelock, J. M. (2018). The Role of Heparan Sulfate in Inflammation, and the Development of Biomimetics as Anti-Inflammatory Strategies. *Journal of Histochemistry & Cytochemistry*, *66*(4), 321–336. https://doi.org/10.1369/0022155417740881

54) Fiege, J. K., Thiede, J. M., Nanda, H. A., Matchett, W. E., Moore, P. J., Montanari, N. R., Thielen, B. K., Daniel, J., Stanley, E., Hunter, R. C., Menachery, V. D., Shen, S. S., Bold, T. D., & Langlois, R. A. (2021). Single cell resolution of SARS-CoV-2 tropism, antiviral responses, and susceptibility to therapies in primary human airway epithelium. *PLOS Pathogens*, *17*(1), e1009292. https://doi.org/10.1371/journal.ppat.1009292

55) Finkel, Y., Mizrahi, O., Nachshon, A., Weingarten-Gabbay, S., Morgenstern, D., Yahalom-Ronen, Y., Tamir, H., Achdout, H., Stein, D., Israeli, O., Beth-Din, A., Melamed, S., Weiss, S., Israely, T., Paran, N., Schwartz, M., & Stern-Ginossar, N. (2021). The coding capacity of SARS-CoV-2. *Nature*, *589*(7840), 125–130. https://doi.org/10.1038/s41586-020-2739-1

56) Fogeron, M.-L., Montserret, R., Zehnder, J., Nguyen, M.-H., Dujardin, M., Brigandat, L., Cole, L., Ninot-Pedrosa, M., Lecoq, L., Meier, B. H., & Böckmann, A. (2021). *SARS-CoV-2 ORF7b: Is a bat virus protein homologue a major cause of COVID-19 symptoms?* [Preprint]. Biochemistry. https://doi.org/10.1101/2021.02.05.428650

57) Fosmire, J. A., Hwang, K., & Makino, S. (1992). Identification and characterization of a coronavirus packaging signal. *Journal of Virology*, *66*(6), 3522–3530. https://doi.org/10.1128/jvi.66.6.3522-3530.1992

58) Frazier, M. N., Dillard, L. B., Krahn, J. M., Perera, L., Williams, J. G., Wilson, I. M., Stewart, Z. D., Pillon, M. C., Deterding, L. J., Borgnia, M. J., & Stanley, R. E. (2021). Characterization of SARS2 Nsp15 nuclease activity reveals it's mad about U. *Nucleic Acids Research*, *49*(17), 10136–10149. https://doi.org/10.1093/nar/gkab719

59) Freitas, R. S., Crum, T. F., & Parvatiyar, K. (2022). SARS-CoV-2 Spike Antagonizes Innate Antiviral Immunity by Targeting Interferon Regulatory Factor 3. *Frontiers in Cellular and Infection Microbiology*, *11*, 789462. https://doi.org/10.3389/fcimb.2021.789462

60) Fu, Y.-Z., Wang, S.-Y., Zheng, Z.-Q., Yi Huang, Li, W.-W., Xu, Z.-S., & Wang, Y.-Y. (2021). SARS-CoV-2 membrane glycoprotein M antagonizes the MAVS-mediated innate antiviral response. *Cellular & Molecular Immunology*, *18*(3), 613–620. https://doi.org/10.1038/s41423-020-00571-x

61) Gabriella, M. (2020). Evidence for host-dependent RNA editing in the transcriptome of SARS-CoV-2. *SCIENCE ADVANCES*.

62) Gadhave, K., Kumar, P., Kumar, A., Bhardwaj, T., Garg, N., & Giri, R. (2021). Conformational dynamics of 13 amino acids long NSP11 of SARS-CoV-2 under membrane mimetics and different solvent conditions. *Microbial Pathogenesis*, *158*, 105041. https://doi.org/10.1016/j.micpath.2021.105041

63) Ganser, L. R., Kelly, M. L., Herschlag, D., & Al-Hashimi, H. M. (2019). The roles of structural dynamics in the cellular functions of RNAs. *Nature Reviews Molecular Cell Biology*, *20*(8), 474–489. https://doi.org/10.1038/s41580-019-0136-0

64) Gao, Z., Zhang, W., Chang, R., Zhang, S., Yang, G., & Zhao, G. (2021). Liquid-Liquid Phase Separation: Unraveling the Enigma of Biomolecular Condensates in Microbial Cells. *Frontiers in Microbiology*, *12*, 751880. https://doi.org/10.3389/fmicb.2021.751880

65) Ghosh, S., Dellibovi-Ragheb, T. A., Kerviel, A., Pak, E., Qiu, Q., Fisher, M., Takvorian, P. M., Bleck, C., Hsu, V. W., Fehr, A. R., Perlman, S., Achar, S. R., Straus, M. R., Whittaker, G. R., De Haan, C. A. M., Kehrl, J., Altan-Bonnet, G., & Altan-Bonnet, N. (2020). β-Coronaviruses Use Lysosomes for Egress Instead of the Biosynthetic Secretory Pathway. *Cell*, *183*(6), 1520-1535.e14. https://doi.org/10.1016/j.cell.2020.10.039

66) Gili, R., & Burioni, R. (2023). SARS-CoV-2 before and after Omicron: Two different viruses and two different diseases? *Journal of Translational Medicine*, *21*(1), 251. https://doi.org/10.1186/s12967-023-04095-6

67) Glowacka, I., Bertram, S., Müller, M. A., Allen, P., Soilleux, E., Pfefferle, S., Steffen, I., Tsegaye, T. S., He, Y., Gnirss, K., Niemeyer, D., Schneider, H., Drosten, C., & Pöhlmann, S. (2011). Evidence that TMPRSS2 Activates the Severe Acute Respiratory Syndrome Coronavirus Spike Protein for Membrane Fusion and Reduces Viral Control by the Humoral Immune Response. *Journal of Virology*, *85*(9), 4122–4134. https://doi.org/10.1128/JVI.02232-10

68) González-Alvarez, F., Estañol, B., González-Hermosillo, J. A., Gómez-Pérez, F. J., Tamez-Torres, K. M., Peña, E., Cantú, C., Chiquete, E., Sifuentes-Osornio, J., Alba-Lorenzo, M. D. C., Celestino-Montelongo, D. A., Salazar-Calderón, G. E., & Aceves Buendia, J. D. J. (2024). Complete remission with histamine blocker in a patient with intractable hyperadrenergic postural orthostatic tachycardia syndrome secondary to long coronavirus disease syndrome. *Journal of Hypertension*, *42*(5), 928–932. https://doi.org/10.1097/HJH.0000000000003669

69) Gordon, D. E., Jang, G. M., Bouhaddou, M., Xu, J., Obernier, K., White, K. M., O'Meara, M. J., Rezelj, V. V., Guo, J. Z., Swaney, D. L., Tummino, T. A., Hüttenhain, R., Kaake, R. M., Richards, A. L., Tutuncuoglu, B., Foussard, H., Batra, J., Haas, K., Modak, M., … Krogan, N. J. (2020). A SARS-CoV-2 protein interaction map reveals targets for drug repurposing. *Nature*, *583*(7816), 459–468. https://doi.org/10.1038/s41586-020-2286-9

70) Gori Savellini, G., Anichini, G., Gandolfo, C., & Cusi, M. G. (2021). SARS-CoV-2 N Protein Targets TRIM25-Mediated RIG-I Activation to Suppress Innate Immunity. *Viruses*, *13*(8), 1439. https://doi.org/10.3390/v13081439

71) Graham, A. C., Temple, R. M., & Obar, J. J. (2015). Mast Cells and Influenza A Virus: Association with Allergic Responses and Beyond. *Frontiers in Immunology*, *6*. https://doi.org/10.3389/fimmu.2015.00238

72) Grohman, J. K., Gorelick, R. J., Lickwar, C. R., Lieb, J. D., Bower, B. D., Znosko, B. M., & Weeks, K. M. (2013). A Guanosine-Centric Mechanism for RNA Chaperone Function. *Science*, *340*(6129), 190–195. https://doi.org/10.1126/science.1230715

73) Guan, Y., Zheng, B. J., He, Y. Q., Liu, X. L., Zhuang, Z. X., Cheung, C. L., Luo, S. W., Li, P. H., Zhang, L. J., Guan, Y. J., Butt, K. M., Wong, K. L., Chan, K. W., Lim, W., Shortridge, K. F., Yuen, K. Y., Peiris, J. S. M., & Poon, L. L. M. (2003). Isolation and Characterization of Viruses

Related to the SARS Coronavirus from Animals in Southern China. *Science*, *302*(5643), 276–278. https://doi.org/10.1126/science.1087139

74) Guilarte, M., Sala-Cunill, A., Luengo, O., Labrador-Horrillo, M., & Cardona, V. (2017). The Mast Cell, Contact, and Coagulation System Connection in Anaphylaxis. *Frontiers in Immunology*, *8*, 846. https://doi.org/10.3389/fimmu.2017.00846

75) Habchi, J., Tompa, P., Longhi, S., & Uversky, V. N. (2014). Introducing Protein Intrinsic Disorder. *Chemical Reviews*, *114*(13), 6561–6588. https://doi.org/10.1021/cr400514h

76) Harvey, W. T., Carabelli, A. M., Jackson, B., Gupta, R. K., Thomson, E. C., Harrison, E. M., Ludden, C., Reeve, R., Rambaut, A., COVID-19 Genomics UK (COG-UK) Consortium, Peacock, S. J., & Robertson, D. L. (2021). SARS-CoV-2 variants, spike mutations and immune escape. *Nature Reviews Microbiology*, *19*(7), 409–424. https://doi.org/10.1038/s41579-021-00573-0

77) Herschlag, D. (1995). RNA Chaperones and the RNA Folding Problem. *Journal of Biological Chemistry*, *270*(36), 20871–20874. https://doi.org/10.1074/jbc.270.36.20871

78) Herschlag, D., Khosla, M., Tsuchihashi, Z., & Karpel, R. L. (1994). An RNA chaperone activity of non-specific RNA binding proteins in hammerhead ribozyme catalysis. *The EMBO Journal*, *13*(12), 2913–2924. https://doi.org/10.1002/j.1460-2075.1994.tb06586.x

79) Hoffmann, M., Kleine-Weber, H., & Pöhlmann, S. (2020). A Multibasic Cleavage Site in the Spike Protein of SARS-CoV-2 Is Essential for Infection of Human Lung Cells. *Molecular Cell*, *78*(4), 779-784.e5. https://doi.org/10.1016/j.molcel.2020.04.022

80) Hong, S., Seo, S. H., Woo, S.-J., Kwon, Y., Song, M., & Ha, N.-C. (2021). Epigallocatechin Gallate Inhibits the Uridylate-Specific Endoribonuclease Nsp15 and Efficiently Neutralizes the SARS-CoV-2 Strain. *Journal of Agricultural and Food Chemistry*, *69*(21), 5948–5954. https://doi.org/10.1021/acs.jafc.1c02050

81) Hsin, W.-C., Chang, C.-H., Chang, C.-Y., Peng, W.-H., Chien, C.-L., Chang, M.-F., & Chang, S. C. (2018). Nucleocapsid protein-dependent assembly of the RNA packaging signal of Middle East respiratory syndrome coronavirus. *Journal of Biomedical Science*, *25*(1), 47. https://doi.org/10.1186/s12929-018-0449-x

82) Hsu, J. C.-C., Laurent-Rolle, M., Pawlak, J. B., Wilen, C. B., & Cresswell, P. (2021). Translational shutdown and evasion of the innate immune response by SARS-CoV-2 NSP14 protein. *Proceedings of the National Academy of Sciences*, *118*(24), e2101161118. https://doi.org/10.1073/pnas.2101161118

83) Ikuta, K., Morita, C., Miyake, S., Ito, T., Okabayashi, M., Sano, K., Nakai, M., Hirai, K., & Kato, S. (1989). Expression of human immunodeficiency virus type 1 (HIV-1) gag antigens on the surface of a cell line persistently infected with HIV-1 that highly expresses HIV-1 antigens. *Virology*, *170*(2), 408–417. https://doi.org/10.1016/0042-6822(89)90431-5

84) Iserman, C., Roden, C. A., Boerneke, M. A., Sealfon, R. S. G., McLaughlin, G. A., Jungreis, I., Fritch, E. J., Hou, Y. J., Ekena, J., Weidmann, C. A., Theesfeld, C. L., Kellis, M., Troyanskaya, O. G., Baric, R. S., Sheahan, T. P., Weeks, K. M., & Gladfelter, A. S. (2020). Genomic RNA Elements Drive Phase Separation of the SARS-CoV-2 Nucleocapsid. *Molecular Cell*, *80*(6), 1078-1091.e6. https://doi.org/10.1016/j.molcel.2020.11.041

85) Ivanyi-Nagy, R., Davidovic, L., Khandjian, E. W., & Darlix, J.-L. (2005). Disordered RNA chaperone proteins: From functions to disease. *Cellular and Molecular Life Sciences*, *62*(13), 1409–1417. https://doi.org/10.1007/s00018-005-5100-9

86) Jackson, C. B., Farzan, M., Chen, B., & Choe, H. (2022). Mechanisms of SARS-CoV-2 entry into cells. *Nature Reviews Molecular Cell Biology*, *23*(1), 3–20. https://doi.org/10.1038/s41580-021-00418-x

87) Jamison, D. A., Anand Narayanan, S., Trovão, N. S., Guarnieri, J. W., Topper, M. J., Moraes-Vieira, P. M., Zaksas, V., Singh, K. K., Wurtele, E. S., & Beheshti, A. (2022). A comprehensive SARS-CoV-2 and COVID-19 review, Part 1: Intracellular overdrive for SARS-CoV-2 infection. *European Journal of Human Genetics*, *30*(8), 889–898. https://doi.org/10.1038/s41431-022-01108-8

88) Jangra, S., De Vrieze, J., Choi, A., Rathnasinghe, R., Laghlali, G., Uvyn, A., Van Herck, S., Nuhn, L., Deswarte, K., Zhong, Z., Sanders, N. N., Lienenklaus, S., David, S. A., Strohmeier, S., Amanat, F., Krammer, F., Hammad, H., Lambrecht, B. N., Coughlan, L., … Schotsaert, M. (2021). Sterilizing Immunity against SARS-CoV-2 Infection in Mice by a Single-Shot and Lipid Amphiphile Imidazoquinoline TLR7/8 Agonist-Adjuvanted Recombinant Spike Protein Vaccine**. *Angewandte Chemie International Edition*, *60*(17), 9467–9473. https://doi.org/10.1002/anie.202015362

89) Kang, S., Yang, M., Hong, Z., Zhang, L., Huang, Z., Chen, X., He, S., Zhou, Z., Zhou, Z., Chen, Q., Yan, Y., Zhang, C., Shan, H., & Chen, S. (2020). Crystal structure of SARS-CoV-2 nucleocapsid protein RNA binding domain reveals potential unique drug targeting sites. *Acta Pharmaceutica Sinica B*, *10*(7), 1228–1238. https://doi.org/10.1016/j.apsb.2020.04.009

90) Kassambara, A. (2023). *ggpubr: "ggplot2" Based Publication Ready Plots*. https://CRAN.R-project.org/package=ggpubr

91) Kasuga, Y., Zhu, B., Jang, K.-J., & Yoo, J.-S. (2021). Innate immune sensing of coronavirus and viral evasion strategies. *Experimental & Molecular Medicine*, *53*(5), 723–736. https://doi.org/10.1038/s12276-021-00602-1

92) Kato, K., Ikliptikawati, D. K., Kobayashi, A., Kondo, H., Lim, K., Hazawa, M., & Wong, R. W. (2021). Overexpression of SARS-CoV-2 protein ORF6 dislocates RAE1 and NUP98 from the nuclear pore complex. *Biochemical and Biophysical Research Communications*, *536*, 59–66. https://doi.org/10.1016/j.bbrc.2020.11.115

93) Kautz, T., & Forrester, N. (2018). RNA Virus Fidelity Mutants: A Useful Tool for Evolutionary Biology or a Complex Challenge? *Viruses*, *10*(11), 600. https://doi.org/10.3390/v10110600

94) Kawai, T., & Akira, S. (2010). The role of pattern-recognition receptors in innate immunity: Update on Toll-like receptors. *Nature Immunology*, *11*(5), 373–384. https://doi.org/10.1038/ni.1863

95) Kelly, J. A., Woodside, M. T., & Dinman, J. D. (2021). Programmed −1 Ribosomal Frameshifting in coronaviruses: A therapeutic target. *Virology*, *554*, 75–82. https://doi.org/10.1016/j.virol.2020.12.010

96) Kempuraj, D., Selvakumar, G. P., Ahmed, M. E., Raikwar, S. P., Thangavel, R., Khan, A., Zaheer, S. A., Iyer, S. S., Burton, C., James, D., & Zaheer, A. (2020). COVID-19, Mast Cells,

Cytokine Storm, Psychological Stress, and Neuroinflammation. *The Neuroscientist*, *26*(5–6), 402–414. https://doi.org/10.1177/1073858420941476

97) Khabar, K. S. A., Al-Zoghaibi, F., Al-Ahdal, M. N., Murayama, T., Dhalla, M., Mukaida, N., Taha, M., Al-Sedairy, S. T., Siddiqui, Y., Kessie, G., & Matsushima, K. (1997). *The alpha Chemokine, Interleukin 8, Inhibits the Antiviral Action of Interferon alpha*. *186(7)*, 1077–1085. https://doi.org/doi: 10.1084/jem.186.7.1077

98) Khan, S., Fung, K. W., 馮家維, Rodriguez, E., Patel, R., Gor, J., Mulloy, B., & Perkins, S. J. (2013). The Solution Structure of Heparan Sulfate Differs from That of Heparin. *Journal of Biological Chemistry*, *288*(39), 27737–27751. https://doi.org/10.1074/jbc.M113.492223

99) Kim, D., Lee, J.-Y., Yang, J.-S., Kim, J. W., Kim, V. N., & Chang, H. (2020). The Architecture of SARS-CoV-2 Transcriptome. *Cell*, *181*(4), 914-921.e10. https://doi.org/10.1016/j.cell.2020.04.011

100) Klumperman, J., Locker, J. K., Meijer, A., Horzinek, M. C., Geuze, H. J., & Rottier, P. J. (1994). Coronavirus M proteins accumulate in the Golgi complex beyond the site of virion budding. *Journal of Virology*, *68*(10), 6523–6534. https://doi.org/10.1128/jvi.68.10.6523-6534.1994

101) Konno, Y., Kimura, I., Uriu, K., Fukushi, M., Irie, T., Koyanagi, Y., Sauter, D., Gifford, R. J., Nakagawa, S., & Sato, K. (2020). SARS-CoV-2 ORF3b Is a Potent Interferon Antagonist Whose Activity Is Increased by a Naturally Occurring Elongation Variant. *Cell Reports*, *32*(12), 108185. https://doi.org/10.1016/j.celrep.2020.108185

102) Koonin, E. V., Krupovic, M., & Agol, V. I. (2021). The Baltimore Classification of Viruses 50 Years Later: How Does It Stand in the Light of Virus Evolution? *Microbiology and Molecular Biology Reviews*, *85*(3), e00053-21. https://doi.org/10.1128/MMBR.00053-21

103) Kreimendahl, S., & Rassow, J. (2020). The Mitochondrial Outer Membrane Protein Tom70-Mediator in Protein Traffic, Membrane Contact Sites and Innate Immunity. *International Journal of Molecular Sciences*, *21*(19), 7262. https://doi.org/10.3390/ijms21197262

104) Kuehnert, J., Sommer, G., Zierk, A. W., Fedarovich, A., Brock, A., Fedarovich, D., & Heise, T. (2015). Novel RNA chaperone domain of RNA-binding protein La is regulated by AKT phosphorylation. *Nucleic Acids Research*, *43*(1), 581–594. https://doi.org/10.1093/nar/gku1309

105) Kumar, R., & Reji, M. (2023). Emergence of SARS-CoV-2 variant of concern omicron: Biological features and genomic concern. *Indian Journal of Microbiology Research*, *9*(4), 252–271. https://doi.org/10.18231/j.ijmr.2022.044

106) La Monica, N., Yokomori, K., & Lai, M. M. C. (1992). Coronavirus mRNA synthesis: Identification of novel transcription initiation signals which are differentially regulated by different leader sequences. *Virology*, *188*(1), 402–407. https://doi.org/10.1016/0042-6822(92)90774-J

107) Laine, D., Trescol-Biemont, M.-C., Longhi, S., Libeau, G., Marie, J. C., Vidalain, P.-O., Azocar, O., Diallo, A., Canard, B., Rabourdin-Combe, C., & Valentin, H. (2003). Measles Virus (MV) Nucleoprotein Binds to a Novel Cell Surface Receptor Distinct from Fc∕RII via Its C-Terminal Domain: Role in MV-Induced Immunosuppression. *J. VIROL.*, *77*.

108) Lan, T. C. T., Allan, M. F., Malsick, L. E., Woo, J. Z., Zhu, C., Zhang, F., Khandwala, S., Nyeo, S. S. Y., Sun, Y., Guo, J. U., Bathe, M., Näär, A., Griffiths, A., & Rouskin, S. (2022). Secondary structural ensembles of the SARS-CoV-2 RNA genome in infected cells. *Nature Communications*, *13*(1), 1128. https://doi.org/10.1038/s41467-022-28603-2

109) Lapointe, C. P., Grosely, R., Johnson, A. G., Wang, J., Fernández, I. S., & Puglisi, J. D. (2021). Dynamic competition between SARS-CoV-2 NSP1 and mRNA on the human ribosome inhibits translation initiation. *Proceedings of the National Academy of Sciences*, *118*(6), e2017715118. https://doi.org/10.1073/pnas.2017715118

110) Lester, S. N., & Li, K. (2014). Toll-Like Receptors in Antiviral Innate Immunity. *Journal of Molecular Biology*, *426*(6), 1246–1264. https://doi.org/10.1016/j.jmb.2013.11.024

111) Li, W., Moore, M. J., Vasilieva, N., Sui, J., Wong, S. K., Berne, M. A., Somasundaran, M., Sullivan, J. L., Luzuriaga, K., Greenough, T. C., Choe, H., & Farzan, M. (2003). Angiotensin-converting enzyme 2 is a functional receptor for the SARS coronavirus. *Nature*, *426*(6965), 450–454. https://doi.org/10.1038/nature02145

112) Li, Y., Jiang, Y., Li, Z., Yu, Y., Chen, J., Jia, W., Ng, Y. K., Ye, F., Shen, B., & Li, S. C. (2021). *Both Simulation and Sequencing Data Reveal Multiple SARS-CoV-2 Variants Coinfection in COVID-19 Pandemic* [Preprint]. Bioinformatics. https://doi.org/10.1101/2021.09.06.459196

113) Lin, R., Génin, P., Mamane, Y., & Hiscott, J. (2000). Selective DNA Binding and Association with the CREB Binding Protein Coactivator Contribute to Differential Activation of Alpha/Beta Interferon Genes by Interferon Regulatory Factors 3 and 7. *Molecular and Cellular Biology*, *20*(17), 6342–6353. https://doi.org/10.1128/MCB.20.17.6342-6353.2000

114) Lin, Y., Currie, S. L., & Rosen, M. K. (2017). Intrinsically disordered sequences enable modulation of protein phase separation through distributed tyrosine motifs. *Journal of Biological Chemistry*, *292*(46), 19110–19120. https://doi.org/10.1074/jbc.M117.800466

115) López-Muñoz, A. (2022). Cell surface SARS-CoV-2 nucleocapsid protein modulates innate and adaptive immunity. *SCIENCE ADVANCES*.

116) López-Muñoz, A. D., Santos, J. J. S., & Yewdell, J. W. (2023). Cell surface nucleocapsid protein expression: A betacoronavirus immunomodulatory strategy. *Proceedings of the National Academy of Sciences*, *120*(28), e2304087120. https://doi.org/10.1073/pnas.2304087120

117) Louten, J. (2016). Virus Structure and Classification. In *Essential Human Virology* (pp. 19–29). Elsevier. https://doi.org/10.1016/B978-0-12-800947-5.00002-8

118) Lu, R., Zhao, X., Li, J., Niu, P., Yang, B., Wu, H., Wang, W., Song, H., Huang, B., Zhu, N., Bi, Y., Ma, X., Zhan, F., Wang, L., Hu, T., Zhou, H., Hu, Z., Zhou, W., Zhao, L., … Tan, W. (2020). Genomic characterisation and epidemiology of 2019 novel coronavirus: Implications for virus origins and receptor binding. *The Lancet*, *395*(10224), 565–574. https://doi.org/10.1016/S0140-6736(20)30251-8

119) Lu, S., Ye, Q., Singh, D., Cao, Y., Diedrich, J. K., Yates, J. R., Villa, E., Cleveland, D. W., & Corbett, K. D. (2021). The SARS-CoV-2 nucleocapsid phosphoprotein forms mutually exclusive condensates with RNA and the membrane-associated M protein. *Nature Communications*, *12*(1), 502. https://doi.org/10.1038/s41467-020-20768-y

120) Lu, Y., Zhao, T., Lu, M., Zhang, Y., Yao, X., Wu, G., Dai, F., Zhang, F., & Zhang, G. (2021). The Analyses of High Infectivity Mechanism of SARS-CoV-2 and Its Variants. *COVID*, *1*(4), 666–673. https://doi.org/10.3390/covid1040054

121) Lwoff, A. (1957). The Concept of Virus. *Microbiology*, *17*(2), 239–253. https://doi.org/10.1099/00221287-17-2-239

122) Makino, S., Yokomori, K., & Lai, M. M. (1990). Analysis of efficiently packaged defective interfering RNAs of murine coronavirus: Localization of a possible RNA-packaging signal. *Journal of Virology*, *64*(12), 6045–6053. https://doi.org/10.1128/jvi.64.12.6045-6053.1990

123) Makiyama, K., Hazawa, M., Kobayashi, A., Lim, K., Voon, D. C., & Wong, R. W. (2022). NSP9 of SARS-CoV-2 attenuates nuclear transport by hampering nucleoporin 62 dynamics and functions in host cells. *Biochemical and Biophysical Research Communications*, *586*, 137–142. https://doi.org/10.1016/j.bbrc.2021.11.046

124) Malden, D. E., Bruxvoort, K. J., Tseng, H. F., Ackerson, B., Choi, S. K., Florea, A., Tubert, J., Takhar, H., Aragones, M., Hong, V., Talarico, C. A., McLaughlin, J. M., Qian, L., & Tartof, S. Y. (2021). Distribution of SARS-CoV-2 Variants in a Large Integrated Health Care System—California, March–July 2021. *MMWR. Morbidity and Mortality Weekly Report*, *70*(40), 1415–1419. https://doi.org/10.15585/mmwr.mm7040a4

125) Masters, P. S. (2019). Coronavirus genomic RNA packaging. *Virology*, *537*, 198–207. https://doi.org/10.1016/j.virol.2019.08.031

126) Mateu, M. G. (2013). Introduction: The Structural Basis of Virus Function. In M. G. Mateu (Ed.), *Structure and Physics of Viruses* (Vol. 68, pp. 3–51). Springer Netherlands. https://doi.org/10.1007/978-94-007-6552-8_1

127) Mathews, D. H., Disney, M. D., Childs, J. L., Schroeder, S. J., Zuker, M., & Turner, D. H. (2004). Incorporating chemical modification constraints into a dynamic programming algorithm for prediction of RNA secondary structure. *Proceedings of the National Academy of Sciences*, *101*(19), 7287–7292. https://doi.org/10.1073/pnas.0401799101

128) Matsuyama, S., Nagata, N., Shirato, K., Kawase, M., Takeda, M., & Taguchi, F. (2010). Efficient Activation of the Severe Acute Respiratory Syndrome Coronavirus Spike Protein by the Transmembrane Protease TMPRSS2. *Journal of Virology*, *84*(24), 12658–12664. https://doi.org/10.1128/JVI.01542-10

129) Mayer, O., Rajkowitsch, L., Lorenz, C., Konrat, R., & Schroeder, R. (2007). RNA chaperone activity and RNA-binding properties of the E. coli protein StpA. *Nucleic Acids Research*, *35*(4), 1257–1269. https://doi.org/10.1093/nar/gkl1143

130) McBride, R., van Zyl, M., & Fielding, B. (2014). The Coronavirus Nucleocapsid Is a Multifunctional Protein. *Viruses*, *6*(8), 2991–3018. https://doi.org/10.3390/v6082991

131) Melchjorsen, J., Sørensen, L. N., & Paludan, S. R. (2003). Expression and function of chemokines during viral infections: From molecular mechanisms to in vivo function. *Journal of Leukocyte Biology*, *74*(3), 331–343. https://doi.org/10.1189/jlb.1102577

132) Meyerholz, D. K., & Reznikov, L. R. (2022). Influence of SARS-CoV-2 on airway mucus production: A review and proposed model. *Veterinary Pathology*, *59*(4), 578–585. https://doi.org/10.1177/03009858211058837

133) Miao, Z., Tidu, A., Eriani, G., & Martin, F. (2021). Secondary structure of the SARS-CoV-2 5′-UTR. *RNA Biology*, *18*(4), 447–456. https://doi.org/10.1080/15476286.2020.1814556

134) Micheau, O., & Tschopp, J. (2003). Induction of TNF Receptor I-Mediated Apoptosis via Two Sequential Signaling Complexes. *Cell*, *114*(2), 181–190. https://doi.org/10.1016/S0092-8674(03)00521-X

135) Minkoff, J. M., & tenOever, B. (2023). Innate immune evasion strategies of SARS-CoV-2. *Nature Reviews Microbiology*. https://doi.org/10.1038/s41579-022-00839-1

136) Miorin, L., Kehrer, T., Sanchez-Aparicio, M. T., Zhang, K., Cohen, P., Patel, R. S., Cupic, A., Makio, T., Mei, M., Moreno, E., Danziger, O., White, K. M., Rathnasinghe, R., Uccellini, M., Gao, S., Aydillo, T., Mena, I., Yin, X., Martin-Sancho, L., … García-Sastre, A. (2020). SARS-CoV-2 Orf6 hijacks Nup98 to block STAT nuclear import and antagonize interferon signaling. *Proceedings of the National Academy of Sciences*, *117*(45), 28344–28354. https://doi.org/10.1073/pnas.2016650117

137) Mittag, T., & Parker, R. (2018). Multiple Modes of Protein–Protein Interactions Promote RNP Granule Assembly. *Journal of Molecular Biology*, *430*(23), 4636–4649. https://doi.org/10.1016/j.jmb.2018.08.005

138) Modic, M., Adamek, M., & Ule, J. (2024). The impact of IDR phosphorylation on the RNA binding profiles of proteins. *Trends in Genetics*. https://doi.org/10.1016/j.tig.2024.04.004

139) Mohd Zawawi, Z., Kalyanasundram, J., Mohd Zain, R., Thayan, R., Basri, D. F., & Yap, W. B. (2023). Prospective Roles of Tumor Necrosis Factor-Alpha (TNF-α) in COVID-19: Prognosis, Therapeutic and Management. *International Journal of Molecular Sciences*, *24*(7), 6142. https://doi.org/10.3390/ijms24076142

140) Mohr, S., Stryker, J. M., & Lambowitz, A. M. (2002). A DEAD-Box Protein Functions as an ATP-Dependent RNA Chaperone in Group I Intron Splicing. *Cell*, *109*(6), 769–779. https://doi.org/10.1016/S0092-8674(02)00771-7

141) Morellet, N., Jullian, N., De Rocquigny, H., Maigret, B., Darlix, J. L., & Roques, B. P. (1992). Determination of the structure of the nucleocapsid protein NCp7 from the human immunodeficiency virus type 1 by 1H NMR. *The EMBO Journal*, *11*(8), 3059–3065. https://doi.org/10.1002/j.1460-2075.1992.tb05377.x

142) Mu, J., Fang, Y., Yang, Q., Shu, T., Wang, A., Huang, M., Jin, L., Deng, F., Qiu, Y., & Zhou, X. (2020). SARS-CoV-2 N protein antagonizes type I interferon signaling by suppressing phosphorylation and nuclear translocation of STAT1 and STAT2. *Cell Discovery*, *6*(1), 65. https://doi.org/10.1038/s41421-020-00208-3

143) Muralidar, S., Ambi, S. V., Sekaran, S., & Krishnan, U. M. (2020). The emergence of COVID-19 as a global pandemic: Understanding the epidemiology, immune response and potential therapeutic targets of SARS-CoV-2. *Biochimie*, *179*, 85–100. https://doi.org/10.1016/j.biochi.2020.09.018

144) Neuwirth, E. (2022). *RColorBrewer: ColorBrewer Palettes*. https://CRAN.R-project.org/package=RColorBrewer

145) Pagani, I., Ghezzi, S., Alberti, S., Poli, G., & Vicenzi, E. (2023). Origin and evolution of SARS-CoV-2. *The European Physical Journal Plus*, *138*(2), 157. https://doi.org/10.1140/epjp/s13360-023-03719-6

146) Pancer, K., Milewska, A., Owczarek, K., Dabrowska, A., Kowalski, M., Łabaj, P. P., Branicki, W., Sanak, M., & Pyrc, K. (2020). The SARS-CoV-2 ORF10 is not essential in vitro or in vivo in humans. *PLOS Pathogens*, *16*(12), e1008959. https://doi.org/10.1371/journal.ppat.1008959

147) Parish, C. R. (2006). The role of heparan sulphate in inflammation. *Nature Reviews Immunology*, *6*(9), 633–643. https://doi.org/10.1038/nri1918

148) Payne, S. (2017). Introduction to RNA Viruses. In *Viruses* (pp. 97–105). Elsevier. https://doi.org/10.1016/B978-0-12-803109-4.00010-6

149) Pekar, J. E., Magee, A., Parker, E., Moshiri, N., Izhikevich, K., Havens, J. L., Gangavarapu, K., Malpica Serrano, L. M., Crits-Christoph, A., Matteson, N. L., Zeller, M., Levy, J. I., Wang, J. C., Hughes, S., Lee, J., Park, H., Park, M.-S., Ching Zi Yan, K., Lin, R. T. P., … Wertheim, J. O. (2022). The molecular epidemiology of multiple zoonotic origins of SARS-CoV-2. *Science*, *377*(6609), 960–966. https://doi.org/10.1126/science.abp8337

150) Peng, Y., Du, N., Lei, Y., Dorje, S., Qi, J., Luo, T., Gao, G. F., & Song, H. (2020). Structures of the SARS -CoV-2 nucleocapsid and their perspectives for drug design. *The EMBO Journal*, *39*(20). https://doi.org/10.15252/embj.2020105938

151) Pinto, A. L., Rai, R. K., Brown, J. C., Griffin, P., Edgar, J. R., Shah, A., Singanayagam, A., Hogg, C., Barclay, W. S., Futter, C. E., & Burgoyne, T. (2022). Ultrastructural insight into SARS-CoV-2 entry and budding in human airway epithelium. *Nature Communications*, *13*(1), 1609. https://doi.org/10.1038/s41467-022-29255-y

152) Poltronieri, P., Sun, B., & Mallardo, M. (2015). RNA Viruses: RNA Roles in Pathogenesis, Coreplication and Viral Load. *Current Genomics*, *16*(5), 327–335. https://doi.org/10.2174/1389202916666150707160613

153) Pomin, V. H., Bezerra, F. F., & Soares, P. A. G. (2017). Sulfated Glycans in HIV Infection and Therapy. *Current Pharmaceutical Design*, *23*(23). https://doi.org/10.2174/1381612823666170127113958

154) Qin, L., Meng, J., Ding, X., & Jiang, T. (2022). Mapping Genetic Events of SARS-CoV-2 Variants. *Frontiers in Microbiology*, *13*, 890590. https://doi.org/10.3389/fmicb.2022.890590

155) R Core Team. (2023). *R: A Language and Environment for Statistical Computing*. R Foundation for Statistical Computing. https://www.R-project.org/

156) Rabaan, A. A., Alenazy, M. F., Alshehri, A. A., Alshahrani, M. A., Al-Subaie, M. F., Alrasheed, H. A., Al Kaabi, N. A., Thakur, N., Bouafia, N. A., Alissa, M., Alsulaiman, A. M., AlBaadani, A. M., Alhani, H. M., Alhaddad, A. H., Alfouzan, W. A., Ali, B. M. A., Al-Abdulali, K. H., Khamis, F., Bayahya, A., … Dhawan, M. (2023). An updated review on pathogenic coronaviruses (CoVs) amid the emergence of SARS-CoV-2 variants: A look into the repercussions and possible solutions. *Journal of Infection and Public Health*, *16*(11), 1870–1883. https://doi.org/10.1016/j.jiph.2023.09.004

157) Rajkowitsch, L., Chen, D., Stampfl, S., Semrad, K., Waldsich, C., Mayer, O., Jantsch, M. F., Konrat, R., Bläsi, U., & Schroeder, R. (2007). RNA Chaperones, RNA Annealers and RNA Helicases. *RNA Biology*, *4*(3), 118–130. https://doi.org/10.4161/rna.4.3.5445

158) Rajpal, V. R., Sharma, S., Sehgal, D., Singh, A., Kumar, A., Vaishnavi, S., Tiwari, M., Bhalla, H., Goel, S., & Raina, S. N. (2022). A comprehensive account of SARS-CoV-2 genome

structure, incurred mutations, lineages and COVID-19 vaccination program. *Future Virology*, *17*(9), 687–706. https://doi.org/10.2217/fvl-2021-0277

159) Rana, R., Kant, R., Huirem, R. S., Bohra, D., & Ganguly, N. K. (2022). Omicron variant: Current insights and future directions. *Microbiological Research*, *265*, 127204. https://doi.org/10.1016/j.micres.2022.127204

160) Redondo, N., Zaldívar-López, S., Garrido, J. J., & Montoya, M. (2021). SARS-CoV-2 Accessory Proteins in Viral Pathogenesis: Knowns and Unknowns. *Frontiers in Immunology*, *12*, 708264. https://doi.org/10.3389/fimmu.2021.708264

161) Reeves, K. D., Polk, C. M., Cox, L. A., Fairman, R. T., Hawkins, G. A., Passaretti, C. L., & Sampson, M. M. (2022). Severe acute respiratory coronavirus virus 2 (SARS-CoV-2) infections occurring in healthcare workers after booster vaccination: A comparison of delta versus omicron variants. *Antimicrobial Stewardship & Healthcare Epidemiology*, *2*(1), e143. https://doi.org/10.1017/ash.2022.239

162) Reineke, L. C., & Lloyd, R. E. (2015). The Stress Granule Protein G3BP1 Recruits Protein Kinase R To Promote Multiple Innate Immune Antiviral Responses. *Journal of Virology*, *89*(5), 2575–2589. https://doi.org/10.1128/JVI.02791-14

163) Ren, Y., Wang, A., Fang, Y., Shu, T., Wu, D., Wang, C., Huang, M., Min, J., Jin, L., Zhou, W., Qiu, Y., & Zhou, X. (2021). SARS-CoV-2 Membrane Glycoprotein M Triggers Apoptosis With the Assistance of Nucleocapsid Protein N in Cells. *Frontiers in Cellular and Infection Microbiology*, *11*, 706252. https://doi.org/10.3389/fcimb.2021.706252

164) Ricciardi, S., Guarino, A. M., Giaquinto, L., Polishchuk, E. V., Santoro, M., Di Tullio, G., Wilson, C., Panariello, F., Soares, V. C., Dias, S. S. G., Santos, J. C., Souza, T. M. L., Fusco, G., Viscardi, M., Brandi, S., Bozza, P. T., Polishchuk, R. S., Venditti, R., & De Matteis, M. A. (2022). The role of NSP6 in the biogenesis of the SARS-CoV-2 replication organelle. *Nature*, *606*(7915), 761–768. https://doi.org/10.1038/s41586-022-04835-6

165) Richards, K. F., Bienkowska-Haba, M., Dasgupta, J., Chen, X. S., & Sapp, M. (2013). Multiple Heparan Sulfate Binding Site Engagements Are Required for the Infectious Entry of Human Papillomavirus Type 16. *Journal of Virology*, *87*(21), 11426–11437. https://doi.org/10.1128/JVI.01721-13

166) Roe, M. K., Junod, N. A., Young, A. R., Beachboard, D. C., & Stobart, C. C. (2021). Targeting novel structural and functional features of coronavirus protease nsp5 (3CLpro, Mpro) in the age of COVID-19. *Journal of General Virology*, *102*(3). https://doi.org/10.1099/jgv.0.001558

167) Rump, A., Risti, R., Kristal, M.-L., Reut, J., Syritski, V., Lookene, A., & Ruutel Boudinot, S. (2021). Dual ELISA using SARS-CoV-2 nucleocapsid protein produced in E. coli and CHO cells reveals epitope masking by N-glycosylation. *Biochemical and Biophysical Research Communications*, *534*, 457–460. https://doi.org/10.1016/j.bbrc.2020.11.060

168) Russell, R. (2008). RNA misfolding and the action of chaperones. *Frontiers in Bioscience*, *13*(13), 1. https://doi.org/10.2741/2557

169) Savastano, A., Ibáñez de Opakua, A., Rankovic, M., & Zweckstetter, M. (2020). Nucleocapsid protein of SARS-CoV-2 phase separates into RNA-rich polymerase-containing condensates. *Nature Communications*, *11*(1), 6041. https://doi.org/10.1038/s41467-020-19843-1

170) Sawicki, S. G., & Sawicki, D. L. (1995). Coronaviruses use Discontinuous Extension for Synthesis of Subgenome-Length Negative Strands. In P. J. Talbot & G. A. Levy (Eds.), *Corona- and Related Viruses* (Vol. 380, pp. 499–506). Springer US. https://doi.org/10.1007/978-1-4615-1899-0_79

171) Scherer, K. M., Mascheroni, L., Carnell, G. W., Wunderlich, L. C. S., Makarchuk, S., Brockhoff, M., Mela, I., Fernandez-Villegas, A., Barysevich, M., Stewart, H., Suau Sans, M., George, C. L., Lamb, J. R., Kaminski-Schierle, G. S., Heeney, J. L., & Kaminski, C. F. (2022). SARS-CoV-2 nucleocapsid protein adheres to replication organelles before viral assembly at the Golgi/ERGIC and lysosome-mediated egress. *Science Advances*, *8*(1), eabl4895. https://doi.org/10.1126/sciadv.abl4895

172) Schiavina, M., Pontoriero, L., Tagliaferro, G., Pierattelli, R., & Felli, I. C. (2022). The Role of Disordered Regions in Orchestrating the Properties of Multidomain Proteins: The SARS-CoV-2 Nucleocapsid Protein and Its Interaction with Enoxaparin. *Biomolecules*, *12*(9), 1302. https://doi.org/10.3390/biom12091302

173) Semrad, K. (2011). Proteins with RNA Chaperone Activity: A World of Diverse Proteins with a Common Task—Impediment of RNA Misfolding. *Biochemistry Research International*, *2011*, 1–11. https://doi.org/10.1155/2011/532908

174) Shang, J., Wan, Y., Luo, C., Ye, G., Geng, Q., Auerbach, A., & Li, F. (2020). Cell entry mechanisms of SARS-CoV-2. *Proceedings of the National Academy of Sciences*, *117*(21), 11727–11734. https://doi.org/10.1073/pnas.2003138117

175) Shetty, S., Stefanovic, S., & Mihailescu, M. R. (2013). Hepatitis C virus RNA: Molecular switches mediated by long-range RNA–RNA interactions? *Nucleic Acids Research*, *41*(4), 2526–2540. https://doi.org/10.1093/nar/gks1318

176) Shi, D., Sheng, A., & Chi, L. (2021). Glycosaminoglycan-Protein Interactions and Their Roles in Human Disease. *Frontiers in Molecular Biosciences*, *8*, 639666. https://doi.org/10.3389/fmolb.2021.639666

177) Shi, G., Kenney, A. D., Kudryashova, E., Zani, A., Zhang, L., Lai, K. K., Hall-Stoodley, L., Robinson, R. T., Kudryashov, D. S., Compton, A. A., & Yount, J. S. (2021). Opposing activities of IFITM proteins in SARS-CoV-2 infection. *The EMBO Journal*, *40*(3), e106501. https://doi.org/10.15252/embj.2020106501

178) Shi, J.-H., & Sun, S.-C. (2018). Tumor Necrosis Factor Receptor-Associated Factor Regulation of Nuclear Factor κB and Mitogen-Activated Protein Kinase Pathways. *Frontiers in Immunology*, *9*, 1849. https://doi.org/10.3389/fimmu.2018.01849

179) Shin, D., Mukherjee, R., Grewe, D., Bojkova, D., Baek, K., Bhattacharya, A., Schulz, L., Widera, M., Mehdipour, A. R., Tascher, G., Geurink, P. P., Wilhelm, A., Van Der Heden Van Noort, G. J., Ovaa, H., Müller, S., Knobeloch, K.-P., Rajalingam, K., Schulman, B. A., Cinatl, J., … Dikic, I. (2020). Papain-like protease regulates SARS-CoV-2 viral spread and innate immunity. *Nature*, *587*(7835), 657–662. https://doi.org/10.1038/s41586-020-2601-5

180) Shriver, Z., Capila, I., Venkataraman, G., & Sasisekharan, R. (2012). Heparin and Heparan Sulfate: Analyzing Structure and Microheterogeneity. In R. Lever, B. Mulloy, & C. P. Page (Eds.), *Heparin—A Century of Progress* (Vol. 207, pp. 159–176). Springer Berlin Heidelberg. https://doi.org/10.1007/978-3-642-23056-1_8

181) Sola, I., Almazán, F., Zúñiga, S., & Enjuanes, L. (2015). Continuous and Discontinuous RNA Synthesis in Coronaviruses. *Annual Review of Virology*, *2*(1), 265–288. https://doi.org/10.1146/annurev-virology-100114-055218

182) Stertz, S., Reichelt, M., Spiegel, M., Kuri, T., Martínez-Sobrido, L., García-Sastre, A., Weber, F., & Kochs, G. (2007). The intracellular sites of early replication and budding of SARS-coronavirus. *Virology*, *361*(2), 304–315. https://doi.org/10.1016/j.virol.2006.11.027

183) Syed, A. M., Taha, T. Y., Tabata, T., Chen, I. P., Ciling, A., Khalid, M. M., Sreekumar, B., Chen, P.-Y., Hayashi, J. M., Soczek, K. M., Ott, M., & Doudna, J. A. (2021a). *Rapid assessment of SARS-CoV-2–evolved variants using virus-like particles*.

184) Syed, A. M., Taha, T. Y., Tabata, T., Chen, I. P., Ciling, A., Khalid, M. M., Sreekumar, B., Chen, P.-Y., Hayashi, J. M., Soczek, K. M., Ott, M., & Doudna, J. A. (2021b). *Rapid assessment of SARS-CoV-2–evolved variants using virus-like particles*. 8.

185) Takeuchi, O., & Akira, S. (2009). Innate immunity to virus infection. *Immunological Reviews*, *227*(1), 75–86. https://doi.org/10.1111/j.1600-065X.2008.00737.x

186) Tavares, R. D. C. A., Mahadeshwar, G., Wan, H., Huston, N. C., & Pyle, A. M. (2021). The Global and Local Distribution of RNA Structure throughout the SARS-CoV-2 Genome. *Journal of Virology*, *95*(5), e02190-20. https://doi.org/10.1128/JVI.02190-20

187) Te Velthuis, A. J. W., Van Den Worm, S. H. E., & Snijder, E. J. (2012). The SARS-coronavirus nsp7+nsp8 complex is a unique multimeric RNA polymerase capable of both de novo initiation and primer extension. *Nucleic Acids Research*, *40*(4), 1737–1747. https://doi.org/10.1093/nar/gkr893

188) Terasaki, K., Narayanan, K., & Makino, S. (2023). Identification of a 1.4-kb-Long Sequence Located in the nsp12 and nsp13 Coding Regions of SARS-CoV-2 Genomic RNA That Mediates Efficient Viral RNA Packaging. *Journal of Virology*, *97*(7), e00659-23. https://doi.org/10.1128/jvi.00659-23

189) Thakur, J., & Henikoff, S. (2020). Architectural RNA in chromatin organization. *Biochemical Society Transactions*, *48*(5), 1967–1978. https://doi.org/10.1042/BST20191226

190) Thompson, S., Martínez-Burgo, B., Sepuru, K., Rajarathnam, K., Kirby, J., Sheerin, N., & Ali, S. (2017). Regulation of Chemokine Function: The Roles of GAG-Binding and Post-Translational Nitration. *International Journal of Molecular Sciences*, *18*(8), 1692. https://doi.org/10.3390/ijms18081692

191) Thoms, M., Buschauer, R., Ameismeier, M., Koepke, L., Denk, T., Hirschenberger, M., Kratzat, H., Hayn, M., Mackens-Kiani, T., Cheng, J., Straub, J. H., Stürzel, C. M., Fröhlich, T., Berninghausen, O., Becker, T., Kirchhoff, F., Sparrer, K. M. J., & Beckmann, R. (2020). *Structural basis for translational shutdown and immune evasion by the Nsp1 protein of SARS-CoV-2*.

192) Thoresen, D., Wang, W., Galls, D., Guo, R., Xu, L., & Pyle, A. M. (2021). The molecular mechanism of RIG-I activation and signaling. *Immunological Reviews*, *304*(1), 154–168. https://doi.org/10.1111/imr.13022

193) Tompa, P., & Csermely, P. (2004). The role of structural disorder in the function of RNA and protein chaperones. *The FASEB Journal*, *18*(11), 1169–1175. https://doi.org/10.1096/fj.04-1584rev

194) Tsuchihashi, Z., Khosla, M., & Herschlag, D. (1993). Protein Enhancement of Hammerhead Ribozyme Catalysis. *Science*, *262*(5130), 99–102. https://doi.org/10.1126/science.7692597

195) Vallet, S. D., Clerc, O., & Ricard-Blum, S. (2021). Glycosaminoglycan–Protein Interactions: The First Draft of the Glycosaminoglycan Interactome. *Journal of Histochemistry & Cytochemistry*, *69*(2), 93–104. https://doi.org/10.1369/0022155420946403

196) Versteeg, G. A., Bredenbeek, P. J., Van Den Worm, S. H. E., & Spaan, W. J. M. (2007). Group 2 coronaviruses prevent immediate early interferon induction by protection of viral RNA from host cell recognition. *Virology*, *361*(1), 18–26. https://doi.org/10.1016/j.virol.2007.01.020

197) VIRELIZIER, J. L., ALLISON, A. C., OXFORD, J. S., & SCHILD, G. C. (1977). Early presence of ribonucleoprotein antigen on surface of influenza virus-infected cells. *Nature*, *266*(5597), 52–54. https://doi.org/10.1038/266052a0

198) Viswanathan, T., Arya, S., Chan, S.-H., Qi, S., Dai, N., Misra, A., Park, J.-G., Oladunni, F., Kovalskyy, D., Hromas, R. A., Martinez-Sobrido, L., & Gupta, Y. K. (2020). Structural basis of RNA cap modification by SARS-CoV-2. *Nature Communications*, *11*(1), 3718. https://doi.org/10.1038/s41467-020-17496-8

199) V'kovski, P., Kratzel, A., Steiner, S., Stalder, H., & Thiel, V. (2021). Coronavirus biology and replication: Implications for SARS-CoV-2. *Nature Reviews Microbiology*, *19*(3), 155–170. https://doi.org/10.1038/s41579-020-00468-6

200) Wajant, H., & Siegmund, D. (2019). TNFR1 and TNFR2 in the Control of the Life and Death Balance of Macrophages. *Frontiers in Cell and Developmental Biology*, *7*, 91. https://doi.org/10.3389/fcell.2019.00091

201) Walls, A. C., Park, Y.-J., Tortorici, M. A., Wall, A., McGuire, A. T., & Veesler, D. (2020). Structure, Function, and Antigenicity of the SARS-CoV-2 Spike Glycoprotein. *Cell*, *181*(2), 281-292.e6. https://doi.org/10.1016/j.cell.2020.02.058

202) Wang, B., Zhang, L., Dai, T., Qin, Z., Lu, H., Zhang, L., & Zhou, F. (2021). Liquid–liquid phase separation in human health and diseases. *Signal Transduction and Targeted Therapy*, *6*(1), 290. https://doi.org/10.1038/s41392-021-00678-1

203) Wang, S., Dai, T., Qin, Z., Pan, T., Chu, F., Lou, L., Zhang, L., Yang, B., Huang, H., Lu, H., & Zhou, F. (2021). Targeting liquid–liquid phase separation of SARS-CoV-2 nucleocapsid protein promotes innate antiviral immunity by elevating MAVS activity. *Nature Cell Biology*, *23*(7), 718–732. https://doi.org/10.1038/s41556-021-00710-0

204) Wang, W., Chen, J., Yu, X., & Lan, H.-Y. (2022). Signaling mechanisms of SARS-CoV-2 Nucleocapsid protein in viral infection, cell death and inflammation. *International Journal of Biological Sciences*, *18*(12), 4704–4713. https://doi.org/10.7150/ijbs.72663

205) Weinstock, L. B., Brook, J. B., Walters, A. S., Goris, A., Afrin, L. B., & Molderings, G. J. (2021). Mast cell activation symptoms are prevalent in Long-COVID. *International Journal of Infectious Diseases*, *112*, 217–226. https://doi.org/10.1016/j.ijid.2021.09.043

206) Weiss, S. R., & Navas-Martin, S. (2005). Coronavirus Pathogenesis and the Emerging Pathogen Severe Acute Respiratory Syndrome Coronavirus. *Microbiology and Molecular Biology Reviews*, *69*(4), 635–664. https://doi.org/10.1128/MMBR.69.4.635-664.2005

207) White, J. P., & Lloyd, R. E. (2012). Regulation of stress granules in virus systems. *Trends in Microbiology*, *20*(4), 175–183. https://doi.org/10.1016/j.tim.2012.02.001

208) Wickham, H. (2023). *forcats: Tools for Working with Categorical Variables (Factors)*. https://CRAN.R-project.org/package=forcats

209) Wickham, H., Averick, M., Bryan, J., Chang, W., McGowan, L. D., François, R., Grolemund, G., Hayes, A., Henry, L., Hester, J., Kuhn, M., Pedersen, T. L., Miller, E., Bache, S. M., Müller, K., Ooms, J., Robinson, D., Seidel, D. P., Spinu, V., … Yutani, H. (2019). Welcome to the tidyverse. *Journal of Open Source Software*, *4*(43), 1686. https://doi.org/10.21105/joss.01686

210) Wickham, H., François, R., Henry, L., Müller, K., & Vaughan, D. (2023). *dplyr: A Grammar of Data Manipulation*. https://CRAN.R-project.org/package=dplyr

211) Willett, B. J., Grove, J., MacLean, O. A., Wilkie, C., De Lorenzo, G., Furnon, W., Cantoni, D., Scott, S., Logan, N., Ashraf, S., Manali, M., Szemiel, A., Cowton, V., Vink, E., Harvey, W. T., Davis, C., Asamaphan, P., Smollett, K., Tong, L., … Thomson, E. C. (2022). SARS-CoV-2 Omicron is an immune escape variant with an altered cell entry pathway. *Nature Microbiology*, *7*(8), 1161–1179. https://doi.org/10.1038/s41564-022-01143-7

212) Witteveldt, J., Blundell, R., Maarleveld, J. J., McFadden, N., Evans, D. J., & Simmonds, P. (2014). The influence of viral RNA secondary structure on interactions with innate host cell defences. *Nucleic Acids Research*, *42*(5), 3314–3329. https://doi.org/10.1093/nar/gkt1291

213) Wolf, Y. I., Kazlauskas, D., Iranzo, J., Lucía-Sanz, A., Kuhn, J. H., Krupovic, M., Dolja, V. V., & Koonin, E. V. (2018). Origins and Evolution of the Global RNA Virome. *mBio*, *9*(6), e02329-18. https://doi.org/10.1128/mBio.02329-18

214) Wong, H. H., Fung, T. S., Fang, S., Huang, M., Le, M. T., & Liu, D. X. (2018). Accessory proteins 8b and 8ab of severe acute respiratory syndrome coronavirus suppress the interferon signaling pathway by mediating ubiquitin-dependent rapid degradation of interferon regulatory factor 3. *Virology*, *515*, 165–175. https://doi.org/10.1016/j.virol.2017.12.028

215) Woo, J., Lee, E. Y., Lee, M., Kim, T., & Cho, Y.-E. (2019). An in vivo cell-based assay for investigating the specific interaction between the SARS-CoV N-protein and its viral RNA packaging sequence. *Biochemical and Biophysical Research Communications*, *520*(3), 499–506. https://doi.org/10.1016/j.bbrc.2019.09.115

216) Woodson, S. A., Panja, S., & Santiago-Frangos, A. (2018a). Proteins That Chaperone RNA Regulation. In G. Storz & K. Papenfort (Eds.), *Regulating with RNA in Bacteria and Archaea* (pp. 383–397). ASM Press. https://doi.org/10.1128/9781683670247.ch22

217) Woodson, S. A., Panja, S., & Santiago-Frangos, A. (2018b). Proteins That Chaperone RNA Regulation. *Microbiology Spectrum*, *6*(4), 6.4.21. https://doi.org/10.1128/microbiolspec.RWR-0026-2018

218) Wu, C., Qavi, A. J., Hachim, A., Kavian, N., Cole, A. R., Moyle, A. B., Wagner, N. D., Sweeney-Gibbons, J., Rohrs, H. W., Gross, M. L., Peiris, J. S. M., Basler, C. F., Farnsworth, C. W., Valkenburg, S. A., Amarasinghe, G. K., & Leung, D. W. (2021). Characterization of SARS-CoV-2 nucleocapsid protein reveals multiple functional consequences of the C-terminal domain. *iScience*, *24*(6), 102681. https://doi.org/10.1016/j.isci.2021.102681

219) Wu, C., Yin, W., Jiang, Y., & Xu, H. E. (2022). Structure genomics of SARS-CoV-2 and its Omicron variant: Drug design templates for COVID-19. *Acta Pharmacologica Sinica*, *43*(12), 3021–3033. https://doi.org/10.1038/s41401-021-00851-w

220) Wu, C.-H., Chen, P.-J., & Yeh, S.-H. (2014). Nucleocapsid Phosphorylation and RNA Helicase DDX1 Recruitment Enables Coronavirus Transition from Discontinuous to Continuous Transcription. *Cell Host & Microbe*, *16*(4), 462–472. https://doi.org/10.1016/j.chom.2014.09.009

221) Wu, J.-L., Kuan, I.-I., Guo, J.-Y., Hsu, W.-C., Tang, W.-C., Chan, H.-J., Chen, Y.-J., Chen, B.-C., Wu, H.-C., & Liao, J. C. (2023). SARS-CoV-2 N protein mediates intercellular nucleic acid dispersion, a feature reduced in Omicron. *iScience*, *26*(2), 105995. https://doi.org/10.1016/j.isci.2023.105995

222) Wu, W., Cheng, Y., Zhou, H., Sun, C., & Zhang, S. (2023). The SARS-CoV-2 nucleocapsid protein: Its role in the viral life cycle, structure and functions, and use as a potential target in the development of vaccines and diagnostics. *Virology Journal*, *20*(1), 6. https://doi.org/10.1186/s12985-023-01968-6

223) Xia, H., Cao, Z., Xie, X., Zhang, X., Chen, J. Y.-C., Wang, H., Menachery, V. D., Rajsbaum, R., & Shi, P.-Y. (2020). Evasion of Type I Interferon by SARS-CoV-2. *Cell Reports*, *33*(1), 108234. https://doi.org/10.1016/j.celrep.2020.108234

224) Xia, H., Wang, P., Wang, G.-C., Yang, J., Sun, X., Wu, W., Qiu, Y., Shu, T., Zhao, X., Yin, L., Qin, C.-F., Hu, Y., & Zhou, X. (2015). Human Enterovirus Nonstructural Protein 2CATPase Functions as Both an RNA Helicase and ATP-Independent RNA Chaperone. *PLOS Pathogens*, *11*(7), e1005067. https://doi.org/10.1371/journal.ppat.1005067

225) Xia, S., Lan, Q., Su, S., Wang, X., Xu, W., Liu, Z., Zhu, Y., Wang, Q., Lu, L., & Jiang, S. (2020). The role of furin cleavage site in SARS-CoV-2 spike protein-mediated membrane fusion in the presence or absence of trypsin. *Signal Transduction and Targeted Therapy*, *5*(1), 92. https://doi.org/10.1038/s41392-020-0184-0

226) Xue, S., Zhou, F., Zhao, T., Zhao, H., Wang, X., Chen, L., Li, J., & Luo, S.-Z. (2022). Phase separation on cell surface facilitates bFGF signal transduction with heparan sulphate. *Nature Communications*, *13*(1), 1112. https://doi.org/10.1038/s41467-022-28765-z

227) Yaron, T. M., Heaton, B. E., Levy, T. M., Johnson, J. L., Jordan, T. X., Cohen, B. M., Kerelsky, A., Lin, T.-Y., Liberatore, K. M., Bulaon, D. K., Van Nest, S. J., Koundouros, N., Kastenhuber, E. R., Mercadante, M. N., Shobana-Ganesh, K., He, L., Schwartz, R. E., Chen, S., Weinstein, H., … Heaton, N. S. (2022). Host protein kinases required for SARS-CoV-2 nucleocapsid phosphorylation and viral replication. *Science Signaling*, *15*(757), eabm0808. https://doi.org/10.1126/scisignal.abm0808

228) Ye, Q., West, A. M. V., Silletti, S., & Corbett, K. D. (2020). Architecture and self-assembly of the SARS-CoV-2 nucleocapsid protein. *Protein Science*, *29*(9), 1890–1901. https://doi.org/10.1002/pro.3909

229) Yu, H., Guan, F., Miller, H., Lei, J., & Liu, C. (2023). The role of SARS-CoV-2 nucleocapsid protein in antiviral immunity and vaccine development. *Emerging Microbes & Infections*, *12*(1), e2164219. https://doi.org/10.1080/22221751.2022.2164219

230) Zachrdla, M., Savastano, A., Ibáñez De Opakua, A., Cima-Omori, M., & Zweckstetter, M. (2022). Contributions of the N-terminal intrinsically disordered region of the severe acute respiratory syndrome coronavirus 2 nucleocapsid protein to RNA-induced phase separation. *Protein Science*, *31*(9), e4409. https://doi.org/10.1002/pro.4409

231) Zeng, W., Liu, G., Ma, H., Zhao, D., Yang, Y., Liu, M., Mohammed, A., Zhao, C., Yang, Y., Xie, J., Ding, C., Ma, X., Weng, J., Gao, Y., He, H., & Jin, T. (2020). Biochemical characterization of SARS-CoV-2 nucleocapsid protein. *Biochemical and Biophysical Research Communications*, *527*(3), 618–623. https://doi.org/10.1016/j.bbrc.2020.04.136

232) Zhang, K., Miorin, L., Makio, T., Dehghan, I., Gao, S., Xie, Y., Zhong, H., Esparza, M., Kehrer, T., Kumar, A., Hobman, T. C., Ptak, C., Gao, B., Minna, J. D., Chen, Z., García-Sastre, A., Ren, Y., Wozniak, R. W., & Fontoura, B. M. A. (2021). Nsp1 protein of SARS-CoV-2 disrupts the mRNA export machinery to inhibit host gene expression. *Science Advances*, *7*(6), eabe7386. https://doi.org/10.1126/sciadv.abe7386

233) Zhang, Q., Chen, C. Z., Swaroop, M., Xu, M., Wang, L., Lee, J., Wang, A. Q., Pradhan, M., Hagen, N., Chen, L., Shen, M., Luo, Z., Xu, X., Xu, Y., Huang, W., Zheng, W., & Ye, Y. (2020). Heparan sulfate assists SARS-CoV-2 in cell entry and can be targeted by approved drugs in vitro. *Cell Discovery*, *6*(1), 80. https://doi.org/10.1038/s41421-020-00222-5

234) Zhang, W., Ma, Z., Wu, Y., Shi, X., Zhang, Y., Zhang, M., Zhang, M., Wang, L., & Liu, W. (2021). SARS-CoV-2 3C-like protease antagonizes interferon-beta production by facilitating the degradation of IRF3. *Cytokine*, *148*, 155697. https://doi.org/10.1016/j.cyto.2021.155697

235) Zhao, F., Lu, J., Lu, B., Qin, T., Wang, X., Hou, X., Meng, F., Xu, X., Li, T., Zhou, H., Zhang, J., Kan, B., Huang, Y., Zhang, Z., & Xiao, D. (2021). A Novel Strategy for the Detection of SARS-CoV-2 Variants Based on Multiplex PCR-Mass Spectrometry Minisequencing Technology. *Microbiology Spectrum*, *9*(3), e01267-21. https://doi.org/10.1128/Spectrum.01267-21

236) Zhao, H., Nguyen, A., Wu, D., Li, Y., Hassan, S. A., Chen, J., Shroff, H., Piszczek, G., & Schuck, P. (2022). Plasticity in structure and assembly of SARS-CoV-2 nucleocapsid protein. *PNAS Nexus*, *1*(2), pgac049. https://doi.org/10.1093/pnasnexus/pgac049

237) Zhao, J., Qiu, J., Aryal, S., Hackett, J., & Wang, J. (2020). The RNA Architecture of the SARS-CoV-2 3′-Untranslated Region. *Viruses*, *12*(12), 1473. https://doi.org/10.3390/v12121473

238) Zhao, X., Zheng, S., Chen, D., Zheng, M., Li, X., Li, G., Lin, H., Chang, J., Zeng, H., & Guo, J.-T. (2020). LY6E Restricts Entry of Human Coronaviruses, Including Currently Pandemic SARS-CoV-2. *Journal of Virology*, *94*(18), e00562-20. https://doi.org/10.1128/JVI.00562-20

239) Zhao, Y., Sui, L., Wu, P., Wang, W., Wang, Z., Yu, Y., Hou, Z., Tan, G., Liu, Q., & Wang, G. (2021). A dual-role of SARS-CoV-2 nucleocapsid protein in regulating innate immune response. *Signal Transduction and Targeted Therapy*, *6*(1), 331. https://doi.org/10.1038/s41392-021-00742-w

240) Zheng, Y., Deng, J., Han, L., Zhuang, M.-W., Xu, Y., Zhang, J., Nan, M.-L., Xiao, Y., Zhan, P., Liu, X., Gao, C., & Wang, P.-H. (2022). SARS-CoV-2 NSP5 and N protein counteract the RIG-I signaling pathway by suppressing the formation of stress granules. *Signal Transduction and Targeted Therapy*, *7*(1), 22. https://doi.org/10.1038/s41392-022-00878-3

241) Zheng, Y., Zhuang, M.-W., Han, L., Zhang, J., Nan, M.-L., Zhan, P., Kang, D., Liu, X., Gao, C., & Wang, P.-H. (2020). Severe acute respiratory syndrome coronavirus 2 (SARS-CoV-2) membrane (M) protein inhibits type I and III interferon production by targeting RIG-I/MDA-5 signaling. *Signal Transduction and Targeted Therapy*, *5*(1), 299. https://doi.org/10.1038/s41392-020-00438-7

242) Zheng, Z.-Q., Wang, S.-Y., Xu, Z.-S., Fu, Y.-Z., & Wang, Y.-Y. (2021). SARS-CoV-2 nucleocapsid protein impairs stress granule formation to promote viral replication. *Cell Discovery*, *7*(1), 38. https://doi.org/10.1038/s41421-021-00275-0

243) Zhou, S., Lv, P., Li, M., Chen, Z., Xin, H., Reilly, S., & Zhang, X. (2023). SARS-CoV-2 E protein: Pathogenesis and potential therapeutic development. *Biomedicine & Pharmacotherapy*, *159*, 114242. https://doi.org/10.1016/j.biopha.2023.114242

244) Zhu, N., Zhang, D., Wang, W., Li, X., Yang, B., Song, J., Zhao, X., Huang, B., Shi, W., Lu, R., Niu, P., Zhan, F., Ma, X., Wang, D., Xu, W., Wu, G., Gao, G. F., & Tan, W. (2020). A Novel Coronavirus from Patients with Pneumonia in China, 2019. *New England Journal of Medicine*, *382*(8), 727–733. https://doi.org/10.1056/NEJMoa2001017

245) Ziebuhr, J. (2005). The Coronavirus Replicase. In L. Enjuanes (Ed.), *Coronavirus Replication and Reverse Genetics* (Vol. 287, pp. 57–94). Springer Berlin Heidelberg. https://doi.org/10.1007/3-540-26765-4_3

246) Zinzula, L., Basquin, J., Bohn, S., Beck, F., Klumpe, S., Pfeifer, G., Nagy, I., Bracher, A., Hartl, F. U., & Baumeister, W. (2021). High-resolution structure and biophysical characterization of the nucleocapsid phosphoprotein dimerization domain from the Covid-19 severe acute respiratory syndrome coronavirus 2. *Biochemical and Biophysical Research Communications*, *538*, 54–62. https://doi.org/10.1016/j.bbrc.2020.09.131

247) Znaidia, M., Demeret, C., Van Der Werf, S., & Komarova, A. V. (2022). Characterization of SARS-CoV-2 Evasion: Interferon Pathway and Therapeutic Options. *Viruses*, *14*(6), 1247. https://doi.org/10.3390/v14061247

248) Zúñiga, S., Cruz, J. L. G., Sola, I., Mateos-Gómez, P. A., Palacio, L., & Enjuanes, L. (2010). Coronavirus Nucleocapsid Protein Facilitates Template Switching and Is Required for Efficient Transcription. *Journal of Virology*, *84*(4), 2169–2175. https://doi.org/10.1128/JVI.02011-09

249) Zúñiga, S., Sola, I., Cruz, J. L. G., & Enjuanes, L. (2009). Role of RNA chaperones in virus replication. *Virus Research*, *139*(2), 253–266. https://doi.org/10.1016/j.virusres.2008.06.015

250) Zúñiga, S., Sola, I., Moreno, J. L., Sabella, P., Plana-Durán, J., & Enjuanes, L. (2007a). Coronavirus nucleocapsid protein is an RNA chaperone. *Virology*, *357*(2), 215–227. https://doi.org/10.1016/j.virol.2006.07.046

6. List of figures

7. List of tables

8. Abbreviations

α	Alpha
γ	Gamma
δ	Delta
β	Beta
°C	Degree Celsius
Amp	Ampicillin
APS	Ammonium persulfate
ATP	Adenosine-triphosphate
BSA	Bovine Serum Albumin
C-terminus	Carboxy-terminus
Cam	Chloramphenicol
CoV	Coronavirus
COVID-19	Coronavirus disease 2019
CTD	C-terminal domain
CV	Column volume
Cy	Cyanin
DAMP	Danger-associated molecular pattern
DLS	Dynamic light scattering
DMSO	Dimethylsulfoxide
DMV	Double membrane vesicles
DNA	Desoxyribonucleic acid
dNTP	2′-desoxyribonucleotide-triphosphate
dsRNA	Double-stranded RNA
E	Envelope
E. coli	*Escherichia coli*
EDTA	Ethylenediaminetetraacetic acid
EMSA	Electrophoretic mobility shift assay
ER	Endoplasmic reticulum
ERGIC	ER-to-Golgi intermediate compartment
EtOH	Ethanol
Fw	Forward
g	Gram
GAG	Glycosaminoglycan
GFP	Green fluorescent protein
gRNA	Genomic RNA
h	Hour
H	Heparin
hCoV	Human CoV
HCV	Hepatitis C virus
His-tag	Histidine tag
HIV-1	Human immunodeficiency virus type 1
HS	Heparan sulfate
HSPG	Heparan sulfate proteoglycan
IDR	Intrinsically disordered region
IPTG	Isopropylthigalactoside
K_D	Dissociation constant

kDa	Kilodalton
LB	Lysogeny broth
LLPS	Liquid-liquid phase separation
LLPS	Liquid-liquid phase separation
M	Molar
M (protein)	Membrane
mAU	Milli-absorbance-units
mg	Milligram
MHV	Mouse hepatitis virus
min	Minute
ml	Milliliter
mM	Millimolar
MNase	Micrococcal nuclease
mRNA	Messenger RNA
MST	MicroScale Thermophoresis
MW	Molecular weight
MWCO	Molecular weight cut off
N (protein)	Nucleocapsid
N-terminus	Amino-terminus
nanoDSF	Nano differential scanning fluorimetry
Ni-NTA	Nickel-nitroacetic acid
nl	nanoliter
nM	Nanomolar
nm	Nanometer
Nsp	Non-structural protein
ORF	Open reading frame
PAA	Poly acryl amide
PAGE	Polyacrylamide gel electrophoresis
PAMP	Pathogen-associated molecular pattern
PBS	Phosphate-buffered saline
PCR	Polymerase chain reaction
PS	Packaging signal
RBD	RNA binding domain
Rcf	Relative centrifugal force
RdRp	RNA-dependent RNA polymerase
Rev	Reverse
RLR	RIG-I-like receptor
RNA	Ribonucleic acid
RO	Replication organelle
Rpm	Rounds per minute
RT	Room temperature
RTC	Replication transcription complex
s	Second
S (protein)	Spike
SARS-CoV-2	Severe acute respiratory syndrome-CoV-2
SD	Standard deviation
SDS	Sodium dodecyl sulfate
sgRNA	Subgenomic RNA

SL	Stem loop
ssRNA	Single-stranded RNA
Taq	*Thermus aquaticus*
Tat	Transactivator of transcription
TBE	Tris Borate EDTA
TCEP	Tris(2-carboxyethyl)-phosphine
TEMED	N,N,N′,N′-tetramethylethylenediamine
TLR	Toll-like receptor
Tris	Tris(hydroxymethyl)aminomethane
TRS	Transcription regulatory sequence
U	Unit
UTR	Untranslated region
vRNP	Viral ribonucleic particle
w/v	Weight per volume
WT	Wild type (Wuhan)
κ	Kappa
µl	Microliter
µM	Micromolar

9. Amino acids representation codes

Amino acid	Three letter code	Single letter code
Alanine	Ala	A
Arginine	Arg	R
Asparagine	Asn	N
Aspartate	Asp	D
Cysteine	Cys	C
Glutamate	Glu	E
Glutamine	Gln	Q
Glycine	Gly	G
Histidine	His	H
Isoleucine	Ile	I
Leucine	Leu	L
Lysine	Lys	K
Methionine	Met	M
Phenylalanine	Phe	F
Proline	Pro	P
Serine	Ser	S
Threonine	Thr	T
Tryptophan	Trp	W
Tyrosine	Tyr	Y
Valine	Val	V

10. Supplement

10.1. Supplementary Tables

Supplementary Table 1: K_D values of RNA3 binding of N (truncation) proteins

Name	ssRNA3		dsRNA3	
	K_D (nM)	K_D confidence (nM)	K_D (nM)	K_D confidence (nM)
N_WT	1259	+/- 722	647	+/- 151
N_BA.5	270	+/- 126	139	+/- 48
N_IRIC	465	+/- 200	191	+/- 51
N_RICI	654	+/- 396	325	+/- 132
N_RIC	343	+/- 189	228	+/- 89
N_IRI	456	+/- 142	2947	+/- 1090
N_RI	710	+/- 379	3842	+/- 1398
N_IC	7781	+/- 1284	3293	+/- 1452
N_CI	-	-	4572	+/- 1544
N_RBD	-	-	-	-
N_CTD	4288	+/- 427	2554	+/- 567
N_WT_PM	6156	+/- 4058		
N_BA.5_PM	1267	+/- 635		

Supplementary Table 2: K_D values of RNA20 binding of N (truncation) proteins

Name	ssRNA20		dsRNA20	
	K_D (nM)	K_D confidence (nM)	K_D (nM)	K_D confidence (nM)
N_WT	425	+/- 186	398	+/- 157
N_BA.5	840	+/- 463	632	+/- 295
N_RIC	135	+/- 56	442	+/- 179
N_RI	321	+/- 150	1587	+/- 723
N_RBD	-	-	-	-
N_CTD	8535	+/- 4519	3300	+/- 394

Supplementary Table 3: K_D values of RNA22 binding of N (truncation) proteins

Name	ssRNA22		dsRNA22	
	K_D (nM)	K_D confidence (nM)	K_D (nM)	K_D confidence (nM)
N_WT	291	+/- 121	344	+/- 132
N_BA.5	601	+/- 342	634	+/- 257
N_RIC	243	+/- 147	406	+/- 68
N_RI	368	+/- 129	3341	+/- 1206
N_RBD	-	-	-	-
N_CTD	2731	+/- 588	1845	+/- 252

10.2. Supplementary Figures

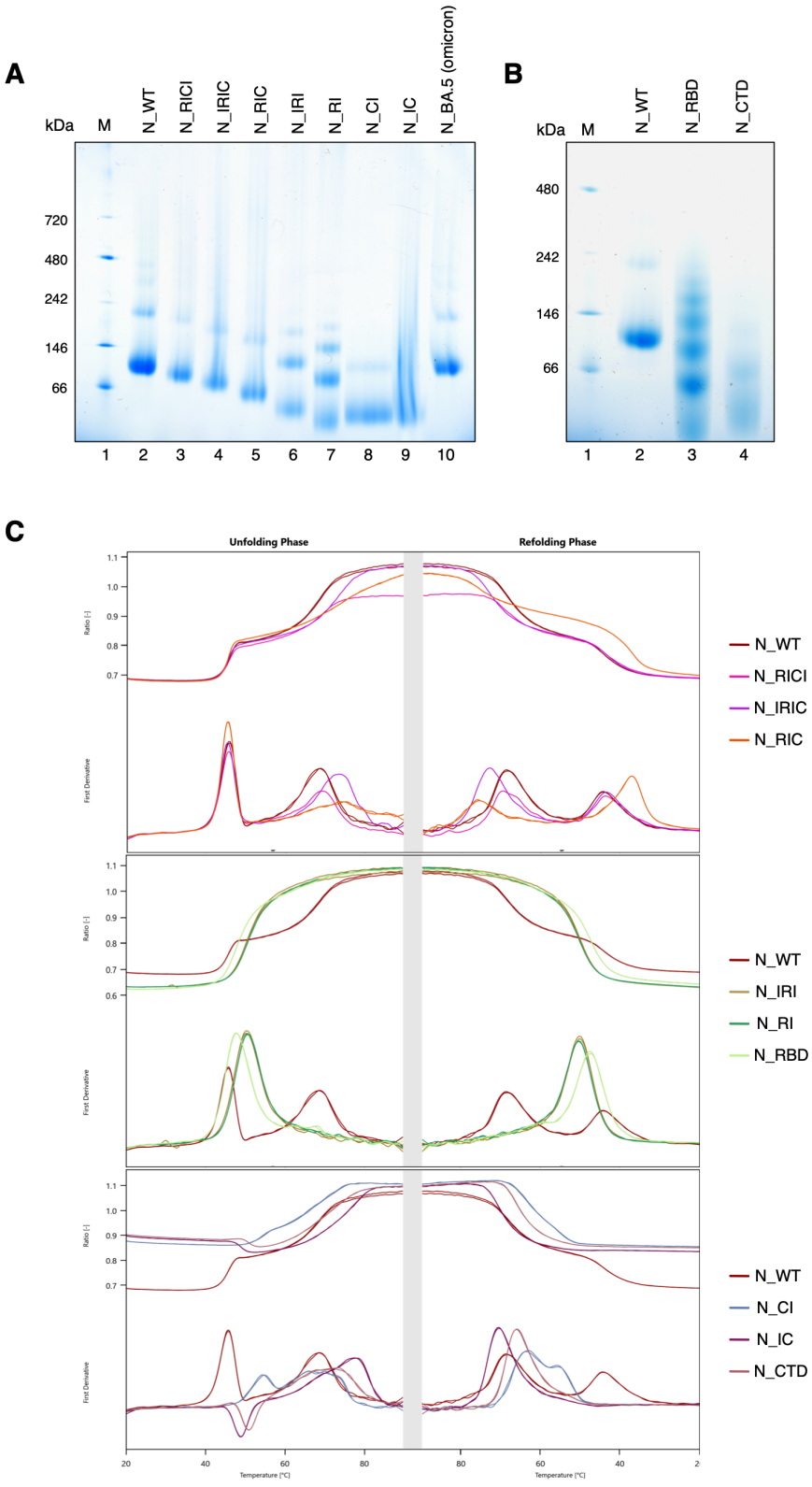

Supplementary Figure 1: native PAA gels and nanoDSF traces of N truncation proteins

(A) Native PAA gel of N_WT and its respective truncation proteins, as well as N_BA.5. A total of 2 µg of each protein was applied and protein oligomerization was observed for all of them. **(B)** Native PAA gel of N_WT and its structured domains N_RBD and N_CTD. A total of 2 µg of each protein was applied and each structured domain exhibited protein oligomerization. **(C)** Unfolding and refolding properties of SARS-CoV-2 N (truncation) proteins related to Figure 2C. The refolding properties of the proteins are consistent with their unfolding properties.

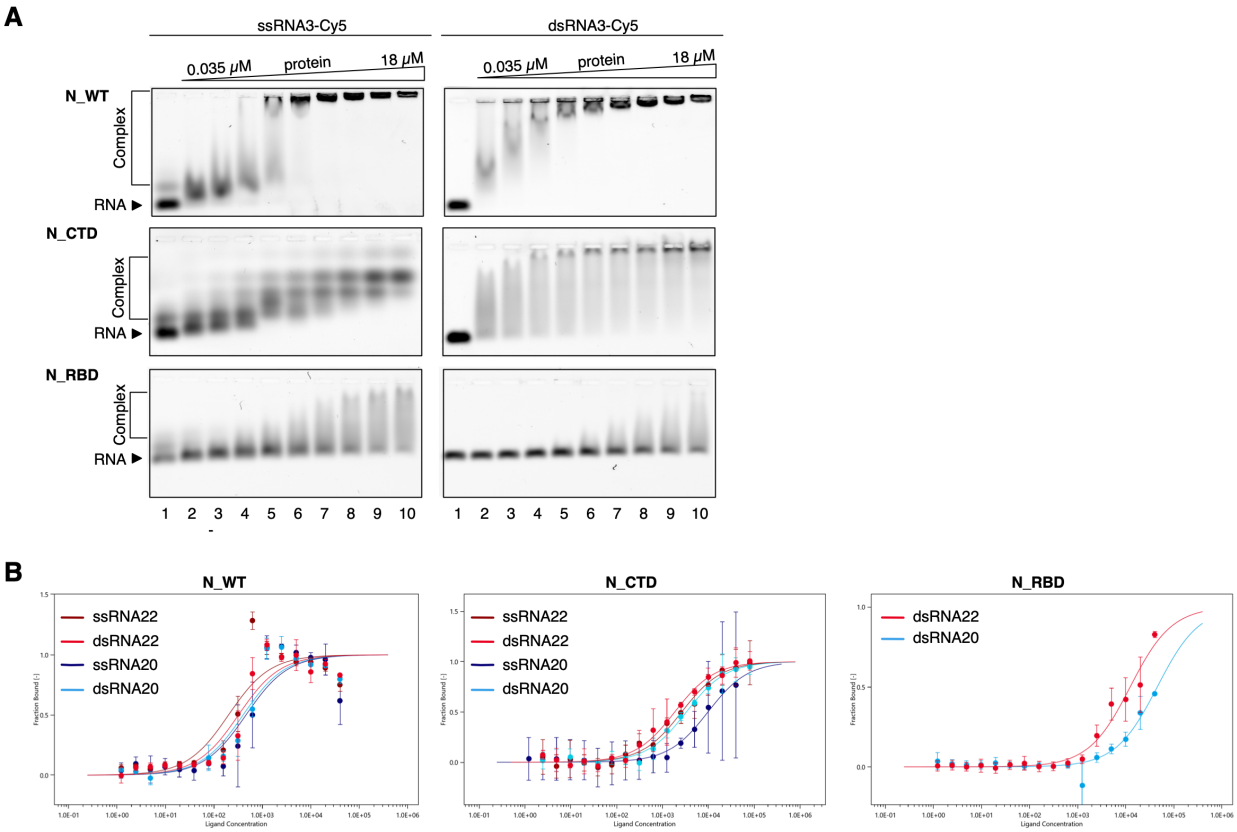

Supplementary Figure 2: ssRNA and dsRNA binding abilities of SARS-CoV-2 N, RBD, and CTD

(A) The ssRNA3 and dsRNA3 binding properties of N_WT and its respective structured domains N_CTD and N_RBD were analyzed using an EMSA approach. A constant amount of 40 nM Cy5-labeled ssRNA3 or dsRNA3 was mixed with varying concentrations (0.035 – 18 µM) of protein and incubated for 90 minutes. N_WT and N_CTD demonstrated high efficiency in binding to both ssRNA3 and dsRNA3, with a slight preference for dsRNA. The RBD domain exhibited only weak RNA binding. **(B)** The binding affinities of N_WT, N_CTD and N_RBD to either ssRNA20 (dark blue), dsRNA20 (light blue), ssRNA22 (dark red), and dsRNA22 (light red) were determined using MST. The plots present the ligand (protein) concentration on the x-axis and the fraction bound on the y-axis. The fitted K_D values for N_WT are as follows: 425 +/- 186 nM (ssRNA20), 398 +/- 157 nM (dsRNA20), 291 +/- 121 nM (ssRNA22) and 344 +/- 132 nM (dsRNA22). Fitted K_D values for N_CTD are: 8535 +/- 4510 nM (ssRNA20), 3300 +/- 394 nM 8 (dsRNA20), 2731 +/- 588 nM (ssRNA22) and 1845 +/- 252 nM (dsRNA22). For N_RBD, only the binding to dsRNA could only be fitted, as indicated.

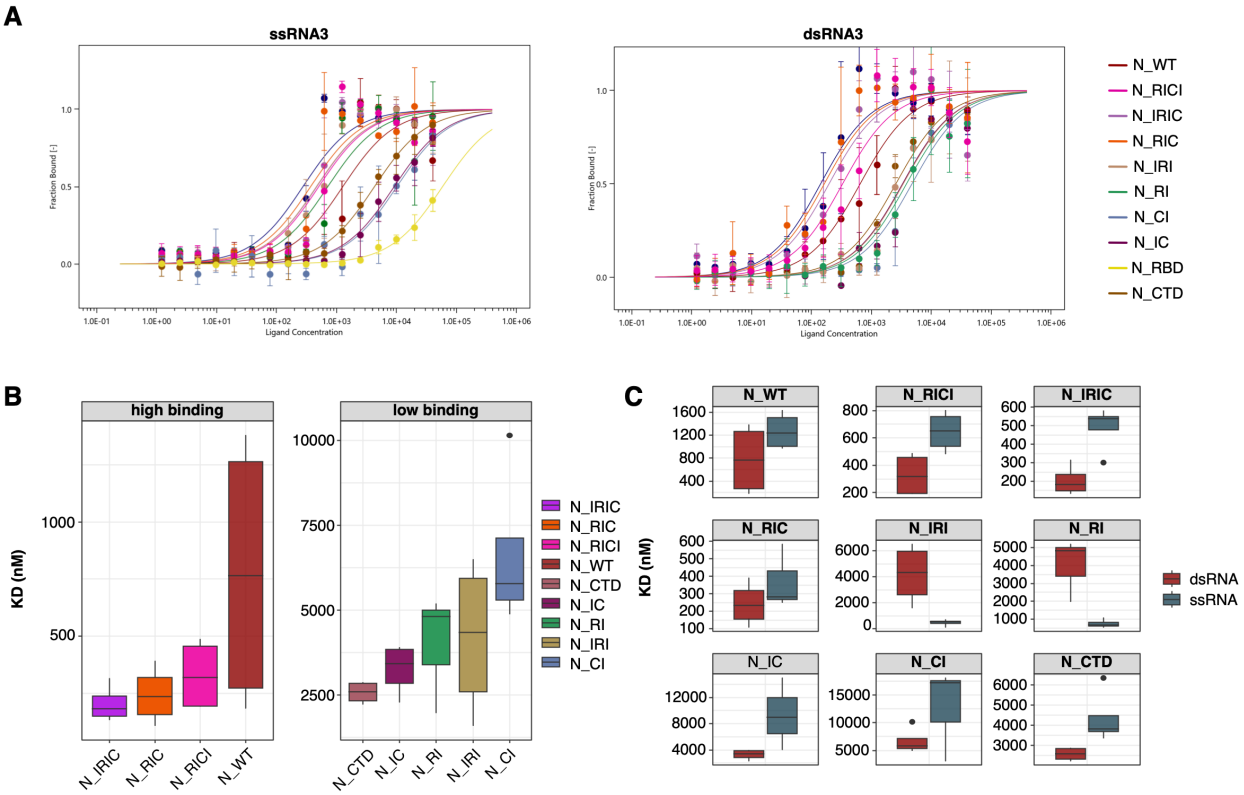

Supplementary Figure 3: RNA binding properties of all generated N truncation proteins

(A) The binding affinities of all N (truncation) proteins (N_WT (dark red), N_RICI (pink), N_IRIC (purple), N_RIC (orange), N_IRI (beige), N_RI (green), N_CI (blue-grey), N_IC (dark purple), N_RBD (yellow) and N_CTD (brown)) to either ssRNA3 (left) or dsRNA3 (right) were determined using MST. All K_D values and the K_D confidence are provided in supplementary table 1. Plots present the ligand (protein) concentration on the x-axis and the fraction bound on the y-axis. **(B)** Comparative boxplot of N (truncation) proteins towards dsRNA3 based on MST data. Each boxplot contains four MST runs with their individual K_D values. Each boxplot represents the interquartile range (IQR), with the median indicated by a horizontal line inside the box. Upper and lower whiskers extend to a maximum of 1.5 times above and below the upper and lower quartiles, respectively. Outliers beyond this range are depicted as individual data points. Proteins are divided into "high binding" and "low binding" groups according to their K_D. Proteins with no or only indicated binding are excluded from the analysis. The x-axis of the plots gives the protein while the K_D is given on the y-axis. Dimensions of the y-axis are different for the groups. Proteins are arranged according to their median K_D value. Only N_IRIC (purple), N_RICI (pink) and N_RIC (orange) display comparable dsRNA binding affinity to N_WT, all other truncation proteins display a reduced affinity towards dsRNA. **(C)** Comparative boxplot of the RNA-binding N (truncation) proteins towards ssRNA3 (blue-grey) and dsRNA3 (dark red), based on MST data. Each boxplot contains four MST runs. Each boxplot represents the interquartile range (IQR), with the median indicated by a horizontal line inside the box. Upper and lower whiskers extend to a maximum of 1.5 times above and below the upper and lower quartiles, respectively. The x axis of the plots gives the RNA while the K_D is given on the y-axis. Dimensions of the y-axis are different for the individual proteins. Except for N_IRI and N_RI, which exhibit higher affinity to ssRNA, dsRNA is the preferred substrate for most N protein truncation proteins.

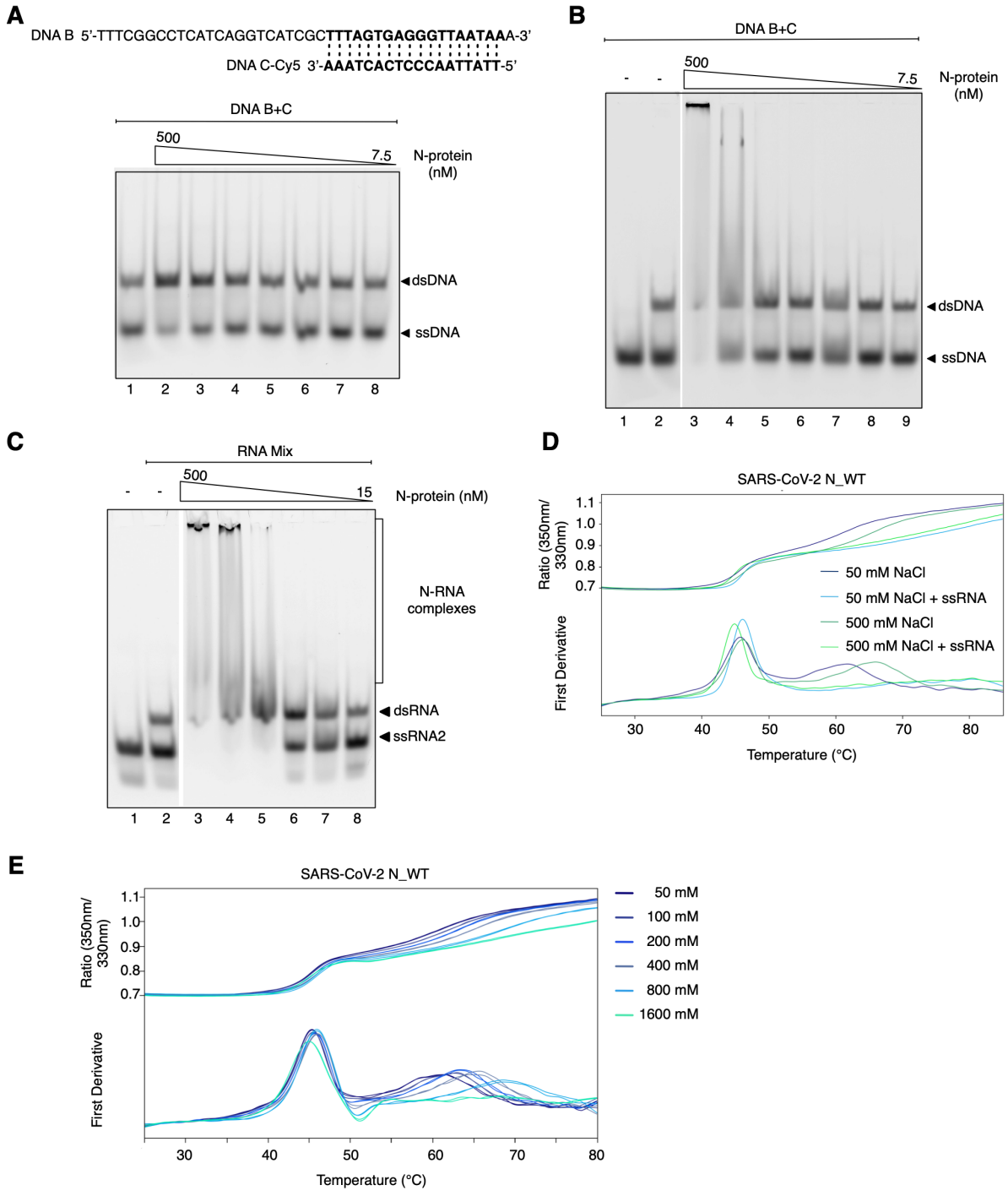

Supplementary Figure 4: DNA chaperone activity, RNA binding and influence of ionic surroundings to N

(A) Analysis of N_WT RNA chaperone activity. Complementary ssDNAB and ssDNAC-Cy5 were mixed and incubated with decreasing N_WT concentrations (lanes 2-8)..Following completion of the reaction, samples were applied to a native 6% PAA gel. RNA hybridization was enhanced in presence of high concentrations (250 nM, 500 nM) of SARS-CoV-2 N protein. Lane 1 served as dsDNAC-Cy5 control. **(B)** Binding of the N_WT towards hybridized dsDNAC (lane 2). A protein concentration range of 500 – 15 nM (lanes 3-8) were applied to the DNA Mix. The binding shift can be observed starting at 250 nM N_WT (lane 4). **(C)** Binding of N_WT towards hybridized dsRNA2 (lane 2). A protein concentration range of 500 – 15 nM (lanes 3-8) was applied to the RNA mix. A binding shift can be observed starting at 125 nM N_WT (lane 5). **(D)** N_WT protein stability was assessed with nanoDSF over a temperature range from 20 - 85°C. Stability was analyzed at 50 mM (blue curves) and 500 mM (green curves) NaCl in absence (dark blue/dark green) or presence (light blue/light green) of ssRNA. In each case, RNA binding was observed independently of salt concentration. **(E)** Protein stability of N_WT was assessed using nanoDSF with a temperature gradient from 25 – 80°C. under increasing NaCl concentrations from 50 – 1600 mM. The stability of the CTD was found to be affected by high salt concentration.

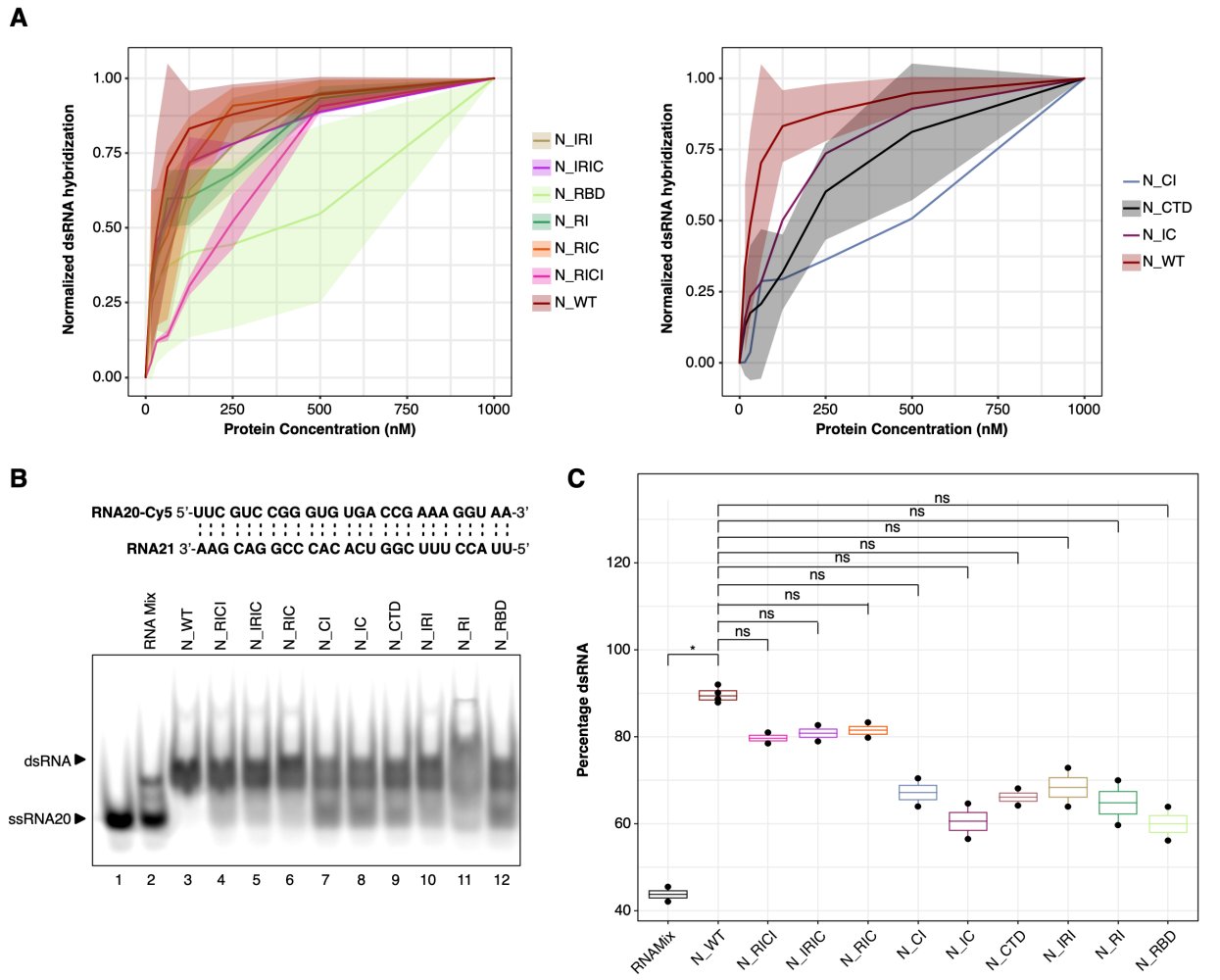

Supplementary Figure 5: RNA chaperone activity of N truncation proteins with ssRNA20/ssRNA21

(A) Chaperone activity of individual N truncation proteins with ssRNA2/ssRNA3 was titrated over a protein concentration range from 0 – 1000 nM. Two individual chaperone assay gels (except for N_CI and N_IC with only one each) were analyzed according to their dsRNA band intensities using Fiji and plotted against the protein concentration. Each dataset was normalized to the RNA Mix control as a baseline. The normalized values are represented on the y-axis and the protein concentration is indicated on the x-axis. N truncation proteins still containing the RBD are displayed in the left plot, while proteins without RBD are shown in the right plot in comparison with N_WT. For each protein, the normalized mean dsRNA hybridization is represented as a thick line and the standard deviation as a ribbon. **(B)** RNA chaperone assay comparing the activity of N truncation proteins at equimolar protein concentrations. An RNA Mix (ssRNA20-Cy5, ssRNA21) was incubated in the absence (lane 2) or presence (lanes 3-12) of 250 nM N (truncation) protein for 3 min at 25°C. Afterwards, samples were analyzed on a 6% native PAA gel and visualized by fluorescent readout using the Typhoon™ FLA 9500 reader (GE Healthcare). The RNA Mix (lane 2) served as a control for spontaneous RNA hybridization, while N_WT (lane 3) represented the fully hybridized state. Additional complete RNA annealing was observed for N_RICI (lane 4), N_IRIC (lane 5) and N_RIC (lane 6), although a visible smear at ssRNA height. Partial hybridization was detectable for N_CI (lane 7), N_IC (lane 8),N_CTD (lane 9), N_IRI (lane 10), N_RI (lane 1), and N_RBD (lane 12). **(C)** Boxplot representing the percentage of hybridized dsRNA. Band intensities were analyzed using Fiji. Each boxplot contains two biological replicates of the chaperone assay. Each boxplot represents the interquartile range (IQR), with the median indicated by a horizontal line inside the box. The upper and lower whiskers extend to a maximum of 1.5 times above and below the upper and lower quartiles, respectively. The x-axis represents the respective N truncation protein, while the percentage of dsRNA is indicated on the y-axis. A significant difference in dsRNA formation was observed between the RNAMix control (black) and N_WT (dark red). Observed differences for the other proteins relative to N_WT were statistically not significant (n.s.). Statistical analysis was performed by applying a t-test using the Benjamini-Hochberg (BH) procedure. 'n.s.' = 0.05 < p; '*' = 0.05 <= p >0.01; '**' = 0.01 <= p > 0.001; '***' = 0.001 <= p > 0.0001; '****' = 0.0001 <= p.

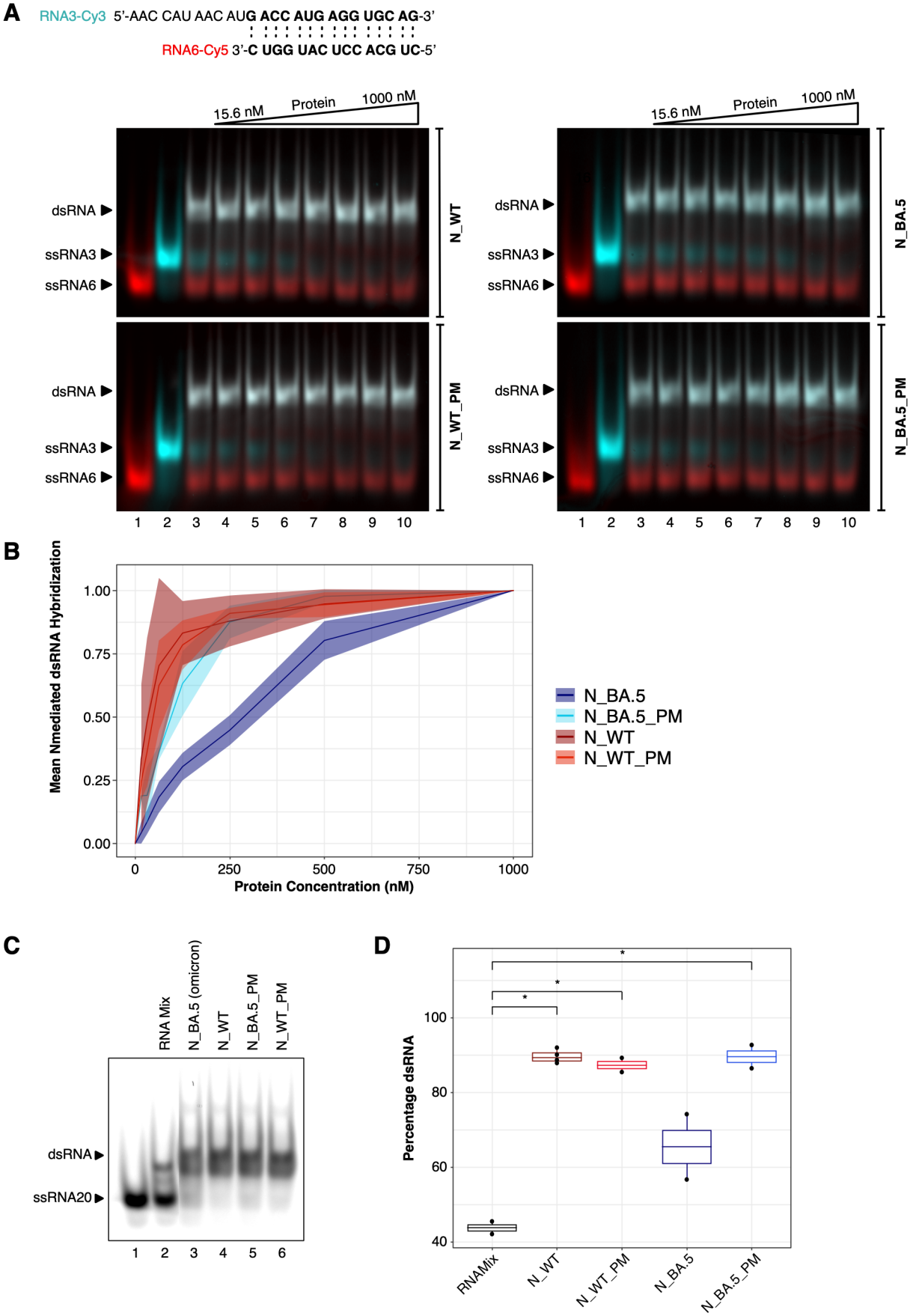

Supplementary Figure 6: Differences in RNA chaperone activity between Wuhan and Omicron BA.5 N and their phosphomimetic variants

(A) N_WT, N_BA.5 and their respective phosphomimetic variants N_WT_PM and N_BA.5_PM were compared in terms of their RNA chaperone activity. The assay was performed with a RNA Mix of ssRNA3-Cy3 and ssRNA6-Cy5,

which was incubated in the presence of increasing protein concentration from 15 – 1000 nM (lanes 4-10). For N_WT and N_WT_PM, complete RNA hybridization could be observed at 125 nM protein (lane 7). For N_BA.5, complete hybridization was detectable starting at 500 nM of protein (lane 9), whereas N_BA.5_PM displayed a complete RNA annealing starting at 125 nM (lane 7). **(B)** dsRNA band intensities of two biological replicates of the chaperone assays for N_WT, N_BA.5, N_WT_PM and N_BA.5_PM were analyzed using Fiji and the normalized dsRNA hybridization values (y-axis) were plotted against the protein concentration (x-axis). Each titration series was normalized to the RNA mix control. Normalized values are represented as a thick line flanked by the standard deviation indicated as a ribbon. N_BA.5 (dark blue) displayed the weakest dsRNA hybridization efficiency. **(C)** RNA chaperone assay comparing the activity of Wuhan and Omicron BA.5 N proteins along with their respective phosphomimetic variants at equimolar protein concentrations. An RNA Mix (ssRNA20-Cy5, ssRNA21) was incubated in the absence (lane 2) or presence of 250 nM N_BA.5 (lane 3), N_WT (lane 4), N_BA.5_PM (lane 5) or N_WT_PM (lane 6) for 3 min at 25°C. Afterwards, samples were analyzed on a 6% native PAA gel and visualized by fluorescent readout using the Typhoon™ FLA 9500 reader (GE Healthcare). RNA Mix (lane 2) served as a control for spontaneous RNA hybridization, while N_WT (lane 4) represented the fully hybridized state. Additional almost complete RNA annealing was observed for N_WT_PM (lane 6) and N_BA.5_PM (lane 5). Partial hybridization was detectable for N_BA.5 (lane 3). **(D)** Boxplot representing the percentage of hybridized dsRNA. ssRNA and dsRNA band intensities were analyzed using Fiji. Each boxplot contains two biological replicates of the chaperone assay. Each boxplot represents the interquartile range (IQR), with the median indicated by a horizontal line inside the box. The upper and lower whiskers extend to a maximum of 1.5 times above and below the upper and lower quartiles, respectively. The x-axis represents the respective N truncation protein, while the percentage of dsRNA is indicated on the y-axis. Except for N_BA.5, each protein displayed a significant enhancement in RNA hybridization relative to the RNA mix control. The difference between N_BA.5 and the other proteins appears not significant. Non-significant comparisons are excluded in the illustration. Statistical analysis was performed by applying a t-test using the Benjamini-Hochberg (BH) procedure. 'n.s.' = 0.05 < p; '*' = 0.05 <= p >0.01; '**' = 0.01 <= p > 0.001; '***' = 0.001 <= p > 0.0001; '****' = 0.0001 <= p.

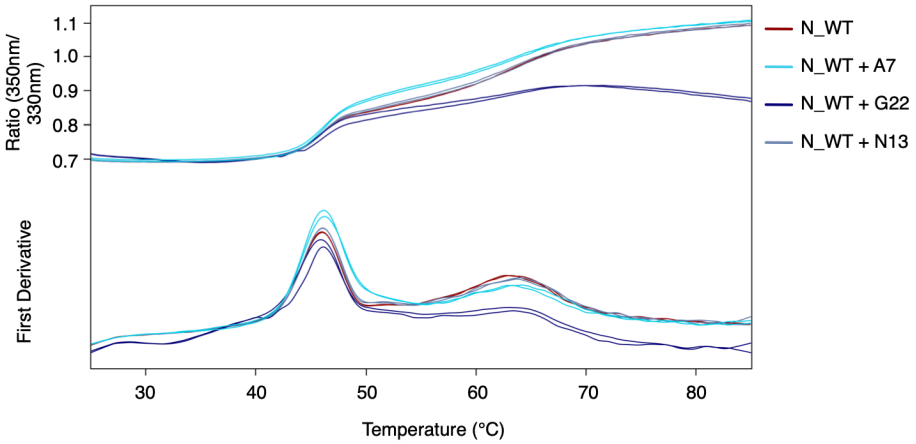

Supplementary Figure 7: Impact of N-RNA LLPS inhibitors on N protein stability

The stability of N_WT was elaborated by nanoDSF in presence of inhibitors impairing LLPS-mediated N-RNA interaction. A temperature range of 25 – 85°C was set. Inhibitors A7 (light blue), G22 (dark blue) and N13 (purple) appear to have only minor effect on the RBD and the CTD of N_WT (dark red). The overall protein integrity persisted in presence of the inhibitors.

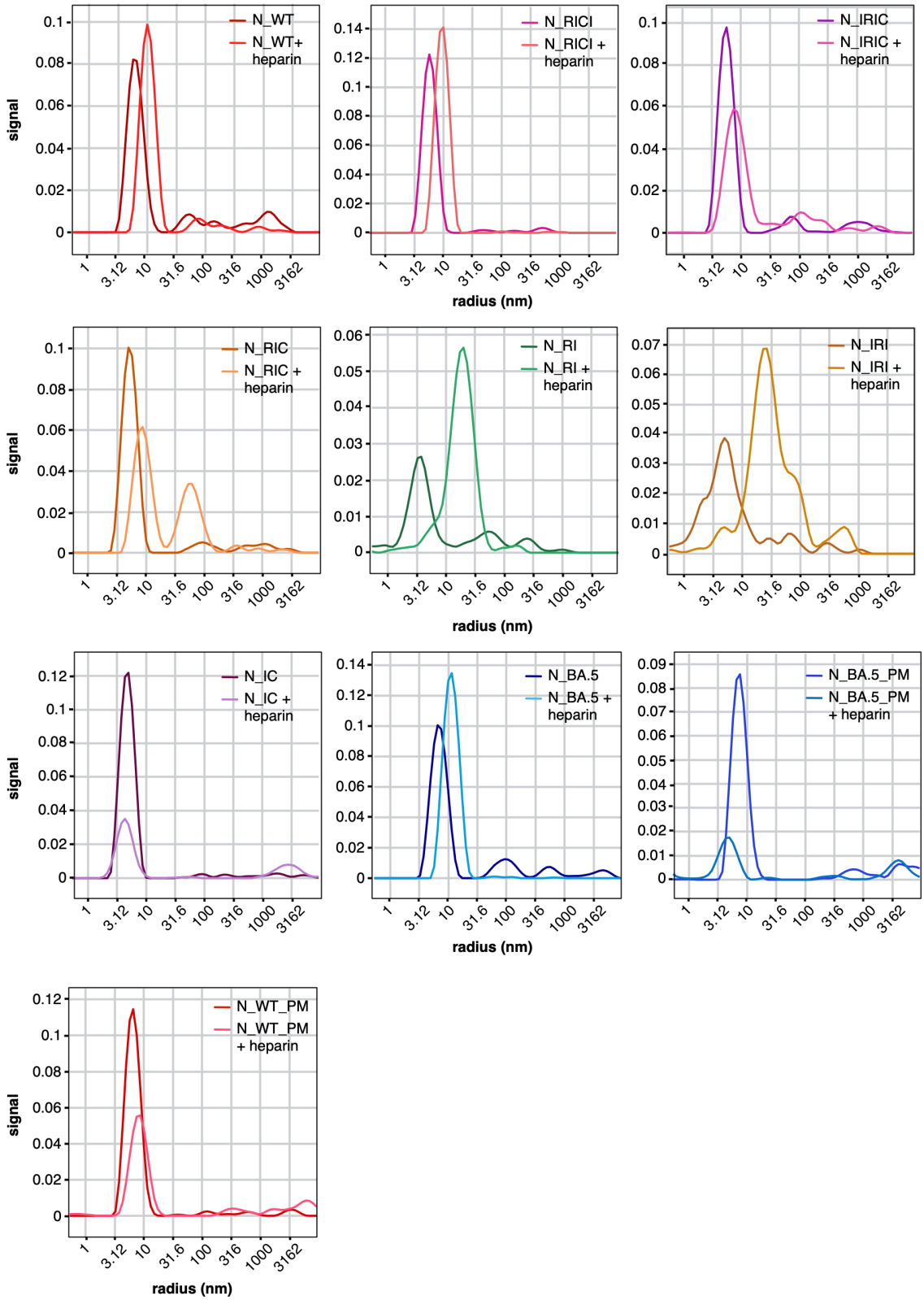

Supplementary Figure 8: DLS measurements of N (truncation) proteins with heparin

Protein particle sizes were assessed by dynamic light scattering (DLS). For this, 10 µM of protein were mixed with 5 µM of heparin (H) in assay buffer (50 mM HEPES pH 7.4, 100 mM NaCl, 0.01% Pluronic F-127). Of each sample, 10 µl were filled into Prometheus High Sensitivity Capillaries (NanoTemper) and measurements were carried out at 100% laser intensity and 37°C. Size distribution within each capillary is depicted in the plots with the signal intensity indicated on the y-axis and the radius in nm on the x-axis. Protein alone is represented in darker color while the curve following addition of H is displayed in lighter color. Addition of H to the protein resulted in an increase in particle radius for most proteins.

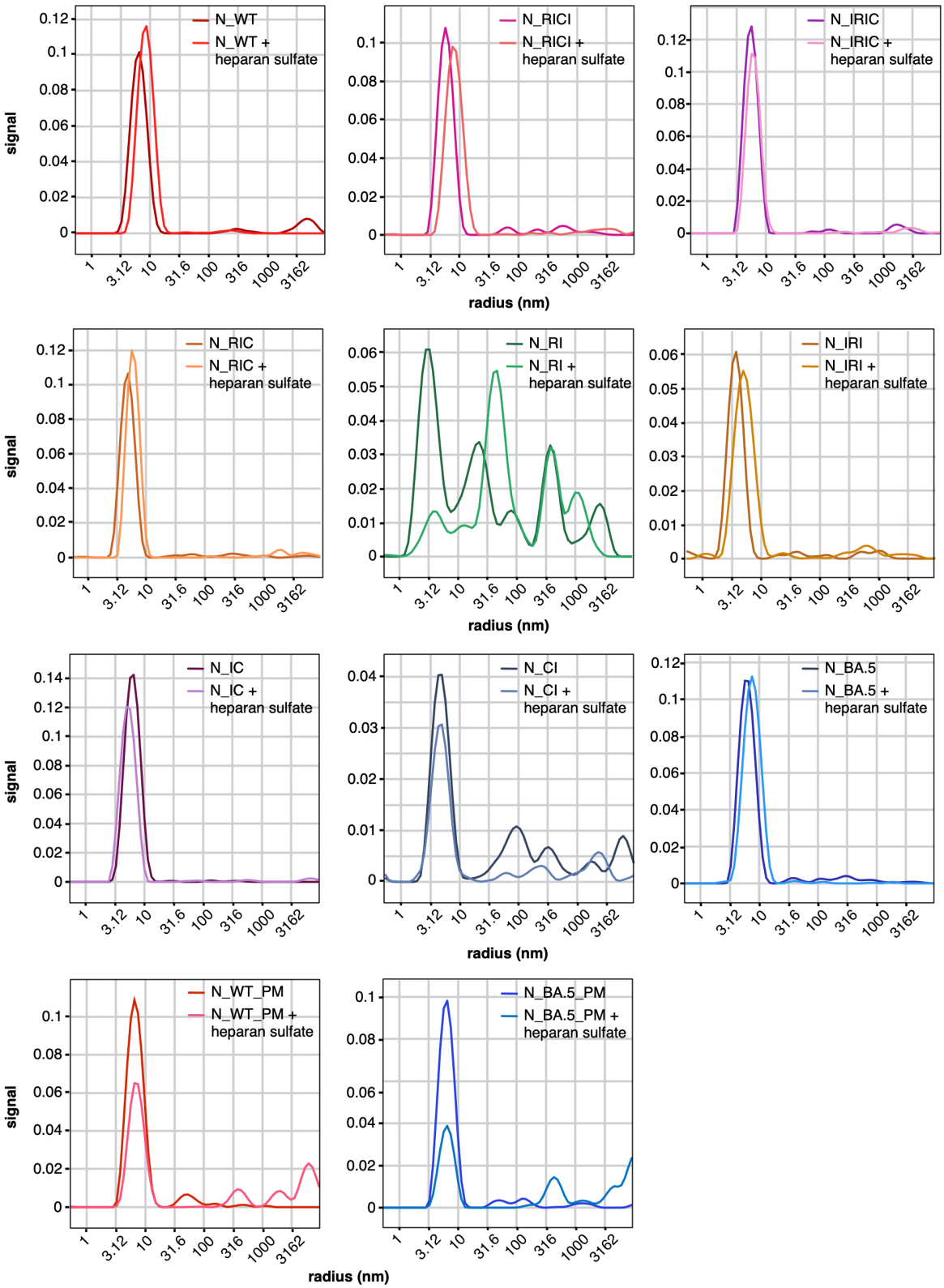

Supplementary Figure 9: DLS measurements of N (truncation) proteins with heparan sulfate

Protein particle sizes were assessed by dynamic light scattering (DLS). For this, 10 µM of protein were mixed with 5 µM of heparan sulfate (HS) in assay buffer (50 mM HEPES pH 7.4, 100 mM NaCl, 0.01% Pluronic F-127). Of each sample, 10 µl were filled into Prometheus High Sensitivity Capillaries (NanoTemper) and measurements were carried out at 100% laser intensity and 37°C. Size distribution within each capillary is depicted in the plots with the signal intensity indicated on the y-axis and the radius in nm on the x-axis. Protein alone is represented in darker color while the curve following addition of HS is displayed in lighter color. Addition of HS to the protein resulted in an increase in particle radius for most proteins.

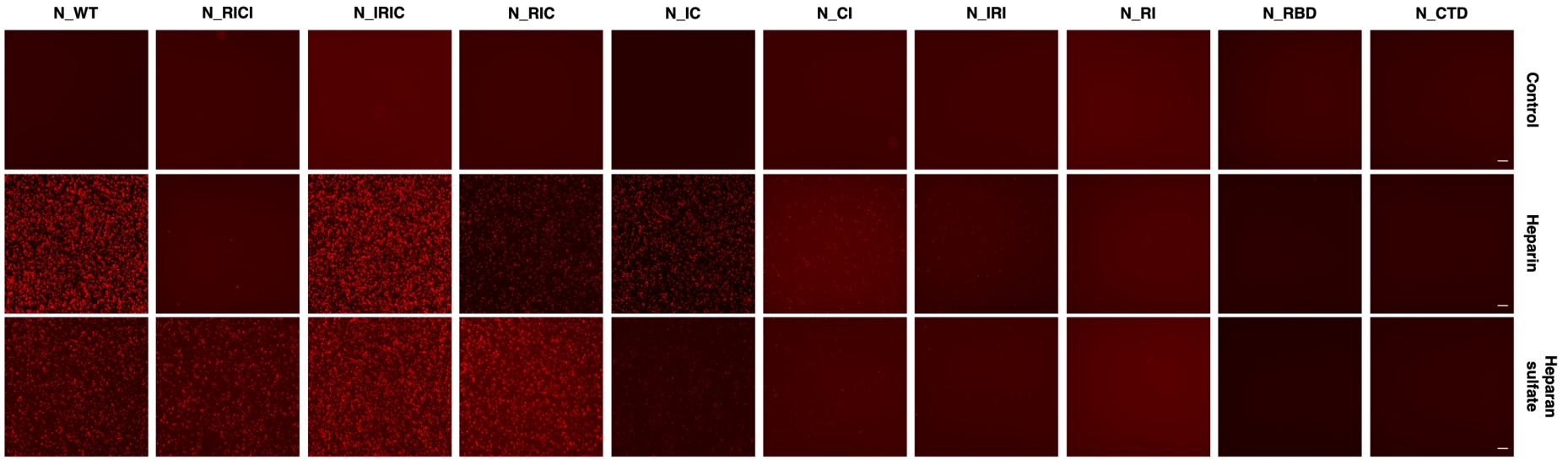

Supplementary Figure 10: LLPS properties of N truncation proteins with heparin and heparan sulfate

N truncation proteins were analyzed regarding their ability to form droplet in *in vitro* LLPS. To conduct this, a constant concentration of 500 nM N protein (with a ratio of 1:4 of 647-labeled to unlabeled N protein) was mixed with either 50 nM heparin (H) or 100 nM heparan sulfate (HS) in a total volume of 12 µl 1x LLPS buffer (50 mM HEPES pH 7.4, 100 mM NaCl, 0.01% Pluronic F-127). The 647-labeled protein, without the addition of H/HS, served as a control. Droplet formation was visualized using fluorescent microscopy (Keyence BZ-X800) with the Cy5 filter at 40x magnification (BZ-PF40LP Plan Fluorite 40X LD PH, Keyence). In case of N_WT, droplet formation was stronger induced with H than HS. This trend was observed for most N truncation proteins. N_RICI did not exhibit droplet formation with H but did so with HS. In contrast, N_CI displayed efficient LLPS with H but showed weaker interaction with HS. N_CI, N_IRI displayed only weak interaction with both H and HS. No droplet formation was detectable for N_RI, N_RBD, and N_CTD. Scale bar = 25 µm.

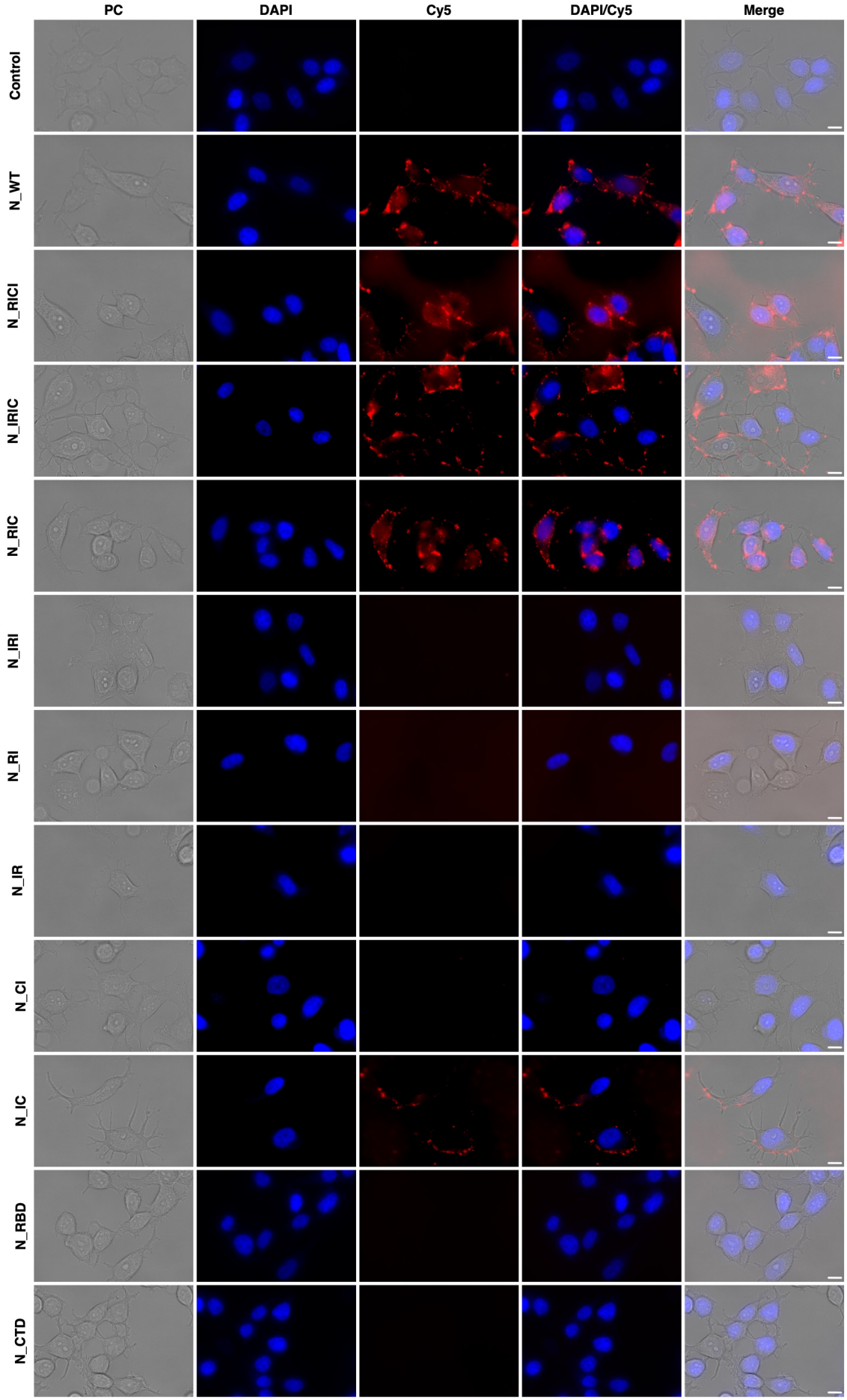

Supplementary Figure 11: Immunostaining of MCF-7 cells with N truncation proteins

Immunofluorescence images depict MCF-7 cells treated with 647-labeled N truncation proteins. The cells were exposed to a total of 500 nM of each 647-labeled protein for 20 min at 37°C with 5% CO_2. Following treatment, cells were fixed using 4% PFA and the cell nuclei were stained with DAPI (5 µg/ml). Fluorescent signals were visualized using fluorescent microscopy (Keyence BZ X-800) with the 100X Oil objective (Keyence, BZ-PA100). The images include phase contrast (PC), individual views of the DAPI and Cy5 channels, as well as the merged DAPI/Cy5 and total merged images. N_WT, N_RICI, N_IRIC, N_RIC and N_IC exhibited a 647-N protein signal on the cell surface. The remaining N truncation proteins did not exhibit a signal on the cell surface. Untreated cells stained with DAPI were included as a control. Scale bar = 25 µm.

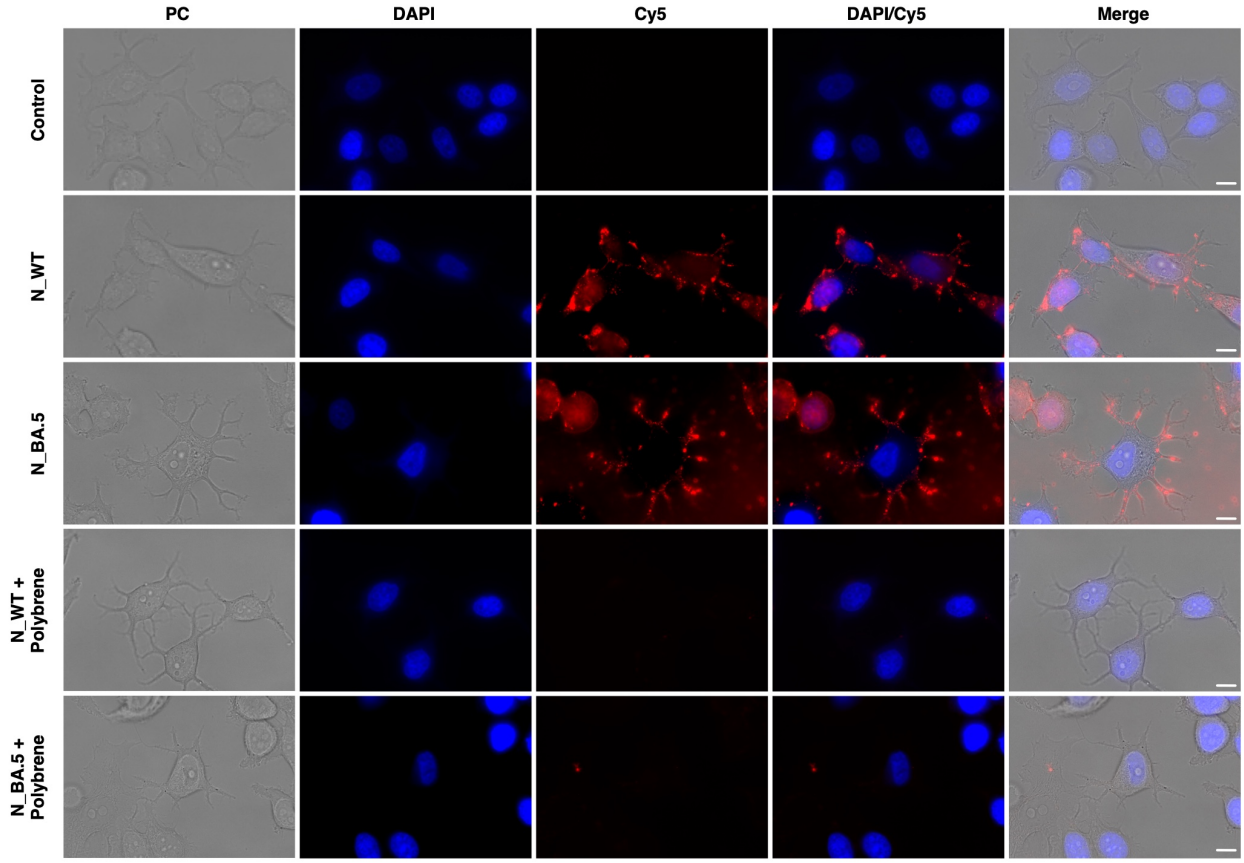

Supplementary Figure 12: Polybrene treatment of MCF-7 cells inhibits binding of the N protein to the cell surface

Immunofluorescence images of untreated and polybrene treated MCF-7 cells. For polybrene treated cells, polybrene was added at a concentration of 10 µg/ml and incubated with the cells for 1h at 37°C, 5% CO_2. Afterwards, MCF-7 cells were incubated with a total of 500 nM of each 647-labeled N_WT and N_BA.5 for 20 min at 37°C, 5% CO_2. Following incubation, cells were fixed with 4% PFA and the cell nuclei were stained with DAPI (5 µg/ml). Fluorescent signals were visualized by fluorescent microscopy (Keyence BZ X-800) with the 100X Oil objective (Keyence, BZ-PA100). The images include phase contrast (PC), individual views of the DAPI and Cy5 channels as well as the merged DAPI/Cy5 and total merged images. Polybrene treatment resulted in the inhibition of binding of both N_WT and N_BA.5 proteins to the cell surface, as evidenced by the absence of detectable signals in the treated cells. Conversely, untreated cells displayed a clear fluorescent signal indicating the presence of bound N proteins. Control images of untreaded cells stained with DAPI were included as a control. Scale bar = 25 µm.

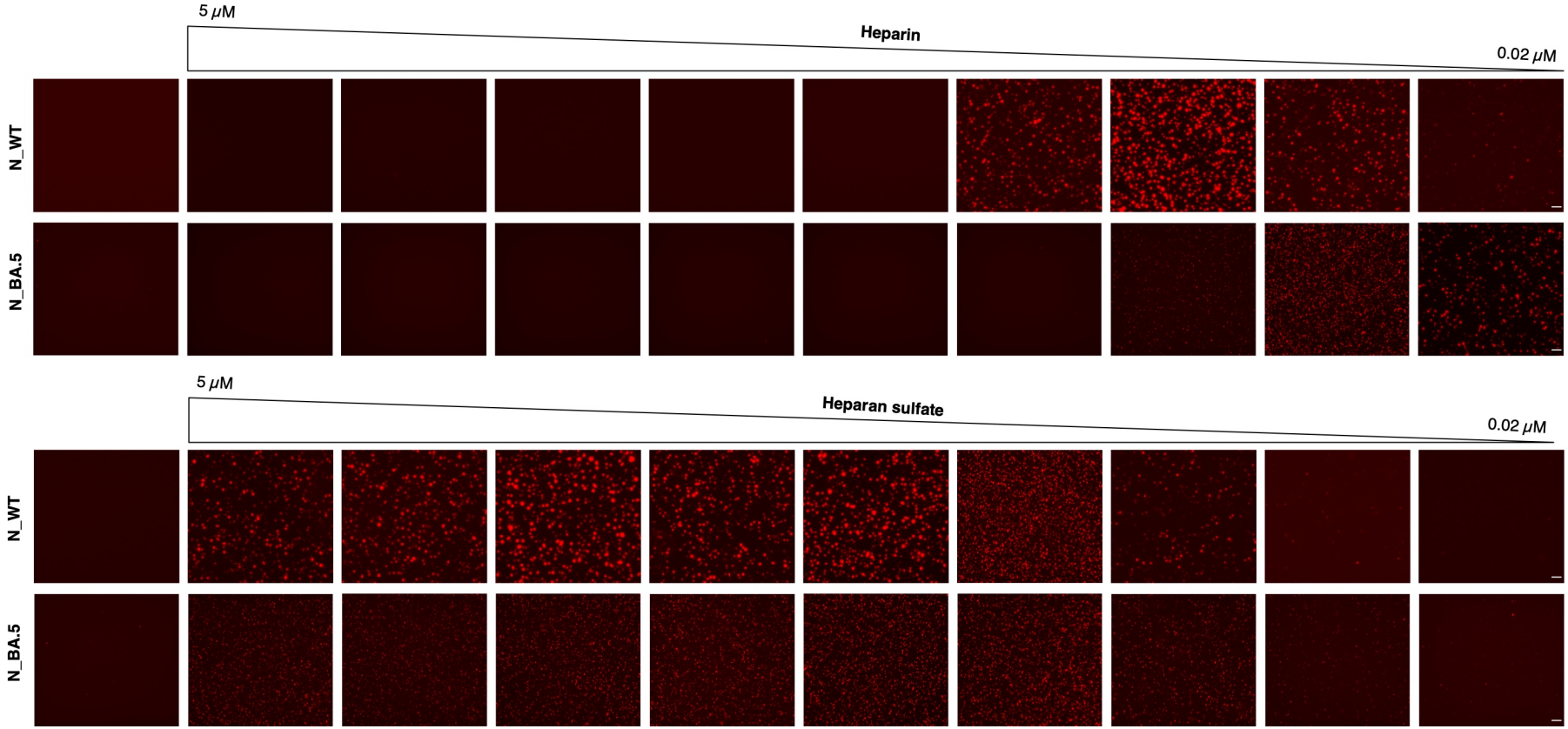

Supplementary Figure 13: Comparative LLPS titration for Wuhan and Omicron BA.5 N protein with heparin and heparan sulfate

The figure presents the results of the analysis conducted to assess the droplet formation capabilities of N_WT and N_BA.5 proteins in in vitro LLPS. To perform this analysis, a constant concentration of 500 nM N protein (with a ratio of 647-labeled to unlabeled N protein of 1:4) was mixed with increasing concentrations of heparin (H) and heparan sulfate (HS) ranging from 0.02 to 5 μM. These mixtures were prepared in a total volume of 12 μl of 1x LLPS buffer (composed of 50 mM HEPES pH 7.4, 100 mM NaCl, and 0.01% Pluronic F-127). Controls were established using the 647-labeled proteins without the addition of H/HS.
Observation of droplet formation was conducted using fluorescent microscopy (Keyence BZ-X800) with the Cy5 filter at 40x magnification (BZ-PF40LP Plan Fluorite 40X LD PH, Keyence). The results indicate that both proteins exhibited droplet formation, with N_BA.5 displaying a weaker overall signal compared to N_WT. Notably, droplet formation occurred over a broader concentration range for HS (0.08 - 5 μM) compared to H (0.04 – 0.16 μM) for both proteins. Scale bar = 25 μm.

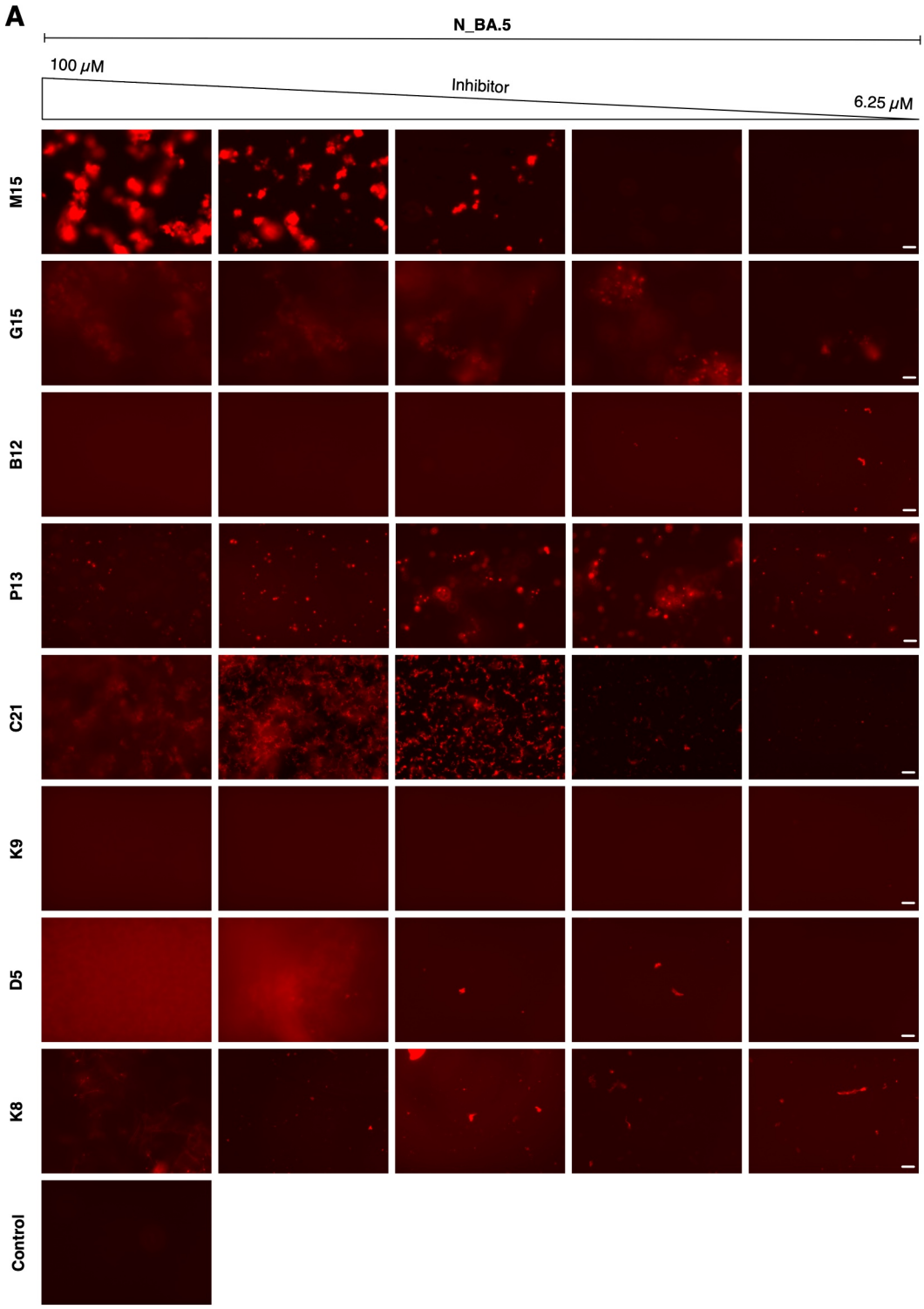
A
N_BA.5
100 μM
Inhibitor
6.25 μM
M15
G15
B12
P13
C21
K9
D5
K8
Control

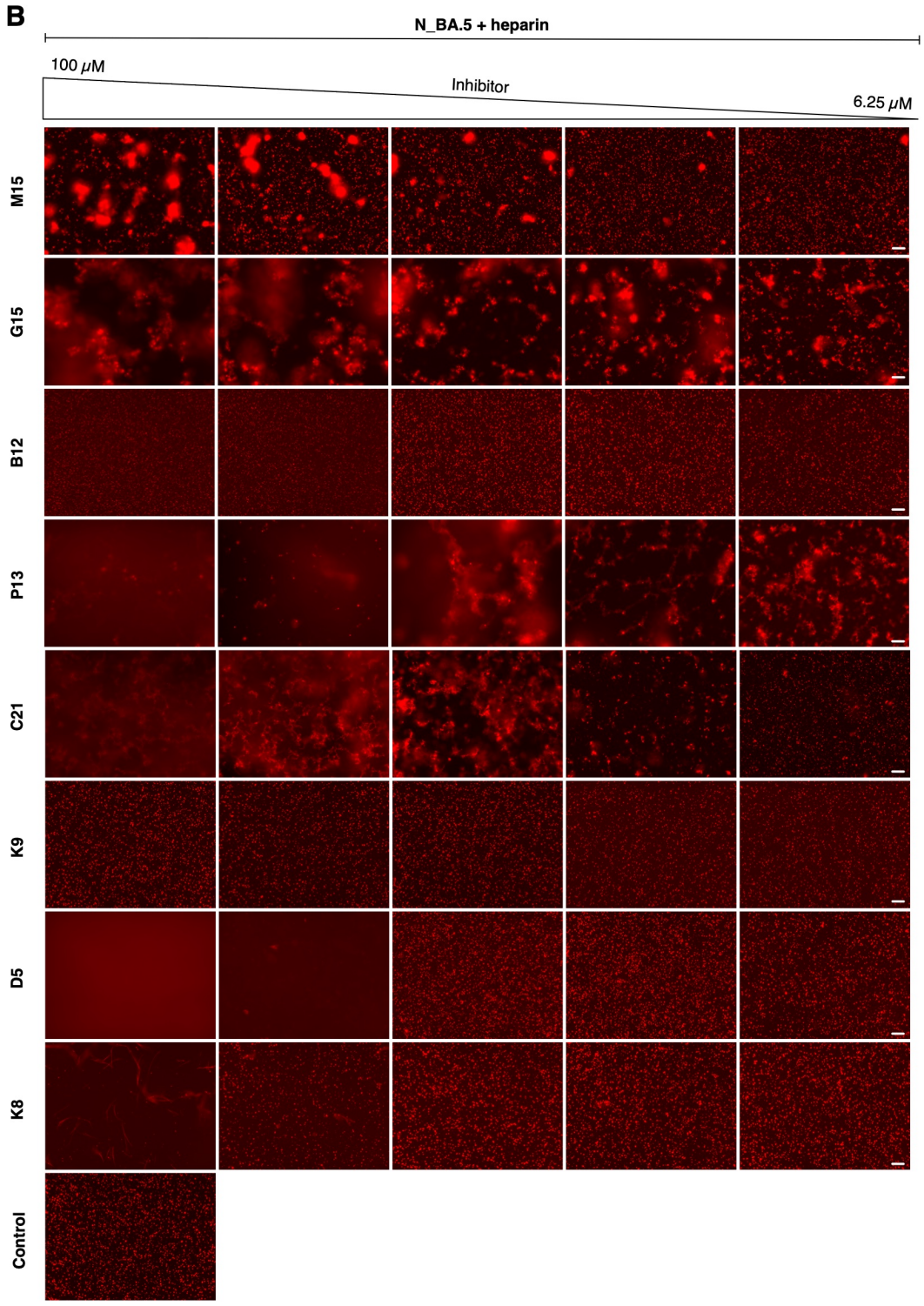
B
N_BA.5 + heparin
100 μM
Inhibitor
6.25 μM
M15
G15
B12
P13
C21
K9
D5
K8
Control

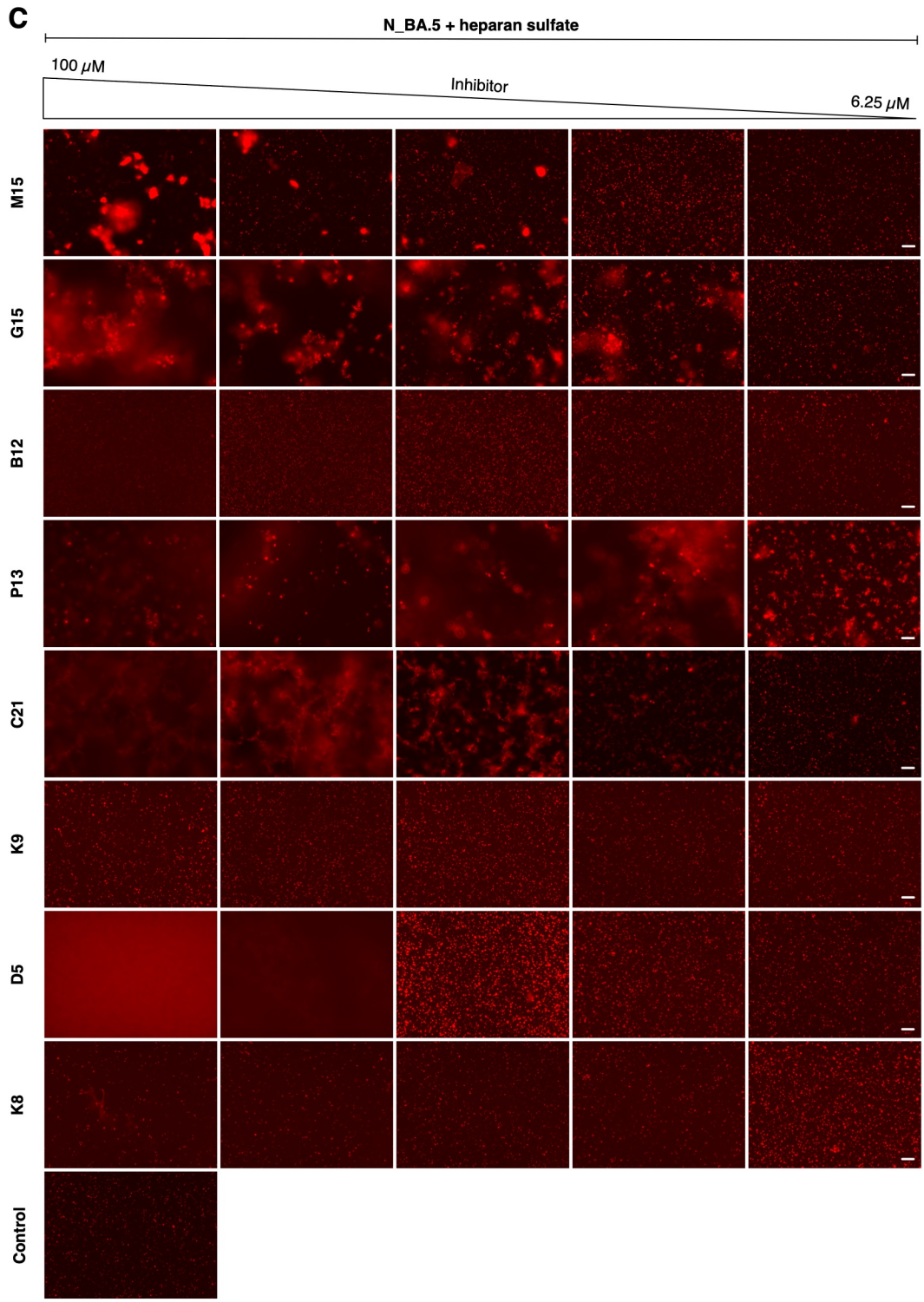

Supplementary Figure 14: Impact of LLPS inhibitors on the interaction of the Omicron BA.5 N protein with heparin and heparan sulfate

Positive hit inhibitors of a 2,500-compound library screen targeting N_BA.5 H/HS LLPS-mediated interaction were evaluated for their phase separation inhibition capabilities on a small scale. The inhibitors tested include M15 (NVP-BHG712), G15 (SU11274), B12 (Fenticonazole Nitrate), P13 (SGI-1027), C21 (Eltrombopag Olamine), K9 (RAF265), D5 (Nelfinavir Mesylate), and K8(Chloroquinaldol). Inhibitors were added to the samples at concentrations ranging from 6.25 – 100 μM. Each well contained a final DMSO concentration of 1% in 50 mM HEPES pH 7.4, 100 mM NaCl, 0.01% Pluronic. Samples were then incubated for 2h at RT prior to visualization with the Cy5 filter of the Keyence BZ-X800 fluorescent microscope at 40x magnification (BZ-PF40L Plan Fluorite 40X LD PH, Keyence). Scale bars = 25 μm.

(A) Effect of inhibitors on N_BA.5 without H/HS. Samples containing 500 nM 647-labeled N_BA.5. (with a labeled to unlabeled ratio of 1:4) were incubated with increasing concentrations of the inhibitors. A control sample containing

647-labeled N_BA.5 alone was included. Most inhibitors induced protein aggregation, except for B12, K9, and D5.
(B) Effect of inhibitors on droplet formation of N_BA.5 with H. Samples containing 500 nM 647-labeled N_BA.5 (with a labeled to unlabeled ratio of 1:4) were incubated with 50 nM H and increasing concentrations of the inhibitors. A control sample containing 647-labeled N_BA.5 with H alone was included. Droplet formation was still observed in most cases, except for G15, P13, and D5.
(C) Effect of inhibitors on droplet formation of N_BA.5 with HS. Samples containing 500 nM of 647-labeled N_BA.5 (with a labeled to unlabeled ratio of 1:4) were incubated with 100 nM HS and increasing concentrations of the inhibitors. A control sample containing N_BA.5 with HS alone was included. Droplet formation was observed in most cases, except for G15, P13, and D5.

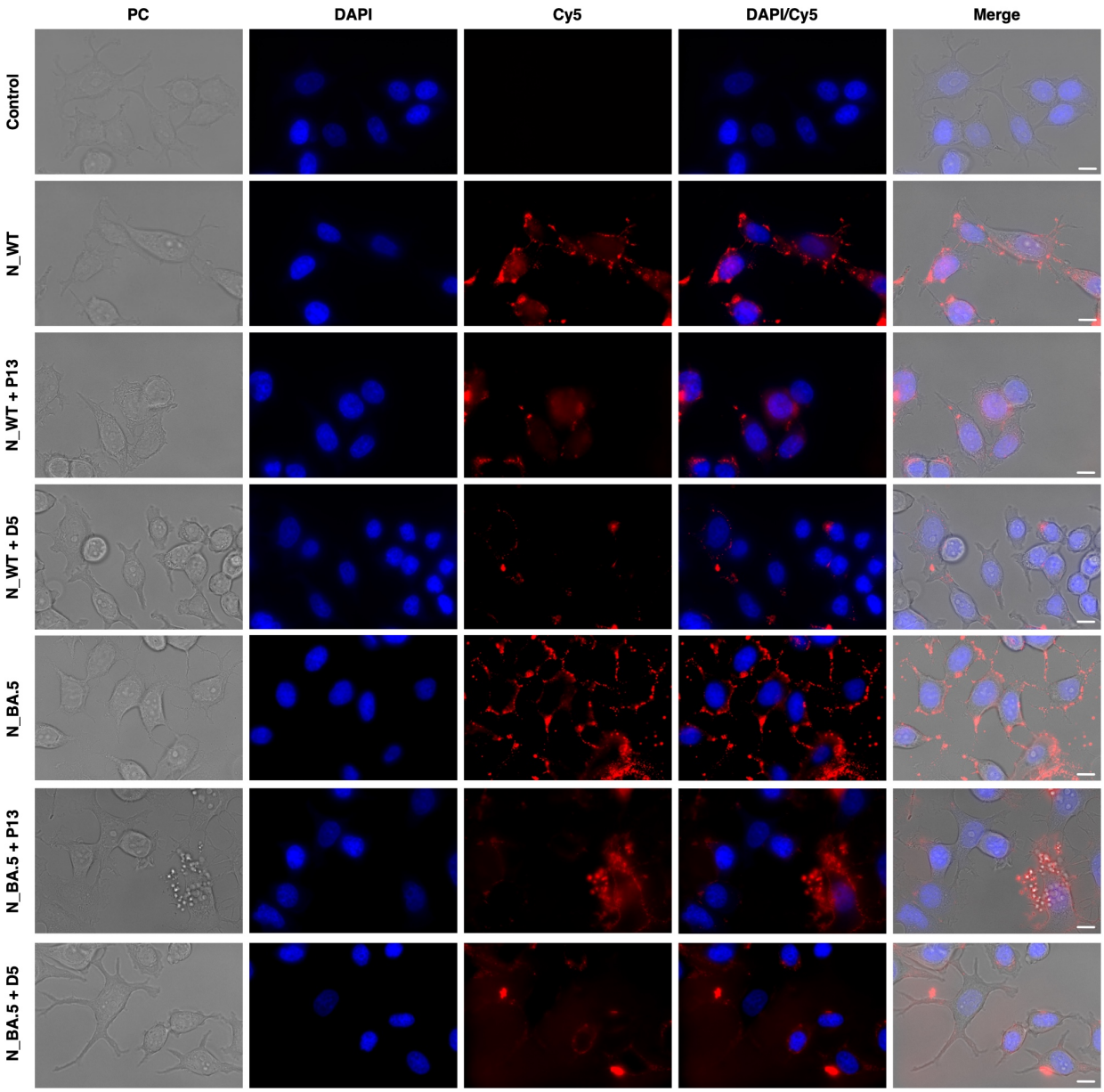

Supplementary Figure 15: Influence of LLPS inhibitors D5 and P13 on cell surface binding abilities of Wuhan and Omicron BA.5 N proteins

MCF-7 cells were treated with 500 nM of each 647-labeled N_WT and N_BA.5, along with 100 μM of inhibitors D5 and P13, for 20 min at 37°C under 5% CO_2. Following incubation, cells were fixed with 4% PFA and the cell nuclei were stained with DAPI (5 μg/ml). Fluorescent signals were visualized by fluorescent microscopy (Keyence BZ X-800) with the 100X Oil objective (Keyence, BZ-PA100). The images include phase contrast (PC), individual views of the DAPI and Cy5 channels as well as the merged DAPI/Cy5 and total merged images. Both inhibitors were observed to reduce the Cy5 signal for N_WT and to a lesser extent for N_BA.5. In combination with N_BA.5, P13 seemed to induce cell death. Untreated cells stained with DAPI served as a control. Scale bar = 25 μm.

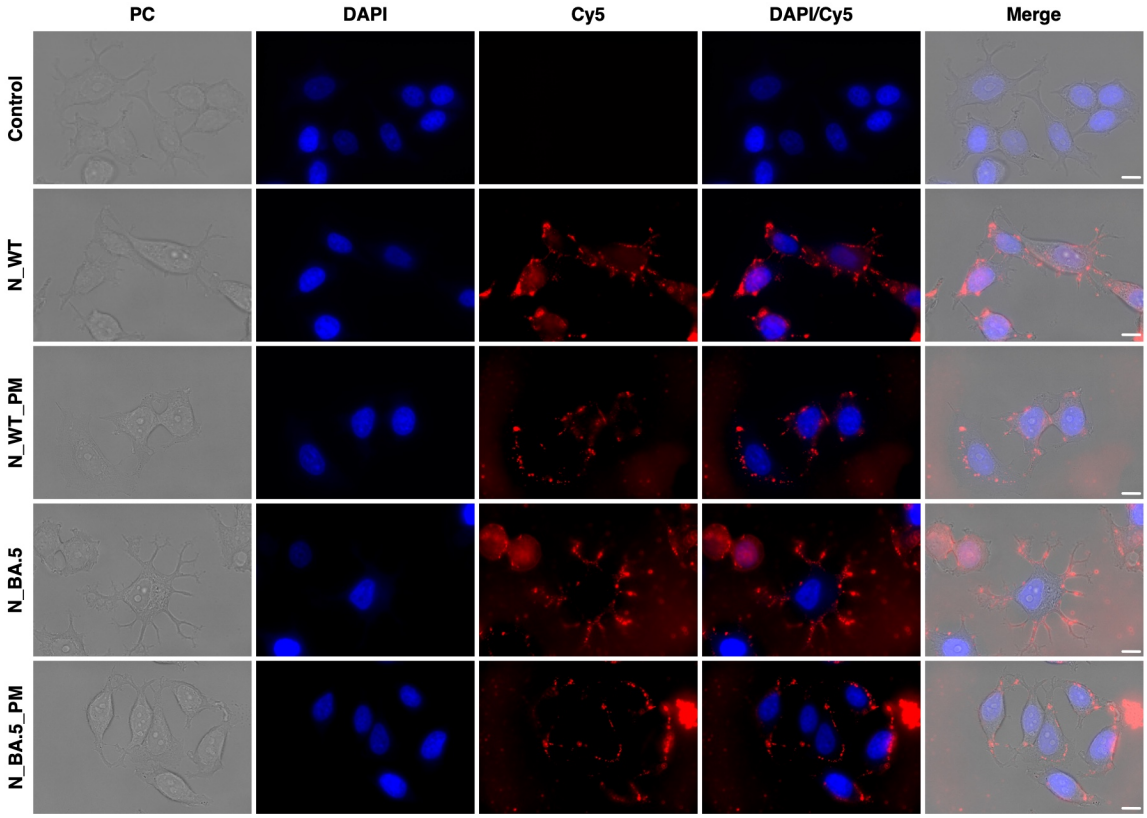

Supplementary Figure 16: Immunostaining of pseudo-phosphorylated N proteins on MCF-7 cells

MCF-7 cells were treated with a total of 500 nM of 647-labeled N_WT, N_WT_PM, N_BA.5, and N_BA.5_PM for 20 min at 37°C under 5% CO_2. Following incubation, cells were fixed with 4% PFA and the cell nuclei were stained with DAPI (5 μg/ml). Fluorescent signals were visualized by fluorescent microscopy (Keyence BZ X-800) with the 100X Oil objective (Keyence, BZ-PA100). The images include phase contrast (PC), individual views of the DAPI and Cy5 channels as well as the merged DAPI/Cy5 and total merged images. Pseudo-phosphorylation of the proteins did not impair the cell surface binding ability of the proteins. Untreated cells stained with DAPI served as a control. Scale bar = 25 μm.

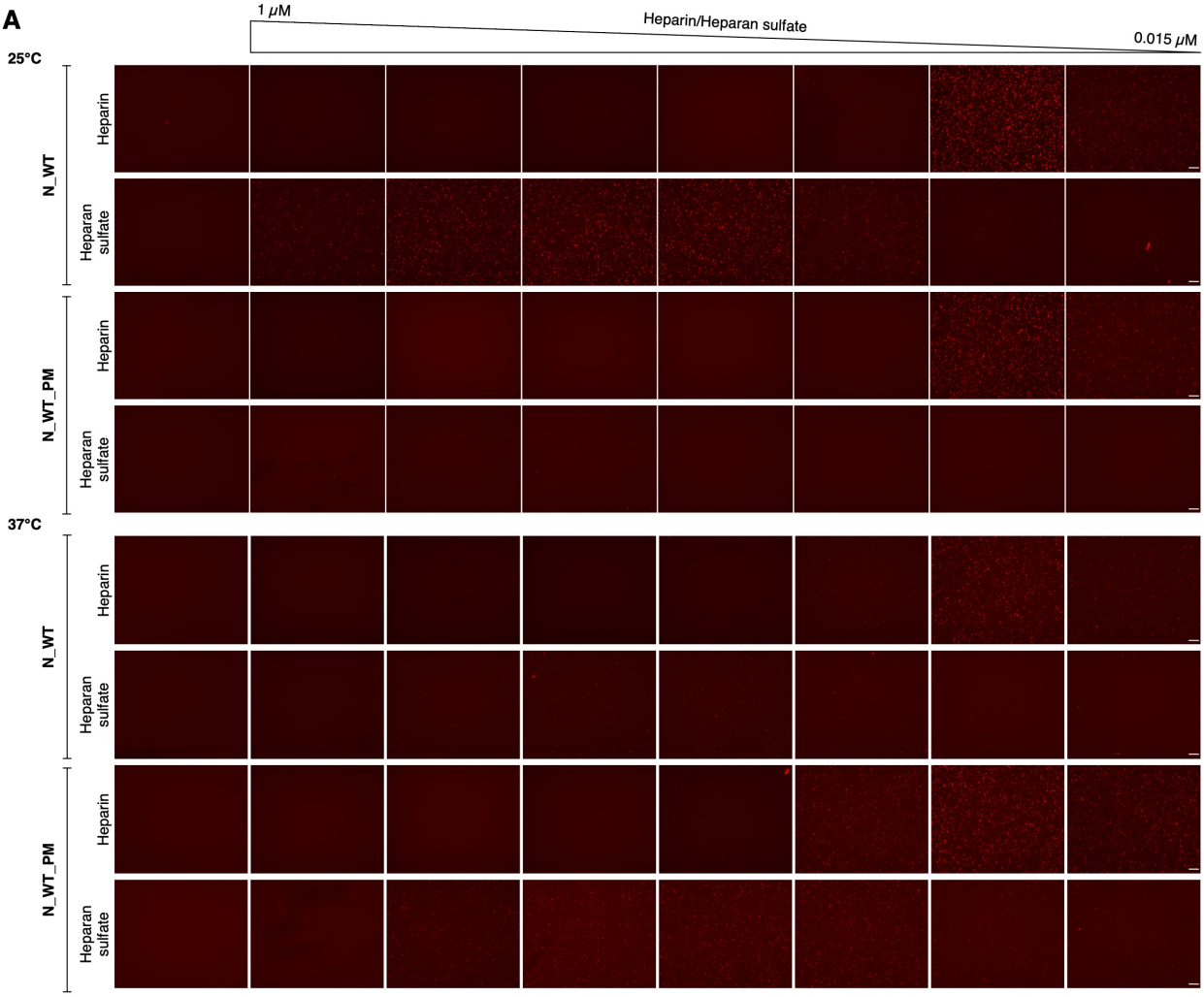
A
1 μM
Heparin/Heparan sulfate
0.015 μM
25°C
N_WT
Heparin
Heparan sulfate
N_WT_PM
Heparin
Heparan sulfate
37°C
N_WT
Heparin
Heparan sulfate
N_WT_PM
Heparin
Heparan sulfate

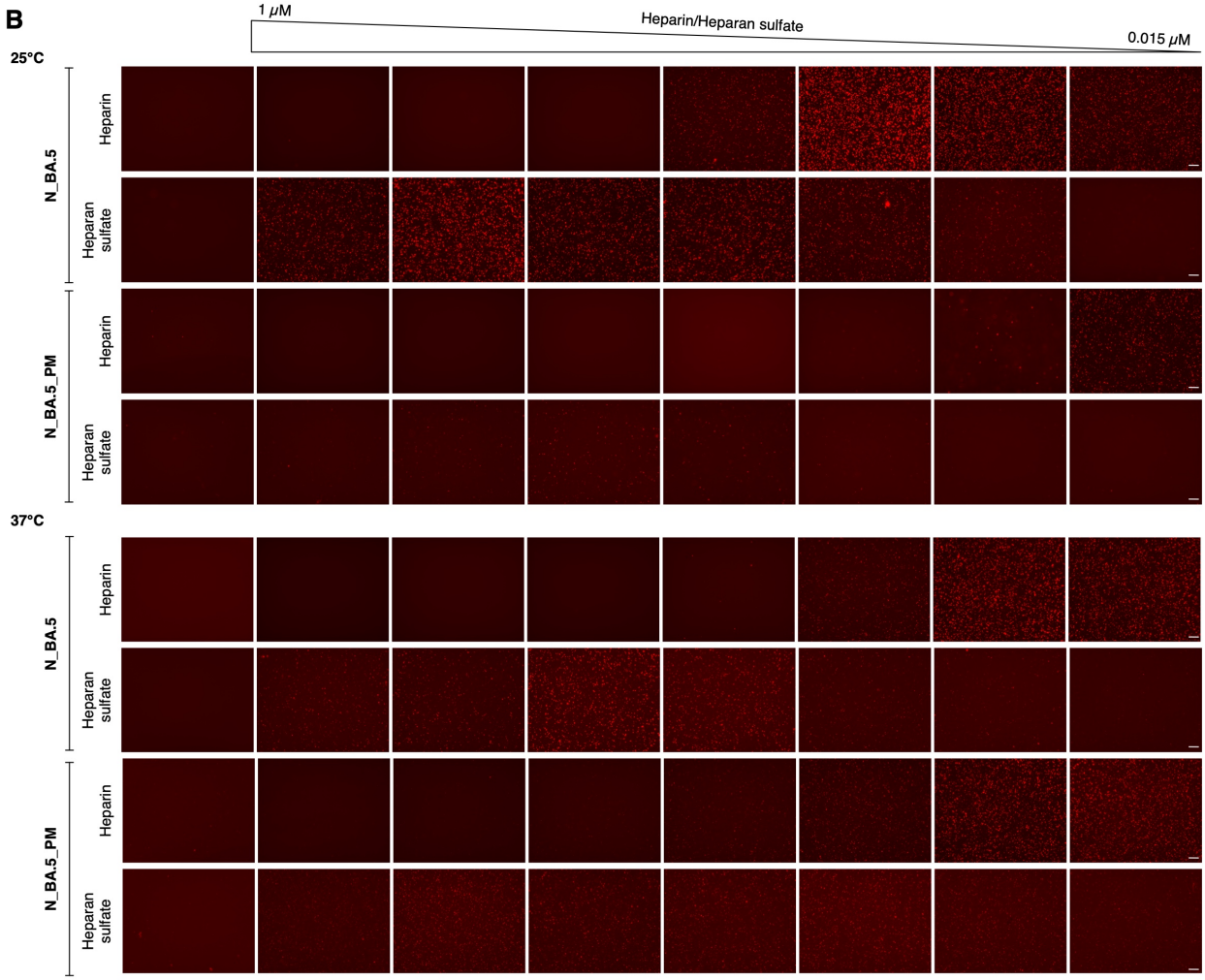

Supplementary Figure 17: Analysis of LLPS capabilities of unmodified and pseudo-phosphorylated Wuhan and Omicron BA.5 N proteins with heparin and heparan sulfate

N_WT, N_WT_PM **(A)**, N_BA.5 and N_BA.5_PM **(B)** were analyzed regarding their droplet formation capabilities in *in vitro* LLPS conducted at temperatures of 25°C (top) and 37°C (bottom). For this, a constant concentration of 500 nM 647-labeled N protein (with a ratio of labeled to unlabeled protein of 1:4) was mixed with increasing concentrations of heparin (H) and heparan sulfate (HS) ranging from 0.015 – 1 μM in a total volume of 12 μl 1x LLPS buffer (50 mM HEPES pH 7.4, 100 mM NaCl, 0.01% Pluronic F-127). The 647-labeled proteins, without the addition of H/HS, served as controls. Droplet formation was visualized using fluorescent microscopy (Keyence BZ-X800) with the Cy5 filter at 40x magnification (BZ-PF40LP Plan Fluorite 40X LD PH, Keyence). Results indicate that both N_WT_PM and N_BA.5_PM exhibited diminished droplet formation with H and HS at 25°ÄC, with slightly more droplets detected with H than with HS. At 37°C, the phosphomimetic N variants displayed more efficient phase separation. Droplet formation for N_WT decreased at 37°C. Scale bar = 25 μm.

11. Danksagung

An dieser Stelle möchte ich mich bei allen bedanken, die mich die letzten Jahre begleitet und maßgeblich zum Gelingen meiner Dissertation beigetragen haben.

Zuerst möchte ich mich bei meinem Doktorvater Prof. Gernot Längst bedanken. Danke, dass du mir die Möglichkeit gegeben hast nach meiner Masterarbeit auch die Doktorarbeit bei dir im Labor anzufertigen. Deine Unterstützung und die Freiheiten, die du mir in meiner Forschung gegeben hast, haben maßgeblich zu meiner persönlichen und fachlichen Weiterentwicklung beigetragen. Danke, dass du für alle Fragen und Probleme jederzeit ein offenes Ohr hattest und ich immer direkt auf dich zukommen konnte!

Ein weiterer Dank gilt Prof. Ralf Wagner unter anderem für die Unterstützung als Mentor, für die Kollaboration innerhalb des Projekts und natürlich für die Übernahme des Zweitgutachtens. Des Weiteren möchte ich mich bei Prof. Peter Becker für die Unterstützung als Mentor in den letzten Jahren bedanken.
Ein herzliches Dankeschön gilt Antonia Senninger, Silvia Materna-Reichelt, Dr. Nataša Stojanović Gužvić, Durdam Das, Prof. Harald Wodrich und Nicolas Landrein für die großartige Zusammenarbeit und ihre individuellen Beiträge zu verschiedenen Teilen des Projekts.

Danke an alle meine Kolleginnen und Kollegen am Lehrstuhl BC III und besonders im Längst Lab. Ein großes Danke an Elisabeth Silberhorn und Regina Gröbner-Ferreira für die Unterstützung bei jeglichen Fragen und Experimenten im Labor. Ein riesiges Dankeschön geht an meine PhD-Leidensgenossen Nora, Fabi und Simon. Ohne euch wären die letzten Jahre bei Weitem nicht so lustig gewesen! Fabi, dir danke ich besonders für die unzähligen lustigen Kaffeepausen, Meme-Battles, R-Unterrichtsstunden und all die anderen Momente, die selbst die schlechtesten Tage gut und die guten Tage im Labor noch besser gemacht haben.